Analysis and numerical simulation of long-term creep tests on concrete beams

Tim Van Mullem

Supervisors: Prof. dr. ir. Robby Caspeele, Prof. dr. ir. Luc Taerwe
Counsellors: Ir. Pieterjan Criel, Nicky Reybrouck

Master's dissertation submitted in order to obtain the academic degree of
Master of Science in Civil Engineering

Department of Structural Engineering
Chair: Prof. dr. ir. Luc Taerwe
Faculty of Engineering and Architecture
Academic year 2015-2016

UNIVERSITEIT
GENT

Analysis and numerical simulation of long-term creep tests on concrete beams

Tim Van Mullem

Supervisors: Prof. dr. ir. Robby Caspeele, Prof. dr. ir. Luc Taerwe
Counsellors: Ir. Pieterjan Criel, Nicky Reybrouck

Master's dissertation submitted in order to obtain the academic degree of
Master of Science in Civil Engineering

Department of Structural Engineering
Chair: Prof. dr. ir. Luc Taerwe
Faculty of Engineering and Architecture
Academic year 2015-2016

UNIVERSITEIT
GENT

The true path to success is through the fear of failure. If you aren't scared enough of failing, you are unlikely to succeed.

Shah Rukh Khan

Acknowledgements

This master dissertation is the crown piece of five years of intensive studying, hard work, frustration, unique opportunities, technical jokes, moments of inspiration, moments of desperation,… , or as it is more commonly known: five years of engineering education.

The subject of this master dissertation is the time-dependent deformation of concrete. This is something that all civil engineers are familiar with. However, the subject is so complex, that what is taught during the lectures should be considered as a “version for dummies”. It is this what drew me to the subject: everyone has heard of the matter, yet no one knows the details.

I would like to take the time to thank my supervisors prof. dr. ir. Robby Caspeele and prof. dr. ir. Luc Taerwe for entrusting me with an unique and invaluable dataset. Particularly, I would like to extend my appreciation to prof. dr. ir. Robby Caspeele for the reflective discussions and the fast replies to posed questions. Your personal approach was appreciated greatly. I would also like to specifically acknowledge Prof. dr. ir. Luc Taerwe for the interesting remarks suggested during a preliminary presentation of the results.

Towards my counsellors, ir. Nicky Reybrouck and ir. Pieterjan Criel, I would like to extend the deepest gratitude; without your help this dissertation would not be what it is now, if it would be finished at all. Nicky, thank you for the many occasion on which you helped and guided my through the computer code when I couldn’t see the forest for its trees . Pieterjan, thank you for the philosophical discussions and for cheering me up and keeping me sane.

I’m also very grateful for having such amazing friends who entertained me and were there for me when I needed them most. Some of them are so awesome they deserve a recognition here. Anna, thank you for guiding me through the subtleties of the English language and for being so kind and understanding. Christophe, thank you for your unwavering faith in me and for being my coach in the gym where you motivated me to get to the end of numerous intensive workouts. Karen, thank you for the many hours of mutual misery in the library, your presence made everything much more bearable. I also credit you for the amazing quote I stole, which can be found at the end of this work.

Last but not least, I would like to acknowledge my family who has supported me from the moment I was born. The teachings of my family, and especially my parents, have indubitably made me the person I am today. Mom, thank you for always being there for me and being such a wonderful mother. Dad, thank you for helping me out in the hours of need and for being an incredible dad.

7th May 2016

Overview

Master's dissertation submitted in order to obtain the academic degree of Master of Science in Civil Engineering

Title: Analysis and numerical simulations of long-term creep tests on concrete beams
Author: Tim Van Mullem
Supervisor: Prof. dr. ir. Robby Caspeele, Prof. dr. ir. Luc Taerwe
Counsellors: ir. Pieterjan Criel, ir. Nicky Reybrouck
Department: Department of Structural Engineering
Chairman: Prof. dr. ir. Luc Taerwe

Faculty of Engineering and Architecture
Ghent University
Academic year 2015-2016

Summary

Concrete is an aging linear viscoelastic material; under sustained loading it will have a time-dependent behaviour, which is caused by shrinkage and creep. Different material models have been formulated in literature to predict the creep and shrinkage deformations. In this master dissertation the predictions of the time-dependent deformations of reinforced and prestressed beams were compared against measurements.

These predictions were calculated with the use of a cross-sectional calculation method which employs the age-adjusted effective modulus. With regard to the age-adjusted effective modulus the difference between a calculated and a constant aging coefficient was considered. Since the stress in the reinforced beams was far above the service level, the effectiveness of a method taking into account the effects of nonlinear creep was studied.

For the prestressed beams the influence of a non-centric placing of the post-tensioning strands was examined. Additionally, a simplified analysis was performed in order to investigate the effect of the relaxation of the prestressing steel.

Keywords

Reinforced and prestressed beams, long-term creep test, age-adjusted effective modulus, creep and shrinkage models

Analysis and numerical simulation of long-term creep tests on concrete beams

Tim Van Mullem

Supervisor(s): Prof. dr. ir. Robby Caspeele, Prof. dr. ir. Luc Taerwe, ir. Pieterjan Criel, ir. Nicky Reybrouck

***Abstract*- The time-dependent deformations of reinforced and prestressed beams were predicted according to six different material models: CEB-FIP Model Code 1990-1999 (MC90-99), FIP Model Code 2010 (MC2010), Eurocode 2 (EC2), Bažant's and Baweja's model B3 (B3), Gardner Lockmann 2000 (GL 2000), and ACI 209 (ACI). These predictions were calculated with the use of a cross-sectional calculation method which employs the age-adjusted effective modulus. Using measurements obtained from an extensive research programme the accuracy of the predicted deformations was analysed.**

***Keywords*- Reinforced and prestressed beams, long-term creep test, age-adjusted effective modulus, creep and shrinkage models, nonlinear creep**

I. INTRODUCTION

Concrete is an aging linear viscoelastic material; under sustained loading it will have a time-dependent deformation caused by creep and shrinkage. Different material models have been proposed in literature to predict these. One of the main issues of these material models is that they have been calibrated on compression tests performed on small specimens without reinforcement. A large-scale analysis of the validity of these models for beams with practical dimensions is missing in literature. Another issue is that the material models are calibrated on data in the service stress range and thus do not take nonlinear creep into account.

Measurements which were available at the Magnel Laboratory for Concrete Research were used to analyse and compare the predictions according to different material models: MC90-99 [1], MC2010 [2], EC2 [3], B3 [4], GL 2000 [5], and ACI [6].

II. MATERIALS

The universities of Ghent, Brussels, Leuven, and Liège collaborated in a large scale research programme. The goal of this experimental investigation was to study the time-dependent behaviour of i.a. reinforced and prestressed beams under different levels of loading. Every university focused on beams with a specific cross-section and/or specific reinforcement ratio and/or specific degree of prestressing.

Each of the universities tested 12 reinforced beams: two beams in a static test at 28 days and ten beams in a long-term test between two and four years. Additionally, also eight prestressed beams were tested: two beams in a static test at 28 days and six beams in a long-term test between two and four years.

All the coarse aggregates, the sand, the cement, the reinforcement, and the prestressing steel were ordered at the same time and were then distributed over the four laboratories. The same concrete mixture was used for all reinforced beams. A different mixture was used for all the prestressed beams.

Figure 1 shows the cross-section of the reinforced beams which were tested at Ghent University. The reinforced beams all had a height of 280 mm and a width of 150 mm.

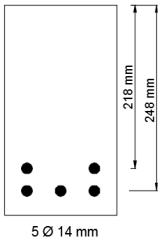

Figure 1. Cross-section of reinforced beams tested at Ghent University.

Figure 2 shows the cross-section of the I-shaped beams from Ghent University. These were prestressed at 7 or 14 days using six strands.

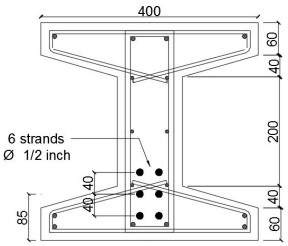

Figure 2. Cross-section of a pre-tensioned I-shaped beams.

The span of the reinforced beams was equal to 2.8 m. The span of the prestressed beams was 8.0 m. Both the reinforced beams and the prestressed beams were subjected to a long-term four point bending test. For the reinforced beams the point loads were placed at respectively one third and two thirds of the span. For the prestressed beams the point loads were placed one fourth of the span from the left and right support.

III. METHODS

The predictions of the time-dependent deformations were calculated using a cross-sectional method.

The instantaneous strain ε_0 and curvature ψ at a reference fibre 0 can be calculated by [7]:

$$\begin{bmatrix}\varepsilon_O\\ \psi\end{bmatrix} = \frac{1}{E_{ref}\cdot(A\cdot I - S^2)}\cdot\begin{bmatrix}I & -S\\ -S & A\end{bmatrix}\cdot\begin{bmatrix}N_{eq.}\\ M_{eq.}\end{bmatrix} \qquad (1)$$

with E_{ref} a reference modulus of elasticity which is taken equal to the modulus of elasticity of concrete measured at 28 days, $N_{eq.}$ and $M_{eq.}$ the equivalent normal force and moment on the cross-section taking into account the prestressing force, and with A, S, and I respectively: the transformed area of the cross-section, the transformed static moment about an axis through O, and the transformed moment of inertia about an axis through O.

Due to creep and shrinkage the strain and curvature will change over time. Assume that these deformations are restrained by an artificial axial force ΔN and an artificial moment ΔM applied in the reference point O. The changes of the strain and curvature can then be calculated using formula (1), by replacing $N_{eq.}$ and $M_{eq.}$ by ΔN and ΔM. Because the restraining forces are not applied immediately at full strength, E_{ref} needs to be replaced by the age-adjusted effective modulus $\overline{E_c}(t,t_0)$, and similarly A, S, and I need to be replaced by their age-adjusted counterpart. $\overline{E_c}(t,t_0)$ can be calculated according to [8]:

$$\overline{E_c}(t,t_0) = \frac{E_c(t_0)}{1+\chi(t,t_0)\cdot\varphi(t,t_0)} \qquad (2)$$

where $E_c(t_0)$ is the instantaneous modulus of elasticity at time of loading t_0, $\varphi(t,t_0)$ is the creep coefficient according to one of the material models and $\chi(t,t_0)$ is an aging coefficient.

The calculation of the aging coefficient is computationally intensive. Therefore, the aging coefficient was in a first instance assumed to be constant and equal to 0.8. The deflections were also computed using a calculated aging coefficient and it was observed that this had an almost unnoticeable influence on the results.

The prestressed beams remained uncracked, but all reinforced beams cracked under loading. From the moment the beams were cracked the strain and curvature were calculated using the principle of tension stiffening.

Once the strain and curvature in the reference fibre were known, the strain in any fibre of the cross-section could be calculated. The deflection of the beams was derived from the curvature over the length of the beam using the principle of elastic weights.

When the stresses become too high the creep becomes nonlinear. In order to take the nonlinearity into account, an equation based on EN 1992-1-1 [3] was used The linear creep coefficient $\varphi(\infty,t_0)$ is replaced by a nonlinear creep coefficient $\varphi_k(\infty,t_0)$:

$$\varphi_k(\infty,t_0) = \varphi(\infty,t_0)\cdot\exp(1.5\cdot(k_\sigma - 0.45)) \qquad (3)$$

in which k_σ is the stress-strength ratio $\sigma_c/f_{ck}(t_0)$, where σ_c is the compressive stress. This correction was only applied for the part of the cross-section which surpassed the limit value of $0.45f_{ck}(t_0)$, with $f_{ck}(t_0)$ the characteristic concrete compressive stress at the moment of loading. EN 1992-1-1 considers this value to be the boundary of linear creep.

In the calculations compression was assumed to be negative and tension was assumed to be positive. A downward deflection was chosen positive, and similarly a moment (and the corresponding curvature) that induces tension at the bottom and compression at the top was considered to be positive.

IV. RESULTS

A. *Reinforced beams*

Figure 3 shows both the deflection measurements and some of the predictions for three of the reinforced beams tested at Ghent University. The predictions have been calculated using a normal linear creep coefficient. Prior to the application of the load (28 days), the beams underwent a small deflection as a result of the restrained shrinkage. At the moment of load application the predicted instantaneous deformation agrees well with the measurements, although it is slightly underestimated for the beam loaded at 90% of the failure load. All the models underestimate the time-dependent deformation; furthermore, the underestimation increases in function of the applied load.

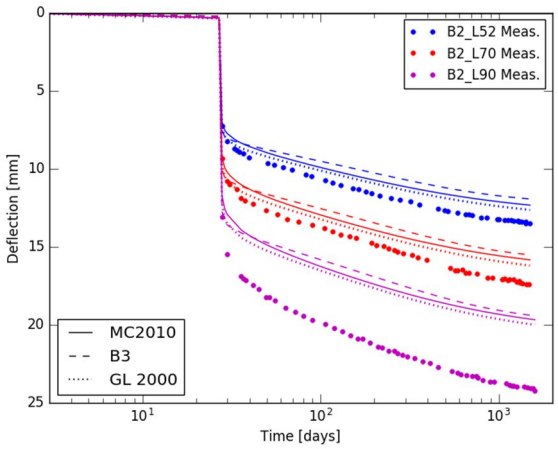

Figure 3. Comparison of measured and predicted deflections of three of the reinforced beams tested at Ghent University.

The predictions of the stresses at the top fibre for the three beams tested at Ghent University are represented in Figure 4. There is also a horizontal line indicating the value of $0.45f_{ck}(t_0)$, All three beams are above this value by approximately 5, 10, and 15 MPa respectively. Note that the concrete stresses decrease over time due to the relaxation of the concrete stress caused by creep and due to some stress redistribution to the reinforcement cage.

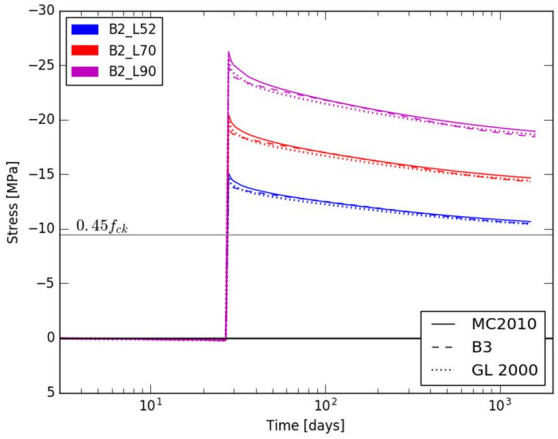

Figure 4. Predictions of the stress near the top fibre of three of the reinforced beams tested at Ghent University.

Figure 5 shows the predicted values using both a linear and a nonlinear creep coefficient. It can be seen that significantly better results are obtained when a nonlinear creep coefficient is used. The deflection predictions of the beam subjected to the highest load also agree better with the measurements, although the deflection is still underestimated.

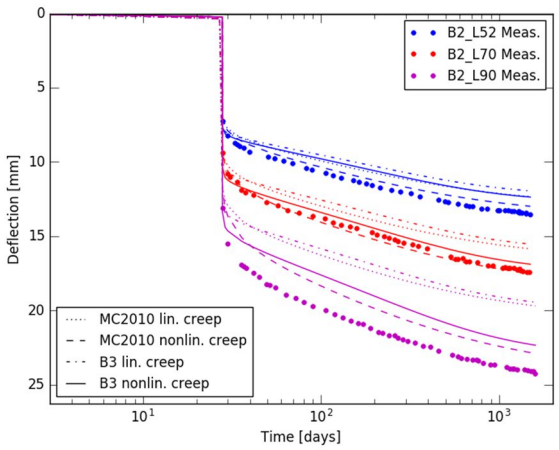

Figure 5. Comparison of predicted values with and without a correction for nonlinear creep for three of the reinforced beams tested at Ghent University.

B. *Prestressed beams*

In a first analysis the prestressed beams were assumed uncracked and the nonlinearity of creep and the relaxation of prestress were neglected.

Figure 6 shows both the predictions and the measurements of the I-shaped beams pre-tensioned at 14 days. The predictions of the beam which is only prestressed are somewhat divergent. It is also observed that the instantaneous deflection predicted by the B3 model and the GL 2000 model do not agree well with the measurements. These models also overestimate the instantaneous deflection due to loading at 28 days. This partially explains why the time-dependent deflection of the two loaded beams (resp. 100% and 50% of the calculated service moment) is predicted almost perfectly.

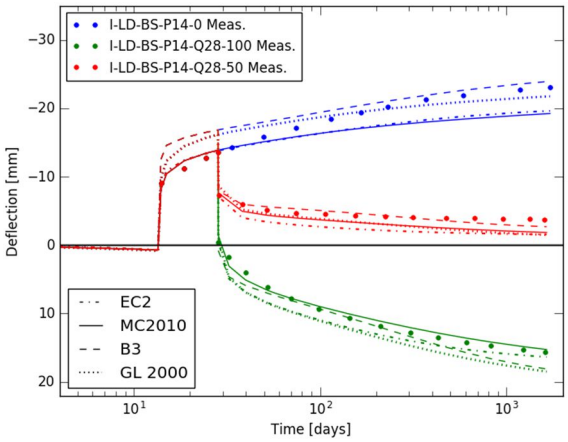

Figure 6. Comparison of deflection predictions and measurements for the I-shaped beams pre-tensioned at 14 days.

A prediction of the stresses at the bottom- and the top fibre of the three beams is given in Figure 7. The stresses at the top fibre are marked by an 'x'. The stresses exceed the value of $0.45f_{ck}(t_0)$ but in a much lesser degree than the reinforced beams. Looking at the lower loaded reinforced beam, it can be concluded that a nonlinear creep calculation for the prestressed beams would hardly result in any accuracy gain of the predictions.

The values of the stress stay above the mean concrete compressive stress f_{ctm}. Hence, the beams are indeed uncracked, as was initially assumed.

From the graph it can also be noted that the compressive stress in the bottom fibre decreases significantly over time, while the stress in the top fibre stays approximately constant.

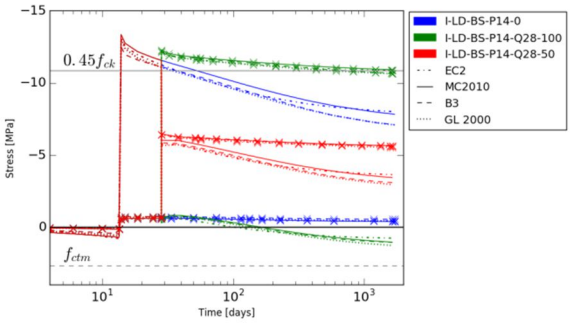

Figure 7. Stress predictions of the I-shaped beams pre-tensioned at 14 days.

In the experimental programme relaxation tests were carried out on the prestressing steel. From these tests it is known that the theoretical relaxation of the prestress stayed below 2% throughout the entire testing period.

The influence of relaxation on the predictions was, in a simplified way, studied by reducing the initial prestress by 2%. The result of these calculations for the I-shaped beams pre-tensioned at 7 days can be seen in Figure 8. From this figure it can be deduced that the relaxation has only a limited influence on the deflections.

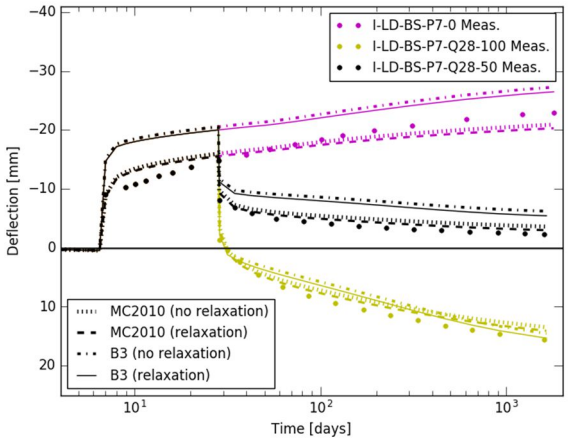

Figure 8. Deflection predictions with and without relaxation for the I-shaped beams pre-tensioned at 7 days.

V. DISCUSSION

A. *Reinforced beams*

When the nonlinearity of the creep is not corrected, the models predict the time-dependent behaviour of the lower loaded beams reasonably well. For the higher loaded beams, the predictions underestimate the time-dependent behaviour, resulting in an increased difference of the predicted values and the measured values over time.

The underestimations of the deflections are possibly explained by the fact that the linear relationship which was assumed between the stress and the strain is no longer valid at higher load levels. The material models are also calibrated on data in the service stress range. It has been shown that many of the beams in this dataset are outside of this service stress range. Therefore, the material models may no longer be valid and thus introduce inaccuracies.

From all the studied models, the ACI model gives the best predictions at early and medium age. At a later age the predicted values according to the GL 2000 model lie the closest to the measured values. The rate of creep at this later age is best described by the B3 model, followed by the GL 2000 model.

The accuracy of the predicted deflections were substantially increased by the use of a nonlinear creep correction. Using a nonlinear creep correction caused the deflections and their rates to be overestimated on average. MC2010 predicts the absolute values of the deflection the best, except for the deflections near the end of loading which are best predicted by GL 2000. The rate of the time-dependent behaviour is the best predicted by the GL 2000 model. At a later age, the B3 model gives the second best predictions of the rate of creep. These results are comparable to what can be found in literature [5, 9, 10, 11].

B. Prestressed beams

The predictions of the deflection for the beams which remain unloaded are divergent. However, the difference is smaller for the loaded beams.

The divergence between the predictions is mainly caused by the diverse predictions of the instantaneous deflection at prestressing. These different instantaneous deflections can be explained by the large variation of the moduli of elasticity and creep coefficients of the different models at early ages. The B3 model has for example a relatively low modulus of elasticity at 7 days and a high creep coefficient at 7 or 14 days for the studied beams.

The predictions are more similar for the loaded beams. This can be justified by the fact that two time-dependent deformations are superimposed on each other: the upward deflection due to prestressing and the downward deflection due to loading.

Despite their initial overestimation the GL 2000 model and the B3 model, together with MC2010, most accurately predict the time-dependent behaviour of the studied beams. In general MC90-99, EC2, and ACI underestimate the deflections slightly.

The stress in the bottom fibre decreases significantly over time. This can mainly be attributed to the time-dependent prestress loss due to creep and shrinkage deformations. The influence of the prestress on the stress in the top fibre is much more limited. This explains why the stress remains almost constant.

For the beams loaded at 50% of the calculated service moment the stress is approximately constant over the entire cross-section, explaining why the time-dependent deformations are so limited.

By a simplified calculation, it was shown in Figure 8 that the influence of the relaxation of prestress on the deflections will be small. Note that in reality the influence will be even smaller than what was shown in Figure 8 because the relaxation will be induced over time and will be smaller than the theoretical value due to the effects of creep and shrinkage.

VI. CONCLUSIONS

A. Reinforced beams

- The difference between a calculated aging coefficient and a constant aging coefficient equal to 0.8 is negligible for the studied beams.
- Without the use of a nonlinear creep correction, the highest loaded beams cannot be accurately predicted.
- The use of the nonlinear creep correction method, which was used here, significantly increases the accuracy of the predictions.
- Correcting the creep, the absolute values at a young and medium age are best predicted by MC2010. The rates throughout the entire testing period are best predicted by the GL 2000 model. At later ages the B3 model gives the second best predictions of the rate.

B. Prestressed beams

- There is some divergence between the predictions of the deflections of the unloaded beams. This is caused by the large difference in the moduli of elasticity and the creep coefficients of the different models.
- The predictions are more similar for the loaded beams due to the superposition of two different deformations.
- MC2010, the GL 2000 model and the B3 model most accurately predict the time-dependent deflections.
- A simplified analysis has indicated that the influence of the relaxation of prestress on the deflections of the studied beams is negligible.

REFERENCES

[1] CEB. (1999). Structural Concrete - Textbook on Behaviour, Design and Performance. Updated Knowledge of the CEB/FIP Model Code 1990 fib Bulletin 2. Lausanne, Switzerland

[2] CEB-FIP. (2013). fib Model Code for Concrete Structures 2010: John Wiley &Sons.

[3] EN 1992-1-1. (2004). Eurocode 2: Design of concrete structures. Part 1-1: General – common rules for buildings and civil engineering structures. London: British Standards Institution.

[4] Bažant, Z. P., & Baweja, S. (2000). Creep and Shrinkage Prediction Model for Analysis and Design of Concrete Structures: Model B3. Paper presented at the Adam Neville Symposium: Creep and Shrinkage—Structural Design Effects, Michigan, USA

[5] Gardner, N. J. (2004). Comparison of prediction provisions for drying shrinkage and creep of normal-strength concretes. Canadian Journal of Civil Engineering, 31(5), pp. 767-775.

[6] ACI Committee 209. (2008). ACI Report 209.2R-08: Guide for Modeling and Calculating Shrinkage and Creep in Hardened Concrete: American Concrete Institute.

[7] Ghali, A., Favre, R., & Elbadry, M. (2002). Concrete Structures: Stresses and Deformations

[8] Bažant, Z. P. (1972). Prediction of Concrete Creep Effects Using Age-Adjusted Effective Modulus Method. Journal of the ACI, 69, pp. 212-217.

[9] Bažant, Z. P., & Li, G.-H. (2008b). Unbiased statistical comparison of creep and shrinkage prediction models. ACI materials Journal, 105(6), 610-621.

[10] Fanourakis, G. C. (2011). Validation of international concrete creep prediction models by application to South African concretes. Journal of the South African Institution of Civil Engineering, 53, 23-30.

[11] Goel, R., Kumar, R., & Paul, D. K. (2007). Comparative Study of Various Creep and Shrinkage Prediction Models for Concrete. Journal of Materials in Civil Engineering,

Table of contents

List of abbreviations

Latin symbols

a	aggregate content in the concrete
a_0	instantaneous deflection in the midspan
a_t	deflection in the midspan at time t
c	cement content in the concrete
$d\sigma_c(\tau)$	increment of stress at time τ
$E_{c,eff}$	effective modulus
E_{cm28}	mean modulus of elasticity at 28 days
$\overline{E_c}(t,t_0)$	age-adjusted effective modulus of elasticity
$E_c(t_0)$	instantaneous modulus of elasticity at time of loading t_0
$E_c(\tau)$	modulus of elasticity at time τ
E_i	modulus of elasticity of section i
E_{ns}	modulus of elasticity of reinforcement steel
E_{ref}	reference modulus of elasticity
$f_{c\ cub\ 200}$	compressive strength of a cube (200x200x200 mm)
$f_{c\ cil}$	compressive strength on a standard cylinder (diameter 150 mm, height 300 mm)
f_{cm}	mean compressive strength of concrete at an age of 28 days, tested on a standard cylinder
f_{ctm}	mean tensile strength of concrete
f_{ptk}	characteristic tensile strength of the steel
f_x	compressive strength of the desired specimen
h_0	notional size of the member, equal to two times the cross-section divided by the perimeter of the concrete member
I_i	moment of inertia of section i
$J(t,t_0)$	creep function or compliance function
k_σ	the stress-strength ratio $\sigma_c/f_{ck}(t_0)$
M	constant moment applied throughout the testing period
$M_{u,0}$	failure moment determined by a static test at 28 days
$M_{u,t}$	failure moment determined by a static test at time t
n	number of prestressing wires
N	normal force
O	reference point
p_d	disjoining pressure
P_i	prestressing force
$P_{m,0}(x)$	mean initial prestress force at a location x from the active anchorage

P_{max}	the maximum prestress force during prestressing
$P_{m,t}(x)$	mean value of the prestressing force at a certain time t at a location x from the active anchorage
$(1/r)_0$	the instantaneous curvature
$(1/r)_t$	the curvature at time t
Q	load
Q_i	load at a node i
Q_{ser}	calculated service load
RH	relative humidity
S	microprestress
S_i	static moment of section i
s_1	bottom reinforcement
s_2	top reinforcement
t	moment of interest
t_c	end of moist curing or the beginning of drying
t_0	time of loading
w	water content in the concrete
x_e	height of the compression zone (relative to top fibre)

Greek symbols

Δ	relative difference between deflection predictions and measurements, calculated by equation (7.2)
Δe	loss of eccentricity due to the non-centric placement of the prestressing wires
$\Delta\sigma_c(t)$	total stress increase at moment t, relative to t_0
$\Delta\sigma_{pr\infty}$	intrinsic prestressing loss at infinity
$\Delta\sigma_{pr}$	prestressing loss in an ideal case
$\Delta\bar{\sigma}_{pr}$	prestressing loss in a concrete member
$\Delta\sigma_{ps}$	stress loss in the prestressed steel
ΔM	total restraining moment
ΔN	total restraining normal force
$\Delta P_{c+s+r}(x)$	sum of all the time-dependent prestress losses at a location x from the active anchorage
ΔP_{el}	prestress loss due to elastic shortening of the concrete at the moment when the prestress is transferred
$\Delta P_i(x)$	immediate prestress losses at a location x from the active anchorage
$\Delta P_{int.}(x)$	prestress loss due to interaction between creep, shrinkage, and relaxation mutually, but also with the present passive reinforcement
ΔP_r	prestress loss due to short-term relaxation of the prestressing steel at the moment between tensioning of the steel and force transfer

$\Delta P_c(x)$	prestress loss at location x from the active anchorage due to creep deformation
$\Delta P_R(x)$	prestress loss at location x from the active anchorage due to relaxation of the prestressing steel
$\Delta P_s(x)$	prestress loss at location x from the active anchorage due to shrinkage deformation
ΔP_{sl}	prestress loss due to slip at the anchorages
$\Delta P_\mu(x)$	prestress loss due to friction of the prestressing steel in the cable duct and due to friction at the deflection points
ε	strain
$\varepsilon_c(t_0)$	instantaneous concrete strain at moment of load application t_0
$\varepsilon_c(t)$	concrete strain at random moment t
$\varepsilon_{cs}(t, t_0)$	free shrinkage between t_0 and t
ε_{c0}	instantaneous strain of the outermost compression fibre
ε_{ct}	strain of the outermost compression fibre at time t
$\varepsilon_{c,top}$	strain at the top fibre
ε_O	strain at the reference point
$\varepsilon_O(t_0)$	instantaneous strain at the reference point
ε_{sm}	mean strain in the tensile reinforcement
η	coefficient dependent on the quality of the steel
ξ	relative creep rate of predicted values against measurements, calculated according to equation (7.3)
ρ_1	tension reinforcement ratio
ρ_2	compression reinforcement ratio
σ_c	concrete compressive stress
$\sigma_c(t_0)$	instantaneous concrete compressive stress at moment of load application t_0
$\sigma_{ct}(t_0)$	total stress
σ_{p0}	initial tension stress in the steel
$\sigma_{ps,\ init.}$	initial prestress in steel before force transfer
τ	intermediate time between the moment of loading t_0 and the moment of interest t
$\varphi(t, t_0)$	creep coefficient at time of interest t after loading at time t_0
$\varphi(t, \tau)$	creep coefficient at time of interest t with loading at time τ
$\varphi_k(\infty, t_0)$	nonlinear, fictive creep coefficient
ϕ_i	internal cable duct diameter
$\phi_{nom,wire}$	nominal diameter of a prestressing wire
$\chi(t, t_0)$	dimensionless aging coefficient
ψ	curvature of the cross-section
ψ_1	curvature out of the cross-sectional parameters of an uncracked section (state 1)
ψ_2	curvature out of the cross-sectional parameters of a cracked section (state 2)
ψ_m	mean curvature
$\psi(t_0)$	instantaneous curvature
ω	percentage of the concrete in compression which undergoes linear creep

1. Introduction

Concrete is an aging linear viscoelastic material. Under loading in the service range, the concrete will have an elastic deformation. If the loading is maintained the concrete will also undergo a time-dependent deformation. This time-dependent deformation is mainly the result of creep and shrinkage of the concrete. For loaded concrete members the creep phenomenon is dominant at later ages. This phenomenon has been studied for decennia. Yet, up until now still no universally accepted creep theory has been formulated. That an accurate prediction of the time-dependent behaviour is required is illustrated by the failure of the Koror-Babeldaob bridge on Palau. This bridge failed due to the underestimation of the long-term deflection, as a result of an inaccurate creep design (Bažant et al., 2011).

Due to the lack of insight in the time-dependent phenomena, different material models have been developed in order to predict the creep and shrinkage behaviour. A problem connected to the use of the different material models is their empirical component. Whether the models are completely empirical or they have a theoretical basis, all of them are calibrated against large datasets. The problem is that these datasets are assembled on compression tests on small specimens without reinforcement. However, the material models are used to assess the behaviour of elements which are an order bigger than the specimens used for calibration. The question thus rises if these material models can indeed be used to accurately predict the behaviour of reinforced concrete elements which have a practical size of several meters.

Tests on beams with a practical size are scarcely found in literature. If such tests are reported, the time of loading is usually too small to make a credible time-dependent analysis. The Magnel Laboratory for Concrete Research participated in a large-scale experimental programme. The goal of this programme was to study the time-dependent behaviour of reinforced, prestressed, and partially prestressed beams under different levels of loading. The experimental programme studied beams with different cross-sections and/or specific reinforcement ratios and/or specific degrees of prestressing. In this dissertation the results of the tests on reinforced and prestressed beams were analysed.

The analysis of the reinforced and the prestressed beams was performed using a cross-sectional calculation method which employs the age-adjusted effective modulus. In an initial stage the calculation method was used in a slightly simplified form. In a later stage different optimisation methods were proposed and tested on their effectiveness in improving the accuracy of the deflection predictions. The creep coefficients, shrinkage strains and moduli of elasticity according to six different material models (CEB-FIP Model Code 1990-1999, FIP Model Code 2010, Eurocode 2, Bažant's and Baweja's model B3, Gardner Lockmann 2000, and ACI 209) were used to calculate: the deflection, the strain, the stress, the axial shortening, and the deformation. The results of these calculations were compared against the available measurements of the experimental programme. This allowed to come to a general conclusion with regard to the accuracy of the models for beams with practical dimensions. The tool which was developed during the study and the analysis allows to perform a complete time-dependent analysis in a limited calculation time.

2. General overview: time-dependent phenomena

Generally, the time-dependent behaviour of concrete is attributed to three different phenomena: creep of concrete, shrinkage of concrete and relaxation of prestressing steel (Ghali et al., 2002). Although the focus of this dissertation is on the creep of concrete, a thorough understanding of the shrinkage and relaxation is also essential. These phenomena are strongly interlinked and influence each other. It is thus required to take them all into account even if one is only interested in one of the phenomena.

A short overview of the structure of concrete at the microscopic level is provided hereunder. This to have a firm base of understanding for the phenomena which will then be discussed.

2.1. Microstructure of concrete

Know that it is known that concrete is a composite material containing coarse aggregates (gravel) in a matrix of mortar. This mortar consist out of smaller aggregates (sand) and a cement paste, which has an important role in the creep process. At the microscopic level, the cement paste is a mixture of unhydrated cement and capillary pores in a cement gel of hydrated cement particles. At the submicroscopic level, this cement gel is mainly comprised out of calciumhydroxide and hydrated calcium silicates (CSH), also called tobermorite. Two or three monomolecular layers of tobermorite form a tobermorite sheet.

Figure 2.1 illustrates the arrangement of tobermorite sheets proposed by Feldman and Sereda (1968). The water which was added during the mixing of the concrete is found at different locations. The centre of Figure 2.1 depicts a capillary pore. Capillary pores can contain free, unbounded water, depending on the relative humidity of the environment. Adsorbed water is held at the surface of the gel particles by van der Waals forces. Between the tobermorite layers and sheets interlayer or zeolitic water is found. The adsorbed water and the zeolitic water combined are called gel water. Additionally, there is also chemically bounded water. This water has reacted with the cement particles to form the hydration products.

In general, most of the chemically bounded water and a little part of the water that is not chemically bounded is considered as non-evaporable. The free water, the adsorbed water and the interlayer water can be removed when the concrete is subjected to high temperatures. Hence, this water is called evaporable water(Neville et al., 1983).

Many of the theories, which have been developed over time, trying to explain the creep and shrinkage behaviour, use one or more of these types of water in their formulation. The theories regarding the shrinkage can be found in section 2.2. A selection of the most accepted theories regarding creep can be found in section 2.3.1.

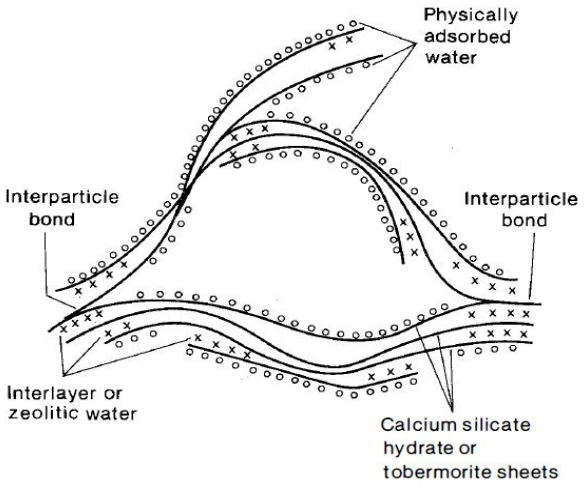

Figure 2.1. Proposed structure of concrete at the submicroscopic level according to Feldman and Sereda (1968).

2.2. Shrinkage of concrete

Concrete suffers from a volume reduction in function of time without being subjected to any loads, this phenomenon is referred to as shrinkage. This shrinkage of the concrete is attributed to four physical processes: autogenous shrinkage, drying shrinkage, carbonation shrinkage, and thermal shrinkage. The first three are related to a loss of water.

As long as the shrinkage can happen freely, no global stresses will be induced in the concrete. However, when the concrete is restrained and deformations cannot happen freely, macroscopic stresses will be induced. The concrete can be externally restrained: fixed supports in the case of beams, the ground in the case of floor slabs, etc. It is also possible that the concrete is internally restrained by reinforcement, which is much stiffer than concrete. Different parts of the concrete member can also restrain one another. This is explained in section 2.2.2.

2.2.1. Autogenous shrinkage

The mixing of cement and water will start a hydration process. The volume of the formed hydration products is smaller than the volume of the original cement and water. In other words, there is a volume reduction, called chemical shrinkage (Tazawa, 1999). This chemical shrinkage creates internal pores but is not macroscopically visible. If no external water is provided the water which is present in the pores of the concrete will be used for the continuation of the hydration process. Note that even when external water is provided, it will take time for the water to migrate inside the concrete elements. The larger the elements are, the longer it will take for the water to migrate to the inside of the concrete element. This self-desiccation causes a capillary tension. These stresses are local and cause macroscopic deformations at an early age of the concrete when the modulus of elasticity has not yet completely developed (Koenders, 1997).These macroscopic deformations are called autogenous shrinkage. Note that the autogenous shrinkage is caused by the chemical shrinkage and happens almost at the same time as the chemical shrinkage. Although the chemical shrinkage is larger than the autogenous shrinkage, the difference is not macroscopically visible due to the creation of the internally capillary pores (Tazawa, 1999).

De Schutter (2012) mentions that the water-cement ratio is the most important factor contributing to the autogenous shrinkage. The lower the water-cement ratio of the concrete, the less water is available and thus the higher the capillary tension will be. Therefore, autogenous shrinkage is more a problem for high-strength concretes. Another influencing factor is the type of cement and the used admixtures since they influence the hydration reaction. Also the paste volume plays a role because shrinkage is limited to the cement paste. The autogenous shrinkage is however independent of the member size and the relative humidity.

2.2.2. Drying shrinkage

Drying shrinkage takes a longer time to develop than autogenous shrinkage and, unlike autogenous shrinkage, it requires a moisture exchange with the environment. The vapour pressure difference between the environment and the concrete causes the capillary water of the concrete to be expelled. This results in a small volume decrease. When the vapour pressure difference remains, the gel water will also be evacuated out of the concrete. This causes a larger volume decrease (De Schutter, 2012). The removal of the interlayer water brings the tobermorite layers closer to each other. This proximity results in the formation of extra bonds, which explain the irreversible part of shrinkage (Taerwe & De Schutter, 2006). Drying shrinkage requires more time than autogenous shrinkage since the water has to migrate out of the concrete.

Due to the different migration lengths of surface water and core water, the drying shrinkage will have a non-uniform character. The surface loses its water quickly and wants to shrink, but it is restrained by the core, which still has most of its water. Therefore tension originates at the surface and compression at the core. As a result of this tension, cracks could occur at the surface. The cracking causes deformations in the opposite direction of the shrinkage. P. Rossi and Acker (1988) reported that because of this, the measured shrinkage is less than the expected shrinkage without cracking.

As opposed to autogenous shrinkage, a lower water-cement ratio has a beneficial influence on the drying shrinkage (De Schutter, 2012). A higher water-cement ratio results in a more extended pore network filled with water after hydration. Thus, more water can be expelled. Comparable to autogenous shrinkage an increase in the cement paste will result in a higher shrinkage. Since the difference in vapour pressure is the driving force, the humidity of the environment will have a large influence. Likewise, the geometry is an important factor; long, thin concrete specimens will shrink faster than compact specimens. The core water of compact specimens requires after all a longer time to migrate to the surface compared to the core water of thin specimens. Also the curing method and curing time play a role: drying at an earlier age will cause a higher amount of shrinkage because more water is available.

2.2.3. Carbonation shrinkage

When concrete is exposed to the air, the carbon dioxide in the air will react with the calcium hydroxide and hydrated calcium silicates in the concrete. This carbonation reaction creates calcium carbonate and water. When this water leaks out of the concrete, the concrete will shrink. (Pham & Prince, 2014) Since carbonation shrinkage only effects the most outer layers, its contribution to the overall shrinkage can usually be neglected (Taerwe & De Schutter, 2006).

2.2.4. Thermal shrinkage

The hydration reaction of cement and water is an exothermal process. This means the concrete will expand and then contract again at an early age. This can be the cause for early-age thermal cracking due to internal or external restraint (De Schutter, 2012). Commonly this causes problems for massive concrete structures and concrete walls which are casted on non-deformable floors etc. For beams which can deform freely at an early age this generally causes no problems. Thermal shrinkage is neglected in the rest of this work.

2.3. Creep of concrete

Creep is the phenomena which causes an increase in strain in a concrete member under a constant stress (Taerwe & De Schutter, 2006). This results in increased deflections but can also cause a redistribution of stress.

As it is mentioned above, creep and shrinkage influence each other. On the other hand, to study creep it is desirable to assume creep and shrinkage as two disconnected phenomena which are additive, since this simplifies the analysis greatly. Therefore, creep is defined as the time-dependent deformation which cannot be attributed to shrinkage. Shrinkage is measured on unloaded specimens. Creep then needs to be split up in two different phenomena: basic creep and drying creep. Basic creep is the creep which will happen even if there is no exchange of moisture, like creep on concrete which is stored under water. Drying creep is the creep which can be attributed to moisture exchange (Neville et al., 1983). The dying creep is sometimes also called the Pickett effect.

During concrete calculations in service conditions, the stress and the strain are assumed to be proportional to one another (Ghali et al., 2002). The instantaneous strain $\varepsilon_c(t_0)$ can then be expressed as:

$$\varepsilon_c(t_0) = \frac{\sigma_c(t_0)}{E_c(t_0)} \tag{2.1}$$

in which: $\sigma_c(t_0)$ is the instantaneous stress, $E_c(t_0)$ is the instantaneous modulus of elasticity and t_0 is the moment of application of the instantaneous stresses. Normally the modulus of elasticity increases as the age of the concrete increases, but it is usually assumed to be constant.

When taking into account the time-dependent behaviour due to creep, the equation for the strain needs an extra term compared to equation (2.1). The strain at a random time t can be calculated as:

$$\varepsilon_c(t) = \frac{\sigma_c(t_0)}{E_c(t_0)} \cdot [1 + \varphi(t, t_0)] \tag{2.2}$$

The creep coefficient $\varphi(t, t_0)$ is a dimensionless factor which expresses, relatively to the initial strain, the increase of strain due to creep. This factor depends on the time of loading t_0 and the time of interest t. Note that shrinkage has been neglected here. In design codes and literature many different formula for $\varphi(t, t_0)$ have been proposed. Figure 2.2 gives a representation of equation (2.2). At time t_0 there is an instantaneous increase of the strain. This strain then increases due to creep, so that at the time of interest t the total strain is equal to the sum of the instantaneous strain $\varepsilon_c(t_0)$ and the strain due to creep $\varphi(t, t_0) \cdot \varepsilon_c(t_0)$. Bažant (1988) determined that the creep

is linear as long as the prevailing stresses stay below 0.4 times the strength of the concrete. This value is discussed in literature. EN 1992-1-1 (2004) reports a value of 0.45 times the characteristic concrete strength, but ACI Committee 209 (2008) and CEB-FIP (2013) endorse the value of 0.4 times the mean concrete strength. More recently it has also been reported that creep can be nonlinear below 0.4 times the strength for certain variable stress histories (CEB-FIP, 2013).

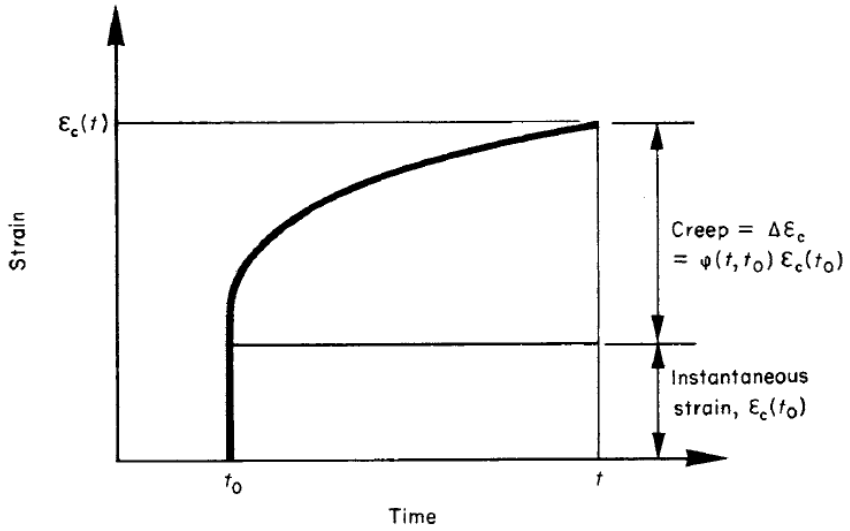

Figure 2.2. Influence of creep on the development of strain over time (Ghali et al., 2002).

Equation (2.2) can be written in a more convenient form by the use of the creep function or compliance function $J(t, t_0)$ (Bažant, 1982, 1988):

$$\varepsilon_c(t) = \sigma_c(t_0) \cdot J(t, t_0) \tag{2.3}$$

$$J(t, t_0) = \frac{1 + \varphi(t, t_0)}{E_c(t_0)} \tag{2.4}$$

The creep function gives the amount of strain at time t for a unit stress applied at t_0.

Note that in this section it was assumed that the stresses are constant. In practice situations this will often not be the case due to changing loads. The reasons why the loads can be changing are multiple: the load is mobile, a construction is not erected at once but has different construction stages, changes in the magnitude of the load,… The theory discussed here then needs to be adapted for changing stresses. This is discussed in section 3.1.

For more general cases Figure 2.2 gets an extra addition, like in Figure 2.3. At the moment of the application of the load there is an instantaneous deformation. Usually this deformation is elastic, but it can also contain a non-elastic part. Then, there is a primary creep. During the primary creep the rate of creep decreases remarkably. When there is a minimum creep rate, the primary creep is followed by a secondary creep. Normally the primary creep is not so large, and the secondary creep is dominant. In this case the secondary creep can be modelled approximately as a straight line. It is this secondary creep which represent the steady state creep. If the stresses are high enough, more than 40% of the failure strength, microcracking can cause a tertiary creep. Under normal conditions, the stresses will be low enough so that there is no tertiary creep, and so that the difference

between primary and secondary creep becomes undistinguishable. Figure 2.3 then becomes like Figure 2.2. (Neville et al., 1983)

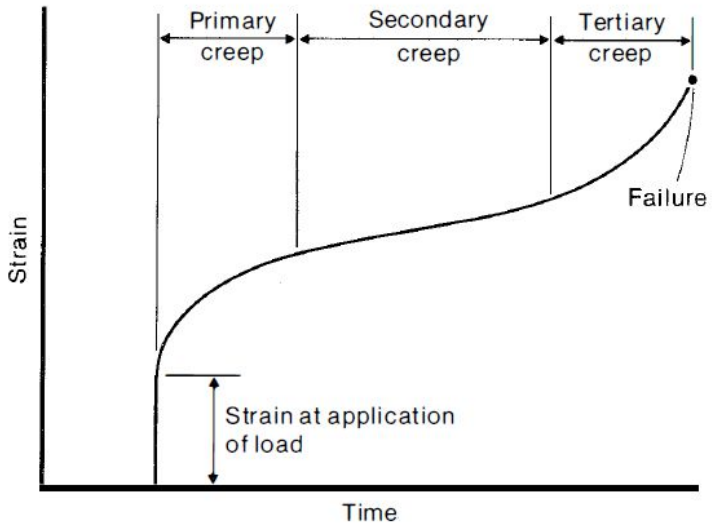

Figure 2.3. Creep phenomenon at higher load levels: primary - , secondary - and tertiary creep (Neville et al., 1983).

The effects of creep are not only limited to strain changes. When a strain is imposed on the concrete element, the induced concrete stress can be calculated using equation (2.1). If the strain is maintained constant, the stress of the element will decrease as a function of time because of creep. The stress can be calculated by:

$$\sigma_c(t) = r(t, t_0) \cdot \varepsilon_c \tag{2.5}$$

where $r(t, t_0)$ is a relaxation function. This principle is illustrated in Figure 2.4.

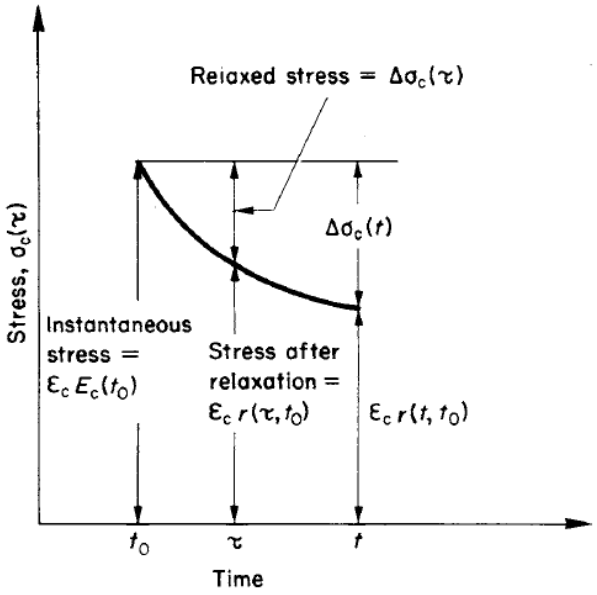

Figure 2.4. Relaxation of concrete stress due to creep under a constant maintained strain (Ghali et al., 2002).

2.3.1. Mechanisms of creep

Creep of concrete is a complex phenomenon. Consensus on the mechanics behind this phenomenon is not yet reached. Moreover, since it is believed to be related to changes on the microscopic level, these mechanics are difficult to study. Neville et al. (1983) cite different mechanisms of creep: mechanical deformation theory, viscous flow, plastic flow, seepage of gel water, delayed elasticity, and microcracking. None of these theories is able to describe the complete creep phenomenon and some of these have been rejected completely, like e.g. the mechanical deformation theory. Others do describe parts of the phenomenon rather well, and therefore combined mechanism theories have been proposed. These combined theories are out of the scope of this thesis. However, hereunder a short description is given of the seepage theory and the viscous flow theory, which Taerwe and De Schutter (2006) report to be the most important mechanisms for the basic creep. They attribute microcracking as the most important factor for drying creep. Be that as it may, research by Pierre Rossi et al. (2012) and Pierre Rossi et al. (2013) gives possible evidence that microcracking is also the main cause for basic creep. Bažant and Prasannan (1989a) proposed the solidification theory which was later incorporated in the microprestress-solidification theory (Bažant, Hauggaard, & Baweja, 1997; Bažant, Hauggaard, Baweja, et al., 1997). Up until now, the microprestress-solidification theory gives the most complete explanation for creep of concrete.

2.3.1.1. Viscous flow theory

The viscous flow mechanism treats concrete as a very viscous material. Hydration products will flow over one another aided by the zeolitic water, which acts as a sort of lubricant (Taerwe & De Schutter, 2006). The creep is thus located in the cement paste. Thomas (as cited by Neville et al., 1983) explains that as the concrete creeps, the stress is transferred from the cement paste to the aggregates, which do not show creep behaviour. As more and more of the stress is transferred to the aggregates, the driving force decreases, which explains the lower creep rates at later times.

Neville et al. (1983) report two main problems related to this theory. The first one being that the material could not undergo volume changes, which is for instance not the case in axial creep. Second, that it is necessary for the creep strain to be proportionally related to the stress. This being only valid for lower stress levels, as already discussed above.

2.3.1.2. Seepage theory

The seepage theory treats the cement paste as a rigid gel. Under load, there is an expulsion (or seepage) of the gel water. This causes a stress redistribution from the water to the skeleton. This mechanism is very similar to drying shrinkage. Although, the driving force here is the applied pressure, not the vapour pressure difference between the environment and the concrete. As more water is squeezed out, the stress on the solid increases. The water takes less stress, and hence the driving force decreases. It is emphasised, that it is the gel water, and not the capillary water, which causes creep. After all, the removal of capillary water causes no deformation.

As the water seeps out the cement paste, particles come closer together and new bonds are formed. This explains the irrecoverable part of creep. However, this theory does not explain why

concrete specimens dried in air and subsequently loaded in water creep double as much as specimens which were both stored and loaded under water (Neville et al., 1983).

2.3.1.3. Microcracking

By the use of acoustic emissions, Pierre Rossi et al. (2012) have proposed that it is microcracking which is the main cause of autogenous creep. These microcracks are created at the moment the static load is applied. These microcracks are vacuums at the moment of their creation, causing both a gradient of pressure and a gradient of concentration of water molecules. These gradients cause a movement of liquid water due to Darcy's law and a movement of water vapour due to Fick's law. This causes a self-drying process in the concrete which results in extra shrinkage. This shrinkage causes a pressure field in the cement paste. The granulates induce stress due to the restraining of the cement paste, which can cause the formation of new microcracks. The initial microcracks can also propagate due to the water reducing their stabilising cohesion force. The propagation of the initial microcracks or the creation of new microcracks increase the self-drying shrinkage even more.

2.3.1.4. Solidification theory and microprestress-solidification theory

Bažant and Prasannan (1989a) developed the solidification theory. This theory does not infringe on the laws of thermodynamics, unlike many other theories. Their creep theory is based on the aging of concrete, since it has been noticed that creep is intensely related to the aging, see also section 2.3.2.3. However, they do not treat the solidified matter (cement gel) as an aging substance because this would result in unmanageable thermodynamic formulations. Instead, they assume the solidified matter to be non-aging. The aging is considered as a growth in solidified matter. During a certain time interval, an amount of reaction products precipitate due to the hydration of the cement. These products adhere to the previously solidified matter and thus form a new layer on top of it. As more and more layers are deposited on the already solidified matter, the concrete becomes macroscopic stiffer and more viscous. This explains the decrease in the rate of creep over time. One of the key hypotheses of this theory is that from the moment the solution of cement in water solidifies, it is subjected to the same strain as the previously solidified matter. It is important to note that the newly solidified layer is in the beginning free of stress: a liquid cannot solidify in a stressed state.

Bazant and Prasannan translated their theory in a model. This model considered the creep strain as a sum of aging and nonaging viscoelastic strain and aging viscous strain. The creep predictions of this model were compared against experimental results (Bažant & Prasannan, 1989b). It gave good predicitions over a broad range of conditions.

Despite the good results, Bažant, Hauggaard, and Baweja (1997) reported two physical shortcomings of the solidification theory. The first one being the inability of the theory to describe the drying creep. The second one being the inability to describe the long-term creep. The age at the moment of loading has an influence on the creep, even after many years. While the formation of hydration products is already strongly reduced after a month and stops after about a year.

In order to theoretically explain the long-term creep, Bažant, Hauggaard, and Baweja (1997) developed the concept of microprestress. In order to explain this concept it is necessary to go back to the structure of concrete. Concrete is a highly hydrophilic porous material: the internal surface of

the pores can easily amount up to 500 m² for 1 cm³. As a result, the capillary forces and the adsorption forces can be very high, much higher than a stress which has been induced by a load. As discussed in section 2.1, concrete consists out of a cement gel and capillary pores. These capillary pores are larger than 1 µm. There are also subcapillary pores, which are smaller than 1 µm, inside of the cement gel. The adsorption forces result in water layers being adsorbed to the pore walls. However, many of the subcapillary pores are not big enough to allow the full thickness of the adsorbed water layers to develop. These pores are given the name micropores. The hindered adsorbed water layers cause a transverse compressive stress on the micropore walls. This stress is called the disjoining pressure p_d, see also Figure 2.5. The crystal growth pressure, which is induced by the growth of crystalline products precipitated out of the hydration reaction, works in the same way as the disjoining pressure. As mentioned in section 2.1, there is also interlayer water. Hindered adsorbed water layers will also cause a disjoining pressure at the location of the interlayer water. The disjoining pressure and the crystal growth pressure need to be compensated by tensile forces. Partially, these tensile forces are carried by the structure of the cement gel. Partially, they are transferred by bonds between the micropore walls, see Figure 2.5. The tensile forces in the transverse bonds cause the cement gel to be prestressed, causing a (tensile) microprestress in the concrete. This is an explanation for the weak tensile force of concrete. The tensile forces in the bonds are not only caused by the disjoining and the crystal growth pressure, also high local volume changes due to drying or hydration induce tensile forces.

It is important to note that the microprestress is not dependent on the macroscopic stress (Bažant, Hauggaard, Baweja, et al., 1997). The microprestress is determined by the disjoining pressure. Due to the short diffusion length between the micropore and the capillary pore, the disjoining pressure changes almost instantaneously when there are changes in the relative humidity of the neighbouring capillary pore. Thus, the microprestress is linearly dependent on the rate of change of the relative humidity in the capillary pore. This is related to the drying creep because during drying there is a diffusion of the internal humidity to the environment (Bažant, Hauggaard, & Baweja, 1997).

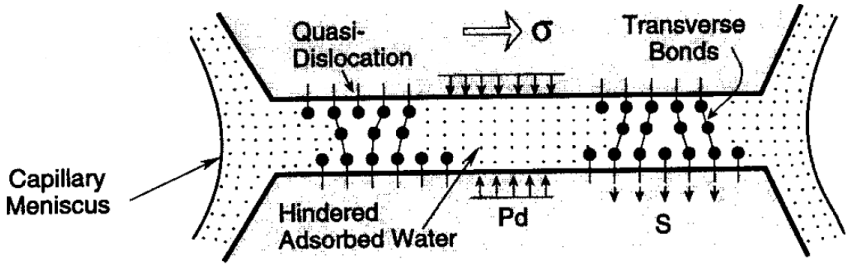

Figure 2.5. Micropore in the cement gel, p_d being the disjoining pressure, S being the microprestress. In reality the walls are more rough (Bažant, Hauggaard, Baweja, et al., 1997).

Bažant, Hauggaard, Baweja, et al. (1997) propose that the hindered adsorbed water layers are slip planes. At these locations shear slips are possible under influence of shear stress and normal stress. In order for the shear slips to be possible the transverse bonds need to break. A lot of these bond breakings cause the concrete to creep on a macroscopic level (or at least causes the long-term flow part of creep). The frequency in which the bonds break, is dependent on the kinetic energy of the thermal vibrations of atoms and on the magnitude of the activation energy barrier. A higher tensile force in the bonds reduces the energy barrier and this results in a faster bond breaking. After the

bond is broken, a new bond will be formed with a neighbouring atom. The breaking and the following bond restoration causes the driving shear stress to be redistributed. This may cause another location to be overstressed, resulting in a new bond breaking. The relaxation of the shear stress and the exhaustion of the overstressed locations causes the creep rate to decline. Another way of phrasing it is saying that as the concrete creeps the microprestress relaxes. This causes the rate of slips to decrease and also causes more and more of the locations where bond breaking happens to become inactive. This inactivity then causes a reduction of the creep rate and is manifested as aging.

It is of course also possible that the bonds are not restored when the stresses are outside the service range. In this case cracks will be formed which reduce the stiffness of the concrete. This causes a nonlinear creep.

As mentioned above the drying creep can be partially explained by the relative humidity. The other part is reasoned to come from cracking (Bažant, Hauggaard, & Baweja, 1997). In case of small elements smeared cracking can be assumed. For more massive elements and for larger structural members localization of the cracking into continuous cracks can happen. In this case the assumption of smeared cracking is invalid and one is required to use fracture mechanics.

Bažant, Hauggaard, and Baweja (1997) formulated the microprestress-solidification theory by combining the solidification theory, the microprestress concept and the cracking. The microprestress concept explains the long-term creep, as well as part of the drying creep. The solidification theory is dominant at early age when there is volume growth of the hydration products. The cracking explains the other part of the drying shrinkage.

The microprestress-solidification theory was tested against an experimental database and was observed to give good results. Figure 2.6 shows the contributions of the different phenomena, which are included in the microprestress-solidification theory, to the creep compliance.

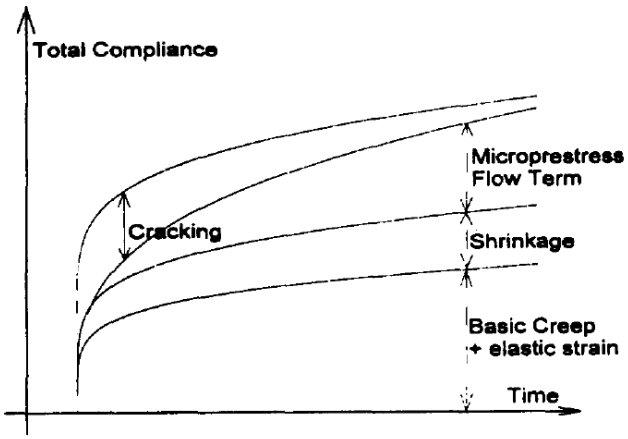

Figure 2.6. Contributions of the different phenomena included in the microprestress-solidification theory to the compliance (Bažant, Hauggaard, & Baweja, 1997).

Jirásek and Havlásek (2014) gave a good rheological representation of the microprestress-solidification model of Bažant, Hauggaard, Baweja, et al. (1997) (Figure 2.7). They studied axially compressed prisms under non-isothermal conditions. In such a loading case the prisms are not expected to crack and they therefore neglected the cracking term. They did however

take into account a temperature term in order to correctly asses the effects of the non-thermal conditions. ε_α is the instantaneous elastic deformation modelled by a non-aging elastic spring. This is unlike the classical static elastic modulus, which is indeed age-dependent. It should be seen as an asymptotic modulus and follows from the extrapolation of experimental data to very short times, which are even shorter than the ones which are used for the determination of the dynamic modulus. The ε_v term is the solidification part of the concrete creep or in other words the sort-term creep. It is represented by a solidifying Kelvin chain where E represents the modulus of elasticity and η represents the viscosity. The reason why a Kelvin chain is used is to be able to write the compliance function as Dirichlet series, which simplifies the mathematical modelling. The third part ε_f is an aging dashpot with viscosity dependent on the microprestress S. This represents the long-term creep explained by the microprestress theory. As mentioned above, this originates from shear slips which are influenced by both the shear stress and the normal stress. ε_{sh} represents the free shrinkage. The last term ε_T represents the thermal expansion, which can be neglected for isothermal tests.

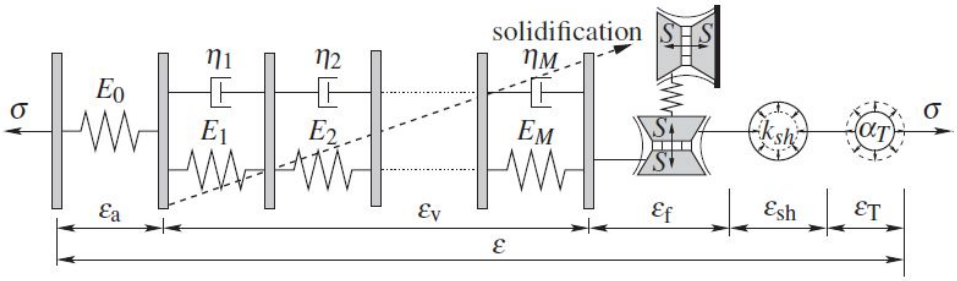

Figure 2.7. Rheological representation of the microprestress-solidification theory with the exclusion of the strain due to cracking (Jirásek & Havlásek, 2014).

Jirásek and Havlásek (2014) rewrote the equation of the microprestress-solidification theory in function of the viscosity. This approach keeps the constitutive law equivalent to the original approach. The microprestress is however eliminated from the equation, which is beneficial since the microprestress cannot be measured directly. This approach leads also to a reduced number of modal parameters which results in a more simplified structure. This new form of the microprestress-solidification theory was compared with non-isothermal creep tests, as already mentioned above. Jirásek and Havlásek discovered that the microprestress-solidification theory severely overestimates the strain in case of loading under cyclic temperature. In the initial stage of concrete higher temperatures result in an increased speed of the hydration process. In other words, the concrete will develop its maturity faster and the creep deformation will be lower. If concrete is however subjected to higher temperatures for longer periods of time the creep rate will increase. The bond breakings will indeed happen easier due to higher microprestress. Be that as it may, the temperature cannot generate additional microprestress to an infinite amount. Therefore, Jirásek and Havlásek adapted the microprestress-solidification equation by taking into account a factor which corrects for temperature cycles: if the concrete experiences a temperature state it has experienced before the microprestress is limited. This adaption of the microprestress-solidification equation was tested against experimental data, and a significant improvement in relation to the original equation was observed.

In the future it is expected that the microprestress-solidification theory will be updated further. After all, it is possible to do a similar reasoning for cyclic changing relative humidities.

2.3.2. Factors influencing creep of concrete

Neville et al. (1983) gives an extensive overview of research on the influencing factors of creep executed in the past few decades. There are many factors which influence creep: cement, admixtures, aggregates, strength, stress, water-cement ratio, age, size, humidity, temperature, curing, duration of loading,… Not all of these factors are as important. Generally the focus lies on: the strength in relation to the applied stress, the water-cement ratio, the age at loading, the duration of the load and the relative humidity.

2.3.2.1. Stress-strength ratio

It is important to realise that the stress applied on a member or the strength of that member individually do not matter, it is their ratio that decides the creep behaviour. Generally, creep occurs from the moment that there is stress in the concrete specimen; there is no lower limit to creep. As mentioned above, the relationship between the stress in a concrete member and the resulting creep is linear as long as the stress remains below a certain level. This boundary of the linear relation is not precisely determined but Neville et al. (1983) reported that this boundary lies between 0.30 and 0.75 of the stress-strength ratio based on experimental results obtained from literature. Starting from this boundary microcracks start to deform which influence the creep behaviour.

In stress-strength region between 0.7 and 0.9 tertiary creep will be induced and specimens can fail due to an excessive strain. Although it should be noted that the strain in case of a long-term test can be higher than for a short term test as was observed by Gvozdev (as cited in Neville et al., 1983).

2.3.2.2. Water-cement ratio

Two interpretations can be adopted with regard to the influence of the water-cement ratio on the creep behaviour, both leading to the same result. The first interpretation is related to the cement paste. As mentioned above it is this cement paste that undergoes the creep deformation, while the aggregates, which are stiff, try to withstand the deformation. Increasing the water-cement ratio, while keeping the cement content constant, will increase the cement paste and thus creep will increase if the other factors stay the same. On the other hand increasing the water-cement ratio decreases the strength. Thus, if the stress stays the same the creep deformation will be larger (Neville et al., 1983).

2.3.2.3. Age of the concrete at loading

The older the concrete is when loaded, the lower the creep deformation will be. This is because the strength of the concrete develops over time as a result of the hydration process of cement and water. This strength gain is commonly referred to as the ageing effect. In general it is assumed that concrete has reached its maximum potential strength at 28 days. Then it does not matter when the concrete is loaded as long as it is loaded after 28 days. However, the analysis of multiple studies by different researchers done by L'Hermite (1959), as cited in Neville et al. (1983), shows that waiting longer than 28 days before loading has a positive effect on the creep deformation, see Figure 2.8. Although it should be noted that the difference is usually not so big, or even negligible, for loading after 28 days. Davis et al. and Glanville (as reported in Neville et al. (1983)) both noticed that the

rate of creep is significantly larger in the first few weeks for early loaded concrete compared to older concretes.

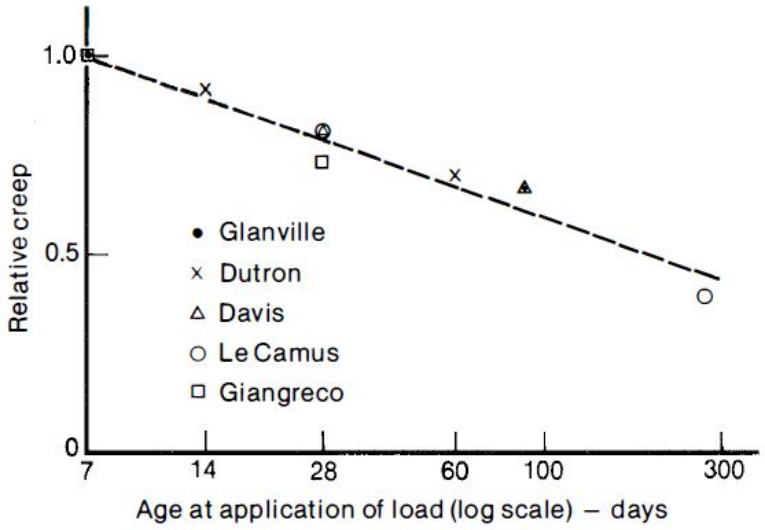

Figure 2.8. Age at the application of the load versus the relative creep, determined using the creep at 7 days. The acting stress is the same for all points (L'Hermite, 1959).

Actually it is the level of hydration which is more important than the age of the concrete. Both are of course related, yet the level of hydration contains more information as it is directly related to the microstructure. De Schutter and Taerwe (2000) for example stated that basic creep is related to the degree of hydration, and that time is not an explicit parameter.

2.3.2.4. Relative humidity of the environment

The relative humidity of the environment influences the relative humidity inside the concrete. When there is an equilibrium between these two, which is called hygral equilibrium, there will be no drying creep. The only form of creep is then basic creep. Concrete that is not in hygral equilibrium will have a higher rate of creep, as well as a higher ultimate creep deformation.

The time it takes to reach hygral equilibrium is dependent on the difference between the relative humidities. Below a certain evaporable water content, increasing the difference in humidities does not cause a proportional increase in water loss. This is because the evaporable water in the concrete is becoming scarce, resulting in an increase of the forces attracting them to the concrete. The size and shape of the specimen also determine the time at which equilibrium is reached. Smaller specimens will reach equilibrium sooner but will have a large rate of drying creep before equilibrium is reached. Larger specimens, on the other hand, have a lower rate of drying creep but this creep continues longer since it takes longer for the water to migrate out of the concrete. (Neville et al., 1983)

Also the humidity of the concrete itself, regardless of the humidity of the environment, plays a role in creep. Different researchers (e.g. Glucklich and Ishai (1962)) monitored a reduced creep deformation when the relative humidity in sealed specimens decreased. Brown and Hope (1976) even observed that cement paste specimens, out of which all the evaporable water has been removed, do not undergo creep deformation.

2.3.3. Creep recovery

When the applied load (or part of it) is removed, an inverse creep process occurs: creep recovery. At the moment of unloading, there will first be an instantaneous recovery, see Figure 2.9. The magnitude of this instantaneous recovery is smaller than the instantaneous strain on application because the modulus of elasticity has increased over time. Bažant (1982) also stated that the instantaneous strain has an irreversible component which is not related to the increase in the modulus of elasticity for high stresses (higher than about half of the strength). After this instantaneous recovery there will be a time-dependent elastic creep recovery: recoverable creep. During the creep process stress is transferred from the creeping cement paste to the granulates, which restrain the creep. This causes a delayed elastic deformation of the granulates. Upon unloading these granulates gradually deform back, thereby attributing to the recoverable creep (Taerwe & De Schutter, 2006). Part of the creep will be unrecoverable. The reason for this is the extra bonds which are formed during the creep deformation and the microcracks which occur.

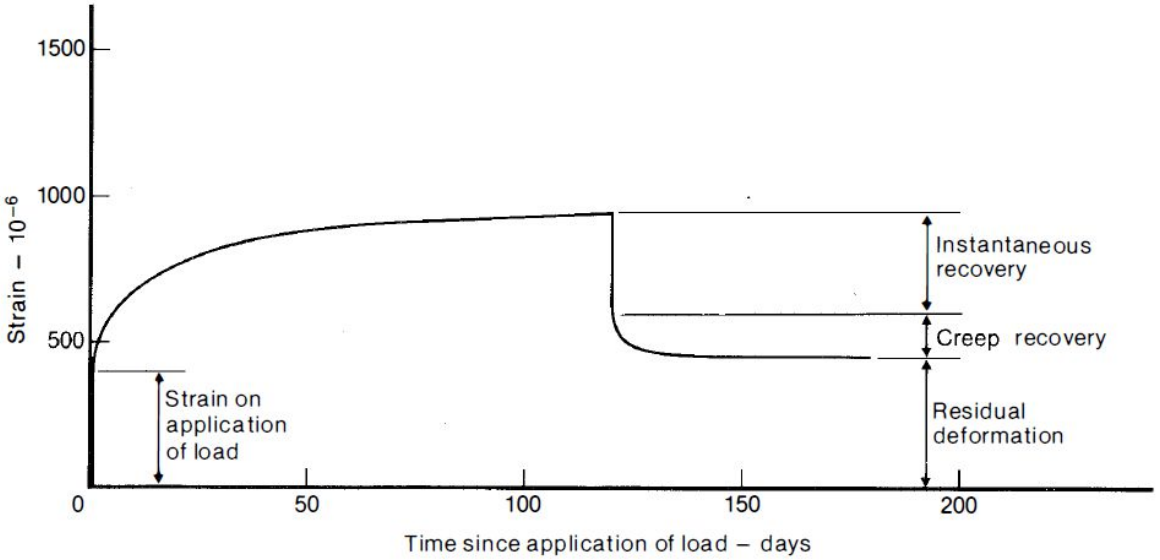

Figure 2.9. Strain curve for unloading (Neville et al., 1983).

2.4. Prestress

Taerwe (2015) defines an element in prestressed concrete as: “A concrete element in which, in a judicious way, initial stresses are created through a system of forces which are in equilibrium and which are permanent in nature.” The term prestressed comes from the fact that high quality steel (prestressing steel), which has been tensioned, induces stresses in the concrete prior to and independent of the applied loads, such as the self-weight and the service loads. The “judicious way” is related to the goal of prestressing. Concrete has a low to negligible tensile strength. During bending, part of the concrete will be in tension and it will crack. The contribution of this concrete to the strength is therefore limited, but the cracked concrete still contributes to the self-weight. The cracks in the concrete can also severely reduce the durability of the concrete element. The goal of prestressing is to avoid these cracks, so that the durability is ensured, and the entire cross-section contributes to the strength of the member. This is done by inducing enough compressive stress in the concrete, in order that the entire cross-section is still in compression even after the introduction of the bending tensile stresses. It is important to underline, that the forces which are exerted on the

concrete element by the prestressing steel are a system of forces in equilibrium. In the case of a statically indeterminate system, secondary forces are induced by the prestressing at the location of external connections. Nonetheless, also these secondary forces are in equilibrium.

From this definition (Taerwe, 2015), it is clear that prestressing in itself is not a time-dependent phenomenon. However, the relaxation of the prestress is a time-dependent phenomenon. Furthermore, the total loss of prestress and the relaxation of prestress have a strong interaction with the time-dependent phenomena.

2.4.1. Prestressing techniques

There are two different kinds of techniques to apply prestress to a concrete element: post-tensioning and pre-tensioning (Taerwe, 2015). Both of these techniques are briefly explained here.

2.4.1.1. Post-tensioning

After the passive reinforcement is placed in the formwork, a duct is attached to the reinforcement cage in the longitudinal direction. This is done prior to casting. When the concrete has been casted the duct forms a cavity in the cross-section. A prestressing cable is then placed in the duct. After the concrete has been hardened sufficiently and has gained enough strength, the prestressing cable is anchored at one side (passive anchorage) and tensioned at the other side using a hydraulic jack. Next the prestressing cable is anchored at the side of the hydraulic jack (active anchorage). It are the anchorages which induce the prestress in the concrete element. Finally, the duct is filled with a grout. The benefit of using a grout is twofold: the grout protects the prestressing steel against corrosion and it creates a bond between the prestressing steel and the element. This last function is important to ensure compatible strains in prestressing steel fibres and adjacent concrete fibres.

2.4.1.2. Pre-tensioning

Wires or strands are kept in tension between two fixed points at the required prestress eccentricity. The concrete is then casted in its required shape around the wires or strands. In other words there is direct contact between the prestressing steel and the concrete. After the concrete has been hardened sufficiently and has gained enough strength, the wires or strands are released from the fixed points and the prestress in the steel is transferred to the concrete by friction and bond stresses.

2.4.2. Relaxation of prestressing steel

A steel tendon which undergoes a fixed deformation, like in the case of prestressing, will have a certain stress. If the strain remains constant over time, the steel stress in the tendon will decrease over time, see also Figure 2.10. This phenomenon is called relaxation of steel. It is attributed to the movement of dislocations or lattice defects in the crystal lattice (Taerwe, 2015).

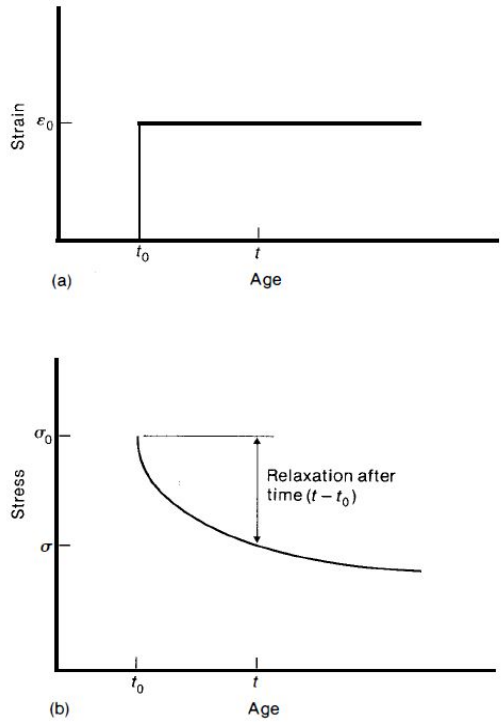

Figure 2.10. Principle of relaxation (Neville et al., 1983). Steel undergoes a constant strain ε_0 (a) and as a result the stress in the steel declines (b).

The relaxation is mainly depended upon the initial steel stress, the quality of the steel, and the ambient temperature. In order to explain the phenomenon the formula below is given (Ghali et al., 2002):

$$\frac{\Delta\sigma_{pr\infty}}{\sigma_{p0}} = -\eta(\lambda - 0.4)^2 \tag{2.6}$$

where σ_{p0} is the initial tension stress in the steel, η is a coefficient dependent of the quality of the steel, $\Delta\sigma_{pr\infty}$ is the intrinsic prestressing loss at infinity, and λ is given by:

$$\lambda = \frac{\sigma_{p0}}{f_{ptk}} \tag{2.7}$$

with f_{ptk} the characteristic tensile strength of the steel. The value of η can be determined out of a long-term test out of which the intrinsic relaxation has been determined. Formula (2.6) is valid for values of λ which are larger than 0.4. For values lower than 0.4 relaxation will not be observed. The formula will result in a value smaller than zero since relaxation is a loss of stress. Standards such as Model Code 90 and Eurocode 2 give values for the relaxation if insufficient data is available.

2.4.3. Interaction of time-dependent deformations

As mentioned above, there is an interaction between the time-dependent phenomena. Figure 2.11 gives a representation of the interaction between relaxation and creep in a stress-strain diagram. Curve one represents a short-term tensile test and curve two represents an infinitely slow tensile test. The infinitely slow test has the purpose of giving the dislocations enough time to move in the crystal lattice. Relaxation causes the stress to decrease under a constant strain. It is represented in the stress-strain diagram by a vertical translation, so point A moves to A_1. Creep is a deformation

under a constant stress. Hence, it is represented by a horizontal translation. Due to creep point A will move to A_2. In a prestressing element, creep will occur under a declining stress, due to relaxation, and relaxation will occur under a declining length, due to creep (and shrinkage). Point A will thus move to point A_3 between point A_1 and point A_2.

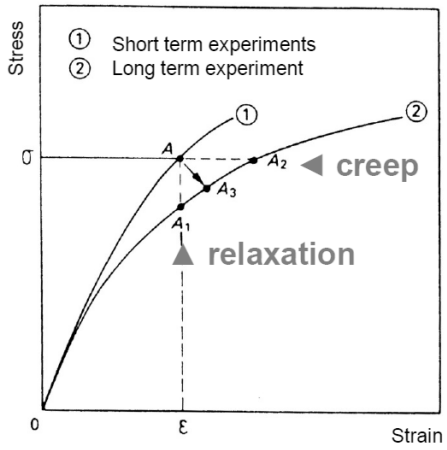

Figure 2.11. Stress-strain diagram representing the interaction between creep and relaxation in a prestressed concrete (Taerwe, 2015).

Instead of looking at just the interaction of creep and relaxation, a more global model for the interaction of time-dependent phenomena is presented in .Figure 2.12. At the moment the prestress is applied to the concrete element, the concrete will elastically shorten. This causes a loss of prestress. The concrete will also shorten over time due to creep and shrinkage. This also causes a loss of prestress, and it makes that the relaxation of the prestress happens under a decreasing length. This is represented in Figure 2.12 by branch r. The decrease of the prestress causes the creep to take place under a decreasing compressive stress. This is shown by branch k. If passive reinforcement is present at the bottom or the top, the creep and shrinkage cannot happen freely but will be restrained. This is represented by branch s_1 and s_2, respectively for bottom reinforcement and top reinforcement.

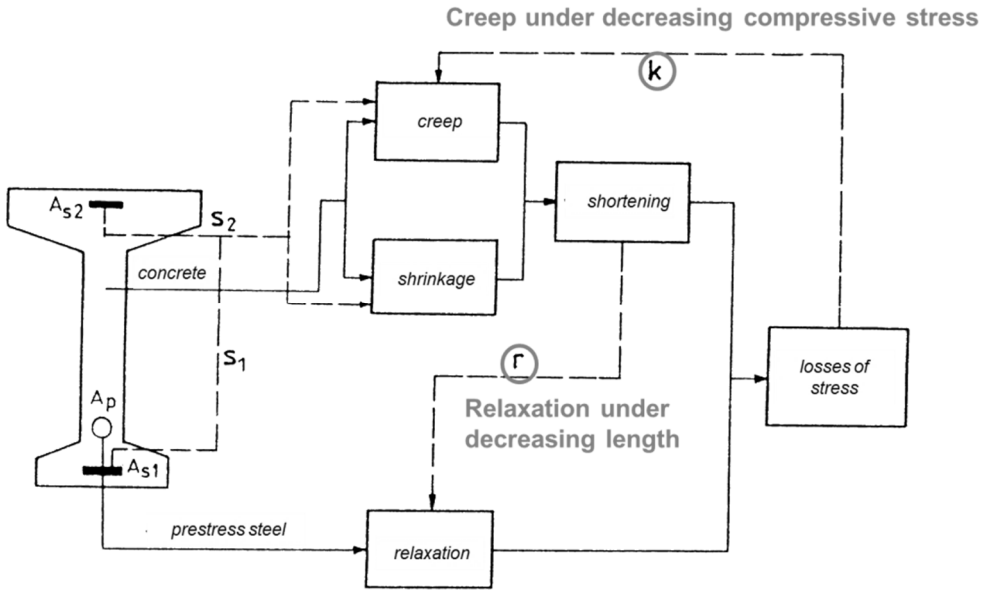

Figure 2.12. Flow chart of the interaction between the time-dependent phenomena (Taerwe, 2015).

Out of this elaboration it is clear that the interaction of the time-dependent phenomena complicates the calculation process significantly. It is required to split up the time domain in intervals and update the stresses and the strains in each time interval for all the phenomena. As an example the updating of the relaxation is given hereunder.

The loss of prestress, as a result of the shortening of the prestressed member due to creep and shrinkage, can be seen as a lower initial tension in the tendon. Hence, the relaxation in a concrete member will be smaller than in a pure theoretical case. The relaxation in a concrete member can thus be calculated as (Ghali et al., 2002):

$$\Delta\bar{\sigma}_{pr} = \chi_r \cdot \Delta\sigma_{pr} \tag{2.8}$$

where $\Delta\bar{\sigma}_{pr}$ is the prestressing loss in a concrete member, χ_r is a dimensionless factor which is smaller than one, and $\Delta\sigma_{pr}$ is the prestressing loss in an ideal case. χ_r is dependent of λ and can be calculated out of tables or graphs.

2.4.4. Prestress losses

As elaborated in the previous section, the interaction of the time-dependent phenomena causes a loss of prestress. There are also other origins of prestress loss. Generally, the prestress losses are split up in two groups: immediate prestress losses and time-dependent prestress losses.

The immediate prestress losses take place at the moment the prestress is transferred from the steel to the concrete. The immediate prestress loss can be split up in four categories (Taerwe, 2015). The first one is the loss due to the elastic shortening of the concrete at the moment when the prestress is transferred (ΔP_{el}). This loss is only present when pre-tensioned steel is used. During tensioning of post-tensioned steel there is also elastic shortening of the concrete, but this does not cause a loss of prestress. The second loss occurs due to friction of the prestressing steel in the cable duct (only for post-tensioned steel) and due to friction at the deflection points ($\Delta P_{\mu}(x)$). The third is the loss due to slip of the prestressing steel at the anchorages and the deformation of the anchorages at the moment of force transfer (ΔP_{sl}). The last loss takes place only in the case of pre-tensioning. It is the loss due to the short-term relaxation of the prestressing steel at the moment between tensioning of the steel and force transfer (ΔP_r).

The mean initial prestress force at a location x from the active anchorage $P_{m,0}(x)$ can be found by subtracting the immediate prestress losses from the maximum prestress force during prestressing P_{max}:

$$P_{m,0}(x) = P_{max} - \Delta P_i(x) \tag{2.9}$$

with $\Delta P_i(x)$ the immediate prestress losses at a location x from the active anchorage:

$$\Delta P_i(x) = \Delta P_{el} + \Delta P_{\mu} + \Delta P_{sl} + \Delta P_r \tag{2.10}$$

Taerwe (2015) attributes the time-dependent prestress losses to: shortening of the concrete due to shrinkage $\Delta P_s(x)$, shortening of the concrete due to creep $\Delta P_c(x)$, relaxation of the prestressing steel $\Delta P_R(x)$ and interaction of the three previous causes mutually and with the passive reinforcement $\Delta P_{int.}(x)$.

The mean value of the prestressing force at a certain time t at a location x from the active anchorage $P_{m,t}(x)$ can be calculated from:

$$P_{m,t}(x) = P_{m,0}(x) - \Delta P_{c+s+r}(x) \tag{2.11}$$

with $\Delta P_{c+s+r}(x)$ the sum of all the time-dependent prestress losses at a location x from the active anchorage:

$$\Delta P_{c+s+r}(x) = \Delta P_s(x) + \Delta P_c(x) + \Delta P_R(x) + \Delta P_{int.}(x) \tag{2.12}$$

This value is often 15% to 20% of $P_{m,0}(x)$ respectively for outdoor and indoor environmental conditions. Equation (2.9) and (2.11) can be combined to form:

$$P_{m,t}(x) = P_{max} - \Delta P_i(x) - \Delta P_{c+s+r}(x) \tag{2.13}$$

Figure 2.13 and Figure 2.14 show the evolution of the prestress in function of time for respectively post-tensioned and pre-tensioned steel. $P_{m,\infty}(x)$ is the prestressing force at a time infinitely removed from now at a location x from the active anchorage. From the figures it is clear that the rate decreases as the time increases. The difference between post-tensioned and pre-tensioned steel can also be clearly seen. Before force transfer, the pre-tensioned steel already starts relaxation. During this time the concrete can also undergo some (autogenous) shrinkage.

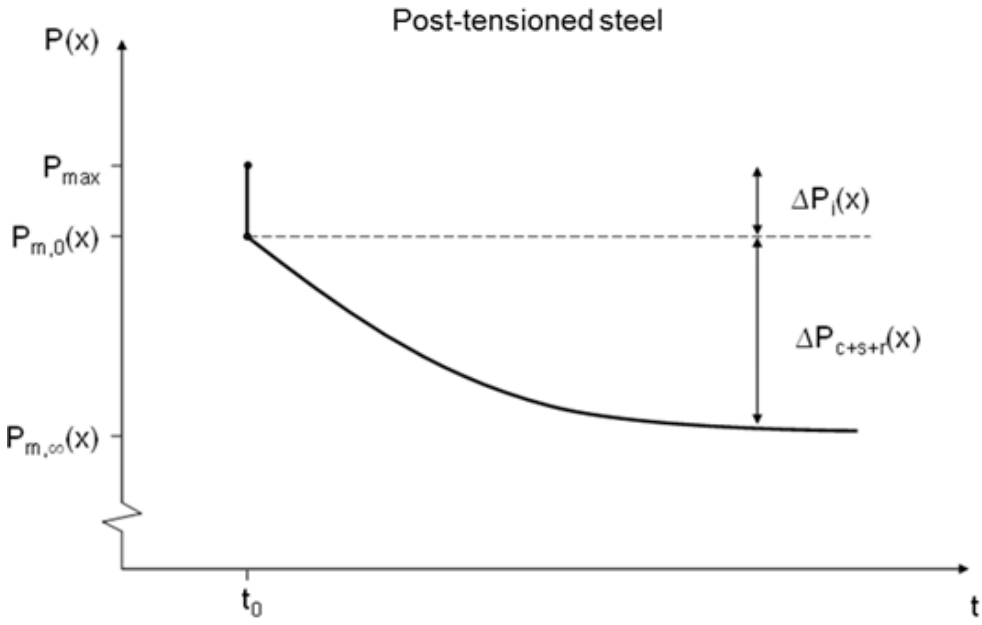

Figure 2.13. Evolution of prestressing force in post-tensioned steel at a certain location x from the active anchorage in function of the time (Taerwe, 2015).

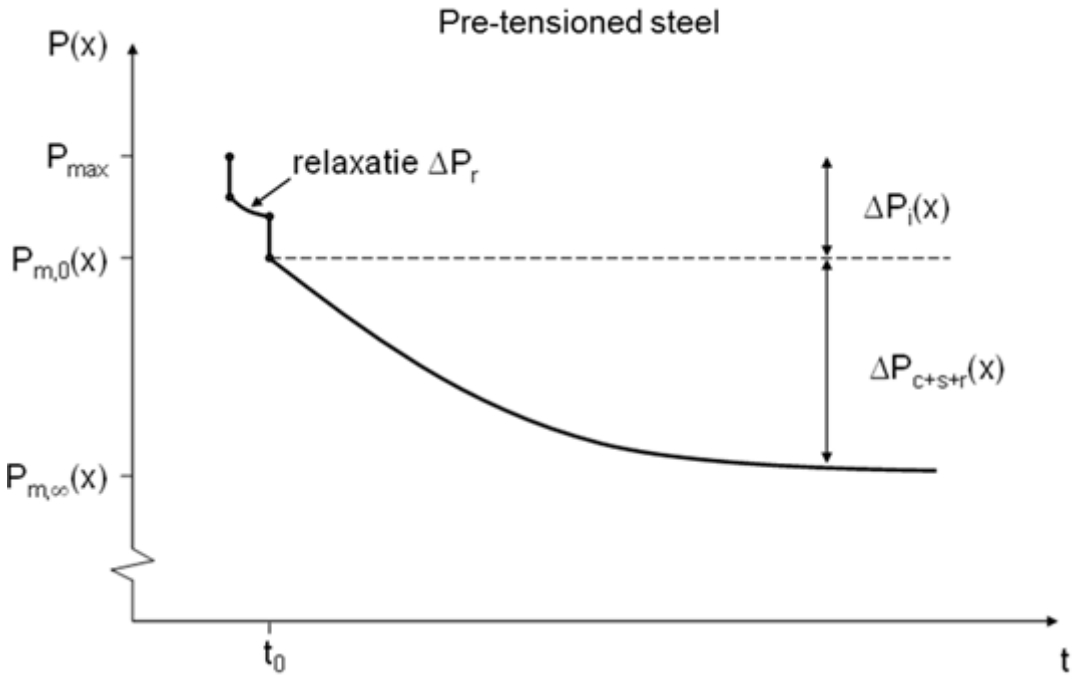

Figure 2.14. Evolution of prestressing force in post-tensioned steel at a certain location x from the active anchorage in function of the time (Taerwe, 2015).

3. Calculation methods to account for time-dependent effects in structural analysis

In this section different forms of the creep law will be discussed using the superposition principle. Another widely used method is the step-by-step method. This method is computationally much more intensive than the superposition principle and therefore was not used.

3.1. Superposition of creep

Concrete behaviour is complex but mostly it is assumed that concrete has an aging linear viscoelastic behaviour. Under this assumption the principle of superposition is valid if four conditions are fulfilled (Bažant, 1982; CEB, 1999):

1) The magnitude of the stresses is in the service range (below about 40% of the strength);
2) The strains do not decrease in magnitude (, although it should be noted that the stresses can);
3) There is no significant drying of the specimen during creep;
4) There is no large increase of the stress a long time after initial loading.

The need for the superposition principle comes from the fact that a concrete element will be subjected to higher loads than just the ones at the first time of loading. For example a concrete slab will first undergo a loading due to its self-weight. Later it will also undergo loading due to service loads etc. To deal with these additional loadings equation (2.2), which gives the strain at a random time t after loading, needs to be extended with an extra term (Ghali et al., 2002):

$$\varepsilon_c(t) = \sigma_c(t_0) \cdot \frac{1+\varphi(t,t_0)}{E_c(t_0)} + \int_0^{\Delta\sigma_c(t)} \frac{1+\varphi(t,\tau)}{E_c(\tau)} d\sigma_c(\tau) + \varepsilon_{cs}(t,t_0) \tag{3.1}$$

where:

$\varepsilon_c(t)$ is the total concrete strain

τ is an intermediate time between the moment of loading t_0 and the moment of interest t

$\Delta\sigma_c(t)$ is the total stress increase at moment t, relative to t_0

$\varphi(t,\tau)$ is the creep coefficient at time of interest t with loading at time τ

$E_c(\tau)$ is the modulus of elasticity at time τ

$d\sigma_c(\tau)$ is the increment of stress at time τ

$\varepsilon_{cs}(t,t_0)$ is the free shrinkage between t_0 and t

A physical representation of this equation is shown in Figure 3.1. The first term on the right side of equation (3.1) is the strain at a random time t due to loading at time t_0. This term is equal to equation (2.2). The last term takes into account the free shrinkage of the specimen. The additional loading after the first time of loading t_0 is taken into account by the integral.

The formulation of superposition assumes that different units of stress increment, imposed on a specimen at the same time and for the same duration, result in a same value of creep. In other words, a linear relationship is assumed. This is valid for stress ranges in the service condition, see

section 2.3. Since part of the creep is irrecoverable, this equation is only valid for stress increments and not for stress decrements.

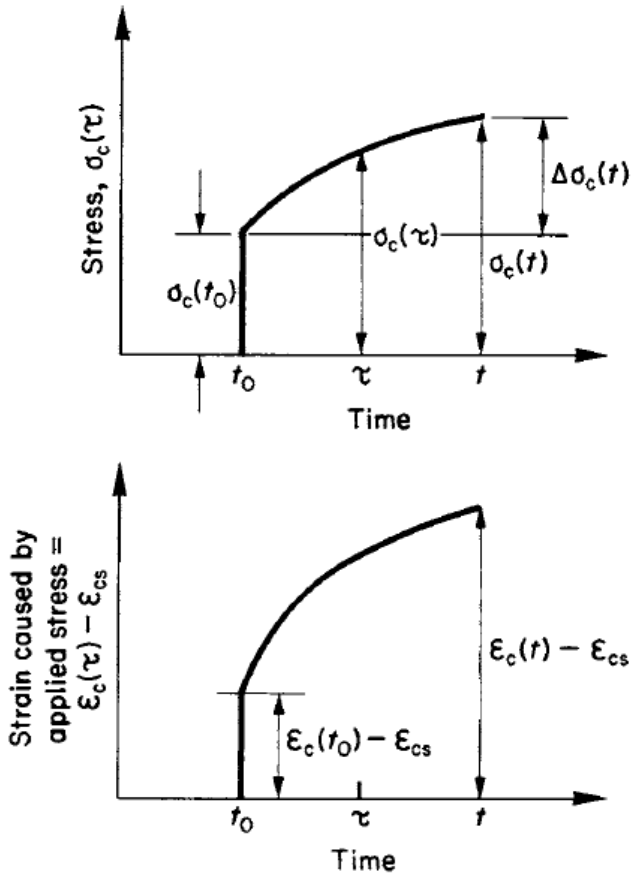

Figure 3.1. Stress versus time, respectively strain versus time of concrete element subjected to stress increase after initial time of loading.(Ghali et al., 2002)

3.2. Aging coefficient

The integral in equation (3.1) makes the practical use of the equation difficult since a continuous set of measurements is required. One can simplify this expression by assuming the incremental stress is fully applied at time t_0 and sustained thereafter. This is of course an overestimation compared to the original case where the incremental stress is applied over time. To take this overestimation into account the dimensionless aging coefficient $\chi(t, t_0)$ is used.

$$\varepsilon_c(t) = \sigma_c(t_0) \cdot \frac{1 + \varphi(t, t_0)}{E_c(t_0)} + \Delta\sigma_c(t_0) \cdot \frac{1 + \chi(t, t_0) \cdot \varphi(t, t_0)}{E_c(t_0)} + \varepsilon_{cs}(t, t_0) \tag{3.2}$$

The aging coefficient generally has a value between 0.6 and 0.9. (Ghali et al., 2002). It can be determined by tables or it can be calculated out of a formula. One of the possible formulas is (Taerwe, 2015):

$$\chi(t, t_0) = \frac{\int_{t_0}^{t} \varphi(t, \tau)\, d\sigma_c(\tau)}{\Delta\sigma_c(t_0) \cdot \varphi(t, t_0)} \tag{3.3}$$

3.3. Age-adjusted effective modulus method

The concept of an age-adjusted modulus of elasticity was first described by Bažant (1972). Under the assumptions of stresses in the normal working range and no unloading, the linear principle of superposition, as described in section 3.1, describes the creep phenomenon. The stress-strain relation is defined if the compliance function and the free shrinkage, or the creep coefficient, the modulus of elasticity and the free shrinkage are known. The age-adjusted effective modulus of elasticity can be defined as:

$$\overline{E_c}(t, t_0) = \frac{E_c(t_0)}{1 + \chi(t, t_0) \cdot \varphi(t, t_0)} \tag{3.4}$$

Putting equation (3.4) into equation (3.2) results in (Ghali et al., 2002):

$$\varepsilon_c(t) = \sigma_c(t_0) \cdot \frac{1 + \varphi(t, t_0)}{E_c(t_0)} + \frac{\Delta\sigma_c(t_0)}{\overline{E_c}(t, t_0)} + \varepsilon_{cs}(t, t_0) \tag{3.5}$$

3.4. Effective modulus method

A more simple approach compared to the age-adjusted effective modulus method is the effective modulus method. The total stress variation is assumed to act at time t_0. The error of this method is large compared to a theoretical solution in case aging concrete is studied (Bažant, 1972). The concrete properties, and thus also the modulus of elasticity, are then still changing. This leads to a significant overestimation, as was already mentioned in section 3.2. Applying the assumptions on equation (3.2) results in:

$$\varepsilon_c(t) = \sigma_{ct}(t_0) \cdot \frac{1 + \varphi(t, t_0)}{E_c(t_0)} + \varepsilon_{cs}(t, t_0) \tag{3.6}$$

where $\sigma_{ct}(t_0)$ is the total stress or: $\sigma_{ct}(t_0) = \sigma_c(t_0) + \Delta\sigma_c(t_0)$. Equation (3.6) can also be derived from equation (3.2) by taking 1 as value for $\chi(t, t_0)$. The effective modulus can be defined as:

$$E_{c,eff} = \frac{E_c(t_0)}{1 + \varphi(t, t_0)} \tag{3.7}$$

Note that this is the inverse of the compliance function, see equation (2.4). By the use of the effective modules and the assumption that all the stress is induced at t_0, equation (3.2) becomes:

$$\varepsilon_c(t_0) = \frac{\sigma_{ct}(t_0)}{E_{c,eff}} + \varepsilon_{cs}(t, t_0) \tag{3.8}$$

4. Material models for creep and shrinkage

There are a lot of material models which are currently used today. The models used in this thesis are: CEB-FIP Model Code 1990-1999 (MC90-99) (CEB, 1999), fib Model Code 2010 (MC2010) (CEB-FIP, 2013), Eurocode 2 (EC2) (NBN EN 1992-1-1, 2005), Bazant's and Baweja's B3 model (Bažant & Baweja, 2000), Gardner's and Lockman's GL 2000 model (Gardner, 2004), and ACI 209.2R-08 (ACI)(ACI Committee 209, 2008). Some are entirely empirical based, such as the GL 2000 model, and others are based on theoretical principles, like the B3 model. There is also a difference in the required input data, the validity range, the accuracy and the calculation method. It is not the goal of this work to give a complete overview of each model. However, since it is the goal of this work to compare the different models against a test base and look at the diverging results, a brief comparison of the models will be provided.

4.1. CEB-FIP Model Code 1990-1999

MC90-99 is an update of the shrinkage and creep model of the Model Code 1990 (MC90) (CEB-FIP, 1993). MC90 was based on research by Müller and Hilsdorf (1990). MC90-99 (CEB, 1999) makes a distinction between autogenous shrinkage and drying shrinkage but it does not differentiate between basic creep and drying creep. Both the model for creep as well as the model for shrinkage are valid for normal-weight plain structural concrete ($15 \leq f_{cm} \leq 120$ MPa), which has been moist cured for a maximum of 14 days. The environment has a mean ambient relative humidity (RH) between 40 and 100 percent, and a temperature between 10°C and 30°C. The model has a correction for the time of loading if the temperature differs from 20°C. Doing the calculations of the creep model of MC90-99 results in a value for the creep coefficient. The code then proposes a formula to calculate the creep function. Note that this formula is slightly different defined then the previously stated formula (2.4) for the calculation of the creep function. The reason for this is that MC90-99 defines the creep coefficient as the ratio of the creep strain over the elastic strain at 28 days. The formula proposed by MC90-99 is equal to:

$$J(t,t_0) = \frac{1}{E_c(t_0)} + \frac{\varphi(t,t_0)}{E_{cm28}} \tag{4.1}$$

This formula now not only includes $E_c(t_0)$ the modulus of elasticity at loading, but also E_{cm28} the modulus of elasticity of the concrete at 28 days.

4.2. FIP Model Code 2010

Unlike MC90-99, MC2010 (CEB-FIP, 2013) differentiates between autogenous shrinkage and drying shrinkage, as well as basic creep and drying creep. The formulas are applicable for normal structural concrete ($20 \leq f_{cm} \leq 130$ MPa) between a relative humidity of 40% and 100%. The concrete may not be moist cured for longer than 14 days at a normal temperature. The temperature should be between 5°C and 30°C, though the model has formulas to deal with temperature effects in the range between 0°C and 80°C. Different cement types result in a different degree of hydration at a certain time. The model takes this into account for creep by adjusting the time of loading. Normally

stresses should not exceed 0.4 times the mean concrete strength at loading in order to remain in the linear creep region. The model can however be extended to take nonlinear creep into account up to 0.6 times the mean concrete strength. It should be noted that this extension neglects the fact that the nonlinearity decreases as the load duration increases. The compliance function can be obtained from the calculated creep coefficient according to formula (4.1).

4.3. Eurocode 2

The models which are used in EC 2 (NBN EN 1992-1-1, 2005) are a combination of MC90-99 and MC2010. The creep model is completely similar to MC90-99. It however has the same extension as MC2010 with regard to nonlinear creep. The only difference is that EC2 considers that nonlinear creep happens at stresses over 0.45 times the characteristic concrete stress at time of loading. This difference results in a small deviation of a constant in the nonlinear creep formula. The shrinkage model is also based on MC90-99, although some formulas are different. The compliance function can be calculated using formula (4.1).

4.4. B3 Model

The model with the strongest theoretical background is the model B3 from Bažant and Baweja. The model was first approved as the international RILEM recommendation in (1995) and was later updated (Bažant & Baweja, 2000). The B3 model is theoretically developed and calibrated with the help of a large computerized database. Unlike the other models, the B3 model gives formulas to calculate the creep function instead of the creep coefficient. If wanted, the creep coefficient can be calculated from equation (2.4). The largest sources resulting in errors are the effect of the concrete composition and the concrete strength on the model parameters. Bažant and Bajewa, however, propose a method to update two model parameters based on the results of short-time creep tests to reduce these errors. The model is valid for Portland cement which has been cured for at least a day with the following characteristics:

$$0.35 \leq \frac{w}{c} \leq 0.85$$

$$2.5 \leq \frac{a}{c} \leq 13.5$$

$$17 \leq f_{cm} \leq 70 \ \ (all\ in\ MPa)$$

$$160 \leq c \leq 720 \ \ (all\ in\ kg/m^3)$$

In which $\frac{w}{c}$ is the water-cement ratio by weight, $\frac{a}{c}$ is the aggregate cement ratio by weight, f_{cm} is the mean compressive strength of a concrete cylinder at the age of 28 days and c is the cement content. The use of the model is restricted to stress values smaller than 0.45 f_{cm}. The model takes the drying creep and the basic creep separately into account. With regards to the shrinkage, the formulas have been developed for drying shrinkage only. Autogenous shrinkage is nonetheless indirectly taken into account because the database for calibration contained the total shrinkage.

4.5. Gardner Lockman 2000 model

Gardner and Lockman (2001) proposed the GL 2000 model. This model was later updated by Gardner (2004). An update of certain constants was later published by Goel et al. (2007). The GL 2000 model is completely empirical. The number of required parameters is minimal. Despite this, the model obtains good results (Goel et al., 2007, see also below). No distinction is made between autogenous shrinkage and drying shrinkage. Instead, a total shrinkage is calculated. The creep component has 3 major terms, from which two are related to the basic creep and the other one is related to the basic creep. The model is valid for normal strength concretes with mean compressive strengths lower than 82 MPa which are not subjected to self-desiccation (ACI Committee 209, 2008). The method can be used irrespective of chemical admixtures or mineral by-products, casting temperature, or type of curing (Gardner & Lockman, 2001). The compliance function can be calculated similar to the MC90-99 model.

4.6. ACI 209.2R-08

The ACI 209R-92 model, with relation to shrinkage and creep, is an empirical model, and was first developed by Branson and Christiason (1971). Later it was updated by ACI Committee 209 (1992) and the model was reapproved by the ACI in 2008 (ACI Committee 209, 2008). No differentiation is made between the different forms of shrinkage and the model also cannot model swelling. Likewise, creep is modelled as a whole and is not split up in basic creep and drying creep. The models for shrinkage and creep consist out of two parts: a time-development factor and an ultimate value. This ultimate value has been developed for a specific, standardised case. Several factors are then utilised to correct for situations deviating from the standardised case. This makes it, by far, the easiest model. In the end, the compliance function can be calculated from equation (2.4). The model is valid for a cement content between 279 and 446 kg/m³ and a relative humidity between 40% and 100%. If the concrete is moist cured, it should be cured for at least a day. If the concrete on the other hand is steam cured, it should be cured between 1 and 3 days. The load should not be applied sooner than 7 days and furthermore, the model is only valid for R and RS concrete. (ACI Committee 209, 2008)

4.7. Comparison of the different models

4.7.1. Parameters

From the previous sections, it is clear that each model has a different validity range, although there is a wide area where they overlap. For MC90-99, MC2010 and EC2 the validity range is almost identical. This is logical since MC2010 and EC2 are based on MC90-99. This can also be seen from the input these three models require: the required parameters are identical. Table 4.1 and Table 4.2 show the required input parameters for shrinkage, respectively creep. For both it has been assumed that all parameters are known. For example, if the modulus of elasticity at 28 days is unknown, most models provide a formula to calculate it from the concrete strength but this approach was not considered. Table 4.2 gives the required parameters to come to the compliance function, since it would otherwise not be possible to compare the different models: the B3 model is a compliance function, while the others are creep coefficient functions.

The GL 2000 model requires the least amount of parameters and does not even require the concrete compressive strength to calculate the creep coefficient. The ACI model does not require the concrete strength at all, neither for the calculation of the shrinkage strain nor the calculation of the creep coefficient. A possible reason for this is that the ACI model provides an ultimate value for the creep and shrinkage, which is then updated depending on the ruling conditions. The other models don't provide an ultimate value for the creep nor for the shrinkage. Instead they provide formula to calculate these values. The ACI model has also a few unique input parameters compared to the other models, namely: the slump of fresh concrete, the fine aggregate content, the cement content and the air content. The B3 model requires the most parameters. It is the only model which takes into account: the shape of the cross-section, the water content, the water-cement ratio, the cement content, and the aggregate to cement ratio. It is also the only model which requires the modulus of elasticity for the calculation of the shrinkage.

Table 4.1. Input variables for the different shrinkage models.

	B3	MC90-99	MC2010	EC2	GL 2000	ACI
Relative humidity	Yes	Yes	Yes	Yes	Yes	Yes
End of curing	Yes	Yes	Yes	Yes	Yes	Yes
Volume to surface ratio	Yes	Yes	Yes	Yes	Yes	Yes
Concrete strength	Yes	Yes	Yes	Yes	Yes	No
Cement type	Yes	Yes	Yes	Yes	Yes	No
Type of curing	Yes	No	No	No	No	Yes
Shape of cross-section	Yes	No	No	No	No	No
Modulus of elasticity	Yes	No	No	No	No	No
Water content	Yes	No	No	No	No	No
Slump of fresh concrete	No	No	No	No	No	Yes
Fine aggregate content	No	No	No	No	No	Yes
Cement content	No	No	No	No	No	Yes
Air content	No	No	No	No	No	Yes

Table 4.2. Input for the different creep models resulting in the compliance function.

	B3	MC90-99	MC2010	EC2	GL 2000	ACI
Relative humidity	Yes	Yes	Yes	Yes	Yes	Yes
Age at loading	Yes	Yes	Yes	Yes	Yes	Yes
Volume to surface ratio	Yes	Yes	Yes	Yes	Yes	Yes
Modulus of elasticity	Yes	Yes	Yes	Yes	Yes	Yes
Concrete strength	Yes	Yes	Yes	Yes	No	No
Cement type	Yes	Yes	Yes	Yes	No	No
End of curing	Yes	No	No	No	Yes	No
Type of curing	Yes	No	No	No	No	Yes
Cement content	Yes	No	No	No	No	No
Water-cement ratio	Yes	No	No	No	No	No
Aggregate-cement ratio	Yes	No	No	No	No	No
Water content	Yes	No	No	No	No	No
Shape of cross-section	Yes	No	No	No	No	No
Slump of fresh concrete	No	No	No	No	No	Yes
Fine aggregate content	No	No	No	No	No	Yes
Air content	No	No	No	No	No	Yes

4.7.2. Accuracy

In his paper where he gives an update of the GL 2000 model, Gardner (2004) also compared: MC90-99 (CEB, 1999), the original B3 model (Bažant & Baweja, 1995), the ACI 209-82 model (ACI Committee 209, 1982), and the GL 2000 model (Gardner, 2004). The ACI 209-82 model is an update of the original model by Branson and Christiason (1971) and is the version before the ACI 209 R-92 model. Gardner did two accuracy comparisons using the same RILEM database: one where he assumed that all data was available (mix proportions, concrete strength development with age and modulus of elasticity) and another one where he assumed that only the mean concrete strength was known. For the "all data" comparison he also took into account the stiffness of the aggregates. This by back-calculating the concrete strength out of the measured modulus of elasticity using the appropriate method valid for the model, and subsequently taking the average of this calculated strength and the reported mean concrete strength. He discerned that using all the data, the GL 2000 model and the B3 model were the best models to predict shrinkage. For the prediction of compliance, the GL 2000 model was the best. If only the mean concrete strength was used, he concluded that the GL 2000 model was most accurate in predicting shrinkage. For compliance, the B3 model and the GL 2000 model had about the same accuracy. Furthermore, the ACI 209-82 model for shrinkage had a lot of scatter as well as an illogical trend: it overestimated at early age and underestimated at older ages. He attributed this to a lack of a size term in the time component of the shrinkage formula. The ACI 209-82 model was also divergent in the fact that including extra information lowered the accuracy of the shrinkage prediction and did not change the prediction of the compliance.

Fanourakis (2011) compared the accuracy of six different models with regards to total creep values, including EC2 (EN 1992-1-1, 2004) and both the original GL 2000 model (Gardner & Lockman, 2001) as well as the adaption of the model by Gardner (2004). This was done using the calculated values for the modulus of elasticity of each of the models. The tested concrete types were typical South African concretes. A database containing six different concrete mixes was used for the comparison. The measurements were done over a measuring period of 168 days. In order to take the aggregate stiffness into account tests were done on samples taken from representative boulders. For the prediction of the modulus of elasticity, Fanourakis determined that EC2 was the least accurate of the models considered, although the difference with the GL 2000 model was rather small. In general it was concluded that the differences between the calculated and measured moduli of elasticity were not significant. The GL 2000 model (Gardner & Lockman, 2001) gave the most accurate result with regards to creep predictions, followed by EC2 and the adapted GL 2000 model (Gardner, 2004).

The predictions for shrinkage and creep of the original B3 model (Bažant & Baweja, 1995), the ACI 209-82 model (ACI Committee 209, 1982), the original GL 2000 model (Gardner & Lockman, 2001), the MC90 (CEB-FIP, 1993) and the MC90-99 (CEB, 1999) were compared by Goel et al. (2007). These creep and shrinkage predictions were compared against the experimental results of Russel and Larson (1989). Goel et al. looked only at the results between 365 days and 5000 days, since they reasoned that shrinkage and creep are long-term effects. For shrinkage it was concluded that the B3 model, the MC90, and the ACI 209-82 model consistently underestimate the experimental values. The best results were obtained by the GL 2000 model, followed by both the B3 model and the MC90-99. The MC90 and the ACI 209-82 model gave the least accurate shrinkage

predictions. With regards to the creep, they observed that the B3 model mostly overestimated the experimental results. While the MC90, the MC90-99, and the ACI 209-82 model in most cases underestimated the creep. Goel et al. (2007) concluded that none of the models is capable to predict creep accurately for all grades of concrete and all durations. However, the GL 2000 model gave usually the best result. Goel et al. (2007) don't mention it explicitly, but from their results it can be concluded that in the majority of the cases MC90 gives a more accurate prediction than MC90-99.

Bažant and Li (2008b) criticised the way in which models were compared: a model that was considered as the most optimal according to one statistical indicator was considered as not optimal according to another. They reasoned that the only correct statistical approach to compare creep and shrinkage models is to use the method of least squares, which is consistent with the central limit theorem. For their comparison they used the NU-ITI Database (Bažant & Li, 2008a), which is an extension of the RILEM database. They however did not use the data out of this database as is; they described a method of weighing. This was required to compensate for the non-uniform character of the data (e.g. there are more short-term tests than long-term tests, there are more tests on specimen with a relative low volume over surface ratio than on specimens with a practical volume over surface ratio,…). The method they described consists of creating four-dimensional boxes and using weight factors for each of the boxes. These boxes are created by splitting up the data in intervals of equal statistical weight by: duration of loading (or duration of drying, dependent on whether you consider creep or shrinkage), start of loading (or start of drying, dependent on whether you consider creep or shrinkage), effective thickness, and relative humidity. This resulted unfortunately in boxes that are nearly or completely empty. This then required a deletion of these boxes which resulted in an inequality of the relative weights of the boxes and of the data set. This problem was still present for three-dimensional boxes. Bažant and Li therefore proposed the use of two-dimensional boxes or even one-dimensional boxes. Furthermore, they proposed three possible transformations of random variables. The first being a scaling to correct for the strength: the data on long-term tests is dominated by older concrete which has a higher water-cement ratio and a different admixture use, compared to the currently used concretes. The second follows from the observation that relative deformation is less dependent on changes in the concrete composition than the total deformation. And the last transformation is motivated by the fact that plots of the creep or shrinkage data against the load duration, respectively drying duration, show a heteroscedastic character. This requires scaling because the statistical analysis works best when the data are homoscedastic. Bažant and Li came to an adapted database by transforming the original database by one of the three aforementioned transformations and by converting this transformed database to one- or two-dimensional boxes. This adapted database was then used to compare five models, including: the B3 model (Bažant & Baweja, 2000), the ACI 209R-92 model (ACI Committee 209, 1992), the MC90-99 (CEB, 1999), and the original GL 2000 model (Gardner & Lockman, 2001). They did comparisons of the models by looking at the coefficients of variation of errors or the correlation coefficients (both defined according to standard regression statistics). These comparisons were done on different combinations of boxes (one-dimensional or two-dimensional) and with or without one of the three possible transformations. In all except one comparison, the B3 model came out as the best creep and shrinkage model. The original GL 2000 model came out as the second best model, followed by the MC90-99 on the third place. The ACI 209R-92 model was the worst model according to the comparison.

As is clear from the above, many researchers devoted their time to the comparison of the different shrinkage- and creep models. It is however also clear that there is not a single comparison using all the latest versions of the models e.g.: Goel et al. (2007) used an outdated version of both the model B3, as well as the GL 2000 model; Bažant and Li (2008b), while using the updated B3 model, used the outdated version of the GL 2000 model; etc. Another problem is that the databases, against which the models were compared, contain a lot of short-term creep test, as well as creep tests performed primarily on small elements. The comparison which is done in this work is therefore quite unique. It is done with the latest versions of the models. But, far more important, the comparison is done using long-term data of beams with dimensions which are used in practice.

5. Available experimental data

5.1. Introduction

The available experimental data is part of the general research programme titled: “The influence of the duration of permanent loading on the behaviour of concrete elements, reinforced concrete elements and prestressed concrete elements”. The original Dutch title is: “Invloed van de werkingsduur van permanente lasten op het gedrag van elementen in beton, in gewapend beton en in spanbeton”. The research programme was executed under supervision of: professor Dehousse, professor Moenaert, professor Reyntjens, and professor Riessauw. The last one also being the spokesman of the research. The programme was funded by “het Fonds voor Collectief Fundamenteel Onderzoek” and took place in the laboratories of the universities of: Brussels, Ghent, Leuven, and Liège. It is possible to identify the programme by its research number: FKFO no. 547.

In a first phase, from 1967 until 1972, the tests on reinforced beams have been performed. In a second phase, from 1975 until 1980, the tests on prestressed beams were executed. In 1980 extra funding was granted in order to extend the programme to also include partially prestressed beams.

In the first part of this chapter the experimental programme for the reinforced beams is described. In the second part the experimental programme for the prestressed beams is described. The idea behind both phases was similar; researching the time-dependent phenomena in concrete. The first phase (with reinforced beams) focused on the influence of the reinforcement density, while the second phase (with the prestressed beams) focused on the influence of the shape of the cross-section and the difference between pre-tensioning and post-tensioning.

This research programme is quite unique; the main focus was on the testing of beams with practical dimensions, whereas most of literature focusses on tests performed on small specimens. Furthermore, the long-term testing was done up to four and a half years, which is longer than the majority of tests reported in literature. As also mentioned above, four laboratories participated in the programme, which endorses the extent and the profoundness of the research programme. The combination of these three factors makes that this experimental data is invaluable.

All the experimental data is accessible at the archive of the laboratory Magnel at Ghent university. A preliminary analysis of the results of the first phase of this programme has already been done by Reybrouck et al. (2015). In this thesis this analysis will be expanded and also extended towards the second phase.

5.2. Reinforced concrete beams

The tests on reinforced beams were in the first place executed to study the influence of the amount of reinforcement and the magnitude of permanent loads on the time-dependent behaviour of concrete. More specifically, the tests measured: the evolution of the deflection, the evolution of the concrete strain, and the evolution of the crack widths. For this dissertation the measurements of the crack widths were omitted.

5.2.1. Material properties

All the reinforced beams were made out of the same concrete composition. All the coarse aggregates (gravel), the sand, the cement and the main reinforcement were ordered at the same time and were then distributed over the four laboratories. The steel quality of the longitudinal reinforcement was equal to BE400a. The stirrups were made out of steel with quality BE220. The design mean compressive strength at 28 days on cubes with a side of 200 mm was 35 MPa. This resulted in the following concrete composition:

Gravel 4/16: 1260 kg
Sand 0/5: 630 kg
Cement P40: 300 kg
Water: 150 l

The cement P40 is an old Belgian cement. In the current European name system it corresponds to CEM I 52.5 N (Holcim, 2010; Keulen, 2011).

5.2.2. Cross-section and reinforcement

All the reinforced beams had a cross-section of 150 mm by 280 mm. The total length of the beams was 3400 mm, and the span was 2800 mm. Each of the four laboratories tested a different section type; the only difference between the types was the reinforcement ratio. Table 5.1 gives an overview of the structural reinforcement of each type. The reinforcement ratios were determined so that failure of the beam would happen due to yielding of the reinforcement (beam types I, II, and IV), or due to simultaneous crushing of the concrete and yielding of the reinforcement (beam type III). Figure 5.1 shows the detailed reinforcement scheme of beam type IV. Figure 5.2 shows a schematic representation of all four beam types. The detailed reinforcement schemes of beam types I, II, and III are given in Appendix A. Note that for the detailed analysis, of which the results are presented in chapter 7, all the longitudinal reinforcement is taken into account. For example, for beam type IV this means that also the four bars of diameter 10 mm in the middle of the beam are taken into account (Figure 5.1), in addition to the structural reinforcement which is presented in Table 5.1 or Figure 5.2.

Table 5.1. Overview of the structural reinforcement of the four types of reinforced concrete beams.

	Tensile reinforcement	Compression reinforcement
Type I	2 Ø 14 mm	/
Type II	5 Ø 14 mm	/
Type III	8 Ø 14 mm	/
Type IV	5 Ø 14 mm	3 Ø 14 mm

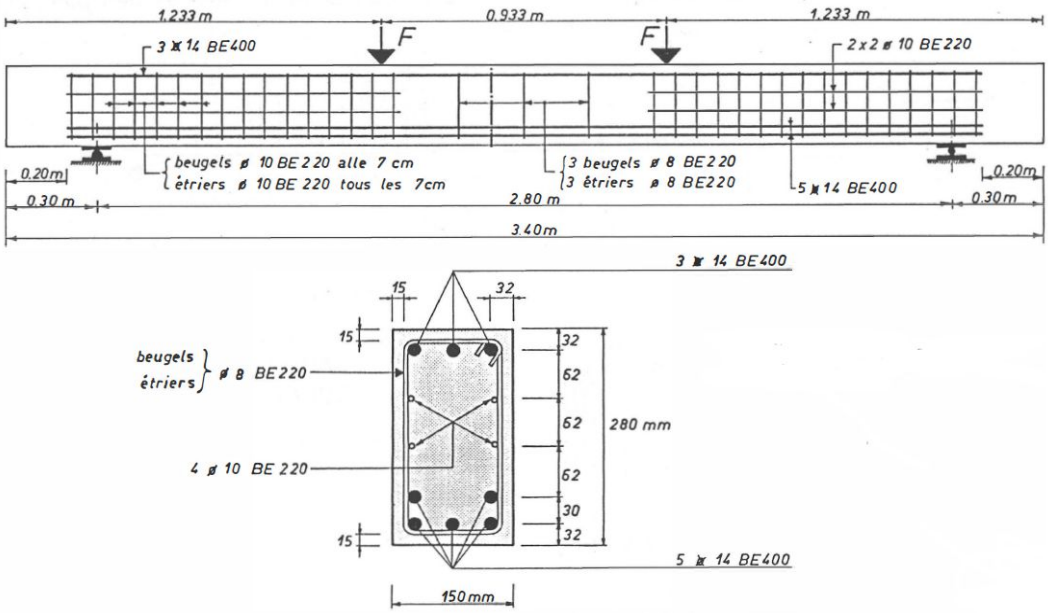

Figure 5.1. Detailed reinforcement scheme of beam type IV. The drawing in the top shows a side view of the beam. The bottom drawing shows the cross-section of the beam. For your information: "beugels" is the Dutch word for stirrups (FKFO no. 547).

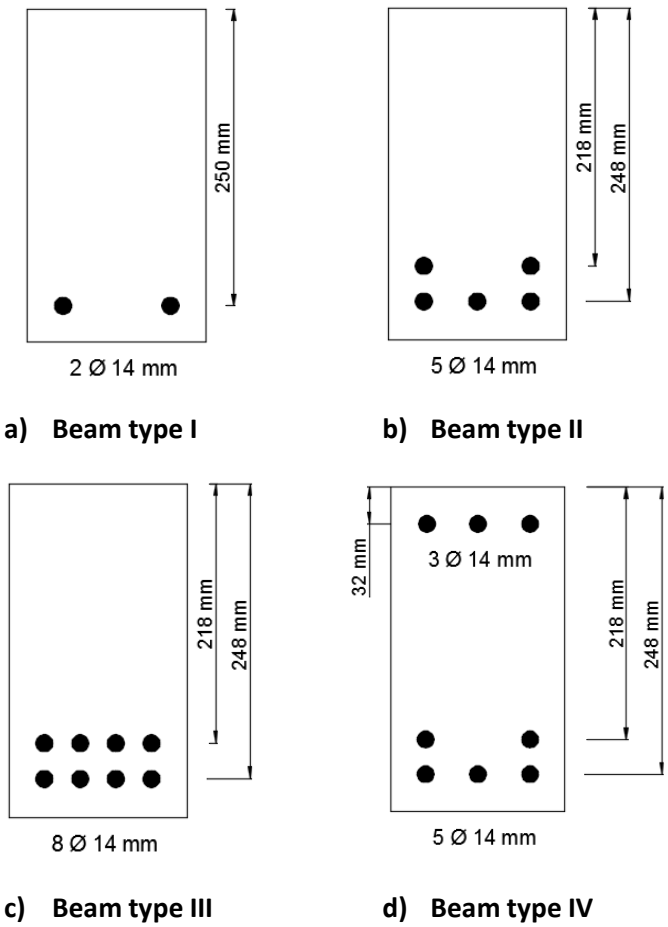

Figure 5.2. Schematic representation of the four different beam types.
All the beams have a width of 150 mm and a height of 280 mm.

5.2.3. Test setup and experimental programme

5.2.3.1. Static tests

From each beam type two beams were subjected to a static test in order to determine the failure moment. The beams were placed on two supports: on the one side a roller support and on the other side a pinned support. The distance between the two supports was 2.800 m. At an age of 28 days, the beams were subjected to a four point bending test. The two point loads were applied at a distance of one third of the left, respectively right support. Figure 5.3 illustrates the four point bending test and the resulting moment line, if the moments imposed by the self-weight of the beams are neglected. The beams were loaded until their service moment in four steps. These service moments were calculated according to the recommendations by CEB (1964). Next, the beams were unloaded completely. Similar as before, the beams were again loaded until their service moment. The load was then increased in steps of about 5% of the theoretical failure load until failure occurred.

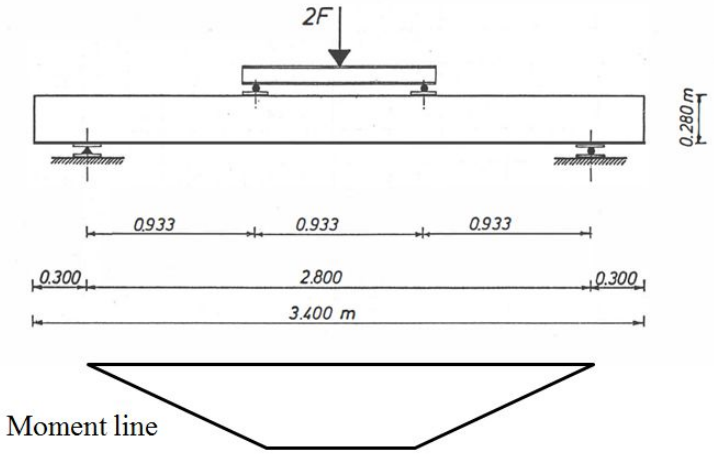

Figure 5.3. Test setup of static tests (adaption of figure from FKFO no. 547).

5.2.3.2. Long-term tests

The long-term tests were executed in an acclimatised room with a temperature of 20°C ± 1°C and a relative humidity of 60% ± 5%. The day after the concrete was casted, the formwork was removed. The tests started at an age of 28 days. The beams were kept under permanent loading between 800 and 1638 days. The test setup can be seen in Figure 5.4, where P represents the force applied by the hydraulic jacks. Two identical beams were tested in the same test setup. The beams were kept in place 300 mm from their end while two hydraulic jacks pushed the beams away from one another. This caused a moment line in both beams similar to the four point bending test described in 5.2.3.1. The span was again 2.800 m, and the loads were again applied at one third of the span. It is important to note that in the top beam the tensile reinforcement was located in the top of the beam, while in the bottom beam the tensile reinforcement was located in the bottom of the beam. This means that in the top beam the gravitational forces acted in a different way than in the bottom beam. The resulting moment in both beams was thus not identical. That is why, the magnitude of the forces applied by the hydraulic jacks was determined, so that the mean moment in the midspan of the two beams was equal to the required moment for the test. This method resulted in a

deviation smaller than 1% between the actual moment in the beams and the mean moment. Figure 5.5 is a picture of the test setup of different beams at the Ghent university.

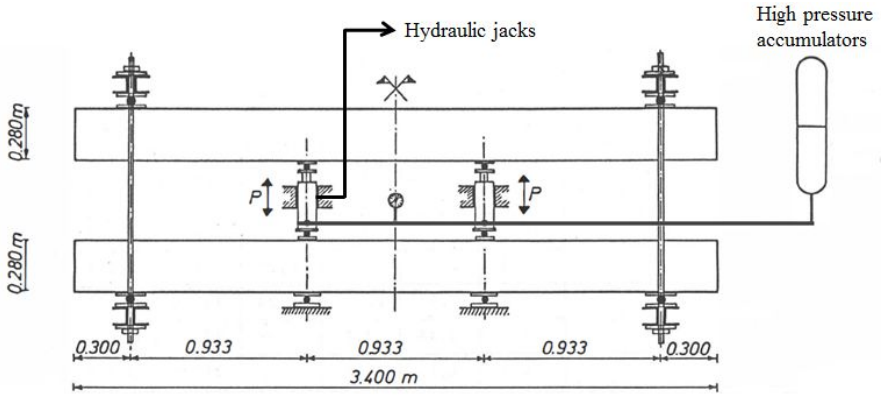

Figure 5.4. Test setup of the long-term tests (FKFO no. 547).

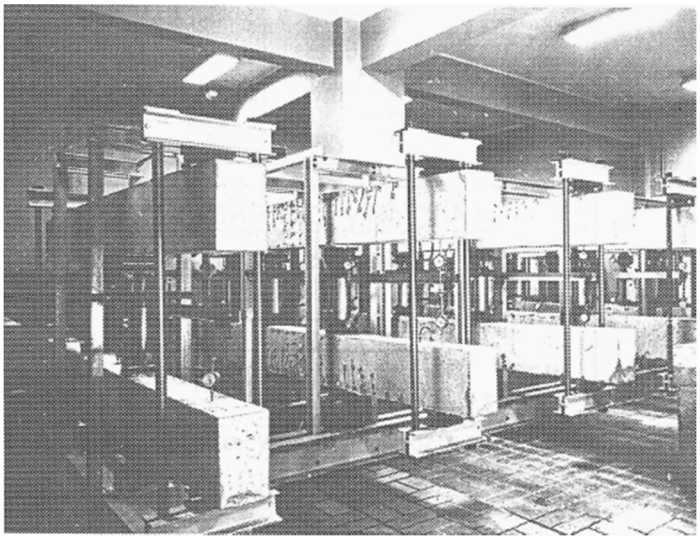

Figure 5.5. Picture of the test setup of the long-term tests at the university of Ghent (FKFO no. 547).

The beams were first loaded until the calculated service moment, as previously described in part 5.2.3.1. Next, the beams were unloaded completely. For the second phase, the beams were loaded immediately until the calculated service moment. The load was then increased in steps of approximately 5% of the theoretical failure load until the desired test moment was obtained. There were four different test moments for each beam type: $0.4 - 0.6\,M_{u,0}$, $\pm\,0.7\,M_{u,0}$, $\pm\,0.8\,M_{u,0}$, $\pm\,0.9\,M_{u,0}$, where $M_{u,0}$ is the experimentally determined failure moment by a static test at 28 days (section 5.2.3.1). In total 32 beams were tested under long-term loading, since the beams were tested in pairs, there were 16 different test setups.

In order to keep the loading constant throughout the entire testing period, while the beams were subjected to shrinkage- and creep deformations, the hydraulic jacks were connected to high pressure accumulators. These accumulators were partially filled with Nitrogen. Deformations in the beams caused volume changes of the Nitrogen. This resulted in small pressure variations. The oil pressure in the hydraulic jacks was checked regularly and, if required, could be adjusted.

During the different loading steps and at regular moments throughout the testing period, the following measurements were done:

- The vertical displacement in five points of the beams (above the supports, under the point loads, and in the middle of the span) was measured using dial gauges with a graduation of 0.01 mm which allowed to determine the absolute displacement of the beams;
- The strains were measured on the side of the beams at the middle of the span and at different locations in the proximity of the upper- and bottom fibre, using a deformeter with a measuring base of 200 mm (Ghent and Leuven) or 300 mm (Brussels and Liège);
- The width of five cracks was measured on each side of the beams, using a measuring microscope with graduation of 0.02 mm.

The location of the measuring points for the four beam types is given in Appendix B.

5.2.3.3. Static test after long-term test

In order to determine the failure moment after the long-term tests the beams were first unloaded. They remained unloaded for 14 days and were then loaded until failure. The loading was done in the following steps: $0.1 \cdot M_{ser,cal}$; $0.5 \cdot M_{ser,cal}$; $1.0 \cdot M_{ser,cal}$; $0.6 \cdot M_{u,0}$; $0.7 \cdot M_{u,0}$; $0.8 \cdot M_{u,0}$; $0.9 \cdot M_{u,0}$; $1.0 \cdot M_{u,0}$. $M_{ser,cal}$ is the service moment calculated according to CEB (1964). $M_{u,0}$ is the experimentally determined failure moment by a static test at 28 days (section 5.2.3.1).

5.2.3.4. Additional tests

Besides the tests which have been described above, additional tests were performed:

- Tensile strength tests on reinforcement bars (Ø 14 mm BE400a);
- Gradation tests for both the sand and the gravel;
- Tests on the cement (i.a. compression- and flexural strength tests);
- Tests on fresh concrete;
- Creep and shrinkage tests on unreinforced prisms (150x150x600 mm);
- Shrinkage tests on unloaded beams with a span of 1.760 m and a total length of 3.400 m;
- Compression tests at the age of 28 days and approximately 4 years on cubes (200x200x200 mm) and prisms (200x200x500 mm).

Mainly the data from the compression tests were crucial for the calculation of the time-dependent deformations.

All material models require the compressive strength at 28 days on standard cylinders (diameter of 150 mm, height of 300 mm). Unfortunately, such tests have not been performed. Using the formula by NBN B15-220 (1970) it is possible to determine a conversion factor to transform the compressive strength of cubes to an equivalent compressive strength on cylinders:

$$\frac{f_x}{f_{c\,cub\,200}} = 0.65 + \frac{0.7}{\left(1 + \frac{\sqrt{A}}{200}\right) \cdot \left(\frac{h}{\sqrt{A}}\right)^{1.05}} \tag{5.1}$$

in which f_x is the compressive strength of the desired specimen, $f_{c\,cub\,200}$ is the compressive strength of a cube (200x200x200 mm), A is the cross-section of the specimen in mm, and h is the height of the specimen in mm. For a standard cylinder with a diameter of 150 mm and a height of 300 mm ($f_{c\,cil}$), this formula gives:

$$\frac{f_{c\,cil}}{f_{c\,cub\,200}} = 0.65 + \frac{0.7}{\left(1 + \frac{\sqrt{75^2 \cdot \pi}}{200}\right) \cdot \left(\frac{300}{\sqrt{75^2 \cdot \pi}}\right)^{1.05}} = 0.83 \quad (5.2)$$

Multiplying the compressive strength of cubes by the factor 0.83 thus gives an equivalent compressive strength for a standard cylinder. Using this factor, the design compressive stress (see section 5.2.1) on a standard cylinder becomes: $f_{c\,cil,design}$ $0.83 \cdot 35 = 29.75\ MPa$.

For each beam type also 2 beams, with a length of 3.400 m, were placed on supports, which were spaced 1.760 m apart. These beams remained unloaded throughout the testing period. They were used to measure the effects of shrinkage. This pure shrinkage date has not been taken into account in this thesis. However, the effects of shrinkage are present in the results of the displacements and the strains.

5.2.4. Results and discussion

The essence of the compression test results is given in Table 5.2. The same concrete was tested in the four different laboratories. The compressive strength has been measured on cubes with dimension of 200x200x200 mm at 28 days and at approximately 4 years. The table also gives the ratio between the compressive strength at 4 years and 28 days. The secant modulus of elasticity has been measured on prisms with dimensions of 200x200x500 mm at 28 days and approximately 4 years. Similar as for the compressive strength, the table also gives the ratio of the modulus at 4 years and 28 days. The compressive strength increases between 10 and 30% over a time period of 4 years. This is due to extra hydration of the cement after 28 days. Normally, the modulus of elasticity should also increase over time (NBN EN 1992-1-1, 2005). This cannot be deduced from the results. The values of type I deviate from the expected trend.

Table 5.2. Mean compressive strength of cubes (200x200x200 mm) and secant modulus of elasticity determined on prisms (200x200x500 mm) for the concrete used for casting the reinforced beams.

	Compressive strength [N/mm²]			Secant modulus of elasticity [kN/mm³]		
	28 days	± 4 years	4 y / 28 d	28 days	± 4 years	4 y / 28 d
Type I	39.4	51.1	1.30	35.5	29.9	0.84
Type II	35.0	44.8	1.28	31.0	/	/
Type III	40.3	44.6	1.11	27.8	35.2	1.27
Type IV	37.7	41.3	1.10	29.2	29.8	1.02
Mean	38.1	45.5	1.20	31.1	31.6	1.04

Table 5.3 gives an overview of the most important data of the long term-tests. M is the constant moment applied throughout the test period, $M_{u,0}$ is the failure moment determined by a static test at 28 days, $M_{u,t}$ is the failure moment determined by a static test at time t, a_0 is the instantaneous deflection in the midspan, a_t is the deflection in the midspan at time t, ε_{c0} is the instantaneous strain of the outermost compression fibre, and ε_{ct} is the strain of the outermost compression fibre at time t. For beam type III there is one set of data missing, namely the data for the beams loaded at the highest load. Most likely these beams failed before the end of the testing period was

reached. Also all the accompanying unreinforced prisms in the creep test failed after only a few hours after 90% of the failure load was applied.

Table 5.3. Summary of the most important data for the long-term tests on reinforced beams.

	$M/M_{u,0}$ [%]	$M_{u,t}$ [kNm]	a_0 [mm]	a_t [mm]	a_t/a_0 [-]	$\varepsilon_{ct}/\varepsilon_{c0}$ [-]	t [days]
Type I $M_{u,0} = 29.9\ kNm$	58	32.12	-	-	-	-	1450
	72	35.78	6.02	10.29	1.71	2.62	1638
	81	34.86	7.39	11.98	1.62	2.62	1372
	91	33.95	8.94	15.02	1.68	2.66	1342
Type II $M_{u,0} = 65.1\ kNm$	52	70.88	7.27	13.49	1.86	2.79	1426
	59	71.45	7.69	14.10	1.83	2.96	1569
	70	71.11	9.36	17.56	1.88	2.77	1499
	80	68.80	10.72	20.24	1.89	2.74	1513
	90	72.44	13.10	24.23	1.85	2.85	1519
Type III $M_{u,0} = 97.8\ kNm$	43	100.76	7.08	14.51	2.06	2.88	1600
	67	101.68	10.58	23.88	2.26	2.72	1600
	77	100.08	13.84	28.74	2.08	2.87	1600
Type IV $M_{u,0} = 72.8\ kNm$	52	76.05	5.98	10.52	1.76	2.09	800
	70	79.03	8.80	13.90	1.58	2.42	800
	80	77.42	11.16	16.96	1.52	-	1000
	90	79.71	12.85	19.28	1.50	-	1000

From Table 5.3 it is clear that the loading level has no negative influence on the failure moment. The failure moment after permanent loading is higher than the failure moment determined at an age of 28 days. The main reason for this is probably the previously discussed increase in compressive strength. This increase in compressive strength needs to be larger than any possible permanent damage caused by the shrinkage- and creep phenomena. Hellesland et al. (1972) reported that sustained load levels could: accelerate the hydration process, improve the healing conditions of cracks in a direction perpendicular to loading, and increase the Van der Waals forces in the concrete due to a closer proximity of the gel particles. All of which lead to an increased strength. Coutinho (1977) also reported an increased strength under sustained loading but attributed this to a change in the solubility of unhydrated cement. Due to the stress, the solubility of the unhydrated cement increases, causing an increased hydration. It can be concluded that the exact phenomenon causing an increased failure moment after sustained loading is unclear, but the hydration of cement plays an important role.

The deflection ratios and the strain ratios are independent of the loading level, as can be seen from Table 5.3. Table 5.4 contains the mean values of the strain ratios and deflection ratios given in Table 5.3. ρ_1 is the tension reinforcement ratio ($A_{s,1}/bd$, with d the effective depth), ρ_2 is the

compression reinforcement ratio ($A_{s,2}/bd$, with d the effective depth), $(1/r)_0$ is the instantaneous curvature, and $(1/r)_t$ is the curvature at time t. Comparing the results for beam types I, II, and III, an increase in the tension reinforcement ratio results in: increased strain-, curvature-, and deflection ratios. This is related to the higher absolute levels of loading for the beams with a higher tension reinforcement ratio. Comparing beam types II and IV, an increase of the compression reinforcement ratio causes a decrease in: strain-, curvature-, and deflection ratios. This is despite the fact that the beams with compression reinforcement are loaded a bit higher. The compression reinforcement takes part of the compression stresses; therefore, the concrete stresses are lower, which results in lower creep levels.

Table 5.4. Reinforcement ratios, strain ratios, curvature ratios, and deflection ratios for the four different beam types.

	$\boldsymbol{\rho_1}$ [%]	$\boldsymbol{\rho_2}$ [%]	$\boldsymbol{\varepsilon_{ct}/\varepsilon_{c0}}$ [-]	$\boldsymbol{\frac{(1/r)_t}{(1/r)_0}}$ [-]	$\boldsymbol{a_t/a_0}$ [-]	$\boldsymbol{t}$ [days]
Type I	0.83	0	2.63	1.75	1.67	1450
Type II	2.17	0	2.82	1.89	1.86	1500
Type III	3.52	0	2.82	1.95	2.05	1600
Type IV	2.17	1.24	2.26	1.75	1.67	800

From Table 5.4 it is also clear that, looking per beam type, the curvature ratios and the deflection ratios are almost identical. They are both significantly smaller than the strain ratios. This is because the strains are measured at the top compression fibre. The deformation is there much larger than at the reinforcement zone. This results in a proportionally smaller increase of the curvature compared to the strains. The reason why the deflection ratios and the curvature ratios are almost identical is because they are related; it is possible to calculate the deflection out of the curvature (see section 6.4). This can for example be done using the integrals of Mohr:

$$a_t = \int \left(\frac{M}{EI}\right)_t \cdot \bar{M} \cdot dx = \int \left(\frac{1}{r}\right)_t \cdot \bar{M} \cdot dx \tag{5.3}$$

where $\bar{M}$ is the moment due to a point load at the location of interest, see Figure 5.6. Between the two point loads of a four point bending test the curvature is constant, and thus also the curvature ratio is constant. Since $\bar{M}$ is the most important at the middle of the span, which is the location of interest, the deflection ratio will be approximately equal to the curvature ratio.

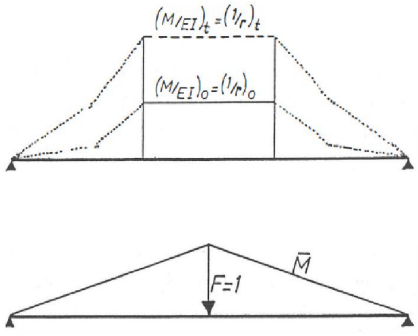

Figure 5.6. Illustration of integrals of Mohr (FKFO no. 547).

5.3. Prestressed concrete beams

The time-dependent behaviour of prestressed beams under permanent loading was also tested. Here the focus lied on the influence of: the shape of the cross-section, the type of prestressing (post-tensioning or pre-tensioning) , the age at prestressing , the age at loading, and the load level. During the testing period the deflections and the deformations were measured.

5.3.1. Material properties

Similar as for the reinforced beams the coarse aggregates (gravel), the sand, the cement, the prestressing steel, and the passive reinforcement were ordered at the same time and were then distributed over the four laboratories. The steel quality of the passive reinforcement was BE400a , which is the same as for the reinforced beams. The concrete composition was chosen in order to have a design mean compressive strength of 50 MPa, measured on cubes with side of 200 mm at 28 days. This resulted in the following concrete composition:

Gravel 4/16:	1250 kg
Sand 0/5:	570 kg
Cement P40 (CEM I 52.5 N):	375 kg
Water:	180 l

5.3.2. Cross-section, reinforcement, and prestressing

Each of the prestressed beams that was tested had a total length of 8.40 m and a span of 8.00 m. In total three different cross-sections were tested: rectangular, T-shaped, and I-shaped cross-sections. All three cross-sections were post-tensioned using a B.B.R.V. cable. Such a cable consisted out of several 7 mm diameter wires, with at their end a cold-formed button head (BBR VT International Ltd, 2016). These wires were fixed in an anchorage head, which was inside a metal duct before the prestressing. As the cable got tensioned by a jack, the anchorage head came out of the duct. When the required prestress was obtained, an anchorage nut was screwed on the anchorage head to block it (Ritzen, 2006). This anchorage system's screwing technique prevented the loss of prestress due to slip (Taerwe, 1999). Figure 5.7 shows an anchored B.B.R.V. cable.

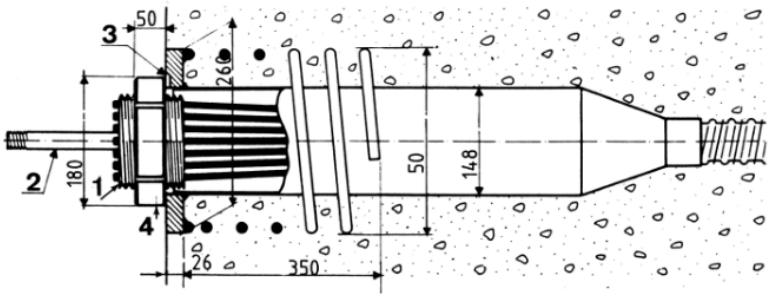

Figure 5.7. Anchored B.B.R.V. cable with 1) the anchorage head, 2) grout injection canal, 3) anchorage plate with small air vent to evacuate air during grouting, and 4) anchorage nut (Ritzen, 2006).

The I-shaped cross-section was also pre-tensioned using six prestressing strands of half an inch (type 12.7 S T.B.R.). The height for all the cross-sections was equal to 400 mm, resulting in a span to height ratio of 20. The prestressing force for each cross-section was determined such that the stress level for the different cross-sections was comparable. Table 5.5 gives an overview of the different types of prestressed beams that were tested as well as the total initial prestressing force. Note that

a beam type is uniquely characterised by its shape and its type of prestressing. Figure 5.8 shows the detailed reinforcement scheme of the four types of beams that were tested during the prestressing programme. In the analysis of these beams (see chapter 8) all the longitudinal reinforcement was taken into account. The I-shaped beams with pre-tensioning had a constant eccentricity of the prestressing force over the length of the beam. This was not the case for the post-tensioned beams. These had a trapezoidal variation of the location of the cable duct and thus, of the location of the prestressing force. The varying eccentricities of the prestressing beams are illustrated in Figure 5.9 for the four types of beams.

Table 5.5. Overview of the different combinations of shapes and types of tensioning that were tested.

Shape	Type of tensioning	Practical tensioning	Total initial prestressing force [kN]
Rectangular (R)	post-tensioning	B.B.R.V. cable with 24 Ø 7 mm wires	1120
T-shaped (T)	post-tensioning	B.B.R.V. cable with 14 Ø 7 mm wires	684
I-shaped (I)	post-tensioning	B.B.R.V. cable with 16 Ø 7 mm wires	750
I-shaped (I)	pre-tensioning	6 strands of 1/2 inch	757

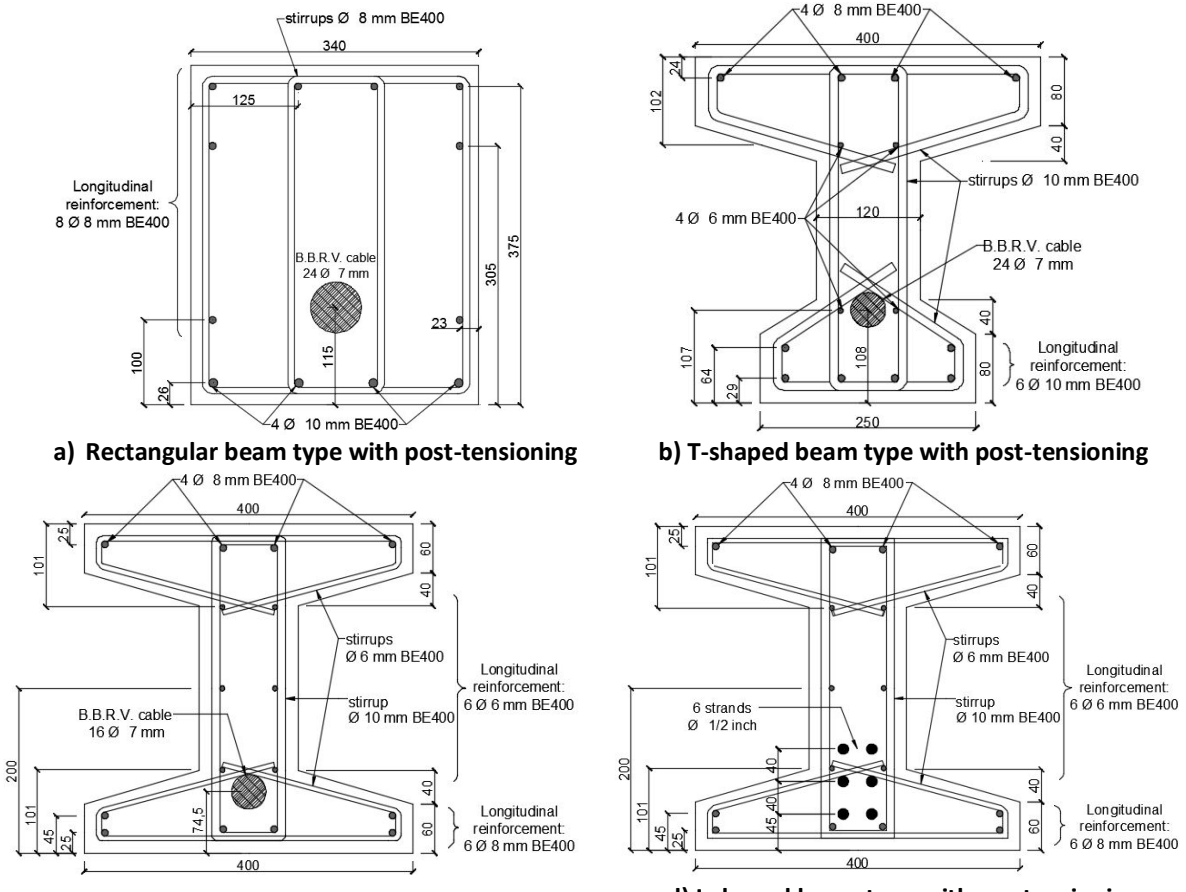

a) Rectangular beam type with post-tensioning

b) T-shaped beam type with post-tensioning

c) I-shaped beam type with post-tensioning

d) I-shaped beam type with pre-tensioning

Figure 5.8. Detailed reinforcement sketch of the four types of prestressed beams. Measurements are in mm. All beams have a height of 400 mm.

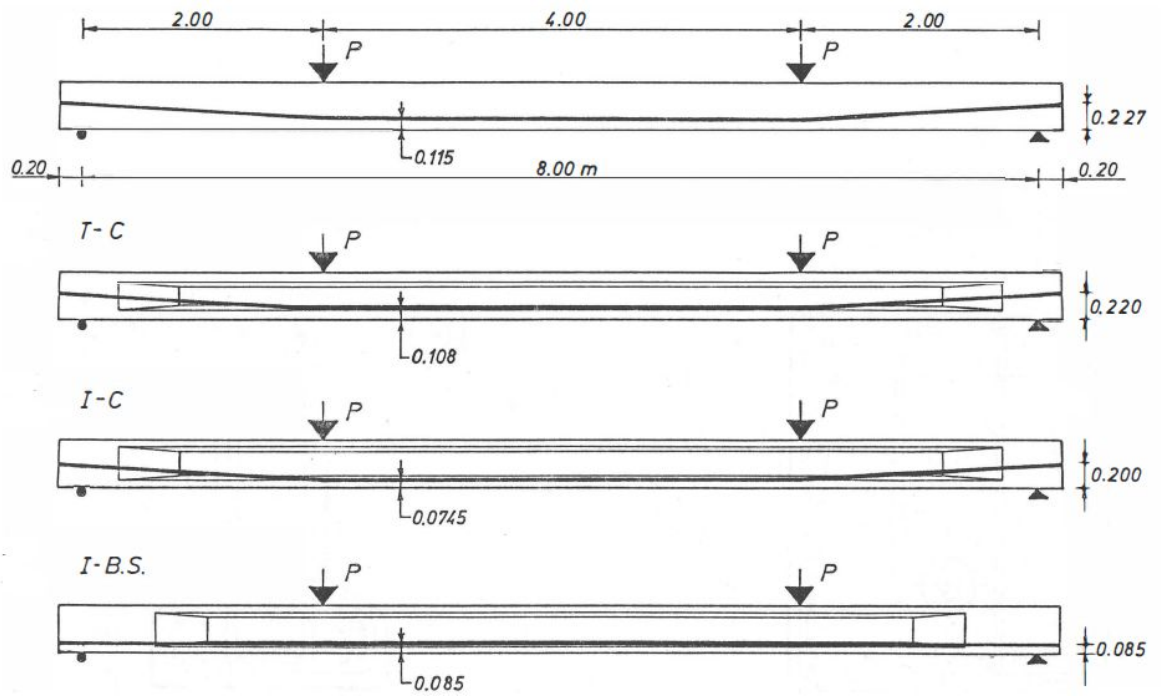

Figure 5.9. Variation of the prestressing eccentricity over the length of the beams (FKFO no. 547).

For the post-tensioned beams the prestress was applied from one side in four steps. At the moment that the required prestress was obtained, a verification of possible prestress losses was done at the other side. If necessary, the cable was tensioned extra at this side.

The strands which were used for pre-stressing were tensioned between two fixed abutments, a day before the casting of the beams, until their required prestressing force. Right before the casting of the concrete the strands were tensioned again until their required initial prestressing force. This re-tensioning step counterbalanced the loss of prestress due to relaxation of the steel and the possible slip between the strands and the anchorages. After the beams were casted and the concrete had obtained sufficient strength, the prestress was transferred to the beams. In order to have a gradual prestressing, hydraulic jacks were used to gradually loosen the anchorages at the abutments.

The magnitude of the prestressing force was not only decided by the intention to have comparable stress levels in the different beam types. During the long-term tests the beams were loaded at: the calculated service load, half of the calculated service load, and no load. Under these three loading levels it was desired to have the stress distributions which are given in Figure 5.10.

a) No load **b) Half of the service load** **c) Complete service load**

Figure 5.10. Desired stress distributions under different levels of loading (FKFO no. 547).

5.3.3. Test setup and experimental programme

5.3.3.1. Static tests

From each beam type two beams were subjected to a static test. For the post-tensioned beams the prestress on all the beams was applied at 14 days. One beam of each beam type was loaded until failure at 28 days and the other beam was loaded at 56 days. Two pre-tensioned beams were both loaded until failure at 28 days. One of the two pre-tensioned beams was prestressed at 7 days and the other was prestressed at 14 days.

Immediately after prestressing the beams were placed on two supports: one pinned support and one roller support. At the prescribed loading date, the beams were subjected to a four point bending test. The two loads were applied 4.00 m away from one another and 2.00 m away from the supports, see Figure 5.11. To apply the loads hydraulic jacks were used. A picture of the test setup at the university of Ghent can be seen in Figure 5.12.

The beams were loaded in five steps until the calculated service moments ($0.10 \cdot Q_{ser}$; $0.25 \cdot Q_{ser}$; $0.50 \cdot Q_{ser}$; $0.75 \cdot Q_{ser}$; $1.00 \cdot Q_{ser}$). Then the beams were unloaded until $0.10 \cdot Q_{ser}$. Next the beams were loaded in steps of 2.5 kN and 5.0 kN until the load Q_w at which the largest crack width was between 0.10 mm and 0.15 mm. Afterwards, ten loading- and unloading cycles between $0.10 \cdot Q_{ser}$ and Q_w were performed. Finally, the beam is loaded until failure in steps of 10 kN per hydraulic jack.

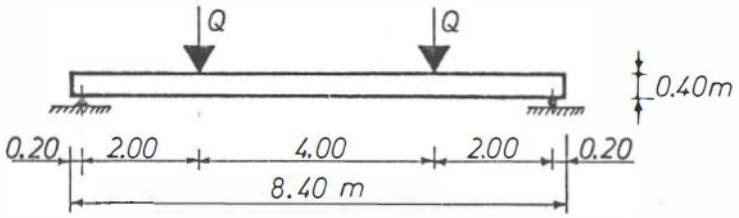

Figure 5.11. Test setup for the prestressed beams (FKFO no. 547).

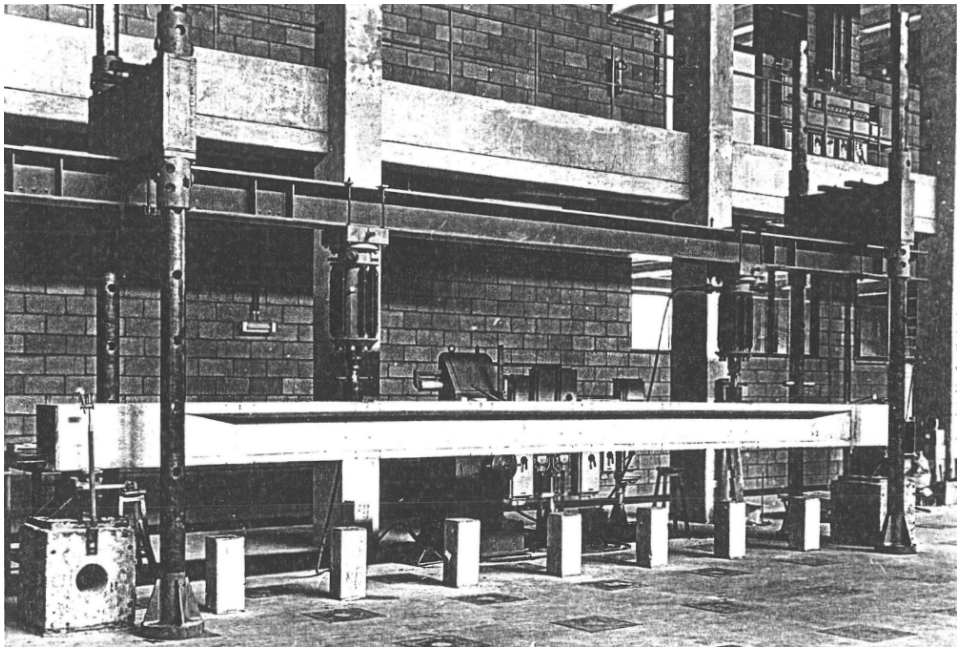

Figure 5.12. Picture of the test setup for prestressed beams at the university of Ghent (FKFO no.547).

During each step of the static test the following measurements were done:

- The vertical displacement in nine points of the beams (above the supports and in seven sections with a distance of 1.00 m from one another) was measured using dial gauges with a graduation of 0.01 mm which allowed to determine the absolute displacement of the beams;
- The strains were measured on the side of the beams at the middle of the span, at the location of the point loads and at different locations in the proximity of the upper- and bottom fibre. This was done using a mechanical extensometer with a measuring base of 8 inches and graduation of $10 \cdot 10^{-6}$ (Ghent, Liège and Leuven) or 12 inches and graduation of $6.6 \cdot 10^{-6}$ (Brussels);
- After the cracking load was applied, the total number of cracks and their crack widths in the zone between the two point loads was measured. This was done using a measuring microscope with graduation of 0.02 mm or using a mechanical deformometer with a measuring base of 2 inches.

The location of the measuring points of the deformations and the strains is given in Appendix C.

5.3.3.2. Long-term tests

Similar as for the static tests the beams were directly placed on a roller and a pinned support immediately after prestressing. The test setup is identical to the test setup of the static tests (see Figure 5.11). Throughout the entire testing period the beams were kept in an acclimatised room with a temperature of 20°C ± 0.5°C and a relative humidity of 60% ± 3%. After (approximately) 28 days or 56 days the long-term loading was applied by two hydraulic jacks at the same location as for the static tests. The prestressed beams were loaded up to 4.5 years under: the calculated service load Q_{ser}, half of the calculated service load $0.5 \cdot Q_{ser}$, or no load. Table 5.6 gives an overview of the testing programme of the prestressed beams. Note that this is a theoretical overview; a deviation of a few days is possible.

Table 5.6. Overview of the testing programme of the prestressed beams.

	Rectangular				T-shaped				I-shaped (post-tens.)				I-shaped (pre-tens.)			
Age at prestressing [days]	14			56	14			56	14			56	7		14	
Age at loading [days]	-	28	56	-	-	28	56	-	-	28	56	-	-	28	-	28
$Q = Q_{ser}$	-	1	1	-	-	1	1	-	-	1	1	-	-	1	-	1
$Q = Q_{ser}/2$	-	1	1	-	-	1	1	-	-	1	1	-	-	1	-	1
$Q = 0$	1	-	-	1	1	-	-	1	1	-	-	1	1	-	1	-

In order to keep the loading constant despite the creep and shrinkage deformations the same technique as for the reinforced beams was used, see section 5.2.3.2. Note that for the testing of the prestressed beams, unlike for the testing of the reinforced beams, the testing did not happen with two beams in one test setup.

The measurements of the concrete deformations and the vertical displacements was done similar as for the static tests at 28 days, see section 5.3.3.1. Also the locations of the measuring points was identical to the locations used in the static test.

After the long-term loading the beams remained unloaded for 6 months. After which they were subjected to a static test until failure, similar to the static test at 28 days.

5.3.3.3. Additional tests

Besides the tests which have been described above additional tests were performed:

- Gradation tests for both the sand and the gravel;
- Tests on the cement (i.a. compression- and flexural strength tests);
- Tests on fresh concrete;
- Shrinkage tests on beams with the same length, cross-section and passive reinforcement as the beams which were tested under loading in a long-term test, but without the prestress and supported at four points instead of two;
- Shrinkage tests on unreinforced beam sections of two meters;
- Compression tests at the age of 28 days and approximately 5 years on prisms (200x200x500 mm) and cylinders (Ø 150 x 300 mm);
- Tensile strength tests on 7 mm wires and 1/2 inch strands;
- Relaxation tests on 7 mm wires and 1/2 inch strands in an acclimatised room (temperature of 20°C ± 0.5°C and a relative humidity of 60% ± 3%).

Mainly the data from the compression tests were crucial for the calculation of the time-dependent deformations.

5.3.4. Results and discussion

The mean compressive strength measured on cylinders (Ø 150 x 300 mm) and the mean secant modulus of elasticity measured on prisms (200x200x500 mm) are given in Table 5.7 for each beam type. The tests were executed at 28 days and at approximately 5 years after casting. The table also shows the ratio of the value obtained at 5 years over the value obtained at 28 days. Note that the mean ratio was not determined by dividing the mean at 5 years by the mean at 28 days. The concrete of the T-shaped type had better properties but was not tested at 5 years. This gives distorted results; the mean at 28 days is high compared to the mean at 5 years. Therefore, the mean ratio is calculated as the mean of the ratios, producing a result which is independent of the concrete of the T-shaped type.

From Table 5.7 it is clear that there is an increase in the compressive strength over time, though this increase is clearly smaller than for the concrete used in the reinforced beams. With regard to the modulus of elasticity there appears to be no evolution in time. Looking at the formulas of the time-dependent modulus of elasticity of the different material models, this is against what is expected.

Table 5.7. Mean compressive strength of cylinders (Ø 150 x 300 mm) and secant modulus of elasticity determined on prisms (200x200x500 mm) for the concrete used for casting the prestressed beams.

	Compressive strength [N/mm²]			Secant modulus of elasticity [kN/mm²]		
	28 days	**± 5 years**	**5 y / 28 d**	**28 days**	**± 5 years**	**5 y / 28 d**
Rectangular	38.7	39.0	1.01	31.1	31.0	1.00
T-shaped	47.1	/	/	36.2	/	/
I-shaped (post-tens.)	33.1	38.7	1.17	29.2	31.3	1.07
I-shaped (pre-tens.)	34.9	40.6	1.16	34.5	33.4	0.97
Mean	38.5	39.4	1.11	32.8	31.9	1.01

The results of the static tests after long-term loading for each of the T-shaped beams is given in Table 5.8. The results of the other types of beams are given in Appendix D. The first column of the tables denotes the name of the beam. For example: T-LD-C-P14-Q31-100%. For the name of the beams the following legend is used in the indicated order:

R, T, and I:	Shape of the cross-section: rectangular, T-shaped, I-shaped;
LD:	Dutch abbreviation for long-term;
Px:	Prestressing happens at the time x;
C, BS:	Type of prestressing system: C stands for the post-tensioned beams and BS stands for the pre-tensioned beams;
Qx:	Four point bending loading happens at time x, when absent the beam is not loaded;
0%, 50%, 100%	percentage of the calculated service load at which the beam is loaded.

Table 5.8. . Results of the static tests after long-term loading of the beams with a T-shaped cross-section.

	$M_{ser.,cal.}$ [kNm]	M_r [kNm]	$M_{u,t}$ [kNm]	$M_{u,t}/M_{ser.,cal.}$ [-]	$M_{u,t}/M_{u,o,m}$ [-]
T-LD-C-P14-Q31-100%	102.0	93	308	3.02	0.99
T-LD-C-P14-Q28- 50%	102.0	77	319	3.13	1.03
T-LD-C-P14- 0%	102.0	75	308	3.02	0.99
T-LD-C-P15-Q56-100%	102.0	77	309	3.03	0.99
T-LD-C-P14-Q56- 50%	102.0	77	289	2.83	0.93
T-LD-C-P56- 0%	102.0	80	310	3.04	1.00
Mean	102.0	80	307	3.01	0.99

The table gives the values of: the calculated service moment $M_{ser.,cal.}$, the cracking moment M_r, the failure moment determined in the static test after the long-term loading $M_{u,t}$, and the failure moment determined in a static test at 28 days $M_{u,o,m}$. What is striking about the table is that the cracking moment is below the service moment. This means that the beams which were loaded at

100% of the service load in the long-term test were cracked. This table further shows that the failure moment does not increase under long-term loading, as was found for the reinforced beams.

The results of the static tests after long-term loading for the other beams can be found in Appendix D.

6. Implementation of a cross-sectional calculation method to determine the time-dependent effects on reinforced and prestressed concrete members

This chapter gives an overview of the method which was used to calculate: the deflection, the strain, the curvature, the stress, and the axial shortening of the beams, which were discussed in chapter 5. First, a cross-sectional method will be explained which allows the calculation of the strain and the curvature for a beam subjected to a moment and a normal force. Second, this method will be expanded, in order to take into account the effects of creep and shrinkage. Next, the influence of prestress (and prestress relaxation) will be taken into consideration. Then, the theory of the elastic weights will be discussed which allows the calculation of the deflection out of the curvatures. Finally, the influence of cracking on the total method will be discussed. The complete method discussed here can also be found in the work of Ghali et al. (2002).

6.1. Cross-sectional method for calculation of strain and curvature

In the sign convention which is adopted here, an axial force N which causes tension is positive. A moment M (and the corresponding curvature ψ) that induces tension at the bottom and compression at the top is positive. Similar to the axial force, tensile stress σ and tensile strain ε are positive.

Consider the cross-section with one axis of symmetry given in Figure 6.1. It has different sections. Every section i is substituted by its transformed section; the original area of the section A_i is replaced by $(E_i/E_{ref}) \cdot A_i$, in which E_i is the modulus of elasticity of section i and E_{ref} is a reference modulus of elasticity. A new cross-section is obtained with modulus of elasticity E_{ref} and an area equal to the sum of the transformed sections. In the analysis of concrete elements E_{ref} can be taken equal to modulus of elasticity of one of the concrete sections E_c. Assume that the cross-section is subjected to a normal force N anywhere on the axis of symmetry. This normal force can be replaced by a statically equivalent normal force N and bending moment M acting at a reference point O. The choice of the location of this reference point is free, as long as it is on the axis of symmetry.

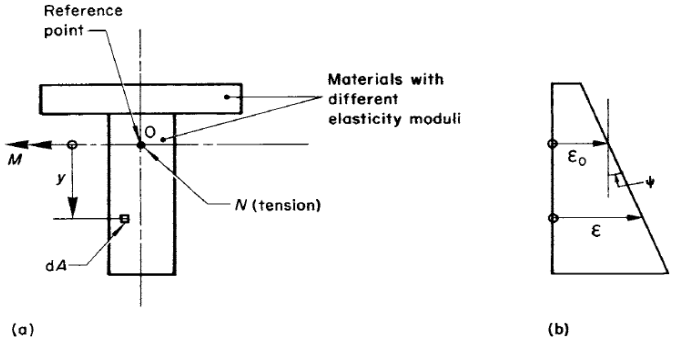

Figure 6.1. a) Composite cross-section with indication of positive N, M, and y; b) corresponding strain distribution (Ghali et al., 2002).

If the strain distribution is assumed linear, and a plane cross-section will thus remain plane, the strain at any fibre can be expressed as:

$$\varepsilon = \varepsilon_O + \psi \cdot y \tag{6.1}$$

in which ε_O is the strain at the reference point, ψ is the curvature of the cross-section, and y is the vertical distance from the fibre to the reference point. This distance is positive if the considered fibre is located below the reference point. When the fibre is located in the ith section, the corresponding stress at the fibre is:

$$\sigma = E_i \cdot (\varepsilon_O + \psi \cdot y) \tag{6.2}$$

By integration of the stress (and the distance y) the normal force (and the bending moment) on the cross-section can be calculated:

$$\begin{aligned} N &= \int \sigma \, dA = \varepsilon_O \cdot \sum_i \left[E_i \int dA \right] + \psi \cdot \sum_i \left[E_i \int y \, dA \right] \\ &= \varepsilon_O \cdot \sum_i [E_i \cdot A_i] + \psi \cdot \sum_i [E_i \cdot S_i] \end{aligned} \tag{6.3}$$

$$\begin{aligned} M = \int \sigma \cdot y \, dA &= \varepsilon_O \cdot \sum_i \left[E_i \int y \, dA \right] + \psi \cdot \sum_i \left[E_i \int y^2 \, dA \right] \\ &= \varepsilon_O \cdot \sum_i [E_i \cdot S_i] + \psi \cdot \sum_i [E_i \cdot I_i] \end{aligned} \tag{6.4}$$

with S_i the static moment of section i about an axis through O and I_i the moment of inertia of section i about an axis through O. The summations in equations (6.3) and (6.4) need to be done over all the sections of the cross-section. The equations can be rewritten:

$$N = E_{ref} \cdot (A \cdot \varepsilon_O + S \cdot \psi) \tag{6.5}$$

$$M = E_{ref} \cdot (S \cdot \varepsilon_O + I \cdot \psi) \tag{6.6}$$

with A, S, and I respectively: the transformed area of the cross-section, the transformed static moment about an axis through O, and the transformed moment of inertia about an axis through O. These are calculated using the ratio E_i/E_{ref}. Equations (6.5) and (6.6) can be combined in a matrix formulation:

$$\begin{bmatrix} N \\ M \end{bmatrix} = E_{ref} \cdot \begin{bmatrix} A & S \\ S & I \end{bmatrix} \cdot \begin{bmatrix} \varepsilon_O \\ \psi \end{bmatrix} \tag{6.7}$$

Mostly, N and M are known and it is required to find ε_0 and ψ. Equation (6.7) can be rearranged:

$$\begin{bmatrix} \varepsilon_O \\ \psi \end{bmatrix} = \frac{1}{E_{ref}} \cdot \begin{bmatrix} A & S \\ S & I \end{bmatrix}^{-1} \cdot \begin{bmatrix} N \\ M \end{bmatrix} = \frac{1}{E_{ref} \cdot (A \cdot I - S^2)} \cdot \begin{bmatrix} I & -S \\ -S & A \end{bmatrix} \cdot \begin{bmatrix} N \\ M \end{bmatrix} \tag{6.8}$$

In the case that there is no normal force N, e.g. a simply supported reinforced beam subjected to simple bending, ε_O and ψ can be calculated as follows:

$$\varepsilon_O = \frac{-S \cdot M}{E_{ref} \cdot (A \cdot I - S^2)} \tag{6.9}$$

$$\psi = \frac{A \cdot M}{E_{ref} \cdot (A \cdot I - S^2)} \tag{6.10}$$

When the strain in the reference point ε_O and the curvature ψ of the cross-section have been calculated, the strain at any fibre (e.g. the centroid) can be calculated using formula (6.1). The concrete stress, respectively the stress in the reinforcement steel, at any fibre can be calculated by:

$$\sigma_c = E_c \cdot (\varepsilon_O + \psi \cdot y) \tag{6.11}$$

$$\sigma_{ns} = E_{ns} \cdot (\varepsilon_O + \psi \cdot y) \tag{6.12}$$

with E_{ns} the modulus of elasticity of the reinforcement steel or in other words the non-prestressed steel.

6.2. Effects of creep and shrinkage on a reinforced section without prestress

The instantaneous strain $\varepsilon_O(t_0)$ and the instantaneous curvature $\psi(t_0)$ at the time of load application t_0 can be calculated as described by the method in section 6.1. The strain and curvature at a random time t after t_0 requires further attention. Due to creep and shrinkage there will be a stress redistribution in the reinforced concrete element. The strain and curvature between time t_0 and t will change. This is denoted by: $\Delta\varepsilon_0$ and $\Delta\psi$. In order to determine these variations, assume that they are restrained by an artificial axial force ΔN and an artificial moment ΔM applied in the reference point O. This restraining force and this restraining moment is then removed by applying the same force and moment but with an opposite sign:

$$\begin{bmatrix} \Delta\varepsilon_O \\ \Delta\psi \end{bmatrix} = \frac{1}{\overline{E_c}(t, t_0) \cdot (\bar{A} \cdot \bar{I} - \bar{S}^2)} \cdot \begin{bmatrix} \bar{I} & -\bar{S} \\ -\bar{S} & \bar{A} \end{bmatrix} \cdot \begin{bmatrix} -\Delta N \\ -\Delta M \end{bmatrix} \tag{6.13}$$

in which $\overline{E_c}(t, t_0)$ is the age-adjusted effective modulus of one of the concrete sections (see section 3.3) and $\bar{A}$, $\bar{S}$, and $\bar{I}$ are respectively: the age-adjusted transformed area of the cross-section, the age-adjusted transformed static moment about an axis through O, and the age-adjusted transformed moment of inertia about an axis through O. These last are calculated using the ratio E_i/E_{ref} with E_{ref} taken equal to $\overline{E_c}(t, t_0)$. The reason why the age-adjusted effective modulus is used instead of the normal modulus of elasticity is because the restraining forces are not applied immediately at full strength. Instead, they develop over time. The total restraining force ΔN and the total restraining moment ΔM can be calculated by summing up the force and moment required to restrain both creep and shrinkage:

$$\begin{bmatrix} \Delta N \\ \Delta M \end{bmatrix} = \begin{bmatrix} \Delta N \\ \Delta M \end{bmatrix}_{creep} + \begin{bmatrix} \Delta N \\ \Delta M \end{bmatrix}_{shrinkage} \tag{6.14}$$

If the creep deformation can happen freely, the strain and curvature at the reference fibre between t_0 and t would change with respectively $\varphi(t,t_0)\cdot\varepsilon_O(t_0)$ and $\varphi(t,t_0)\cdot\psi(t_0)$. The force and moment required to restrain the creep deformation is equal to:

$$\begin{bmatrix}\Delta N\\ \Delta M\end{bmatrix}_{creep} = -\sum_i \overline{E_{ci}}(t,t_0)\cdot\varphi_i(t,t_0)\cdot\begin{bmatrix}A_{ci} & S_{ci}\\ S_{ci} & I_{ci}\end{bmatrix}\cdot\begin{bmatrix}\varepsilon_{O,i}(t_0)\\ \psi_i(t_0)\end{bmatrix} \tag{6.15}$$

with $\overline{E_{ci}}(t,t_0)$ the age-adjusted modulus of elasticity of concrete section i; $\varphi_i(t,t_0)$ the creep coefficient of concrete section i; and A_{ci}, S_{ci} and I_{ci} respectively the area of concrete section i and the static and inertia moment through the reference point O of section i. The summation is done over all the concrete sections.

Since free shrinkage does not change the curvature, the formula to calculate the restraining force and moment is simpler:

$$\begin{bmatrix}\Delta N\\ \Delta M\end{bmatrix}_{shrinkage} = -\sum_i \overline{E_{ci}}(t,t_0)\cdot\varepsilon_{cs}\cdot\begin{bmatrix}A_{ci}\\ S_{ci}\end{bmatrix} \tag{6.16}$$

with ε_{cs} the free shrinkage between time t_0 and t. The summation is again performed over all the concrete sections.

The concrete stress which is required to prevent the creep and shrinkage deformations is equal to:

$$\sigma_{restrained} = -\overline{E_{ci}}(t,t_0)\cdot(\varphi(t,t_0)\cdot\varepsilon_c(t_0) + \varepsilon_{cs}) \tag{6.17}$$

where $\varepsilon_c(t_0)$ is the instantaneous concrete strain which can be calculated using equation (6.1). Formula (6.17) can be applied for any fibre.

Using equations (6.15) and (6.16) to find the total restraining force and moment with equation (6.14), allows to calculate the changes in strain $\Delta\varepsilon_O$ and curvature $\Delta\psi$ during the time period $t - t_0$ with equation (6.13). With $\Delta\varepsilon_O$, $\Delta\psi$ and $\sigma_{restrained}$ determined the stress increments due to creep and shrinkage can be computed. The stress change for concrete, respectively reinforcement steel, at any fibre in any section, is equal to:

$$\Delta\sigma_c = \sigma_{restrained} + \overline{E_{ci}}(t,t_0)\cdot(\Delta\varepsilon_O + y\cdot\Delta\psi) \tag{6.18}$$

$$\Delta\sigma_{ns} = E_{ns}\cdot(\Delta\varepsilon_O + y_{ns}\cdot\Delta\psi) \tag{6.19}$$

For the derivation in this section, it has been assumed that the external forces are all applied at time t_0. If this is not the case, the vector $\varphi_i(t,t_0)\cdot[\varepsilon_O(t_0) \quad \psi(t_0)]$ in formula (6.15) needs to be changed by a summation of the instantaneous stresses and strains multiplied with their corresponding creep coefficients. A similar adaption, but then only for the strain, needs to be done for the term $\varphi(t,t_0)\cdot\varepsilon_c(t_0)$ in formula (6.17).

6.3. Prestress and prestress loss due to relaxation

Section 6.1, which allows to calculate the instantaneous deformation, and section 6.2, which allows to calculate the time-dependent deformations due to shrinkage and creep, can be easily adapted to take into account a prestressing force. First, the influence on the instantaneous deformations will

be reviewed, and then second the influence on the deformations due to the time-dependent effect of relaxation of the prestressing steel will be discussed.

6.3.1. Influence on the calculation of the instantaneous deformation

The prestressing force can be induced into the concrete by one or more layers of prestressed steel. Every layer is characterised by its prestressing force P_i and distance to the reference point $y_{ps,i}$ (remember that the y-axis is positive downwards). Assume that the prestress of all the layers is induced in the concrete at the same time, the time t_0 at which the external loads are applied. In order to apply the method of section 6.1, the prestressing force needs to be converted to an equivalent force and moment at the reference point O:

$$\begin{bmatrix} N_{eq.} \\ M_{eq.} \end{bmatrix} = \begin{bmatrix} N - \sum_i P_i \\ M - \sum_i P_i \cdot y_{ps,i} \end{bmatrix} \tag{6.20}$$

with N and M defined according to section 6.1 as the equivalent axial force and moment (at the reference point) of an external load. The summation needs to be executed over all prestressing layers. This calculated vector $[N_{eq.} \quad M_{eq.}]$ replaces the original vector $[N \quad M]$ in equations (6.7) and (6.8):

$$\begin{bmatrix} N_{eq.} \\ M_{eq.} \end{bmatrix} = E_{ref} \cdot \begin{bmatrix} A & S \\ S & I \end{bmatrix} \cdot \begin{bmatrix} \varepsilon_O \\ \psi \end{bmatrix} \tag{6.21}$$

$$\begin{bmatrix} \varepsilon_O \\ \psi \end{bmatrix} = \frac{1}{E_{ref} \cdot (A \cdot I - S^2)} \cdot \begin{bmatrix} I & -S \\ -S & A \end{bmatrix} \cdot \begin{bmatrix} N_{eq.} \\ M_{eq.} \end{bmatrix} \tag{6.22}$$

When post-tensioning is used, the area of the metal duct and the prestressing steel should not be taken into account for the calculation of A, S, and I. At the moment the prestress is transferred, the duct is usually not yet grouted. Therefore, there is no compatibility of strains and the prestressing steel can move independent of the concrete.

Additional changes to the method described in section 6.1 are not required. The equations to calculate the instantaneous strain and curvature of the concrete stay the same, as do the equations to calculate the stress in the concrete and in the non-prestressed steel. The stress in the prestressing steel, immediately after prestress transfer to the concrete, can be calculated as follows:

$$\sigma_{ps}(t_0) = \sigma_{ps,\ init.} + E_{ps} \cdot (\varepsilon_O(t_0) + \psi(t_0) \cdot t_0) \tag{6.23}$$

where $\sigma_{ps,\ init.}$ Is the initial prestress in the steel before force transfer, E_{ps} is the modulus of elasticity of the prestressing steel and $\varepsilon_O(t_0)$ and $\psi(t_0)$ are calculated according to formula (6.22). The second part of equation (6.23) represents the change in stress due to the elastic shortening of the concrete when the prestress is transferred. This instantaneous loss is not present when post-tensioning is applied due to the incompatibility of strains.

6.3.2. Effect of relaxation of steel on the time-dependent deformation

Remember the assumption of section 6.3.1 that the prestress is applied at the same time as the external loads are applied, namely the time t_0. The method which was described in section 6.2 still holds for a prestressed section. The formula to calculate the restraining forces just needs to be expanded to take into account the relaxation of the prestressing steel:

$$\begin{bmatrix}\Delta N\\ \Delta M\end{bmatrix} = \begin{bmatrix}\Delta N\\ \Delta M\end{bmatrix}_{creep} + \begin{bmatrix}\Delta N\\ \Delta M\end{bmatrix}_{shrinkage} + \begin{bmatrix}\Delta N\\ \Delta M\end{bmatrix}_{relaxation} \tag{6.24}$$

The contribution of the relaxation of the prestressing steel to the restraining forces can be calculated by:

$$\begin{bmatrix}\Delta N\\ \Delta M\end{bmatrix}_{relaxation} = \sum_i \begin{bmatrix}A_{ps,i} \cdot \Delta\overline{\sigma_{pr,i}}\\ A_{ps,i} \cdot \Delta\overline{\sigma_{pr,i}} \cdot y_{ps,i}\end{bmatrix} \tag{6.25}$$

with $A_{ps,i}$ the cross-section of the ith prestressing layer, $y_{ps,i}$ the vertical distance between the ith layer and the reference point O (positive if the layer is below O), and $\Delta\overline{\sigma_{pr,i}}$ the reduced relaxation of the prestressing steel in the ith layer during the time period $t - t_0$:

$$\Delta\bar{\sigma}_{pr} = \chi_r \cdot \Delta\sigma_{pr} \tag{2.8}$$

where χ_r is a dimensionless factor which is smaller than one, and $\Delta\sigma_{pr}$ is the prestressing loss in an ideal case.

The rest of the calculation method described in section 6.2 is similar. One should only remember to correct $\bar{A}$, $\bar{S}$, and $\bar{I}$ for the metal duct in case of post-tensioning. From the moment the duct is grouted the prestressing steel can be taken into account for the calculation of $\bar{A}$, $\bar{S}$, and $\bar{I}$. The grout should not be taken into account; it is not prestressed and will crack when tension is induced in it (Taerwe, 2015).

The stress loss in the prestressed steel during the time period $t - t_0$ can be calculated as follows:

$$\Delta\sigma_{ps} = \Delta\bar{\sigma}_{pr} + E_{ps} \cdot \left(\Delta\varepsilon_O + y_{ps} \cdot \Delta\psi\right) \tag{6.26}$$

with $\Delta\varepsilon_O$ and $\Delta\psi$ calculated according to equation (6.13) and (6.24). Due to the presence of non-prestressed reinforcement this loss is smaller than in a theoretical member with only prestressed steel. The non-prestressed steel takes part of the compressive force which is induced in the concrete by the prestressing steel. As the compressive stress in the concrete reduces over time due to relaxation, this compressive stress is redistributed to the non-prestressed steel, where the compressive stress increases. Therefore, the compressive stress in a member with non-prestressed steel is smaller than in the case no non-prestressed steel would be present. The presence of non-prestressed steel also influences the strain and curvature. Since, the steel does not want to deform the strain and curvature will be smaller.

6.4. Calculation of deflection: method of elastic weights

Once the curvature over the length of the beam is known, it is possible to calculate the deflection of the beam using the method of elastic weights. The beam is replaced by a conjugate beam. The beams which are studied in this dissertation are isostatic beams. In the case of an isostatic beam, the conjugate beam is identical to the original beam, but the load on the beam is replaced by a transversal distributed load equal to the curvature, see Figure 6.2. If the curvature is positive (elongation at the bottom and compression at the top) the applied load needs to act vertically downwards. The shear force V and the moment M at a certain point in the conjugated beam are equal to respectively the rotation θ and the deflection D at the corresponding point in the original beam.

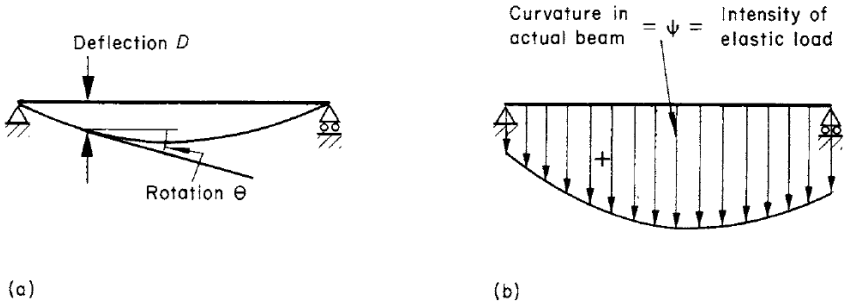

Figure 6.2. a) Isostatic beam with indication of deflection and rotation; b) conjugate beam with distributed load ψ (Ghali et al., 2002).

In the case this method is applied in numerical calculations, the continuous loading needs to be discretised. This can be done by uniformly dividing a number of nodes over the length of the beam. In the nodes an equivalent concentrated load Q is applied. The load at a node i (Q_i) is opposite in sign, but with the same magnitude, as the sum of the reactions on node i from two simply supported beams, from $i-1$ to i and from i to $i+1$, carrying the same load as the conjugate beam, see Figure 6.3. In case of a distributed load which has a parabolic variation, Figure 6.4 gives the equivalent concentrated loads.

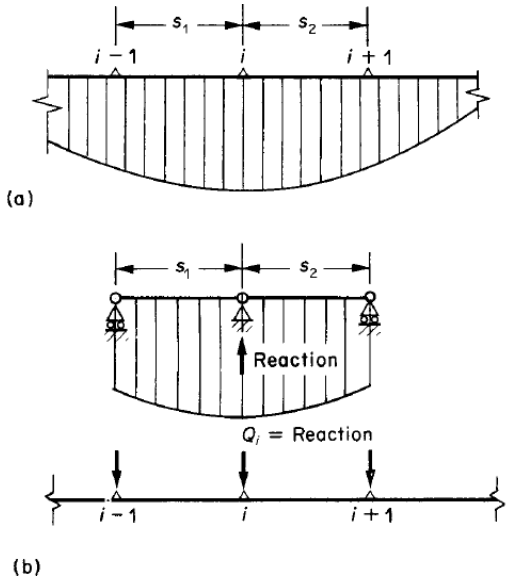

Figure 6.3. Transition from (a) a distributed loading to (b) an equivalent concentrated loading (Ghali et al., 2002).

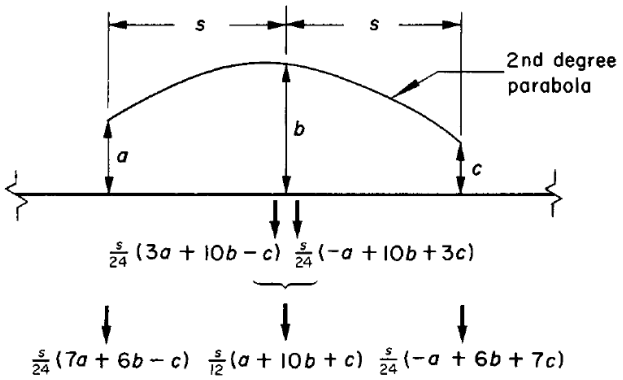

Figure 6.4. Equivalent concentrated loads in case the distributed load varies parabolically (Ghali et al., 2002).

By the use of the principle of concentrated loads, it is possible to derive a set of simplified equations which allows to determine the elongation (D_1), the end rotations (D_2 & D_3), and the deflection at the middle (D_4) of a beam or a section of a beam, see Figure 6.5 (a). The input for these equations are the strain at the centroid of the cross-section $\varepsilon_{centr.}$ and the curvature ψ. These need to be known at three points, see Figure 6.5 (b).

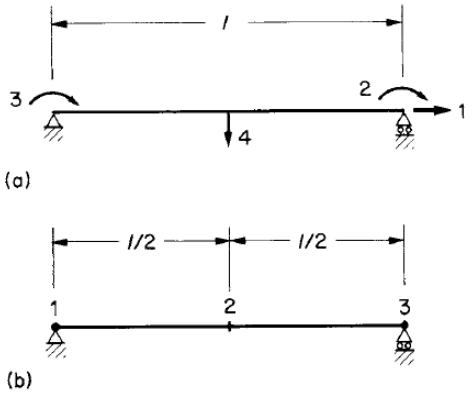

Figure 6.5. a) Simply supported beam with span l and b) its two section equivalent (Ghali et al., 2002).

If $\varepsilon_{centr.}$ and ψ vary linearly between consecutive sections, which is the case in a four point bending test, the elongation, the end rotations and the deflection at the middle can be calculated according:

$$D_1 = \frac{l}{4} \cdot [1 \quad 2 \quad 1] \cdot \{\varepsilon_{centr.}\} \tag{6.27}$$

$$D_2 = \frac{l}{24} \cdot [1 \quad 6 \quad 5] \cdot \{\psi\} \tag{6.28}$$

$$D_3 = \frac{l}{24} \cdot [5 \quad 6 \quad 1] \cdot \{\psi\} \tag{6.29}$$

$$D_4 = \frac{l^2}{48} \cdot [1 \quad 4 \quad 1] \cdot \{\psi\} \tag{6.30}$$

$$\text{with } \{\varepsilon_{centr.}\} = \begin{bmatrix} \varepsilon_{centr.,1} \\ \varepsilon_{centr.,2} \\ \varepsilon_{centr.,3} \end{bmatrix} \text{ and } \{\psi\} = \begin{bmatrix} \psi_1 \\ \psi_2 \\ \psi_3 \end{bmatrix} \tag{6.31}$$

6.5. Curvature due to bending for cracked sections

The tensile strength of concrete is low compared to its compressive strength. Therefore, most non-prestressed concrete beams crack at the moment loading is applied. Cracked concrete is no longer able to transfer tensile forces. The forces which are applied at a cross-section, thus need to be resisted by the concrete in compression and the reinforcement. The cracks will be distributed over the length of the concrete. Cracked cross-sections are alternated by uncracked sections. In the uncracked sections the tensile stress is lower than the tensile strength of the concrete. In these sections, the concrete that is in tension also contributes to the resistance against the forces, and thus it contributes to the stiffness.

For the analysis of cracked members two ideal states are considered. State 1 is the uncracked state in which the entire concrete cross-section is considered for the calculation of the stiffness. In this state there is compatibility between the strains of the concrete and the reinforcement steel. This is the state which has been studied up until now. State 2 is the fully cracked state. All the concrete in tension is ignored; only the concrete in compression and the reinforcement are taken into account for the calculation of the stiffness. The actual state will be somewhere in between these two states and thus interpolation will be required.

First, state 2 will be considered and the neutral axis, at which the strain is zero, will be determined. This will allow to calculate the required parameters (e.g. the stiffness) of state 2. Second, the interpolation principle will be explained in order to calculate the curvature and the deflection.

The derivation for a prestressed concrete section will not be performed. Prestressed elements are generally designed in such a manner that the stress in the concrete never reaches the tensile strength of the concrete. This will be checked in chapter 8 for the studied prestressed beams and it will be concluded that this is indeed the case for the studied beams.

6.5.1. Determination of the neutral axis

Figure 6.6 (a) shows a concrete cross-section with a random shape and several reinforcement layers. At an arbitrary reference point O an axial force N and a moment M are applied so that the top of the cross-section is in compression and the bottom is in tension.

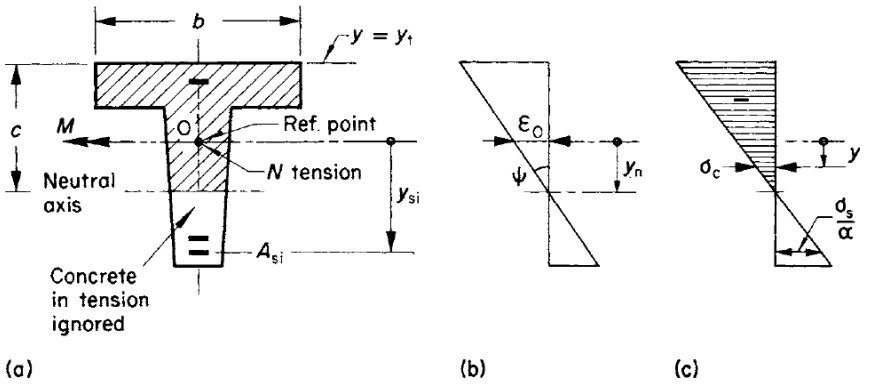

Figure 6.6. a) Concrete section with random shape and indication of the neutral axis; b) corresponding strain of the section; c) corresponding stress of the cross-section (Ghali et al., 2002).

The strain at any fibre, located at a distance y from the reference point O, due to N and M can be calculated according to formula (6.1):

$$\varepsilon = \varepsilon_O + \psi \cdot y \tag{6.1}$$

The vertical coordinate of the neutral axis can be calculated as:

$$y_n = -\varepsilon_O/\psi \tag{6.32}$$

Keeping in mind that the cracked concrete is no longer able to transfer tensile forces, the stress in the concrete becomes:

$$\sigma_c = \begin{cases} E_c \cdot \left(1 - \dfrac{y}{y_n}\right) \cdot \varepsilon_O & for\ y < y_n \\ 0 & for\ y \geq y_n \end{cases} \tag{6.33}$$

The stress of a reinforcement layer at a vertical distance y_{ns} away from the reference point O can be determined by:

$$\sigma_s = E_s \cdot \left(1 - \frac{y_{ns}}{y_n}\right) \cdot \varepsilon_O \tag{6.34}$$

The integration of the concrete stresses and the summation of the steel stresses needs to result in the axial force N. Taking the moment of these stresses around an axis through the reference point O needs to result in the moment M:

$$N = \varepsilon_O \cdot \left\{ E_c \cdot \int_{y_t}^{y_n} \left(1 - \frac{y}{y_n}\right) \cdot dA + E_{ns} \cdot \sum A_{ns} \cdot \left(1 - \frac{y_{ns}}{y_n}\right) \right\} \tag{6.35}$$

$$M = \varepsilon_O \cdot \left\{ E_c \cdot \int_{y_t}^{y_n} y \cdot \left(1 - \frac{y}{y_n}\right) \cdot dA + E_{ns} \cdot \sum A_{ns} \cdot y_{ns} \cdot \left(1 - \frac{y_{ns}}{y_n}\right) \right\} \tag{6.36}$$

with y_t the vertical coordinate of the top fibre, dA an elemental area of concrete in compression, A_{ns} the steel area of a reinforcement layer, E_c the modulus of concrete, and E_{ns} the modulus of the reinforcement steel. The summations need to happen over all the reinforcement layers.

Solving (6.35) and (6.36) as a set of equations results in the vertical coordinate of the neutral axis y_{ns}. Divide for example equation (6.36) by equation (6.35):

$$\frac{\int_{y_t}^{y_n} y \cdot (y_n - y) \cdot dA + \alpha \cdot \sum A_{ns} \cdot y_{ns} \cdot (y_n - y_{ns})}{\int_{y_t}^{y_n} (y_n - y) \cdot dA + \alpha \cdot \sum A_{ns} \cdot (y_n - y_{ns})} - e = 0 \tag{6.37}$$

where equivalence coefficient α is equal to $\frac{E_{ns}}{E_c}$ and eccentricity e is the ratio of the moment over the axial force $\frac{M}{N}$. Note that it is not the individual value of N and M that decides the location of the neutral axis but their ratio.

In the case there is no axial force N, like e.g. a simply supported non-prestressed beam only subjected to bending, y_{ns} can be calculated simpler by substituting N by zero in equation (6.35):

$$\int_{y_t}^{y_n} \left(1 - \frac{y}{y_n}\right) \cdot dA + \alpha \cdot \sum A_{ns} \cdot \left(1 - \frac{y_{ns}}{y_n}\right) = 0 \tag{6.38}$$

The meaning of this equation is that the static moment of the transformed fully cracked section around the neutral axis is zero. In other words the neutral axis is the centre of the transformed fully cracked section. Remember that for a fully cracked section only the reinforcement steel and the concrete in compression are taken into account.

In case of a rectangular cross-section formula (6.38) can be simplified. Define for example a temporary axis system with the origin at the top and the y-axis positive downwards. Assume that x_e is the distance from the top fibre to the neutral axis or in other words assume that x_e is the depth of the compression zone. Formula (6.38) then becomes (Taerwe, 2013):

$$\frac{1}{2} \cdot b \cdot {x_e}^2 + (\alpha - 1) \cdot A_{s2} \cdot (y_n - y_{ns,2}) = \alpha \cdot A_{s1} \cdot (y_{ns,1} - y_n) \tag{6.39}$$

where b is the width of the cross-section, A_{s2} is the area of the compression reinforcement, $y_{ns,2}$ is the distance from the top fibre to the centre of the compression reinforcement, A_{s1} is the area of the tensile reinforcement, and $y_{ns,1}$ is the distance from the top fibre to the centre of the tensile reinforcement. y_n can then be calculated out of x_e by transforming x_e to the original axis system.

Section 6.1 and section 6.2 explained the calculation method for uncracked sections (state 1). If the neutral axis is determined, as explained in this section, the cross-sectional properties (A, S, and I) can be updated. The method of section 6.1 and section 6.2 can then be repeated for the calculation of the cracked section (state 2).

6.5.2. Tension stiffening

A concrete cross-section subjected to bending will crack at the moment the stress in the outermost tensile fibre becomes equal to the mean tensile strength of the concrete f_{ctm} (Taerwe, 2013). The bending moment just before cracking is equal to:

$$M_r = \frac{f_{ctm} \cdot \bar{I}}{y_{nt}} \tag{6.40}$$

in which $\bar{I}$ is the time-dependent transformed section of state 1 and y_{nt} is de vertical distance between the neutral axis and the outermost tension fibre.

In a cracked section the steel stress will be maximum at the location of a crack and will be minimum in between cracks, since the concrete still contributes to the stiffness in the cracked sections. The mean strain in the tensile reinforcement ε_{sm} is thus related to the degree at which cracking occurred. Therefore it can be interpolated out of the reinforcement strain of state 1 ε_{s1} (uncracked) and the reinforcement strain of state 2 ε_{s2} (totally cracked):

$$\varepsilon_{sm} = (1 - \zeta) \cdot \varepsilon_{s1} + \zeta \cdot \varepsilon_{s2} \tag{6.41}$$

in which:

$$\zeta = 1 - \beta_1 \cdot \beta_2 \cdot \left(\frac{M_r}{M}\right)^2 \tag{6.42}$$

in which M is the moment at the critical section, β_1 is a constant which is equal to 1 for high bond bars, which is the case for the studied beams, and β_2 is a constant which is equal to 0.5 for sustained loading.

If a similar effect is assumed on the mean curvature ψ_m it can also be interpolated out of the curvatures of state 1 and 2 (ψ_1, respectively ψ_2):

$$\psi_m = (1 - \zeta) \cdot \psi_1 + \zeta \cdot \psi_2 \tag{6.43}$$

where $\psi_1$is the curvature out of the cross-sectional parameters of an uncracked section (state 1) and ψ_2 is the curvature out of the cross-sectional parameters of a cracked section (state 2).

Figure 6.7 gives a visual representation of equation (6.43). Once the moment surpasses the cracking moment the curvature is interpolated out of two straight lines which represent the uncracked section and the cracked section. The horizontal plateau BC is related to the formulation of the tension stiffening factor ζ.

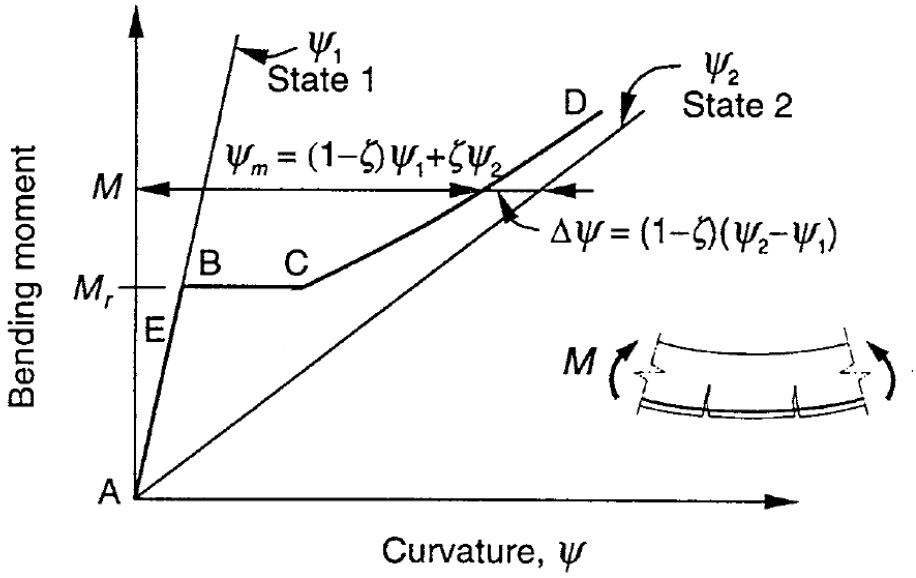

Figure 6.7. Visual representation of equation (6.43) (adapted from Ghali et al., 2002).

7. Modelling of the time-dependent performance of tested reinforced beams; results and discussion

Using the methods discussed in chapter 6 in combination with the material models discussed in chapter 4, the time-dependent behaviour of the reinforced beams of the available dataset (section 5.2) is studied. Six models have been used: GL 2000, MC9099, MC2010, ACI, EC2, and B3. First, the shrinkage model was studied on itself. Similarly, also the creep model was studied on itself. Next, the predictions of the time-dependent behaviour according to these six models versus the actual measured values of the dataset were reviewed. The difference between the use of a simplified aging coefficient and a calculated aging coefficient was examined. Finally, also the influence of the use of a nonlinear creep calculation was investigated.

7.1. Comparison of shrinkage predictions

In Figure 7.1 the shrinkage strain of the six models is plotted up to 1638 days, which is the last day until which static long-term test were executed. Note that the shrinkage strain is negative, in agreement with the sign convention explained in section 6.1. The material parameters necessary for the models can be derived from the information given in section 5.2. The mean of the four types of beams was chosen for: the mean concrete strength f_{cm28}, the modulus of elasticity of concrete E_{cm28}, and the nominal size h. As an overview Table 7.1 gives four important parameters which are used in all material shrinkage models (except for f_{cm28} which is not used by ACI). The ACI model requires, among other parameters, the air content and the slump factor. These two parameters have not been determined. For the air content a value of 2% was assumed and this value has been used for all the following calculations. For the slump factor a value of 300 mm was assumed and this value has also been used for all the following calculations.

Table 7.1. Overview of important input parameters for the material shrinkage models.

Mean concrete strength at 28 days f_{cm28}	31.6 MPa
Nominal size h	95.3 mm
Relative humidity RH	60%
End of curing t_c	1 day

All models except for model B3 have a very similar prediction for the shrinkage at 1638 days. Note that the shrinkage models for MC2010 and MC90-99 are completely identical; therefore, the curve for MC90-99 is not visible in Figure 7.1. EC2 follows a somewhat similar approach as MC2010 and MC90-99, and some of the formulas are approximately similar. Yet, EC2 has a much more pronounced S-shape. The GL 2000 model is the easiest model to calculate shrinkage. Despite this, it predicts the shrinkage strain quite similar to MC2010 and MC90-99, which are more difficult to calculate. Model B3 is the only model that uses the modulus of elasticity at 28 days for the calculation of the shrinkage strain. The prediction of the shrinkage strain for model B3 is significantly lower than for the other models. The reason for this is unclear. The difference between the GL 2000 model, which is the highest predicting model, and the B3 model is more than 50%.

The shrinkage test executed on concrete prisms (150x150x600 mm) for 1600 days resulted in a shrinkage strain of approximately 0.0004 (FKFO no. 547). All the models overestimated this shrinkage. It can be concluded that model B3, which gave the lowest prediction, is the most apt to describe the shrinkage of the concrete used for the reinforced beams.

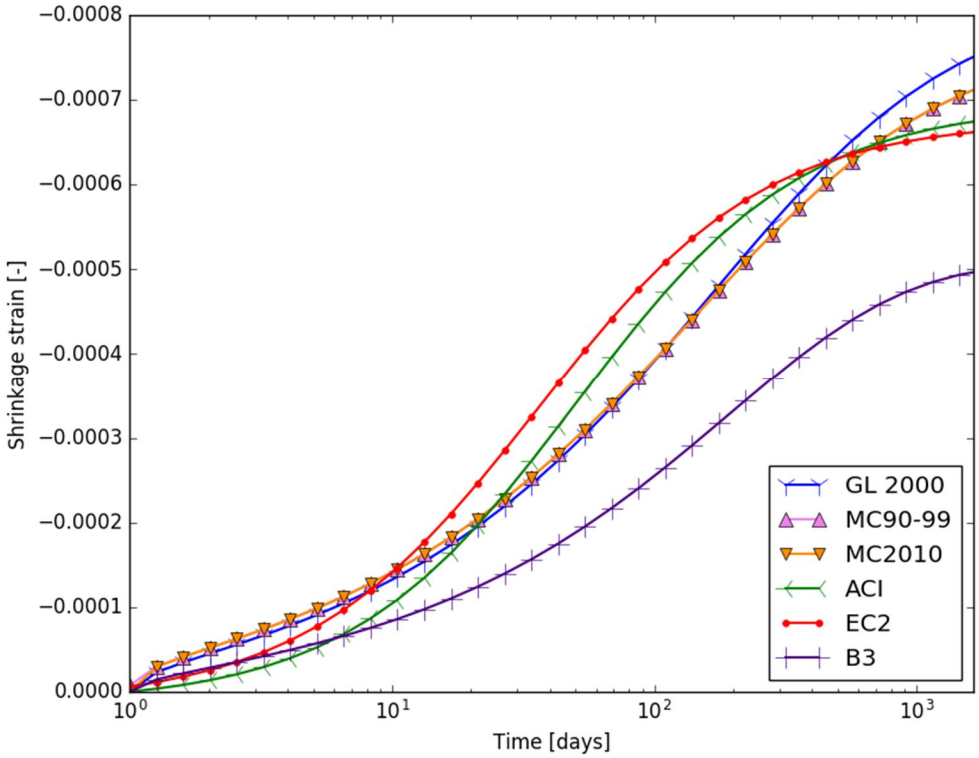

Figure 7.1. Semi-logarithmic plot of the shrinkage strains versus time up until 1638 days.

7.2. Comparison of creep predictions

Figure 7.2 shows the creep coefficient, according to the six models, up to 1638 days. The first part of the curves is equal to zero. The load is applied at 28 days and thus there is no loading before 28 days and hence, also no creep. The same input as in section 7.2 was used for the calculations.

The MC90-99 curve is almost indistinguishable from to the EC2 curve. This is not surprising; after all their mathematical formulations are almost identical. One of the small differences is the correction which is applied to two factors (φ_{RH} and β_H).; both of them being factors dependent on the notional size and the relative humidity. MC90-99 applies the correction for all strength classes of concrete, while EC2 applies the corrections only if the mean concrete strength is larger than 35 MPa. Another small difference is the use of an adjusted time of loading $t_{0,adj.}$. EC2 clearly subscribes for which formulas this adjusted time of loading should be applied and for which formulas it should not be applied. MC90-99 does not have such a clear division. For the values of the creep coefficient according to MC90-99 in Figure 7.2 the adjusted time of loading $t_{0,adj.}$ was applied at every instance the time of loading t_0 was required.

For the type of concrete which was used and for the time period which is represented in Figure 7.2 the highest creep coefficient is obtained by model B3 and the lowest creep coefficient is obtained by the ACI model.

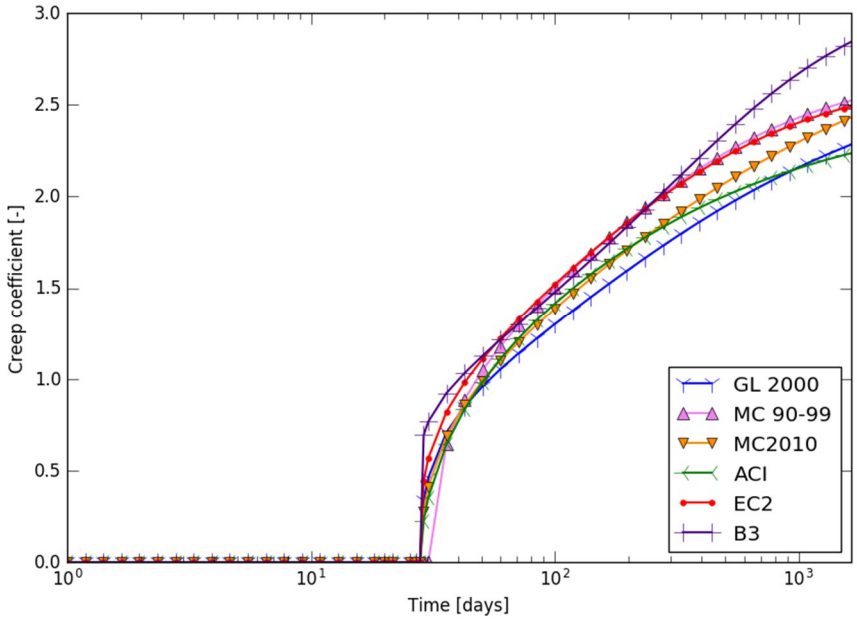

Figure 7.2. Semi-logarithmic plot of the creep coefficients versus time up until 1638 days.

The creep deformation on unreinforced prisms (150x150x600 mm) was measured under a loading of 50% and 70% of the prism compression strength. This loading was applied from 28 days up until 550 days. The reported mean creep coefficient was 2.20. Figure 7.3 shows the creep predictions up until 550 days. Table 7.2 shows the calculated creep coefficient for the different models, as well as the relative difference Δ which is defined as:

$$\Delta = \frac{\varphi_{calc.} - \varphi_{meas.}}{\varphi_{meas.}} \tag{7.1}$$

Table 7.2. Calculated creep coefficients at 550 days and relative difference.

	$\varphi_{calc.}$	Δ
GL 2000	1.979	-0.101
MC90-99	2.269	0.031
MC2010	2.108	-0.042
ACI	2.027	-0.078
EC2	2.248	0.022
B3	2.394	0.088

GL2000, MC2010, and ACI underestimate the creep coefficient at 550 days. MC90-99, EC2, and B3 overestimate the creep coefficient. What is somewhat surprising is that the worst prediction is made by the GL2000 model. This is in contrast with the generally good predictions of the model reported in literature (see section 4.7.2). Model B3 overestimates the measured value most severely. This is as is expected from literature (see again section 4.7.2). The best prediction is done by EC2 which gives only a relative difference of 0.02.

The curve of the creep coefficient calculated according to MC90-99 has a somewhat peculiar behaviour just after loading, where it temporarily remains zero. This is related to the assumption with regard to the use of the adjusted time of loading $t_{0,adj.}$. In the other creep models the creep

coefficient is set to zero if the time is smaller or equal to the time of loading t_0. With the assumption about the adjusted time of loading $t_{0,adj.}$ being used for all the formulas which require t_0, the creep coefficient for MC90-99 is set to zero if the time is smaller than $t_{0,adj.}$. If this would not be done, calculating the creep coefficient for times between t_0 and $t_{0,adj.}$ would result in complex values. To mitigate this deviating behaviour for MC90-99 $t_{0,adj.}$ is henceforth only used in the formula which is stated by EC2. If a new plot would be made, the MC90-99 curve would lie even closer to the EC2 curve than it does now. Therefore MC90-99 will often not be plotted in the figures which can be found later in this chapter.

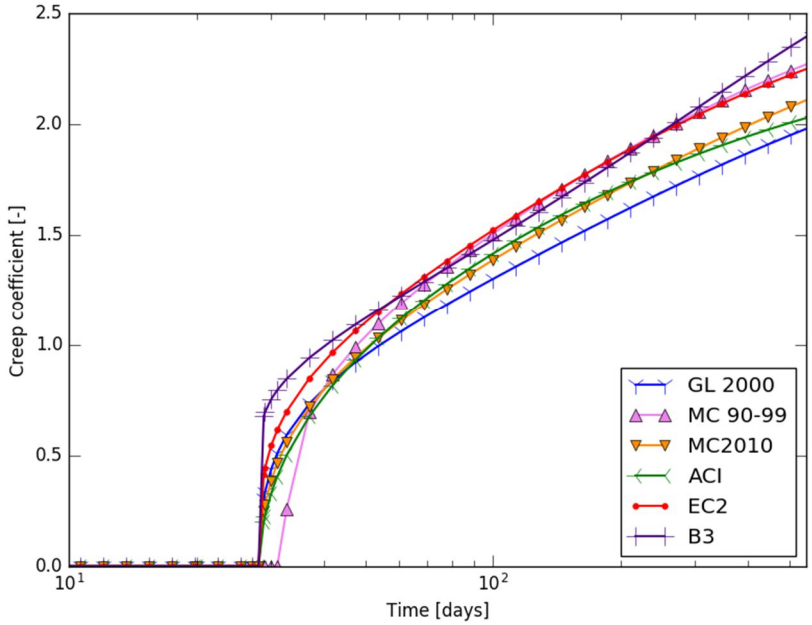

Figure 7.3. Semi-logarithmic plot of the creep coefficients versus time up until 550 days.

As extra information Figure 7.4 shows the creep coefficient curves up to 274 years. The curves for MC90-99, EC2, and ACI flatten out. This is in contrast to the curves according to B3, GL2000, and MC2010. These last three exhibit a linear behaviour after about 2000 days.

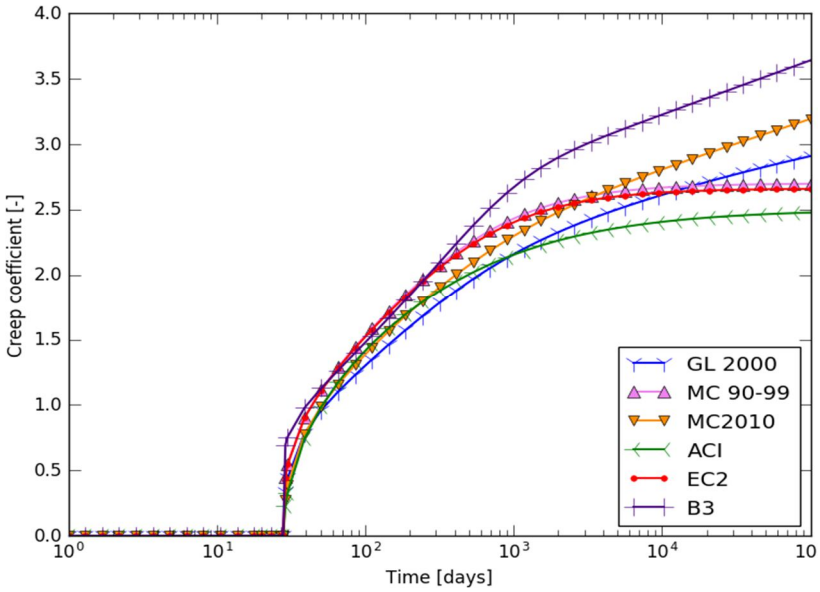

Figure 7.4. Semi-logarithmic plot of the creep coefficients versus time up until 274 years.

7.3. Predictions of calculation models versus available measurements

7.3.1. Assumptions

The deflections and the strains of the different types of reinforced beams were predicted and compared against the measurements of the long-term tests. In order to do this a cross-sectional method which uses the age-adjusted effective modulus was used (see chapter 6). This method assumes a linear relation between stress and strain. For the calculation of the deflection according to the method of the elastic weights the beams were split up in sections. The number of sections was determined by two opposing constraints: being accurate and keeping the calculation time reasonable. It was determined that 30 sections (section length of less than 10 cm) was a good compromise; for a further gain in accuracy the number of sections would have needed to be increased drastically.

The method of chapter 6 requires: the shrinkage strain, the modulus of elasticity, and the creep coefficient; all at different moments in time. These three were calculated according to the different material models. For the calculation of the modulus of elasticity at different times EC2, MC2010, B3, and MC90-99 prescribe formulas consisting out of a time function multiplied with the modulus of elasticity at 28 days. This modulus of elasticity at 28 days can be estimated using formulas, but in order to obtain a higher accuracy it was chosen to take the measured modulus of elasticity depending on the beam type. If for example a beam of type I was calculated, the modulus of elasticity of beam type I was chosen (instead of the mean modulus of elasticity of all the beam types). Note that the ACI model and the GL 2000 model do not require the modulus of elasticity at 28 days. Instead of a time function multiplied with the modulus of elasticity at 28 days, their formulas contain the time-dependent mean compressive strength of the concrete, which is calculated out of the mean compressive strength at 28 days. For this compressive strength at 28 days the measured values depending on the beam type were used, similar as for the modulus of elasticity at 28 days. This method was also used at any other moment the compressive strength was required.

In all the calculations the tangent modulus of elasticity was used as prescribed by EN 1992-1-1 (2004, section 3.1.4) (except for the calculation of the shrinkage strain and the creep compliance according to the B3 model). The time-dependent influence of the modulus of elasticity is thus assumed to be encompassed by the creep – and aging coefficients.

The determination of the aging coefficient $\chi(t, t_0)$ for the age-adjusted effective modulus requires extensive calculations. For a first analysis it was assumed that the aging coefficient was constant and equal to 0.8. This simplification reduced the calculation time by about a factor five.

When the depth of the cracked zone is determined in hand calculations (e.g. Taerwe, 2013) this is done using the long-term equivalence coefficient α with a value between 15 and 21. In order to be more accurate here, the depth of the cracked zone was determined using the age-adjusted effective modulus with a creep coefficient determined for the end of loading of the studied beam.

The long-term tests on reinforced beams were executed on pairs of beams, see Figure 5.4. The results of the tests were always presented as the mean of the results of the pair. By opting for this

approach the influence of the self-weight was cancelled out of the measurements. Since the calculated predictions were compared against these measured mean values, the self-weight did not needed to be taken into account in the calculations.

Finally, the test setup of the long-term tests, see Figure 5.4, was somewhat simplified in order to facilitate the calculations. The parts of the beams extending beyond the supports were neglected, see Figure 7.5. The error resulting out of this simplification was not studied specifically, but based on common engineering practice it is assumed to be small.

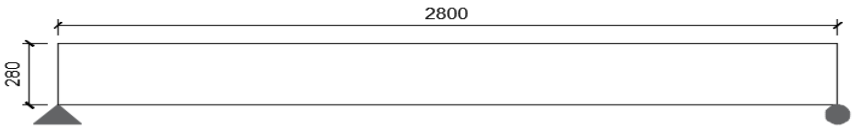

Figure 7.5. Assumed setup of reinforced beams (measurements in mm).

7.3.2. Results out of a linear creep calculation with simplified $\chi(t, t_0)$

7.3.2.1. Deflection

The predictions for the deflection at midspan of the beams of type II (Figure 5.2, p. 37) calculated with a constant aging coefficient $\chi(t, t_0)$ equal to 0.8 can be seen in Figure 7.6 as continuous lines. For reasons of clarity it was chosen to show only four predictions: EC2, MC2010, B3, and GL 2000. Note that a downward deflection in all the graphs will have a positive sign. The measurements are shown in this graph as dots. In all the graphs comparing measurements against predictions, all the measurements and predictions corresponding to a certain beam have the same colour. The name in the uppermost legend indicates the beam. The number after the B indicates the beam type and the number behind the L indicates at which percentage of the failure load the beam was loaded throughout the testing period. Take for example beam B2_L52. This is a beam of beam type II and it was loaded at 52% of the failure load of the beams of type II.

From Figure 7.6 it is clear that the models have a very similar prediction for the deflection. For the lowest load level the predictions are, for the largest part, quite accurate; however, closer to the end of the testing period the predictions underestimate the measured deflections. For the higher load levels the predictions are inaccurate. The models predict the rate of creep badly, resulting in an underestimation of the deflection which becomes more pronounced as the time increases. A possible explanation for these underestimations can be the fact that the linear calculation approach which was used is no longer valid under these higher load levels. The load level is also above the service range and thus outside of the validity range of the models, which could also explain the underestimation of the rate of creep.

The trend in the predictions of the deflections of beam types I and III is very similar to the trend of beam type II. Their graphs can be found in Appendix E. For the highest load level of beam type III it is not only the deflection over time which is underestimated, also the instantaneous deflection at 28 days is predicted too low. This could also be an indication of the fact that the linear approach is no longer valid. Figure 7.7 shows the predictions according to EC2, MC2010, B3, and MC90-99 for the reinforced beams of type IV. For the higher load levels the same trend of underestimation, seen for the beams of type II, is evident. For the lower load levels there is an overestimation of the creep at earlier ages. Near the end of the testing period the predicted values and the measured values are

almost identical. The explanation of this phenomenon is an overestimation of the instantaneous deflection, resulting in an overestimation of the models at early age, followed by an underestimation of the rate of creep , resulting in better predictions over time. If the tests would have continued over a longer time, the models would most likely have underestimated the creep at a later age, based on the rates of creep near the end of the measuring period.

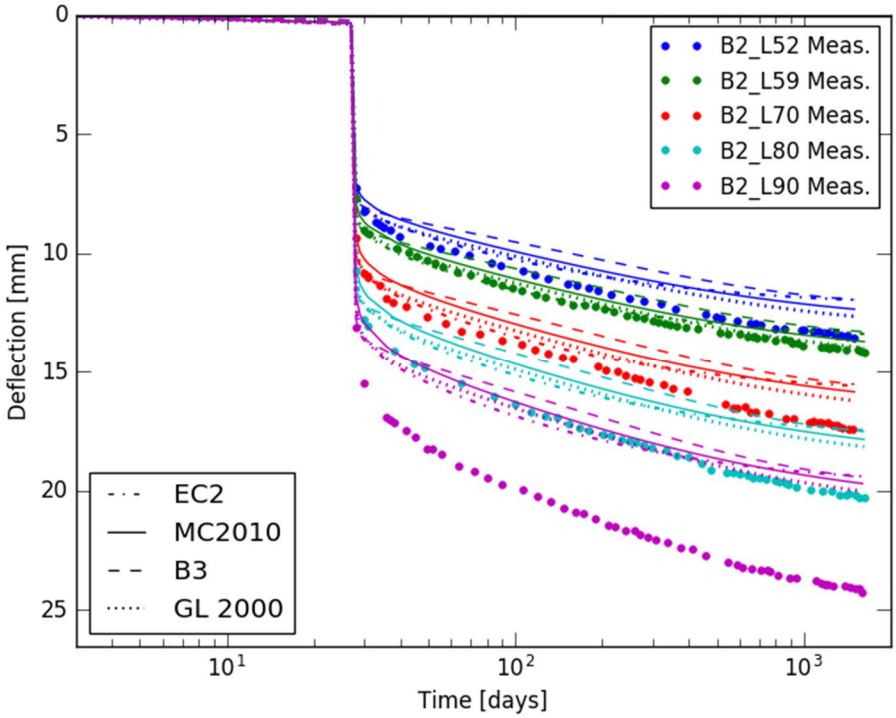

Figure 7.6. Predictions and measurements of the deflection at midspan of the reinforced beams of type II (constant aging coefficient equal to 0.8 and no correction for nonlinear creep).

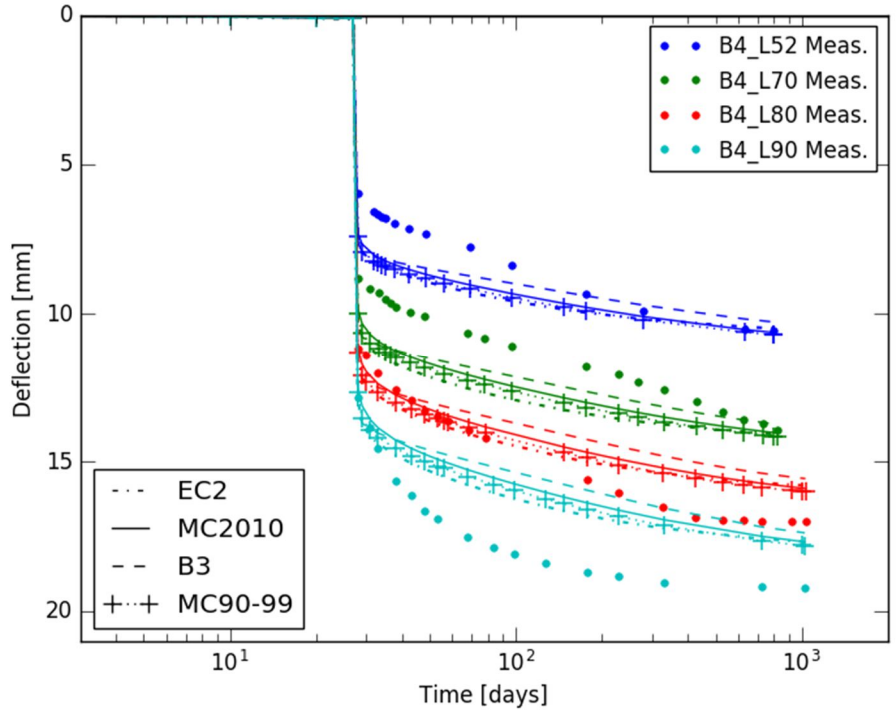

Figure 7.7. Predictions and measurements of the deflection at midspan of the reinforced beams of type IV (constant aging coefficient equal to 0.8 and no correction for nonlinear creep).

Before the time of loading, which is 28 days for the reinforced beams, there is no creep deformation. The deflection graphs; however, show a small deflection before 28 days. This deflection is caused by shrinkage. In unreinforced beams the shrinkage can happen freely and there will be no curvature due to shrinkage, only axial strains. In the case of reinforced beams, the reinforcement steel hinders the shrinkage deformation. For the beams of type I, II, and III the most important fraction of steel is located in the bottom part of the beam. This steel will impede the free shrinkage deformation near the bottom. Near the top the shrinkage deformation will be hindered less. This difference in strain between the bottom and the top presents itself as a curvature which results in a downward deflection. Note that the deflection due to shrinkage of the beams of type IV (Figure 7.7) is much smaller than the deflection of the beams of type II (Figure 7.6) and type I and III (Appendix E). The beams of type IV have the same tensile reinforcement as the beams of type II, but they also have compressive reinforcement. This compressive reinforcement will hinder the shrinkage deformation at the top, resulting in a smaller curvature.

7.3.2.2. Stress

Not taking into account the beam of type IV loaded at 70%, the measured deflections of the beams of type IV (Figure 7.7) have levelled more out than the measured deflections of the beams of type II (Figure 7.6). Figure 7.8 and Figure 7.9 show the predictions of the stress at the top fibre in the midspan of the beams of type II, respectively type IV. According to the sign convention of chapter 6, tensile stresses are positive; therefore, the compressive stress in the concrete is negative. Comparing the two graphs, it can be seen that the stress just after loading is similar for the two beam types. Over time the compressive stresses decrease due to relaxation but this decrease is more pronounced for the beams of type IV. This explains why the deflections of the beams of type IV level out quicker. The absolute level of loading between the two beam types is similar (and is even slightly higher for beam type IV), see Table 5.3. This similar loading explains why the stresses just after loading are comparable. The reason why the compressive stresses over time are lower in the beams of type IV thus needs to be related to the compression reinforcement which is present in the beams of type IV. This compression reinforcement causes a stress redistribution. The concrete in compression wants to creep and is resisted by the compression reinforcement. As this goes on, compression stress which is in the concrete is transferred to the reinforcement, thus resulting in lower compression stresses in the concrete over time. This phenomenon thereby attributes to the relaxation of concrete stress caused by creep. Since this is a long-term phenomenon, the stresses just after loading are similar for the two beam types. Criel et al. (2015) came to a similar conclusion. They tested axially loaded prisms with different reinforcement ratios and concluded that compression reinforcement causes a significant redistribution of the stresses.

In Figure 7.8 and Figure 7.9 it can also be seen that the stress is positive in the time period just before loading. This is caused by the restrained shrinkage, as explained previously. The restrained shrinkage will result in a tensile stress at the top fibre of about 1.5 MPa just before loading in the beams of type IV. The tensile stress in the beams of type I, II, and III is negligible because there is no structural tensile reinforcement hindering the shrinkage.

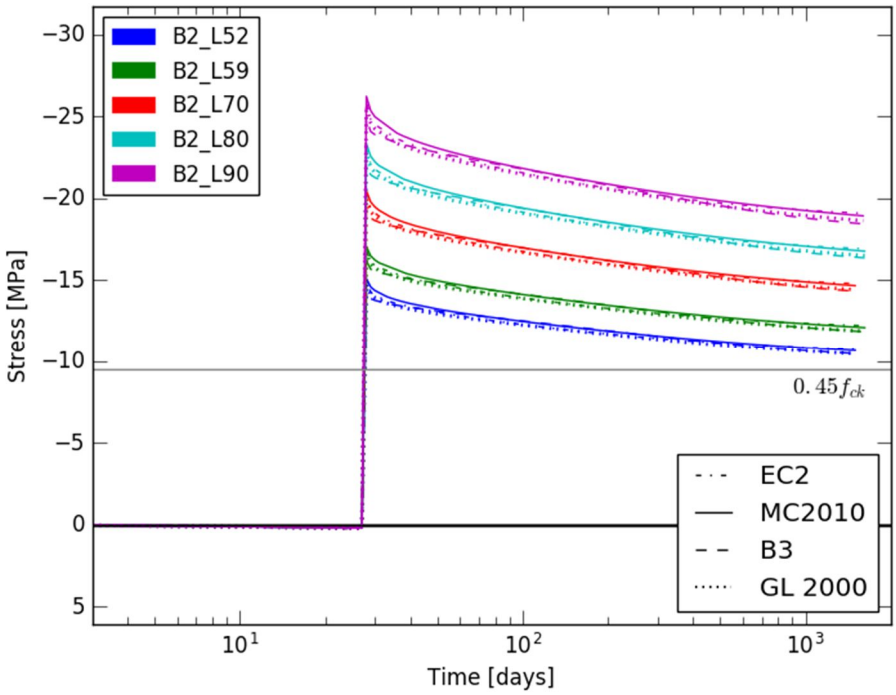

Figure 7.8. Prediction of the stress at the top fibre at midspan of the reinforced beams of type II (constant aging coefficient equal to 0.8 and no correction for nonlinear creep).

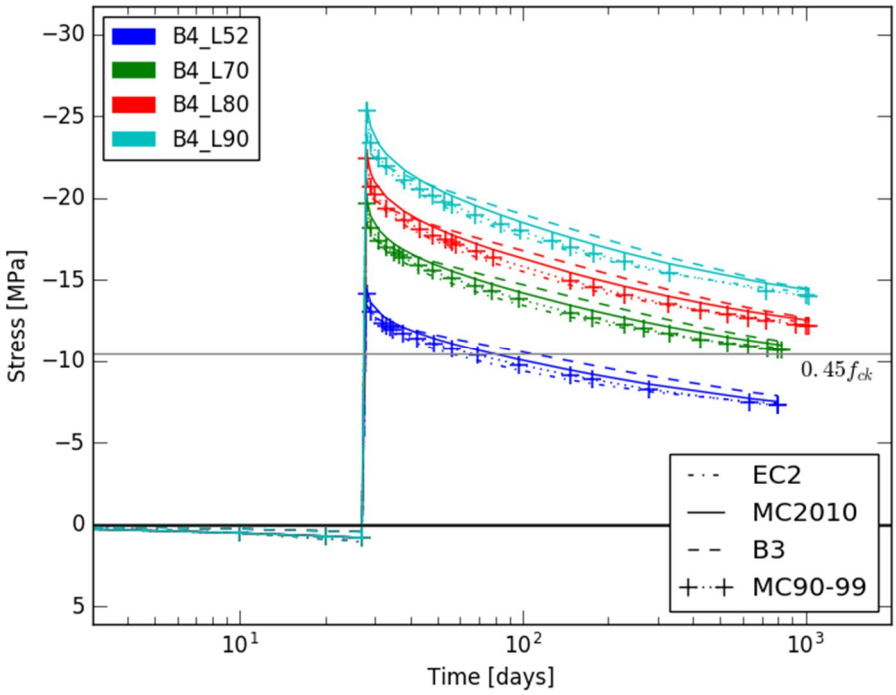

Figure 7.9. Prediction of the stress at the top fibre at midspan of the reinforced beams of type IV (constant aging coefficient equal to 0.8 and no correction for nonlinear creep).

NBN EN 1992-1-1 (2005) advises to keep the concrete compressive stress below 0.45 times the characteristic compressive strength of the concrete at loading $f_{ck}(t_0)$ in the serviceability limit state under the quasi-permanent load combination. If this condition is fulfilled, the creep can be assumed linear. The stress graphs have a grey line which indicates the value of $0.45f_{ck}(t_0)$. When comparing the different beam types, the location of this line varies slightly. This is due to the fact that $f_{ck}(t_0)$

varies somewhat for each beam type. All the beams, except for the beams of type I, have compressive stresses above the value of $0.45 f_{ck}(t_0)$. Most of them even stay above this value even though the compressive stresses decrease significantly over time due to relaxation. For the beams of type I (Figure E.3) only the highest loaded beam has a compressive stress which surpasses the boundary value for a short period of time. Due to a low tensile reinforcement ratio, the beams of type I have a low failure moment in comparison to the other beams. The moments which are imposed for the long-term loading are thus also relatively low, which results in relatively low compressive stresses compared to the other beam types.

7.3.2.3. Strain

Figure 7.10 shows the strains at midspan in the measuring point closest to the top fibre (Appendix B) for the beams of type II. Similar as for the stress, a compressive strain is negative. The strains are predicted with the same trend as the deflections (Figure 7.6). The prediction for the beams loaded at a lower level is reasonably good, although the difference between the measured and calculated values increases over time. For the higher loaded beams the strains are severely underestimated. Due to the linear elastic relationship which was assumed between the stress and the strain in the calculations, the predicted values increase with a constant step for increases in the load level of the same magnitude. The difference between the predictions of for example the beams loaded at 70% and 80% is the same as the difference between beams loaded at 80% and 90%. Figure 7.10 shows that this behaviour was clearly not present in the measured beams. The assumption of a linear elastic relationship between stress and strain is only valid for lower stress- and strain levels, explaining why the higher loaded beams are so severely underestimated.

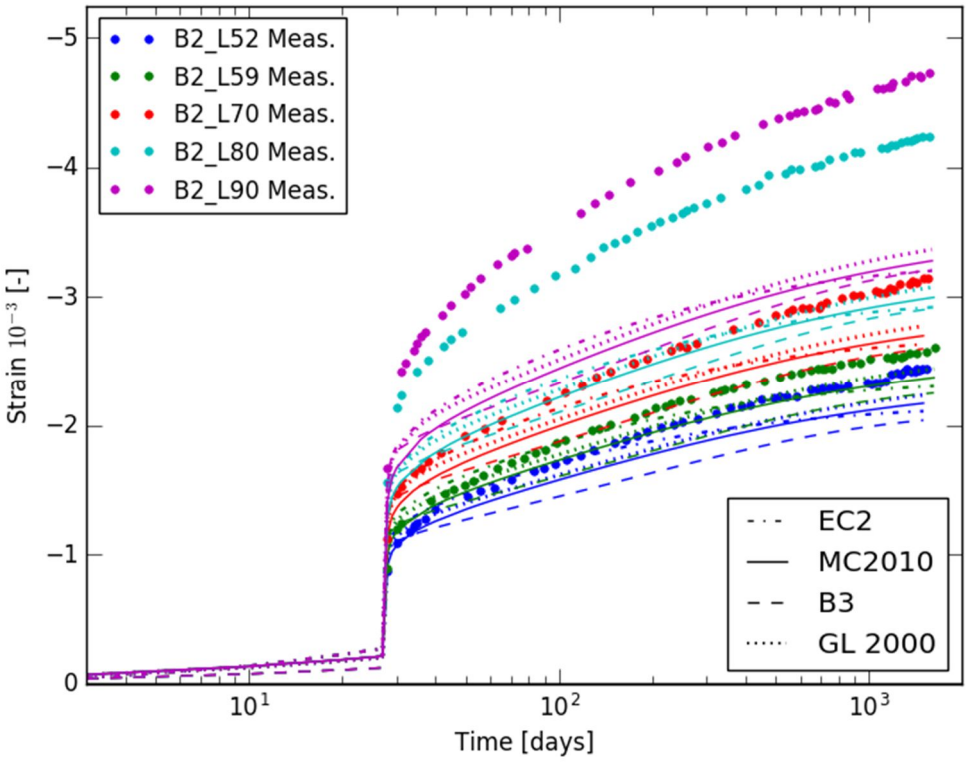

Figure 7.10. Predictions and measurements of the strain near the top fibre at midspan of the reinforced beams of type II (constant aging coefficient equal to 0.8 and no correction for nonlinear creep).

Figure 7.11 shows the measured and calculated strains near the top fibre at midspan for two beams of type IV. The calculated values overestimate the strain. It should be noted that the graph gives a somewhat distorted image due to the scale. The difference between the measured and calculated values of the strain of beam type IV is of the same magnitude as the difference between the measured and calculated values of the beam loaded at 70% of type II. The calculated values have a reasonably good prediction of the rate but overestimate the instantaneous strain at loading. Previously, it was also found for these beams that they overestimate the deflection. It is important to note that the compression steel, which is present in the beams of type IV, significantly reduces the strains, as can be seen by comparing the results of beam type II and beam type IV.

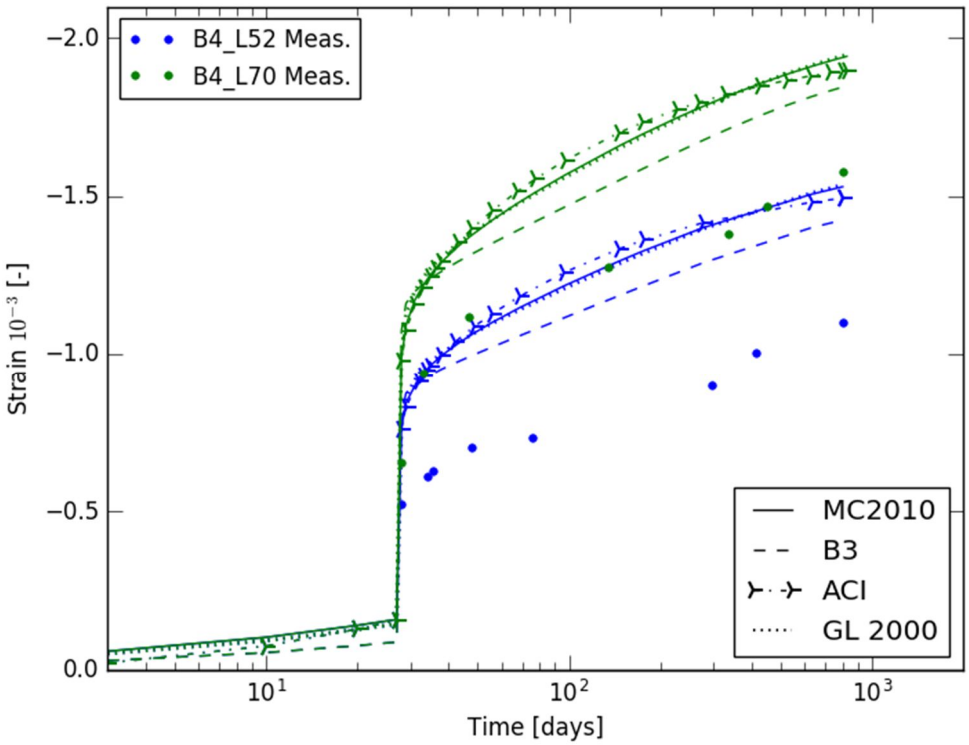

Figure 7.11. Predictions and measurements of the strain near the top fibre at midspan of the reinforced beams of type IV (constant aging coefficient equal to 0.8 and no correction for nonlinear creep).

7.3.2.4. Deformation

The mean deformation at the midspan of the beam of type II, which is loaded at 52% of its failure load, is shown in Figure 7.12. The predicted values according to MC2010 are represented by a solid line. The measured values are represented by a pair of dots: a dot near the top fibre and a dot near the bottom fibre. The dashed line is merely a visual aid that connects the pair of dots. The actual deformation was not linear and showed a kink. The lines do not start at a height of 0 m (they start a few millimetres higher) and they also do not end at 0.280 m (they stop a few millimetres lower). This is because the measuring points of the strains were not at the top- and bottom fibre but slightly below the top fibre, respectively slightly above the bottom fibre, see Appendix B. The compressive strains are underestimated, except for the compressive strain just after loading (28 days) which is slightly overestimated. It can be seen that the degree of underestimation increases over time, as could also be seen in Figure 7.10. This is due to an underestimation of the creep rate. Also the tensile strains, which are positive, are underestimated, though their underestimation is slightly more pronounced. The underestimation of both the compressive strain near the top fibre

and the tensile strain near the bottom fibre results in an underestimation of the curvature. Since the deflections are calculated from the curvatures (see section 6.4), this could also have been concluded looking at the deflection graph (Figure 7.6).

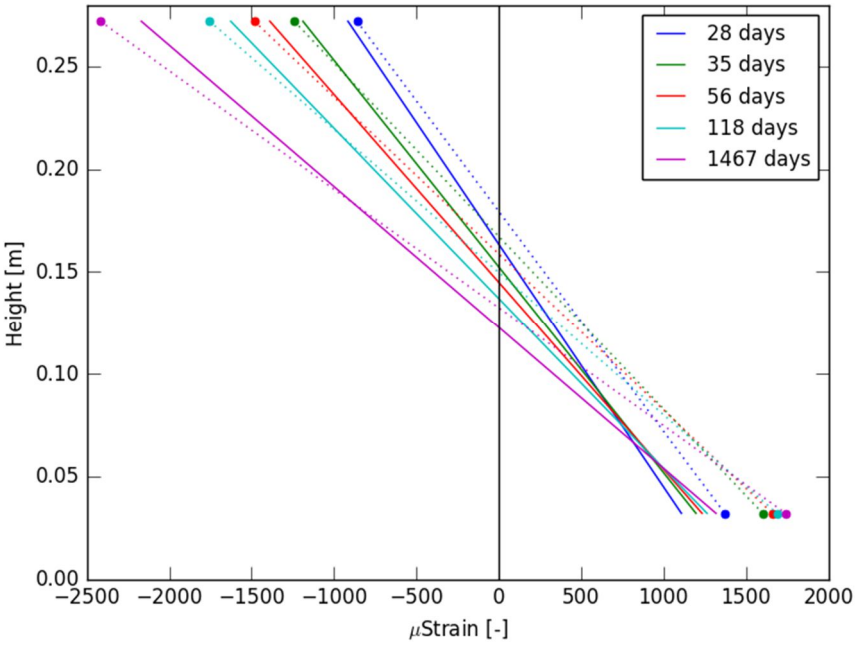

Figure 7.12. Predictions (MC2010) and measurements of the deformation at midspan of the reinforced beam B2_L52 (constant aging coefficient equal to 0.8 and no correction for nonlinear creep).

Figure 7.13 shows the mean deformations of the same beam loaded at 80% of its failure load instead of 52%. The deflection graph (Figure 7.6) showed that the models severely underestimate the deflection of this beam loaded at this level. This can also be deduced from this graph, seeing that it shows a severe underestimation of the curvature.

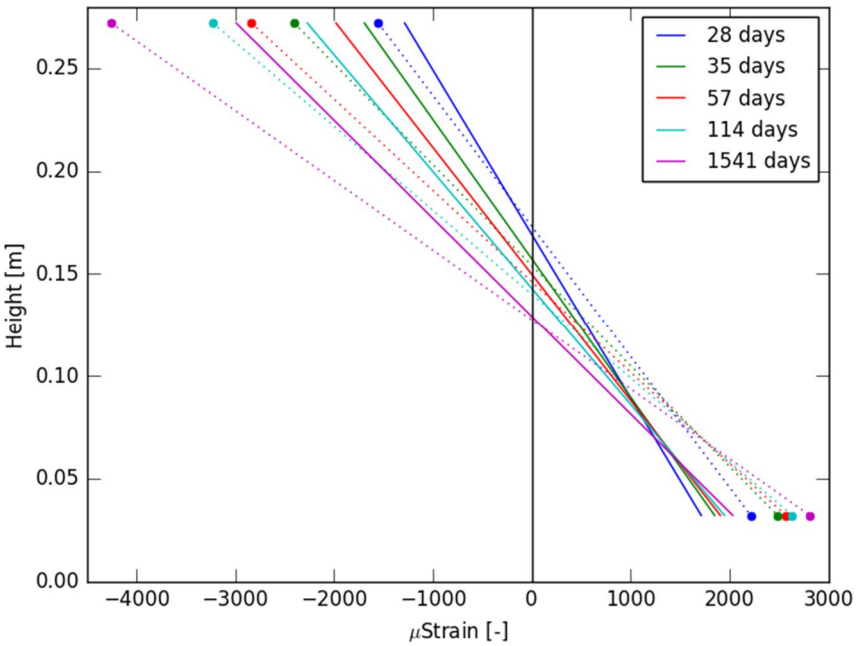

Figure 7.13. Predictions (MC2010) and measurements of the deformation at midspan of the reinforced beam B2_L80 (constant aging coefficient equal to 0.8 and no correction for nonlinear creep).

The mean deformations of the beam of type IV loaded at 52% are shown in Figure 7.14. In contrast to the two beams of type II which were just discussed, this graph shows an overestimation of the curvature of the beam. All the strains are overestimated, except for the tensile strain near the bottom at 788 days which is slightly underestimated. The information presented in this graph is in agreement with the deflection graph (Figure 7.7) and the strain graph (Figure 7.11). The curvature of the measurements can be seen to increase more over time than the curvature according to MC2010. This supports the observation that at an early age the deflection is overestimated and that as the time increases this overestimation diminishes.

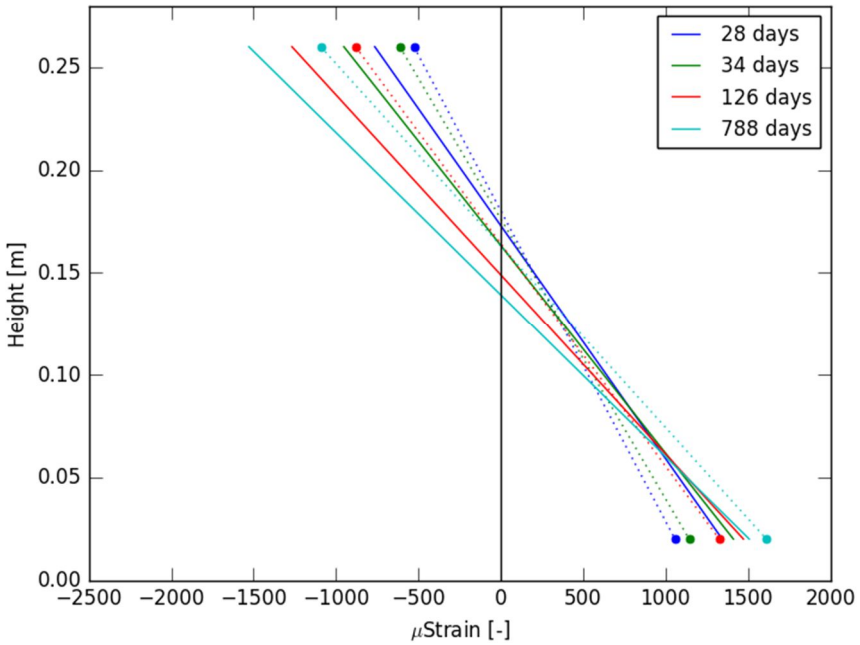

Figure 7.14. Predictions (MC2010) and measurements of the deformation at midspan of the reinforced beam B4_L52 (constant aging coefficient equal to 0.8 and no correction for nonlinear creep).

All the three deformation graphs, which are presented here, clearly demonstrate the phenomenon of the relaxation of concrete compressive stress. As the time increases, the concrete compressive stress decreases, see Figure 7.8 and Figure 7.9. In order to sustain the internal force equilibrium, the depth of the compression zone increases, which can be clearly seen from the presented deformation graphs.

7.3.2.5. Quantification

The graphs give a good indication of the quality of the predictions of the time-dependent deformations. It is; however, not possible to show all the models in the graphs, for reasons of clarity. The graphs also have different scales in order to present the information in the most clear way possible. This, together with the large quantity of information, makes it challenging to make accurate comparisons. Therefore it has been chosen to present the most important data of the deflection graphs in a table. Moreover, the use of a table allows to make a quick and accurate assessment of optimisation methods, see the next sections.

As an example, Table 7.3 gives the comparison of the predictions of EC2, MC2010, B3, ACI, MC90-99, and GL 2000 against the measurements for the beam of type III loaded at 67%, see Figure 7.15. The symbols in the table are defined as:

$$\Delta_i = \frac{p_i - m_i}{m_i} \tag{7.2}$$

$$\xi_{i-j} = \frac{(p_j - p_i) - (m_j - m_i)}{(m_j - m_i)} \tag{7.3}$$

where p_i is the calculated deflection at time i and m_i is the measured deflection at time i. In Table 7.3 t_e is the end of loading.

Following out of the definitions; an underestimation will be negative and an overestimation will be positive. The most accurate predictions are the ones with a relative difference Δ and a relative rate of creep ξ which are as close to zero as possible. In the table the most accurate predictions are underlined. If the measurement at one of the times was not known, it was calculated using linear interpolation. This was not necessary for the predictions because their value was calculated at the exact time of interest.

Table 7.3. Comparison of predictions against measurements of the deflection at midspan of the beam B3_L67 (constant aging coefficient equal to 0.8 and no correction for nonlinear creep).

	EC2	MC2010	B3	ACI	MC90-99	GL 2000
Δ_{28}	0.04	-0.01	0.06	-0.03	0.01	-0.02
ξ_{28-56}	-0.28	-0.34	-0.59	-0.28	-0.32	-0.35
Δ_{56}	-0.06	-0.11	-0.14	-0.11	-0.09	-0.12
ξ_{56-147}	-0.29	-0.29	-0.4	-0.24	-0.28	-0.32
Δ_{147}	-0.09	-0.14	-0.18	-0.13	-0.12	-0.15
ξ_{147-t_e}	-0.66	-0.53	-0.5	-0.67	-0.56	-0.51
Δ_{t_e}	-0.23	-0.23	-0.26	-0.26	-0.23	-0.24

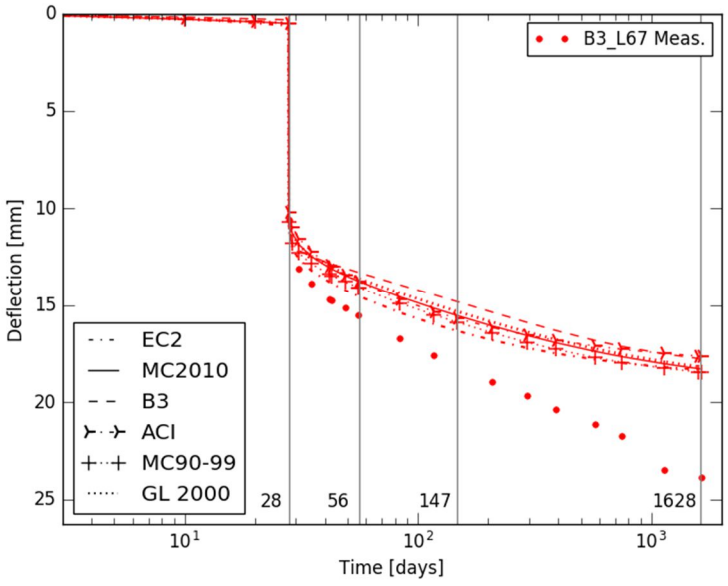

Figure 7.15. Measurements and six predictions of the deflection at midspan of the beam B3_L67 (constant aging coefficient equal to 0.8 and no correction for nonlinear creep)

From Table 7.3 it can be concluded that all the models give a good prediction of the instantaneous deformation at 28 days for beam B3_L67. This is an indication that the reported values of e.g. the modulus of elasticity and the concrete strength determined on small specimens is representative for the concrete of the beam. Further it can concluded that EC2 lies the closest to the measurements and predicts together with ACI the rate of creep the best at an early age. At a medium age the rate of creep is best predicted by ACI, but at a later age B3, followed by GL 2000, predict the rate the best.

Table 7.4 gives an overview of the accuracy of the models for the entire testing base. At an early age the difference between the predictions and the models is relatively small. Over time the difference increases due to a consistent underestimation of the rate of creep, resulting in a significant increase of the relative difference Δ over time. At an early age the ACI model describes the behaviour of the reinforced beams the best. The model gives the smallest difference between measured and predicted values, as well as the best prediction of the rate of creep. At the end of loading the predictions of the GL 2000 model lie the closest to the measured values. The B3 model stands aside from the other models; its predictions become better over time. Especially the prediction of the rate of creep, which the B3 model underestimates the most severe at an early age, improves drastically over time. Even so much so that the B3 model gives the most accurate prediction of the rate of creep at an older age of the concrete.

Table 7.4. Mean comparison of predictions against measurements of the deflection at midspan of all the reinforced beams (constant aging coefficient equal to 0.8 and no correction for nonlinear creep).

	EC2	MC2010	B3	ACI	MC90-99	GL 2000
Δ_{28}	-0.03	-0.01	0.07	0.01	0.01	0.03
ξ_{28-56}	-0.10	-0.15	-0.45	-0.07	-0.14	-0.16
Δ_{56}	-0.06	-0.05	-0.06	-0.02	-0.04	-0.03
ξ_{56-147}	-0.14	-0.12	-0.23	-0.05	-0.11	-0.13
Δ_{147}	-0.08	-0.07	-0.09	-0.03	-0.05	-0.05
ξ_{147-t_e}	-0.47	-0.23	-0.17	-0.47	-0.27	-0.19
Δ_{t_e}	-0.15	-0.11	-0.12	-0.12	-0.10	-0.09

It should be noted that the B3 model prescribes a term to take into account the instantaneous strain in the compliance function which deviates from the general convention (see Bažant & Baweja, 2000). This different method for the calculation of the instantaneous strain was not used. The instantaneous strains of all the models were calculated using the tangent modulus of elasticity with an assumption of a linear relationship between stress and strain. The reason that the B3 predictions deviate at an early age from the other models and the measurements could by related to the shrinkage function, which gives significantly lower values over time than the shrinkage functions of the other models, see section 7.1.

7.3.2.6. Summary

In this section, the results of a cross-sectional linear calculation, using the age-adjusted effective modulus with a constant aging coefficient equal to 0.8, were compared against measurements on

reinforced beams. The predictions for the lower loaded beams are reasonably good although the calculations slightly underestimate the measurements and thus predict values on the unsafe side. For the higher loaded beams, the predictions severely underestimate the time-dependent behaviour, resulting in an increased difference of the predicted values and the measured values over time.

A possible explanation for these underestimations is the fact that the linear relationship which was assumed between the stress and the strain is not valid at higher load levels. The material models are also calibrated on data in the service stress range. It has been shown that many of the beams in this dataset are outside of this service stress range. Therefore, using the material models under these circumstances induces a certain degree of inaccuracy in the calculations.

Of all the six model which were studied (EC2, MC2010, B3, ACI, MC90-99, and GL 2000) the ACI model gives the best predictions at early and medium age. At a later age the predicted values according to the GL 2000 model lie the closest to the measured values. The rate of creep at this later age is best described by the B3 model, followed by the GL 2000 model. This last observation is in agreement by what was found by Gardner (2004), Fanourakis (2011), Goel et al. (2007), and Bažant and Li (2008b).

7.3.3. Influence of the use of a calculated aging coefficient

Up until now the aging coefficient was assumed constant and equal to 0.8. This is a simplification; the aging coefficient is depended on the relaxation function of concrete, the modulus of elasticity and the creep coefficient. Both the modulus of elasticity and the creep coefficient are described by the different material models. Therefore, each material model will have different values of the aging coefficient.

In order to calculate the aging coefficient a module, as proposed by Ghali et al. (2002), was implemented in the calculation software. This module uses a step-by-step method to determine the relaxation function, which is then used to calculate the aging coefficient. The step-by-step method requires a lot of calculations and thus increases the entire calculation time of the time-dependent analysis considerably. In an effort to limit the increase of the calculation time, calculated aging coefficients were stored in a library. Allowing to get the value out of the library, if the input parameters were identical, instead of doing the laborious calculations. Even with this optimisation an analysis with a calculated aging coefficient took at least five times longer than an analysis with a constant aging coefficient.

Figure 7.16 shows both the predictions determined with a calculated aging coefficient and with a constant aging coefficient (equal to 0.8) for the beams of type IV. The predictions have been done according to the B3 model and the ACI model. In Appendix E the comparison between the two calculation methods can be found for the other models. The figures show that the difference between the two calculation models is negligible.

Table 7.5 presents the same information as Table 7.4 but now for the predictions determined by the use of a calculated aging coefficient. About half of the values in Table 7.5 are identical to the values in Table 7.4. The values which are underlined are the values which differ. Except for the relative difference at loading Δ_{28}, the predictions determined by the use of a calculated aging coefficient

are slightly worse than the predictions determined by the use of a constant aging coefficient (equal to 0.8). However, it should be noted that the differences are of an order of magnitude which is negligible.

It can be concluded that the assumption of a constant aging coefficient did not induce errors of any significance. Furthermore, a constant value of 0.8 for the aging coefficient predicts the time-dependent behaviour of the studied beams reasonably well.

Table 7.5. Mean comparison of predictions against measurements of the deflection at midspan of all the reinforced beams (calculated aging coefficient and no correction for nonlinear creep).

	EC2	MC2010	B3	ACI	MC90-99	GL 2000
Δ_{28}	-0.03	-0.01	0.06	0.01	0.01	0.02
ξ_{28-56}	-0.12	-0.16	-0.47	-0.08	-0.16	-0.18
Δ_{56}	-0.07	-0.06	-0.07	-0.02	-0.04	-0.03
ξ_{56-147}	-0.17	-0.13	-0.23	-0.09	-0.14	-0.15
Δ_{147}	-0.09	-0.07	-0.09	-0.04	-0.06	-0.05
ξ_{147-t_e}	-0.49	-0.23	-0.17	-0.49	-0.29	-0.19
Δ_{t_e}	-0.16	-0.11	-0.12	-0.12	-0.11	-0.09

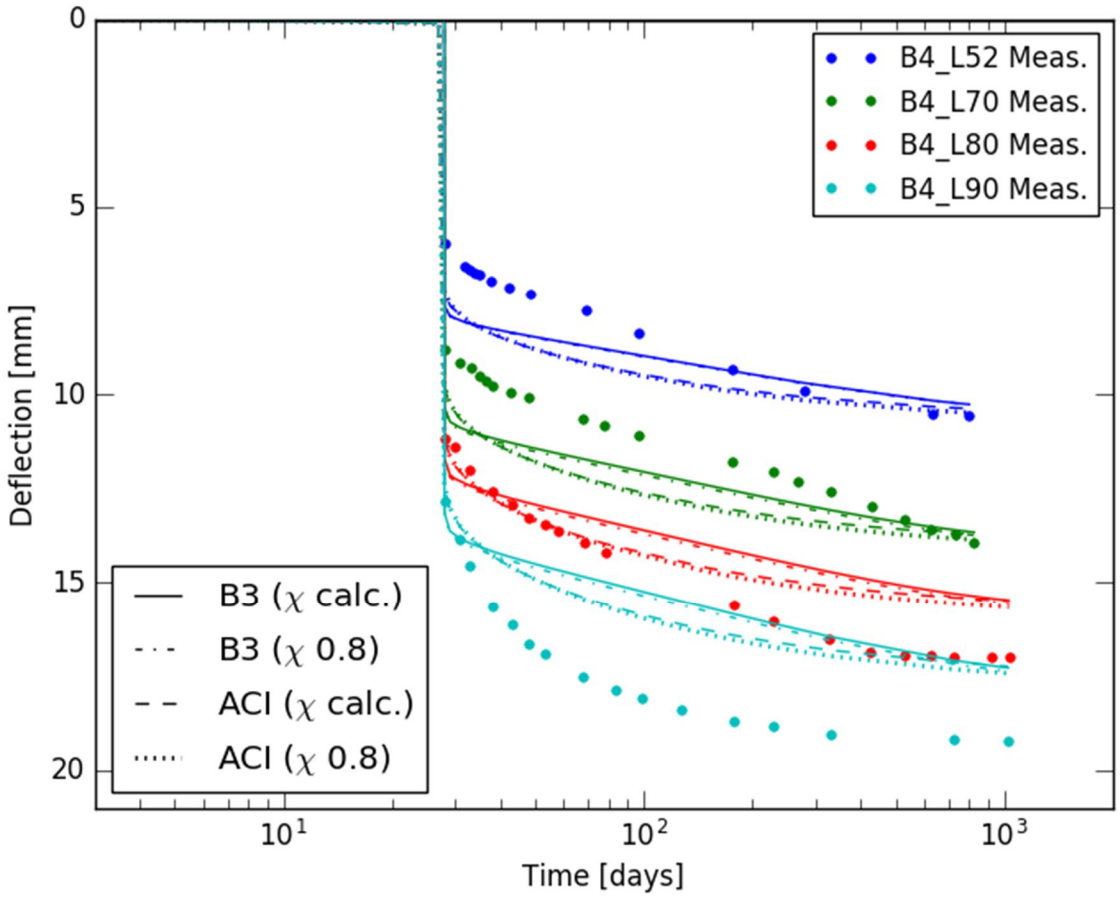

Figure 7.16. Comparison of predicted values with a calculated aging coefficient against predicted values with a constant aging coefficient for beams of type IV.

7.3.4. Influence of a nonlinear creep calculation

All of the material models which are studied here can in their basic form only be used to predict linear creep. It is thus required that the stresses stay in the service range. In case the stresses surpass the service range the creep becomes nonlinear. EC2 and MC2010 are the only two models, of the six which were studied, that provide a practical, ready-to-use formula to correct the creep coefficient for the effects of nonlinear creep.

The Eurocode is the design code for Europe. Therefore, it was chosen to focus the research on the nonlinear creep function described by EC2. This model assumes the creep to be linear up to $0.45f_{ck}(t_0)$, in which $f_{ck}(t_0)$ is the characteristic concrete compressive strength on standard cylinders at the age of loading t_0. The graphs in section 7.3.2.2 showed that most of the beams clearly surpass this limit. In order to take the nonlinearity into account EC2 (NBN EN 1992-1-1, 2005) prescribes a nonlinear, fictive creep coefficient which can be calculated out of the linear creep coefficient:

$$\varphi_k(\infty, t_0) = \varphi(\infty, t_0) \cdot \exp(1.5 \cdot (k_\sigma - 0.45)) \tag{7.4}$$

in which $\varphi(\infty, t_0)$ is the linear creep coefficient which was used up until now and k_σ is the stress-strength ratio $\sigma_c / f_{ck}(t_0)$, where σ_c is the compressive stress.

NBN EN 1992-1-1 (2005) does not describe specifically how to deal with cross-sections in which part of the stress surpasses $0.45f_{ck}(t_0)$ and part of the stress stays below $0.45f_{ck}(t_0)$. It was chosen to apply the correction only for the part of the cross-section which surpasses the limit value of $0.45f_{ck}(t_0)$. If a parabola-rectangle diagram is assumed to describe the relation between concrete stress and strain (NBN EN 1992-1-1, 2005), the following set of equations can be solved to find the strain which corresponds with a stress of $0.45f_{ck}(t_0)$:

$$\begin{cases} \sigma_c = f_{ck} \cdot \left[1 - \left(1 - \dfrac{\varepsilon_c}{2‰}\right)^2\right] \\ \sigma_c = 0.45 \cdot f_{ck}(t_0) \end{cases} \tag{7.5}$$

Note that the first equation of the set is only valid if the instantaneous concrete strain stays below 2‰ at the age of loading. This was the case for all the models in all the calculations, see also section 7.3.2.3.

The solution of the set (7.5) is given the name $\varepsilon_{c\,0.45}$. Assume now again a linear elastic relationship between the stress and the strain (as was also done for everything up until this section). Then, the height of the zone where the creep will be nonlinear can be calculated as:

$$y_{nonlin.} = \frac{|\varepsilon_{c,top}| - |\varepsilon_{c\,0.45}|}{\psi} \tag{7.6}$$

with $\varepsilon_{c,top}$ the strain at the top fibre and ψ the curvature. The percentage of the concrete in compression which undergoes linear creep will be:

$$\omega = 1 - \frac{y_{nonlin.}}{x_e} = 1 - \frac{|\varepsilon_{c,top}| - |\varepsilon_{c\,0.45}|}{\psi \cdot x_e} \tag{7.7}$$

where x_e is the height of the compression zone. Finally, using this percentage, the creep coefficient was adapted in the following manner:

$$\begin{aligned}\varphi_{new}(\infty, t_0) &= \omega \cdot \varphi(\infty, t_0) + (1-\omega) \cdot \varphi_k(\infty, t_0) \\ &= \varphi(\infty, t_0) \cdot [\omega + (1-\omega) \cdot \exp(1.5 \cdot (k_\sigma - 0.45))]\end{aligned} \tag{7.8}$$

For the calculation of the stress-strength ratio k_σ the stress at the top compression fibre was used. The application of formula (7.8) results in an averaged creep coefficient which needs to be used for the entire cross-section. A more accurate approach would be to split up the cross-section in a large number of strips with a differentially small thickness and determine a new creep coefficient for each of the strips.

Despite the somewhat crude approach, the adaption of the creep coefficients, according to the prescribed method, resulted in a significant improvement of the predictions. As an example, Figure 7.17 shows the prediction of MC2010 and B3, with and without the correction for nonlinear creep, for three of the beams of beam type II, including both the highest and lowest loaded beam. For this lowest loaded beam the correction for nonlinear creep has a very limited influence. This is logical since the stress in this beam did not exceed the value of $0.45 f_{ck}(t_0)$ by much, see Figure 7.8. For the medium loaded beam the influence of the correction is already a bit more pronounced. For the highest loaded beam, the influence of the correction is unambiguous. The models still underestimate the absolute value of creep but the underestimation is now much smaller. In addition, the rate of the time-dependent behaviour is much better prescribed; the deflection curve of MC2010 is for the later time period nearly parallel with the measurements.

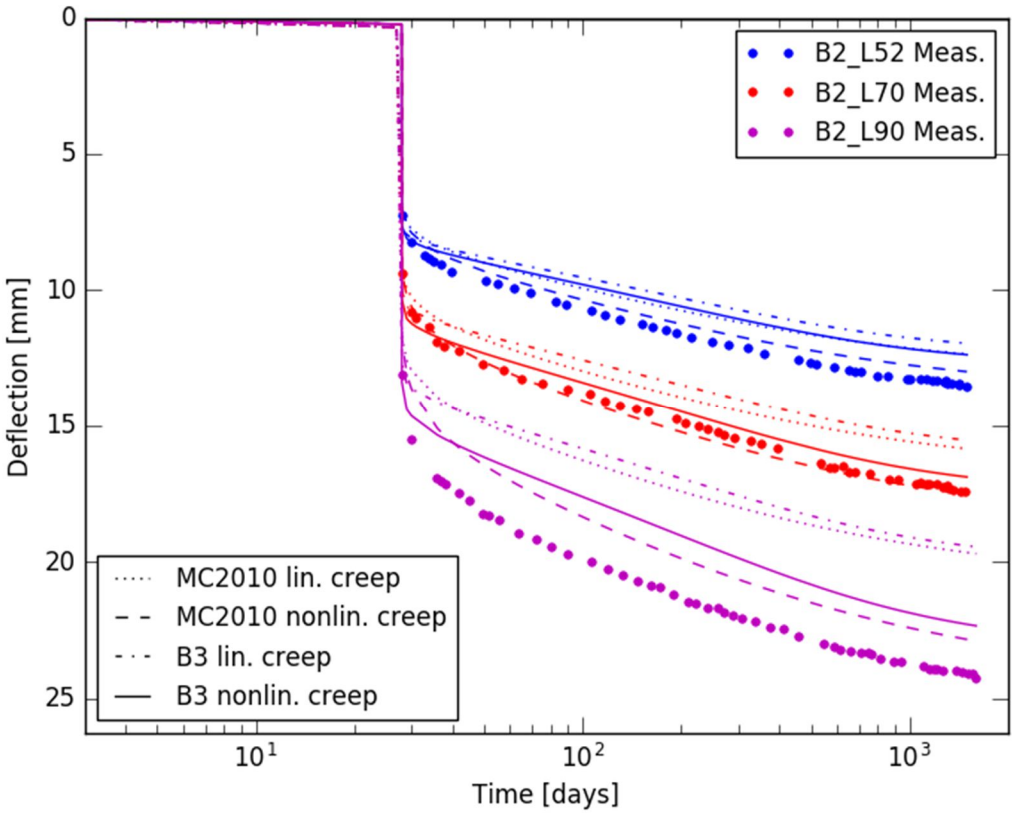

Figure 7.17. Comparison of predicted values with and without a correction for nonlinear creep for three beams of type II (constant aging coefficient equal to 0.8).

It is stressed that the correction for nonlinear creep only influences the time-dependent behaviour and does not influence the instantaneous deformations, as can be seen in Figure 7.18. The correction for nonlinear creep notably increases predictions of the two higher loaded beams of type IV. The correction has no influence on the lower loaded beam, since its compression stress was barely above the boundary level. The absolute value of the deflection is still predicted badly for the beam loaded at 70%; however, the correction did increase the accuracy of the prediction of the rate of creep.

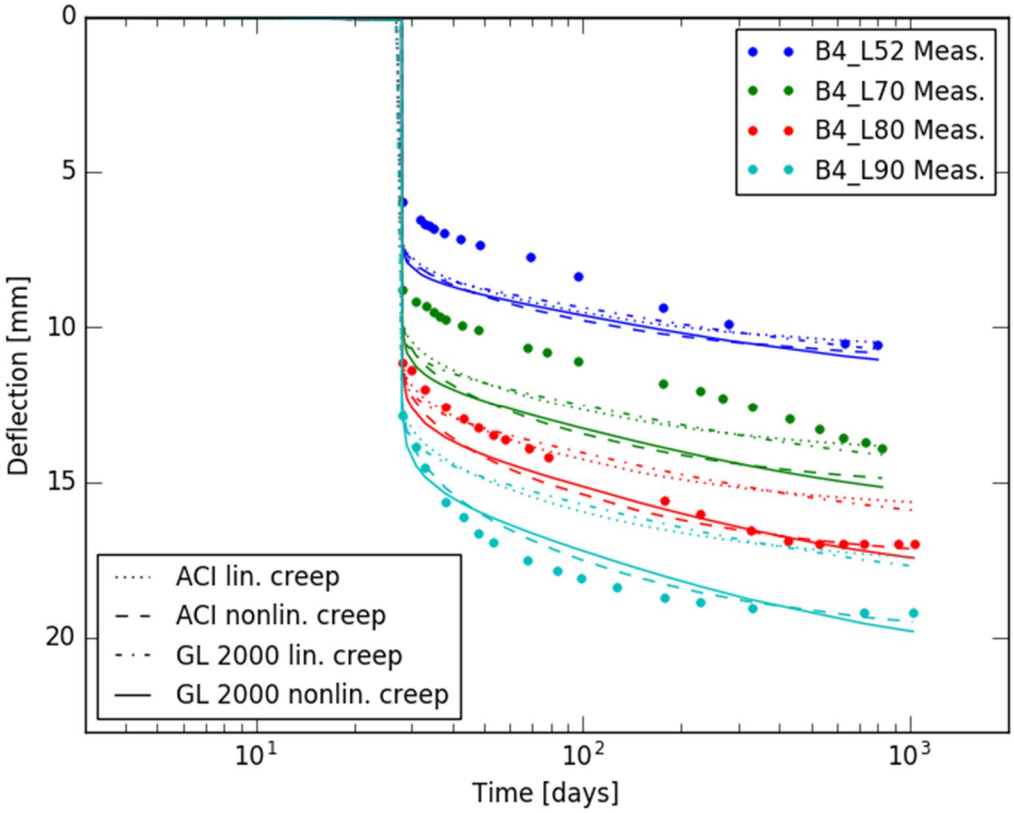

Figure 7.18. Comparison of predicted values with and without a correction for nonlinear creep for the beams of type IV (constant aging coefficient equal to 0.8).

Table 7.6 presents the comparison table of all the models for the predictions using a nonlinear creep correction. From the comparison of this table and Table 7.4, it is clear that correcting the creep coefficient, for nonlinear creep due to stresses outside of the service range, substantially increases the accuracy of the predictions. Note that on average the models now overestimate the deflections and their rates, which is opposite to the underestimations done in the case of no correction for nonlinear creep. The underlined values in Table 7.6 are the most accurate predictions. On average, MC2010 predicts the absolute values of the deflection the best (except for the absolute value at the end of loading). The rate of the time-dependent behaviour is on average the best predicted by the GL 2000 model, which also predicts the absolute deflection at the end of loading the best. The B3 model gives the second best predictions of the rate of creep at a later age. The worst predictions are done by the ACI model. This model gave the best predictions at an early age in case of no correction. For this model correcting for the nonlinear creep results in more inaccurate predictions, except for the rate of creep at later ages, which is predicted better.

Table 7.6. Mean comparison of predictions against measurements of the deflection at midspan of all the reinforced beams (correction for nonlinear creep and constant aging coefficient equal to 0.8).

	EC2	MC2010	B3	ACI	MC90-99	GL 2000
Δ_{28}	-0.02	-0.01	0.10	0.01	0.02	0.03
ξ_{28-56}	0.16	0.08	-0.34	0.18	0.09	0.07
Δ_{56}	0.01	0.00	-0.01	0.04	0.03	0.03
ξ_{56-147}	0.06	0.06	-0.11	0.14	0.06	0.04
Δ_{147}	0.01	0.00	-0.03	0.04	0.02	0.02
ξ_{147-t_e}	-0.32	-0.07	-0.02	-0.34	-0.13	-0.02
Δ_{t_e}	-0.06	-0.03	-0.05	-0.04	-0.02	0.00

8. Modelling of the time-dependent performance of tested prestressed beams; results and discussion

Using the same methods as described in the previous chapter the available dataset on prestressed beams (section 5.3) was studied. The shrinkage predictions were again studied with a special focus on the influence of the notional size h_0. The behaviour of the modulus of elasticity at an early age was also analysed, because the beams were loaded before 28 days. Then, the creep coefficients of the different models were studied with the influence of the notional size and the influence of the age at loading as focal points. With the knowledge of these three parts as a basis, the time-dependent behaviour, as predicted by the different models, was compared against the measured behaviour. This was done using a constant aging coefficient, similar as in the previous chapter. Afterwards the impact of the relaxation of the prestressing steel was considered. In the end, the influence of calculating with an estimated practical eccentricity of the post-tensioning steel instead of a theoretical eccentricity was also studied.

8.1. Comparison of shrinkage predictions

Most of the long-term tests on prestressed beams lasted between 847 and 1644 days. Due to the variation in shape, there is a significant variation in the notional size h_0. The largest difference can be found between the rectangular cross-section and the I-shaped cross-section, see Table 8.1. Note that the notional size of the post-tensioned, I-shaped cross-section is slightly lower than the one of the pre-tensioned cross-section due to the presence of the duct. To study the influence of the notional size on the shrinkage predictions two cases are studied, see Table 8.2. The first case has as an input the notional size of the rectangular cross-section. The second case represents the mean of the T-shaped and the two I-shaped cross-sections.

In both cases the mean of the four types of beams was chosen for the mean concrete strength f_{cm28} and the modulus of elasticity of concrete E_{cm28}. The composition of the concrete was different from the composition of the concrete of the reinforced beams. This was taken into account in the calculations. For the value of the air content and the slump factor the same values as in the previous chapter were assumed, 2% and 300 mm respectively.

Table 8.1. Overview of the notional size for the four different cross-sections of prestressed beams.

Shape	h_0 [mm]
Rectangular	178.3
T-shaped	99.2
I-shaped (post-tens.)	88.8
I-shaped (pre-tens.)	90.4

Table 8.2. Overview of important input parameters for the material shrinkage models for the two studied cases of concrete used for the casting of prestressed beams.

	Case 1	Case 2
Mean concrete strength at 28 days f_{cm28}	38.5 MPa	38.5 MPa
Nominal size h_0	178.3 mm	92.8 mm
Relative humidity RH	60%	60%
End of curing t_c	1 day	1 day

Figure 8.1 and Figure 8.2 show the shrinkage strain predictions up to 1644 days for case 1, respectively case 2. Comparing the two graphs it can be seen that a higher notional size causes the shrinkage strain to build up slower, resulting in lower shrinkage values at 1644 days. The final shrinkage strain does not change for most models as can be seen from comparing Figure 8.3 a) and b). The exception to this rule are EC2 and ACI. Their final shrinkage strain decreases for a higher notional size. For the studied nominal size of 178.3 mm they also become almost identical after 800 days. If the nominal size would increase they would start to differ again: the final shrinkage value of ACI would decrease more than the final shrinkage value of EC2. The reason why the ultimate shrinkage strain of the other models is independent of the notional size is because, for those models, the notional size is only used in time functions. Changes in the notional size thus influence the development rate of the shrinkage but do not change the final strain. In the ACI model and the EC2 model the notional size is not only used in a time function but also in a size term, and a change in the magnitude of the notional size results thus in a change of the ultimate strain.

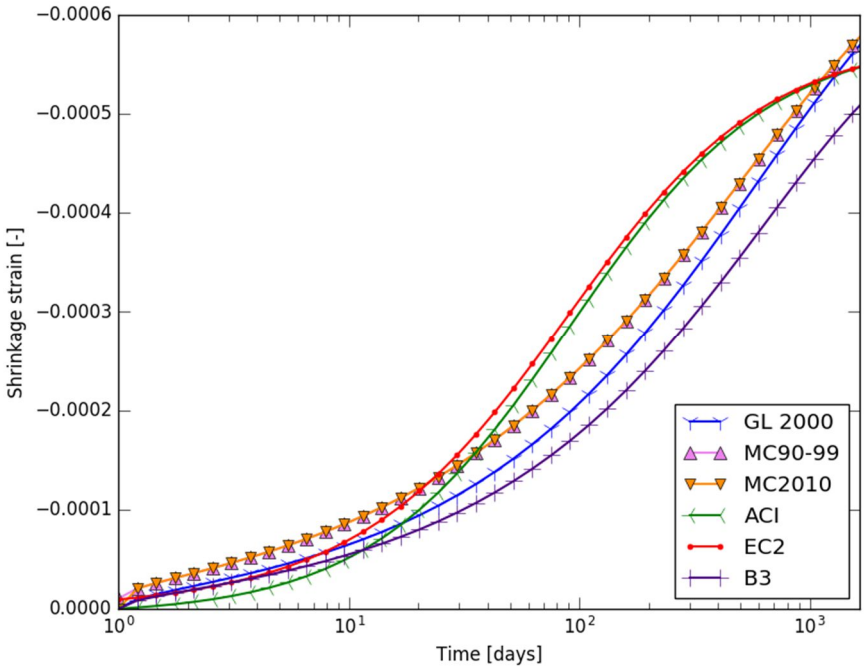

Figure 8.1. Semi-logarithmic plot of the shrinkage strains versus time up until 1644 days for the prestressed concrete case 1 (h_0 = 178.3 mm).

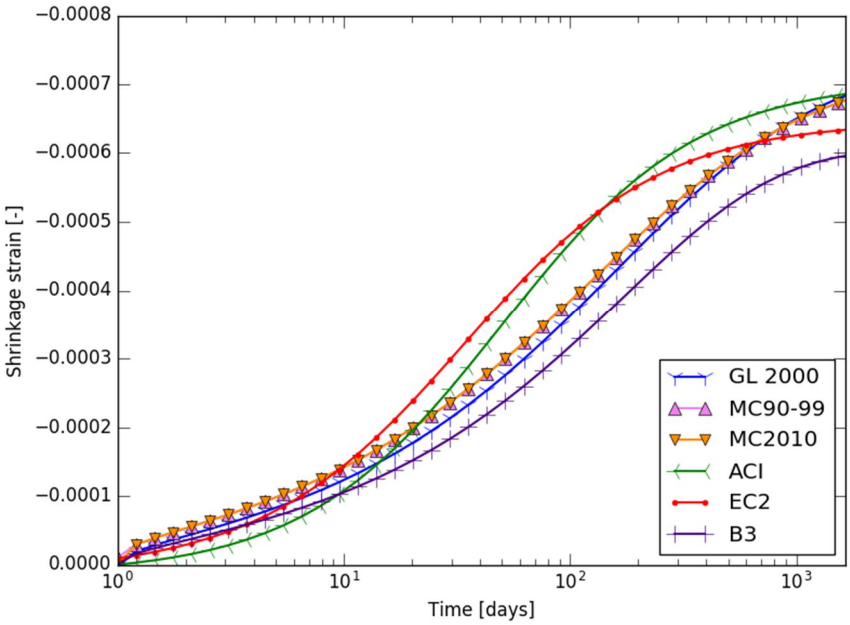

Figure 8.2. Semi-logarithmic plot of the shrinkage strains versus time up until 1644 days for the prestressed concrete case 2 (h_0 = 92.8 mm).

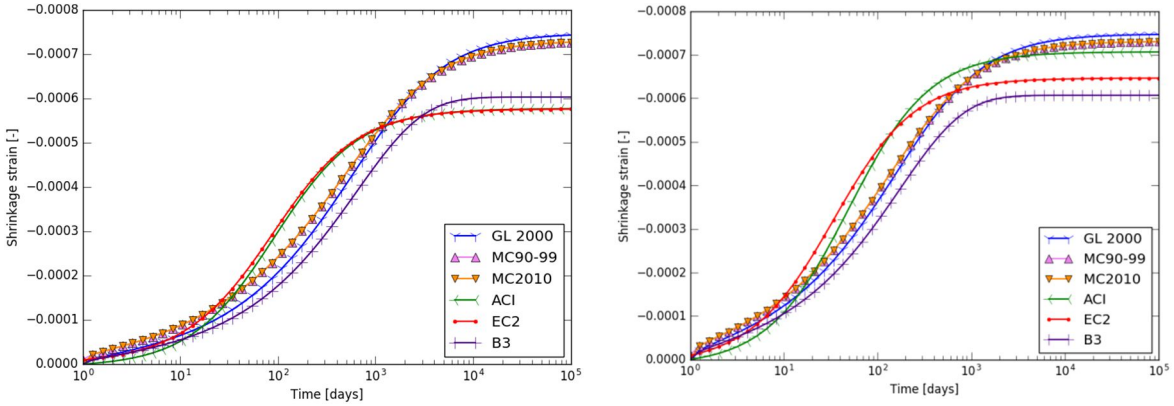

a) Case 1 (h_0 = 178.3 mm) **b) Case 2 (h_0 = 92.8 mm)**

Figure 8.3. Semi-logarithmic plots of the shrinkage strains versus time up until 274 years.

Note that the notional size of case 2 is almost identical to the notional size used in section 7.1 for the investigation of the shrinkage behaviour of the concrete used for the reinforced beams. The comparison of Figure 7.1 and Figure 8.2 shows that the shrinkage predictions for the concrete used in the prestressed beams lie closer to one another than the predictions for the concrete used in the reinforced beams. For case 2 the most extreme predictions are the one from ACI and the one from B3; the ACI prediction is 15% higher than the B3 prediction. This is relatively small compared to the 50% difference obtained between the GL 2000 model and the B3 model for the concrete used for the reinforced beams, see section 7.1. Note that for case 1 the most different predictions are the ones by MC2010 (similar prediction by MC90-99) and B3. Their difference is 14%. One of the main reasons that the difference between the models is smaller for the concrete of the prestressed beams than for the concrete of the reinforced beams is the difference in concrete strength, which is required for all models except ACI. The other main reason is a different water content which influences the B3 predictions. The higher water content of the concrete used in the prestressed beams increases the shrinkage predictions of the B3 model compared to the concrete used in the reinforced beams.

8.2. Comparison of creep predictions

Figure 8.4, respectively Figure 8.5, show the creep coefficient up until 1644 days for the concrete loaded at 28 days for case 1, respectively case 2. The creep coefficient of MC90-99 was corrected for $t_{0,adj.}$ in the way that EC2 prescribes it, as was suggested in section 7.2. This can also be deduced from the graphs, since MC90-99 has its instantaneous step at the same moment as the other models. The higher notional size for case 1 results in a decrease of the value of the creep coefficient at 1644 days relative to case 2. For case 2 the values of the creep coefficient according to all models, except B3, are somewhat grouped together at 1644 days. For case 1, GL 2000 has detached itself from the group and has shifted towards the B3 model. This is because the influence of the notional size on the creep coefficient of GL 2000 is, compared to the creep coefficients of the other models, limited. This results in a higher position of the creep coefficient of the GL 2000 model relative to the other models. Note that even though there is an influence of the instantaneous value of the creep coefficient at 28 days, this influence is limited.

Out of the comparison between Figure 8.5 and Figure 7.2 (reinforced beams) it can be seen that for the concrete composition used for the prestressed beams the predictions of EC2 and MC90-99 are a bit more divergent than for the concrete of the reinforced beams. It can also be noticed that the predictions of the ACI model and the GL 2000 model have shifted upwards relative to the predictions by EC2, MC2010, and MC90-99. Similar to what was already explained in section 8.1, the difference between the creep coefficients is caused by the different concrete strength and concrete composition.

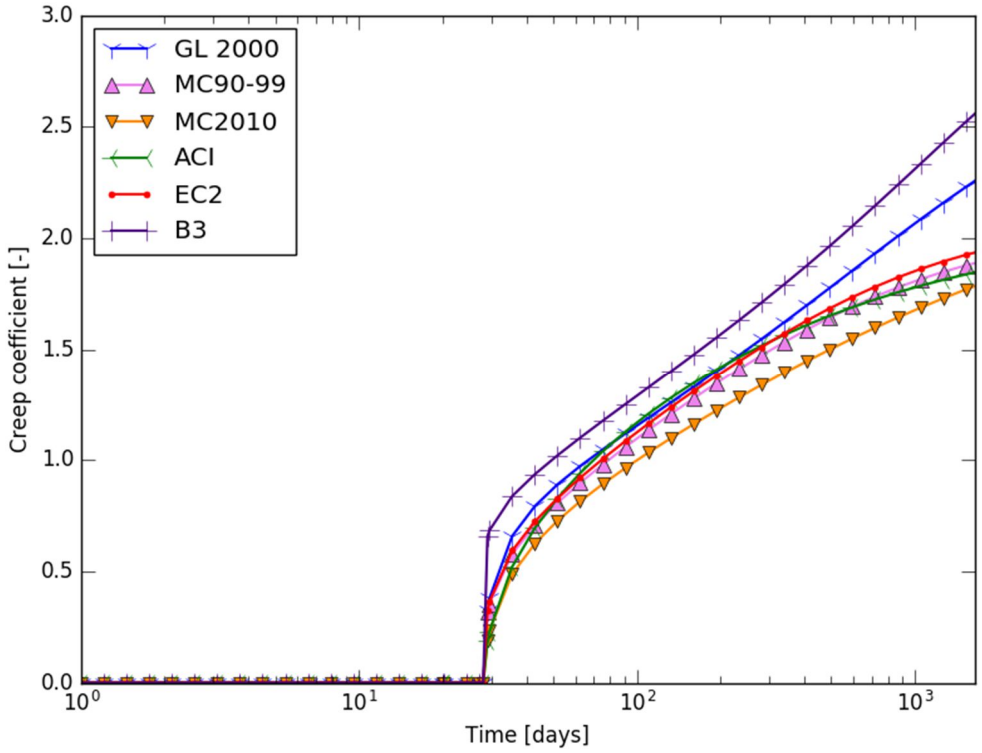

Figure 8.4. Semi-logarithmic plot of the creep coefficients versus time up until 1644 days for the prestressed concrete case 1 (t_0 = 28 days, h_0 = 178.3 mm).

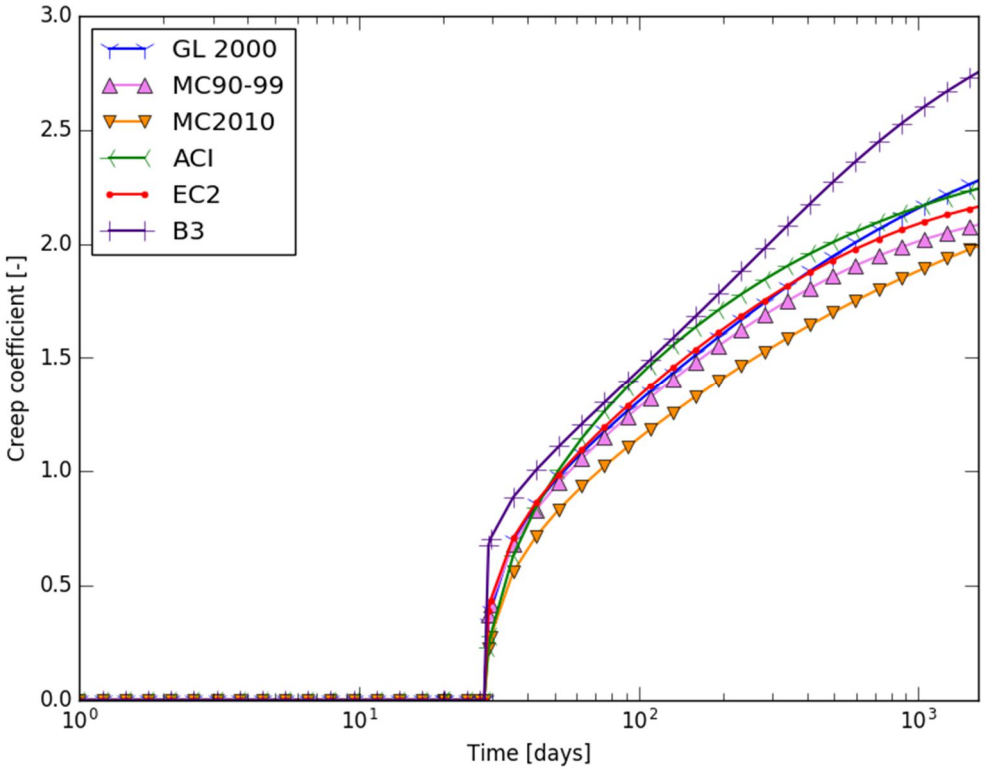

Figure 8.5. Semi-logarithmic plot of the creep coefficients versus time up until 1644 days for the prestressed concrete case 2 (t_0 = 28 days, h_0 = 92.8 mm).

Figure 8.6 shows the creep coefficient for the two cases up until 274 years. The creep coefficients of ACI, EC2, and MC90-99 have an asymptotic behaviour. The increase of the notional size for case 1 results in a slight decrease of the asymptotic value of these three models. The creep coefficients of MC2010, B3, and GL 2000 don't have an asymptotic behaviour; they have a linear long-term behaviour for logarithmic time scales. An increase of the notional size results in a slight decrease of the rate in which their creep coefficients develop. The creep curve of the B3 model has a kink at later ages. The higher notional size causes this kink to shift from approximately 2500 days to approximately 6000 days. Note however that the influence of the notional size on the creep coefficient at 274 years is almost negligible for the creep coefficient of the B3 model.

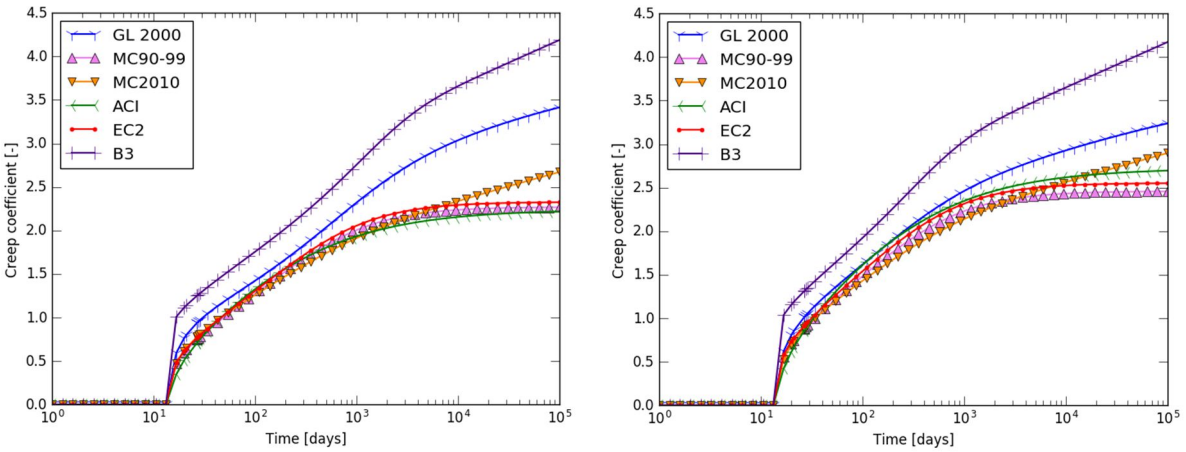

a) Case 1 (h_0 = 178.3 mm) **b) Case 2 (h_0 = 92.8 mm)**

Figure 8.6. Semi-logarithmic plots of the creep coefficients versus time up until 274 years (t_0 = 28 days).

The prestressed beams which were loaded underwent two loading steps: prestressing at 7 or 14 days and loading due to the four point bending test at 28 or 56 days. Throughout this entire thesis, the creep coefficient was defined relative to the definition of the compliance function according to formula (2.4). ACI and B3 follow this same definition. EC2, MC90-99, MC2010, and GL 2000 follow another definition; they define their creep coefficients relative to the definition of the compliance function given by equation (4.1). If the loading is applied at 28 days, there is no difference between the two formulations. For loading at a different time the creep coefficients of EC2, MC90-99, MC2010, and GL 2000 need to be adapted. They were multiplied by the ratio of the modulus of elasticity at time of loading over the modulus of elasticity at the age of 28 days $E_c(t_0)/E_c(28)$, making their definition compatible with the definition used in this thesis.

Figure 8.7 shows the creep coefficients at different times of loading calculated according to EC2 for the notional size of case 2. It can be observed that loading at a later age reduces the creep coefficient. This is because, at a later age the degree of hydration is in a further advanced stage, causing the concrete to be stronger and to creep less, as was also discussed in section 2.3.2.3.

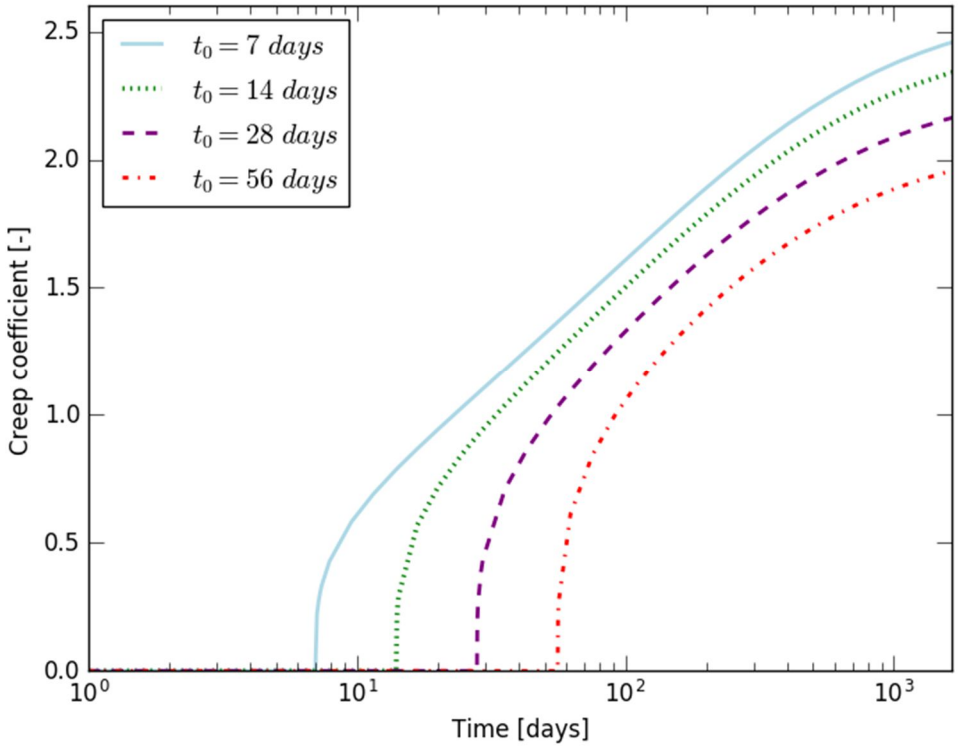

Figure 8.7. Semi-logarithmic plot of the EC2 creep coefficient up until 1644 days for different times of loading (h_0 = 92.8 mm).

The creep coefficients for case 2 in the event of early age loading at 7 days are shown in Figure 8.8. Examining both Figure 8.8 (loading at 7 days) and Figure 8.5 (loading at 28 days), allows to study the influence of the loading age on all the models more closely. Loading at an earlier age causes the predictions of MC90-99, MC2010, ACI, and EC2 to lie closer together. From Figure 8.5 it is clear that the creep coefficient of the B3 model lies somewhat separated from the rest of the models for loading at 28 days. Looking at Figure 8.8 loading at an earlier age results in the B3 model completely dissociating itself from the other models. The GL 2000 model, which has similar values as EC2 and ACI for loading at 28 days, gives values between B3 and the rest of the models for loading at 7 days.

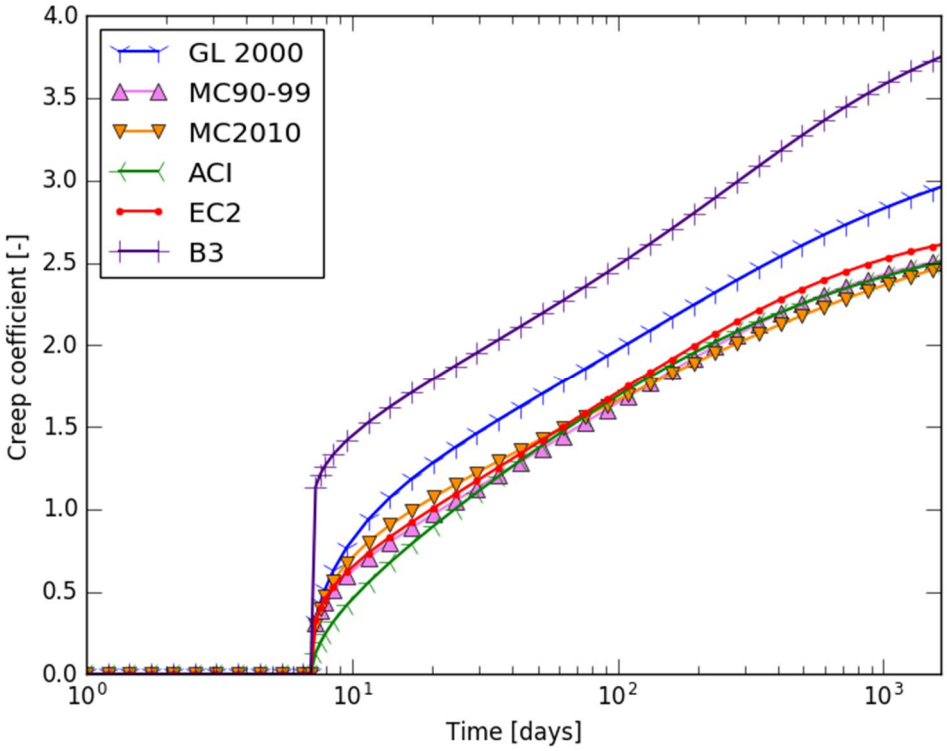

Figure 8.8. Semi-logarithmic plot of the creep coefficients versus time up until 1644 days for the prestressed concrete case 2 (t_0 = 7 days, h_0 = 92.8 mm).

Figure 8.9 gives a better illustration of the creep at early ages in the case of loading at 7 days, respectively 28 days. Similar to what was explained before, this figure also clearly illustrates that the B3 model dissociates itself in the case of earlier loading. Note also that the value of the instantaneous creep coefficient of the B3 model is much higher than that of the other models. The value also increases for earlier loading ages, while the value of the instantaneous creep coefficient of EC2, MC90-99, and GL 2000 stays approximately the same. The value of the instantaneous creep coefficient of ACI undergoes a decrease for earlier loading ages. Contrarily the one of MC2010 undergoes a slight increase.

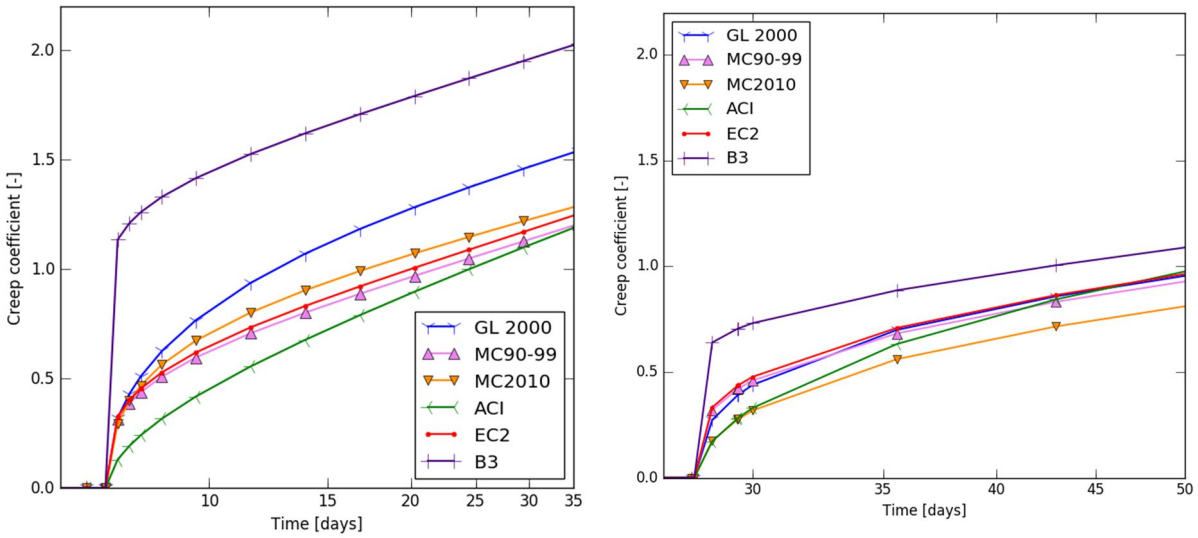

a) t_0 = 7 days **b) t_0 = 28 days**

Figure 8.9. Semi-logarithmic plot of the creep coefficients versus time up until 28 days after loading for the prestressed concrete case 2 (h_0 = 92.8 mm).

8.3. Comparison of the predictions of the modulus of elasticity

The modulus of elasticity is dependent on the level of hydration of the concrete and is thus dependent on time. All models, except for ACI and GL 2000, prescribe a formula to calculate the time-dependent modulus of elasticity out of the product of a time function and the modulus of elasticity at 28 days. This time function is based on the time function used to calculate the time-dependent compressive strength of each model. ACI and GL 2000 calculate the time-dependent modulus of elasticity out of the time-dependent concrete strength. So instead of the modulus of elasticity at 28 days, they use the concrete strength at 28 days.

The time-dependent moduli of elasticity calculated according to the different models are shown in Figure 8.10. MC90-99 and MC2010 are indistinguishable from one another since they use the same formula. The formula prescribed by EC2 is almost identical to the formula of MC90-99; the only difference is a different value of the power in the time function. This causes EC2 to give lower values at later ages. The B3 model uses a totally different formula from EC2, MC90-99, and MC2010, yet it gives almost identical values as these three at later ages. Note that at 28 days the time function of EC2, MC90-99, MC2010, and B3 becomes 1, causing the modulus of elasticity to become equal to modulus of elasticity at 28 days E_{cm28}.

The modulus of ACI and GL 2000 does not become equal to E_{cm28} at 28 days. This is due to their concrete strength based formulation. Note that at later ages their value is also clearly different from the other models.

From the graph it can be seen that at an early age there is some variation between the different models. The moduli also have a substantial rate at early ages. Since the prestressing happened at an early age, it can be that the instantaneous and time-dependent deformations just after prestressing are predicted poorly.

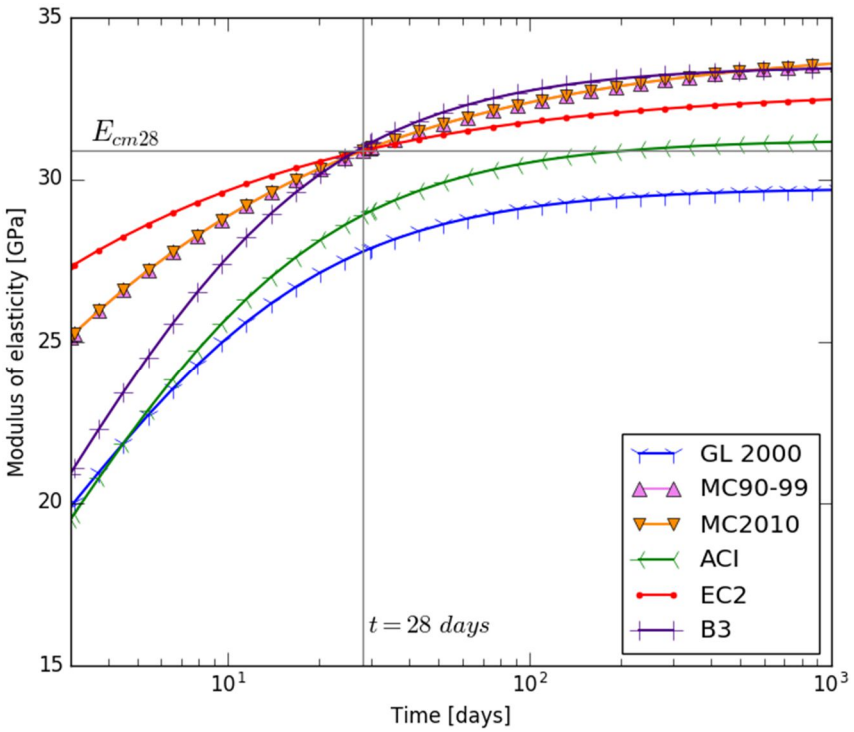

Figure 8.10. Semi-logarithmic plot of the secant moduli of elasticity versus time.

8.4. Predictions of calculation models versus available measurements

8.4.1. Assumptions

For the prediction of the time-dependent behaviour of the prestressed beams many of the assumptions which were stated for the reinforced beams (section 7.3.1) are reused. The same calculation method was used (a cross-sectional linear approach using the age-adjusted effective modulus). In order to take the prestress into account the prestressing force was transformed in an equivalent normal force and moment, as described in section 6.3.1. The same number of sections was used as for the reinforced beams. This made the section length longer than in the case of the reinforced beams (due to the longer span of the prestressed beams). It was tested if the use of more sections changed the accuracy, but it was concluded that this was not the case.

In section 7.3.3 it was shown that the use of a calculated aging coefficient did not improve the accuracy of the predictions compared to a constant aging coefficient equal to 0.8. Therefore, the analysis of the prestressed beams was performed with a constant aging coefficient equal to 0.8, similar as for the reinforced beams. The method which was proposed in section 7.3.4, to correct the creep coefficient for the effects of nonlinear creep, was not used for the analysis of the prestressed beams. More information with regards to this subject can be found in section 8.4.2.2.

The prestressing force of prestressed beams is generally balanced together with the cross-section in such a manner that cracking will not occur under the service load. For the analysis of the prestressed beams it was assumed that the beams remained uncracked throughout the entire testing period. Section 8.4.2.2 will endorse that this assumption was well-founded.

Contrary to the reinforced beams, the self-weight of the prestressed beams needed to be taken into account. In the calculations this self-weight was placed on the beams at the moment of prestressing.

Similar as for the reinforced beams the parts of the beam extending beyond the supports are not taken into account. Figure 8.11 shows the assumed test setup of the reinforced beams. In the case of the post-tensioned beams there is a variable tendon profile. The eccentricity at the end, which is under the assumptions above the supports, was taken equal to the eccentricity above the supports in the original tendon profile. In a first approach it was also assumed that the post-tensioning steel is located centrally in the duct. The influence of placing the steel non-centrically is studied in section 8.4.3.

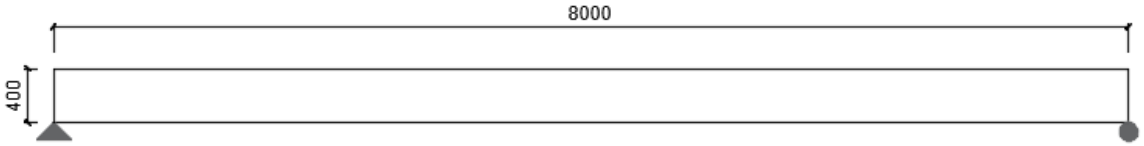

Figure 8.11. Assumed test setup for the prestressed beams (measurements in mm).

In Figure 5.9 it can be seen that the cross-section of the T-shaped and I-shaped beams changes near the supports. Due to the lack of exact measurements and the fact that the change happened outside of the zone with maximum moment, this change in cross-section was not taken into

account. The T-shaped and I-shaped cross-section, as can be seen in Figure 5.8, was thus assumed unchanging over the entire span.

The loss of prestress, in the case of post-tensioning, due to friction in the cable duct and due to friction at the deflection points was neglected. This loss will have been limited due to verification and extra tensioning which was performed at the non-prestressing side. The loss due to slip of the prestressing steel at the anchorages and the deformation of the anchorages at the moment of force transfer was also not taken into account. In the case of post-tensioning this loss will have been small due to the use of the B.B.R.V. system as mentioned in section 5.3.2. In the case of pre-tensioning the influence of slip and the build-up of prestress is assumed to stay limited to the section of the beam close to the supports, where the moments are small. In contrast to the previous two losses, the loss due to the elastic deformation of the concrete in the case of pre-tensioning was taken into account. This loss is intrinsically imbedded in the calculation method. Finally, the influence of the loss of prestress due to relaxation will be discussed in section 8.4.4.

8.4.2. Results out of a linear creep calculation with simplified $\chi(t, t_0)$

Before the results are discussed, a small nuance in the terminology of this section is provided. The prestressed beams undergo two types of loading: prestressing and loading due to the four point bending. The loading due to four point bending will be referred to as “loading”. Prestressing is also an act of loading, but it will be termed “prestressing”. If an unloaded beam is mentioned, this thus means a beam which is prestressed but which is not subjected to four point bending loading. Prestressing results in a negative, upward deflection and loading results in a positive, downward deflection. In case a prediction overestimates (underestimates) the measurements for a beam which is prestressed but not yet loaded, this means that the models predict a higher (lower) upward deflection. In case a prediction overestimates (underestimates) a deflection after loading, this means that the prediction lies under (above) the measurements on the deflection graph, regardless of the sign of the deflection.

8.4.2.1. Deflection

The overview of the testing programme of the prestressed beam was given in Table 5.6. For each combination of prestressing- and loading age one beam was loaded at the full service load and another was loaded at half of the service load. In the deflection graphs which are presented in this section both beams will be plotted on the same graph. In each of the graphs the beam, which is prestressed at the same age but which remains unloaded throughout the entire testing period, is added as a reference.

Figure 8.15 shows the deflection predictions of the I-shaped beams which are pre-tensioned at 7 days and loaded at 28 days. EC2 and MC2010 predict the instantaneous upward deflection at the time of prestressing well. The prediction by GL 2000 is slightly off, and the B3 model totally overestimates the instantaneous upward deflection. Looking mainly at the unloaded beams (and at the early age behaviour of the loaded beams), there is a lot of variation between the predictions. The variation is caused by divergent predictions at an early age. The reason for these divergent predictions is related to both the modulus of elasticity and the creep coefficient. There is a lot of variation between the moduli of elasticity of the models at early age, see section 8.3. This mainly explains the difference between GL 2000 and EC2 (and MC2010). The B3 model also has a lower

modulus of elasticity than EC2 and MC2010. However, more importantly is that for early age loading the creep coefficient of the B3 model is much higher than the creep coefficient from the other models, see Figure 8.9 a). This causes the creep at early ages to be much higher than the creep deformations predicted by the other models. This explains why the deflections predicted by the B3 model for the unloaded beam are so high.

The deflections of EC2 and MC2010 lie close together for the unloaded beam. Figure 8.9 a) and Figure 8.7 indicate that this is the result of their similar creep coefficient for loading at 7 days.

Despite its severely overestimated deflection after prestressing, the B3 model describes the time-dependent behaviour of the unloaded beam and the beam loaded at 50% remarkably well. The time-dependent behaviour of the beam loaded at a 100% is almost perfectly described by the GL 2000 model. Remark that the different predictions are far less divergent for the loaded beams than for the unloaded beam. The highest loaded beam even has the least difference between the predictions at the end of loading. This can be attributed to two reasons. The first being the overestimation of the instantaneous deformation by the B3 model and the GL 2000 model, bringing them closer to the other models. The second reason being related to the rate of creep. After loading the beam creeps downwards. The creep coefficient of the B3 models is significantly higher than the creep coefficient of other models. The difference between the B3 model and the other models thus decreases over time because the B3 model, which after loading has the smallest deflection, has the highest rate of creep at later age, resulting in a larger increase of deflection over time.

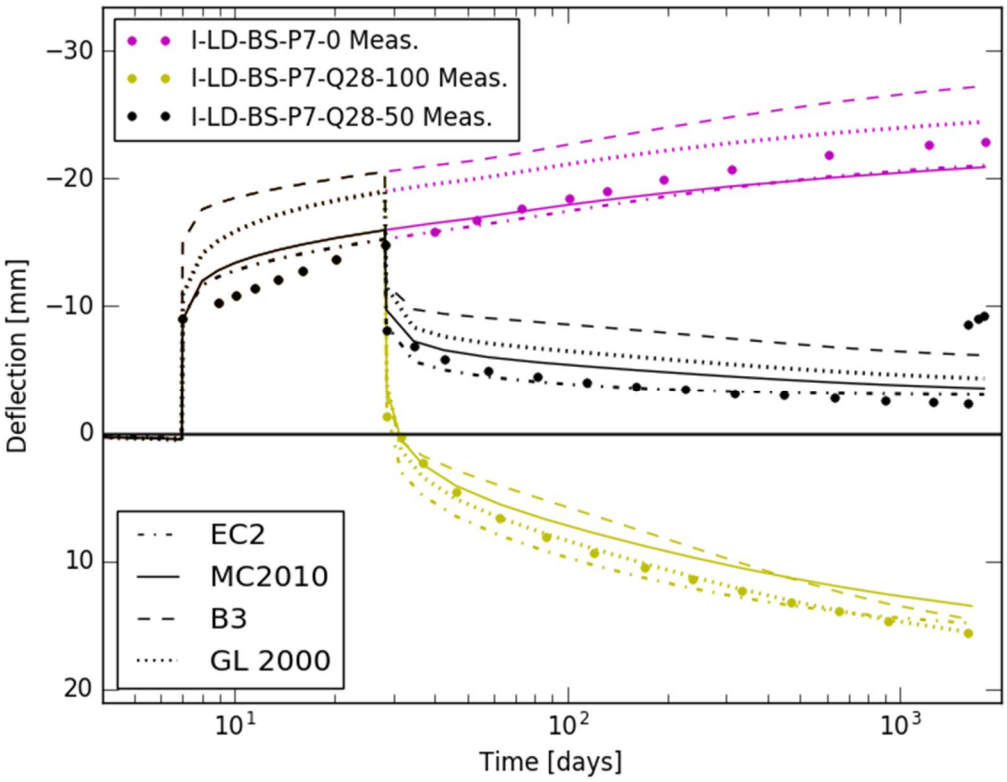

Figure 8.12. Predictions and measurements of the deflection at midspan of the pre-tensioned I-shaped beams prestressed at 7 days (constant aging coefficient equal to 0.8 and no correction for relaxation of prestress).

Figure 8.13 shows the deflections of the I-shaped beams which are pre-tensioned at 14 days and loaded at 28 days. The measured deflections of these beams is very comparable with the ones from Figure 8.12. Note that the variation between the models is slightly smaller than for the beams prestressed at 7 days. This is due to a smaller variation in the creep coefficients and the moduli of elasticity. For these beams the unloaded beam and the beam loaded at 50% are best predicted by the B3 model. The instantaneous deflection prediction after prestressing is again overestimated by the B3 model. The rate of creep of the measurements of the unloaded beam up until an intermediate age (± 300 days) is higher than what is predicted by any of the models. The measured deflections bridge in that time period the difference with the predictions of the B3 model. At a later age the measured rate is approximately the same as the predicted rate by the B3 model, which is why the B3 model prescribes this beam the best.

The predictions of MC2010 represent the time-dependent behaviour of the beam loaded at full service load nearly perfectly. This is due to a good prediction of the instantaneous upward deflection, followed by a very reasonable prediction of the early age creep, proceeded by a good prediction of the instantaneous deflection at loading and finally also a good description of the creep at a medium and later age.

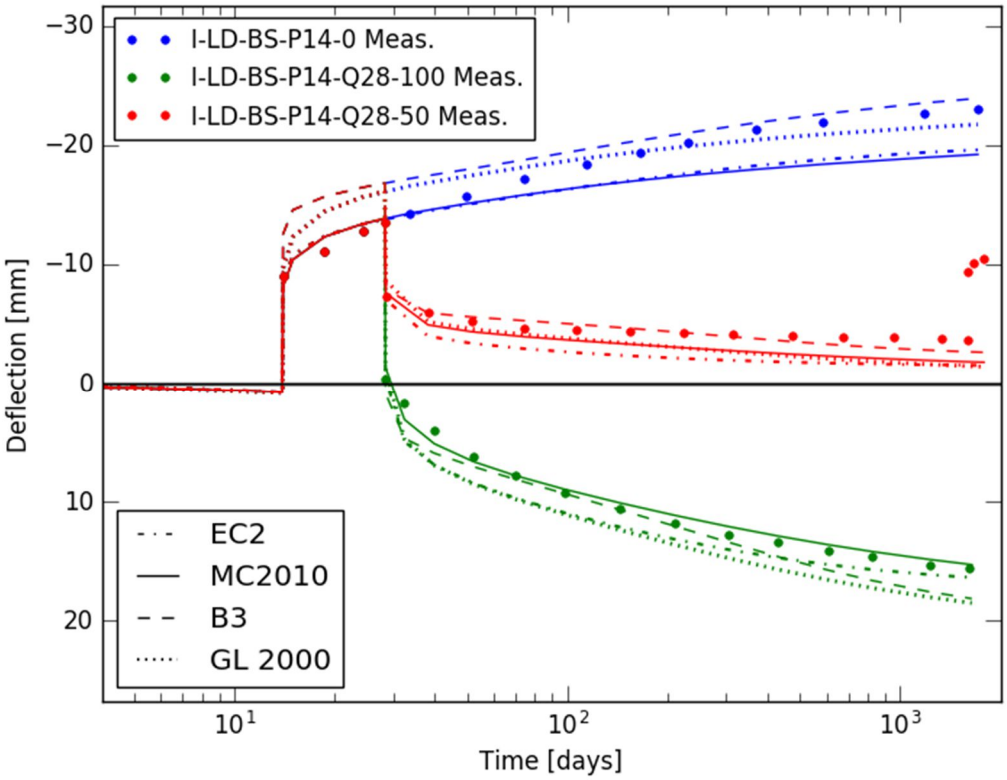

Figure 8.13. Predictions and measurements of the deflection at midspan of the pre-tensioned I-shaped beams prestressed at 14 days (constant aging coefficient equal to 0.8 and no correction for relaxation of prestress).

Figure 8.14 shows the deflections of the I-shaped beams which are post-tensioned at 14 days and loaded at 56 days. Note that the predictions of the models for each of these beams lie close together. This is due to their comparable value of the modulus of elasticity and the creep coefficient. All models overestimate the creep of the unloaded beam. They all predict the instantaneous deflection quite accurate, but they overestimate the early rate of creep. Also at later

ages the rate of creep is higher according to the models than the measurements for the unloaded beam. Studying the measurements of the unloaded beam more closely, it appears that the creep has levelled out at approximately 800 days. The exact reason explaining the difference between measurements and the predictions is unclear. It is possible that the applied initial prestress deviated in a small amount from the reported value or that the difference is caused by a loss of prestress due to friction and/or relaxation. This will be closer studied in section 8.4.4.

The loaded beams in Figure 8.14 are quite well predicted. The deflection at 56 days is underestimated. This is not because the value of the instantaneous deflection step is predicted badly. This is because the deflection before the loading was overestimated, as was explained in the previous paragraph. The early rate of creep immediately after loading is predicted higher than the measured values, thereby compensating for the difference in deflection at 56 days.

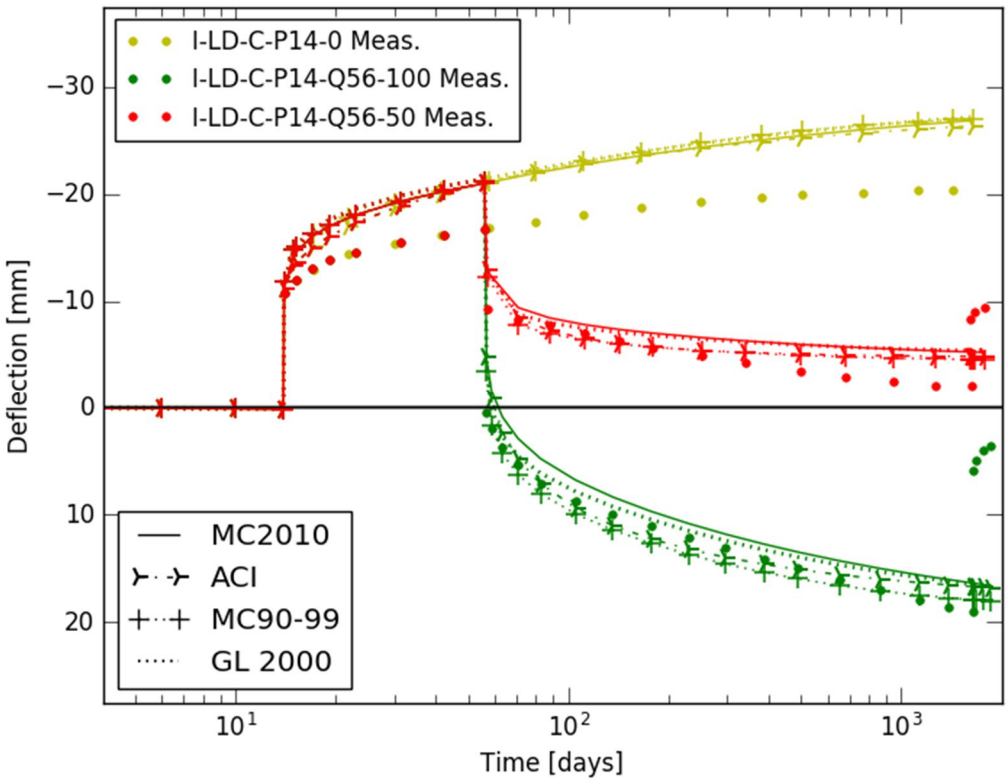

Figure 8.14. Predictions and measurements of the deflection at midspan of the post-tensioned I-shaped beams loaded at 56 days (constant aging coefficient equal to 0.8 and no correction for relaxation of prestress).

The deflections of the T-shaped beams which are loaded at 56 days are shown in Figure 8.15. Compared to the three previous figures, the predictions of the deflections are remarkably inaccurate. First of all, the instantaneous deflection due to prestressing is underestimated. Secondly, the models underestimate the time-dependent deformation at early ages. Also the instantaneous deflection due to loading is underestimated. The rate of creep of the beam loaded at 50% is also underestimated.

A possible explanation for these unreliable predictions can be found in Table 5.7. The concrete strength of the T-shaped beams which was reported is exceptionally high compared to the concrete strength of the other beam types. Also the modulus of elasticity is higher than the moduli of the other beam types, although in a less distinct way than the concrete strength. The difference

between the concrete strength of the T-shaped beam and the post-tensioned I-shaped beam is 42%. For the modulus of elasticity this difference is 24%. Taking this into account, it is possible that the concrete which was used to test the strength and the elasticity was not representative for the concrete which was used for the casting of the beams. This hypothesis is also supported by the reported cracking moments in Table 5.8. The T-shaped beams were the only beams that had a measured cracking moment below their service moment.

The calculations of the prestressed beams were done using only uncracked cross-sections, see also section 8.4.1. The T-shaped beams which were loaded at 100% of the service moment were cracked because the cracking moment was below the service moment. The fact that these beams were cracked can also be deduced form Figure 8.15. In all the previous figures, the value of the measured instantaneous deflection at 100% loading was equal to the double of the measured instantaneous loading at 50%. Here, the instantaneous deflection at 100% is more than double the instantaneous deflection at 50%. The fact that the T-shaped beams loaded at 100% cracked, can also influence the accuracy of the predictions of these beams.

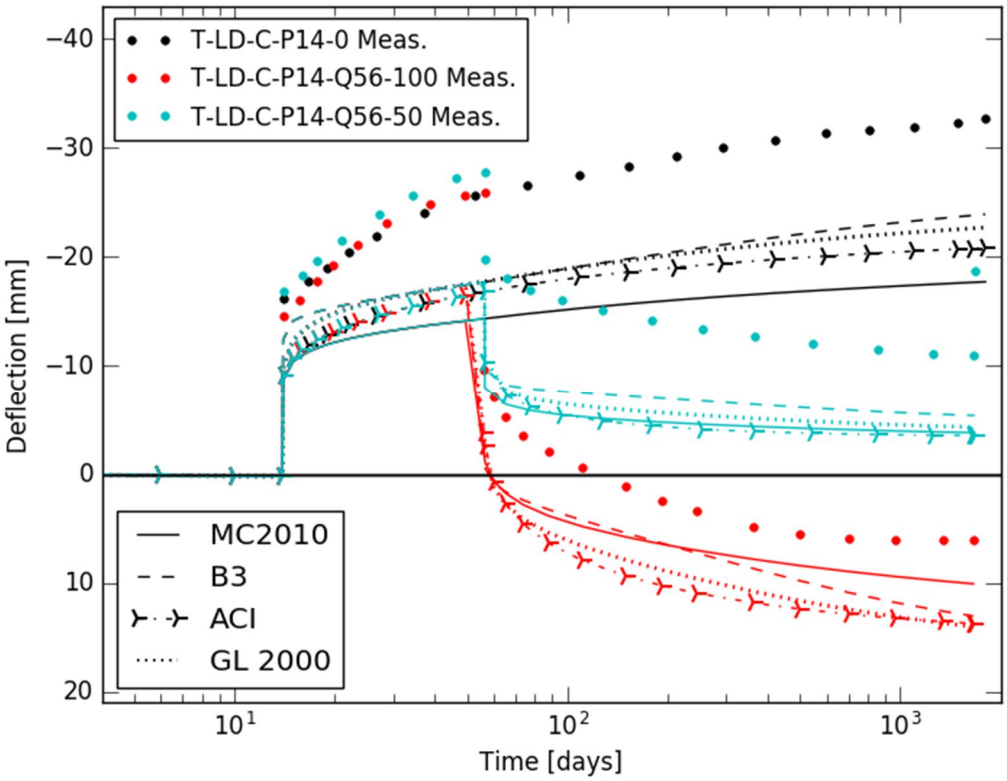

Figure 8.15. Predictions and measurements of the deflection at midspan of the post-tensioned T-shaped beams loaded at 56 days (constant aging coefficient equal to 0.8 and no correction for relaxation of prestress).

Figure 8.16 shows the rectangular beams which are only prestressed and are not loaded. The measurements of these beams show an illogical trend; at 150 days the deflection of the beams prestressed at 45 days becomes larger than the deflection of the beam prestressed at 14 days. The creep coefficient of the beam prestressed at 45 days can theoretically never become larger than the creep coefficient of the beam prestressed at 14 days, see Figure 8.7. Thus, the time-dependent deflection of the beam prestressed at 45 days could theoretically never become larger than the time-dependent deflection of the beam prestressed at 14 days. From Figure 8.16 it is clear that the

instantaneous deflection of the later loaded beam is the highest. This could indicate that the concrete of the beam which is prestressed at 45 days is from a different quality than the beam which is prestressed at 14 days. This difference in quality could explain the illogical trend of the time-dependent deformations.

The predictions in Figure 8.16 show a logical trend; the time-dependent deflection of the later prestressed beam stays below the time-dependent deflection of the earlier prestressed beam. The models underestimate the instantaneous deflection which can be an indication of the fact that the reported parameters of the rectangular beams are not representative for the concrete used in the beams. Note that the variation between the models is smaller for the later prestressed beams. This is because the variation between the creep coefficients decrease for a later time of loading, as was already explained.

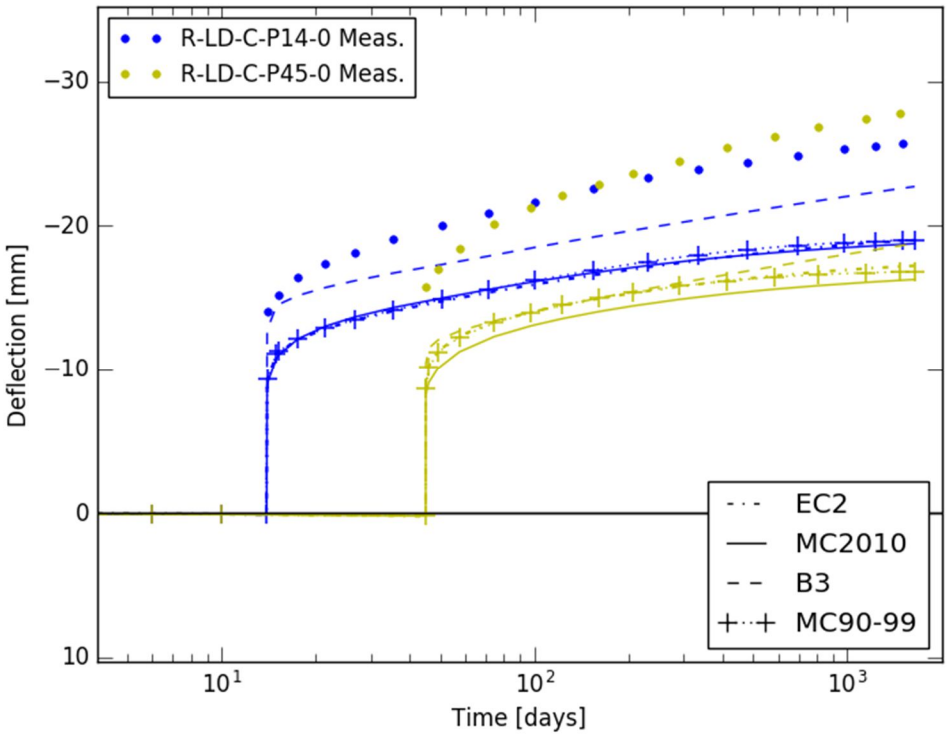

Figure 8.16. Predictions and measurements of the deflection at midspan of the post-tensioned rectangular beams which are not loaded (constant aging coefficient equal to 0.8 and no correction for relaxation of prestress).

8.4.2.2. Stress

Similar as for the reinforced beams, the stresses were calculated. Due to the prestress, both the top and the bottom fibre are in compression. Both of them are displayed in the graphs. The predictions of the top fibre are marked with an "x". The predictions of the bottom fibre are unmarked. Each graph has a grey continuous line indicating the value of $0.45f_{ck}(t_0)$, which was determined at the earliest time of prestressing of the beams represented in the graph. For example, in Figure 8.17 $f_{ck}(t_0)$ was determined for t_0 equal to 14 days. All graphs also have a grey dashed line indicating the mean concrete tensile stress at 28 days f_{ctm}.

In Figure 8.17 the stresses of the unloaded rectangular beams are represented. Up until the moment of prestressing, the stresses in the beams are negligible. The prestress is applied in the

bottom of the beams, and the bottom fibres are thus placed in compression. At the moment of prestressing, the stress in the bottom fibre surpasses the value of $0.45 f_{ck}(t_0)$. Strictly speaking, the boundary which is applicable for the beam loaded at 45 days should lie higher. For this beam the boundary should be determined using the concrete strength at 45 days, instead of the concrete strength at 14 days (as was used in the graph). Comparing the two beams in the figure, it can be remarked that they have a nearly identical behaviour. This is to be expected since the applied prestressing force is equal.

Figure 8.17 indicates that the top fibre is also in compression. The influence of the prestress is limited in this fibre, yet at the moment of prestressing also the self-weight is applied to the beam. Hence the stress in the beams is a combination of the prestress and the self-weight.

Over time, the compressive stress in the bottom fibre decreases. One reason for this is the time-dependent prestress losses, which can amount up to 15% to 20% of the initial prestress (Taerwe, 2015). These losses are caused by the creep and shrinkage deformation. The relaxation of the prestress will also have an influence on the time-dependent losses. In the present calculations this relaxation was neglected; its influence will be studied in section 8.4.4. Note that the stress increases over time in the bottom fibre is almost indistinguishable. This is explained by the limited influence of the prestress on the stress at the top fibre. Another reason for the decrease of the compressive stress in the bottom fibre is the stress redistribution. As the concrete creeps and shrinks, compressive stress is transferred to the passive reinforcement, as was already explained in the previous chapter.

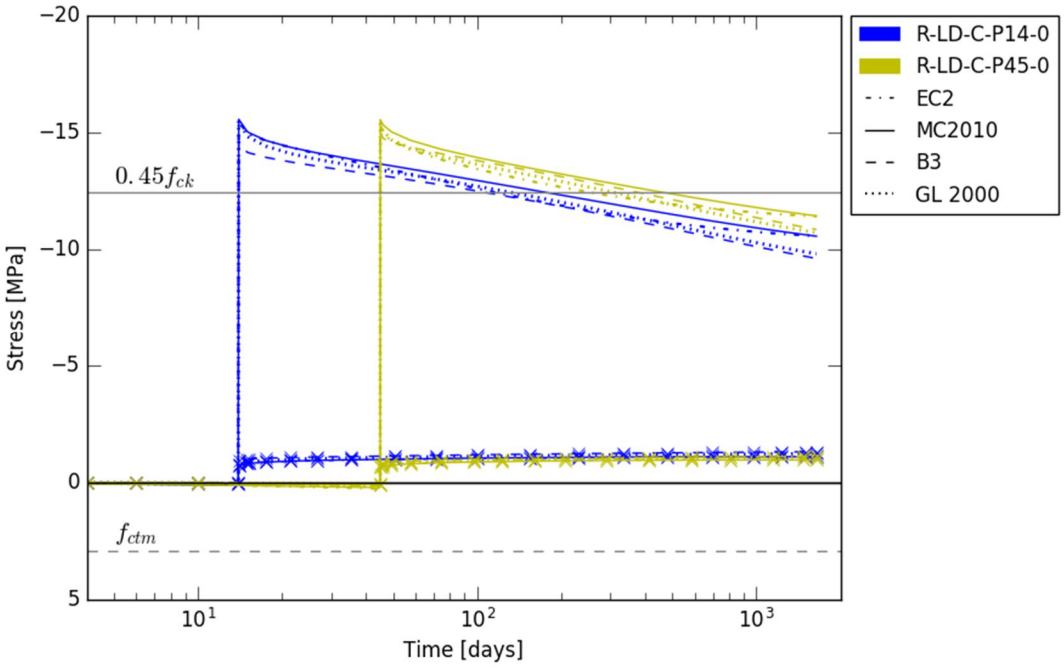

Figure 8.17. Prediction of the stress at the bottom fibre and the top fibre (marked by an x) at midspan of the post-tensioned unloaded rectangular beams (constant aging coefficient equal to 0.8 and no correction for relaxation of prestress).

The stress predictions of the I-shaped beams pre-tensioned at 7 days are presented in Figure 8.18. The stresses of the unloaded beam serve as a reference. The behaviour of the unloaded beam is similar to that of the previously discussed beams. The other two beams presented in the figure are

loaded at 28 days. Due to the loading, compressive stress is induced in the top fibre and tensile stress is induced in the bottom fibre. Note that all beams obtain the desired stress distribution (Figure 5.10) reasonably well. The approximate uniform stress distribution of the beam loaded at 50% explains why the deflection of these beams stays roughly constant over time (Figure 8.12). Note that there is a little bit more variation between the stress predictions of the models than for the beams represented in Figure 8.17. This is due to a larger variation of the moduli of elasticity between the models caused by the earlier age of prestressing.

Comparing the stress in the bottom fibre of the three beams, it can be observed that the stress decrease is lower for the loaded beams. The compressive stresses are lower in them, resulting in smaller time-dependent losses.

For the unloaded beam it can be remarked that the compressive stress in the top fibre stays constant. For the beam loaded at a 100 % the compressive stress decreases slightly due to relaxation of the concrete stress and/or stress redistribution to the passive reinforcement. For the beam loaded at 50% the compressive stress is quite low; therefore, the effects of creep are limited. As a result the concrete compressive stress stays approximately constant.

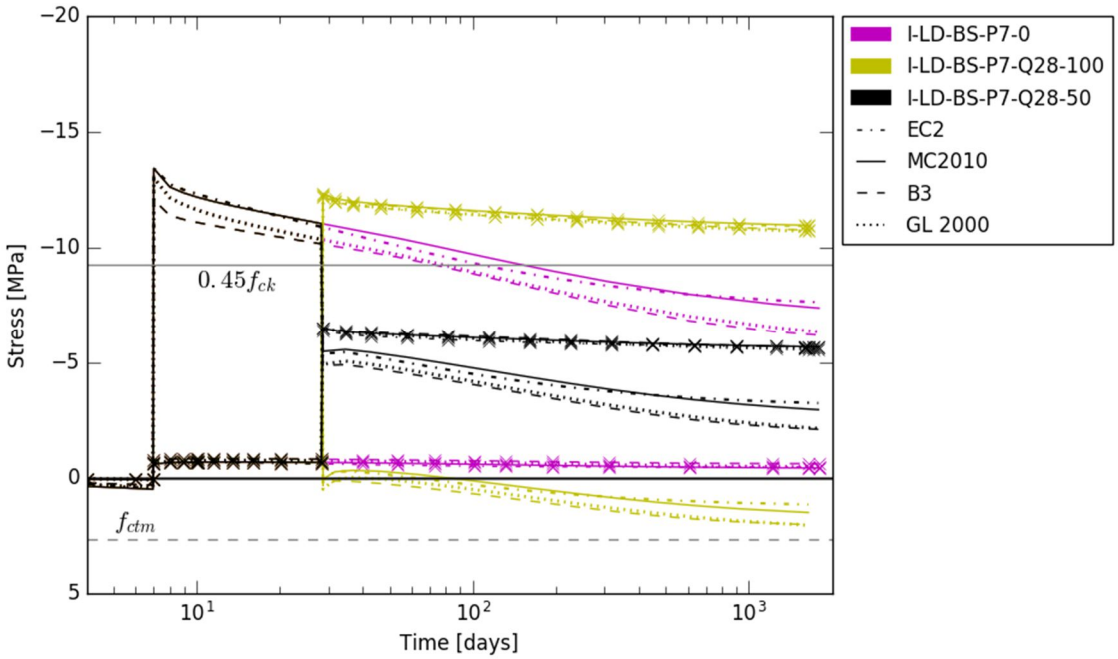

Figure 8.18. Prediction of the stress at the bottom fibre and the top fibre (marked by an x) at midspan of the pre-tensioned I-shaped beams which are prestressed at 7 days (constant aging coefficient equal to 0.8 and no correction for relaxation of prestress).

Table 8.3 shows the calculated elastic stresses as they were reported in the FKFO report. The first three rows are representative for the time just after loading. In the last three rows the factor 0.8 takes into account the time-dependent prestress losses. The last three rows thus represent the stresses a long time after loading. There is a good agreement between the trend reported in the table and the trend visualised in Figure 8.18; however, the table gives higher values for the stress at the bottom fibre. Immediately after prestressing this difference can be explained by the age of the concrete, which was most likely not taken into account for the calculations leading to the reported values in the table. Due to its young age the modulus of elasticity is not yet completely developed, resulting in smaller stresses. The differences between the values just after loading is considered to

be related to the time-dependent prestress losses between the moment of prestressing and the moment of loading. These were taken into account in the graph but were not taken into account for the values in the table. There is also a difference in the reported compressive stresses in the bottom fibre at later ages. The exact explanation for this difference is not entirely clear. Most likely it will be related to neglecting the stress redistribution to the passive reinforcement and neglecting of the time-dependency of the moduli of elasticity for the values in the table.

Table 8.3. Reported calculated elastic stress state for the pre-tensioned I-shaped beams at midspan (FKFO no. 547).

		Top fibre	Bottom fibre
$P_i + g$	[MPa]	-0.71	-14.31
$P_i + g + Q_{ser}/2$	[MPa]	-6.53	-8.71
$P_i + g + Q_{ser}$	[MPa]	-12.36	-3.12
$0.8 \cdot P_i + g$	[MPa]	-0.96	-11.07
$0.8 \cdot P_i + g + Q_{ser}/2$	[MPa]	-6.78	-5.47
$0.8 \cdot P_i + g + Q_{ser}$	[MPa]	-12.61	+0.12

The stresses of the T-shaped beams loaded at 56 days are represented in Figure 8.19. The models predict the deflection of these beams very inaccurate, as was shown in the previous section. The absolute stress level in these T-shaped beams is very comparable to that of the pre-tensioned I-shaped beams which were just discussed. The only difference is that the stress due to prestressing is slightly higher in the T-shaped beams. Comparing the stresses of the I-shaped beams and the T-shaped beams with the stresses of the other beams given in Appendix G, it can be seen that the stresses in the pre-tensioned I-shaped beams are slightly lower than the stresses of the other beams. However, it can be concluded that the absolute stress level for all the beams is comparable. Looking at the stress level relative to the $0.45 f_{ck}(t_0)$ boundary, it can be concluded that the relative stress of the T-shaped beams is lower than that of the other beams. This can be attributed to the high value of the concrete strength of the T-shaped beams in comparison to the other beams.

Table 8.4 show the calculated elastic stresses as reported in the FKFO report for the T-shaped beams. The same remarks as for the I-shaped beams are valid here.

Table 8.4. Reported calculated elastic stress state for the T-shaped beams at midspan (FKFO no. 547).

		Top fibre	Bottom fibre
$P_i + g$	[MPa]	-0.68	-16.45
$P_i + g + Q_{ser}/2$	[MPa]	-6.25	-9.53
$P_i + g + Q_{ser}$	[MPa]	-11.81	-2.61
$0.8 \cdot P_i + g$	[MPa]	-0.94	-12.66
$0.8 \cdot P_i + g + Q_{ser}/2$	[MPa]	-6.51	-5.74
$0.8 \cdot P_i + g + Q_{ser}$	[MPa]	-12.07	+1.18

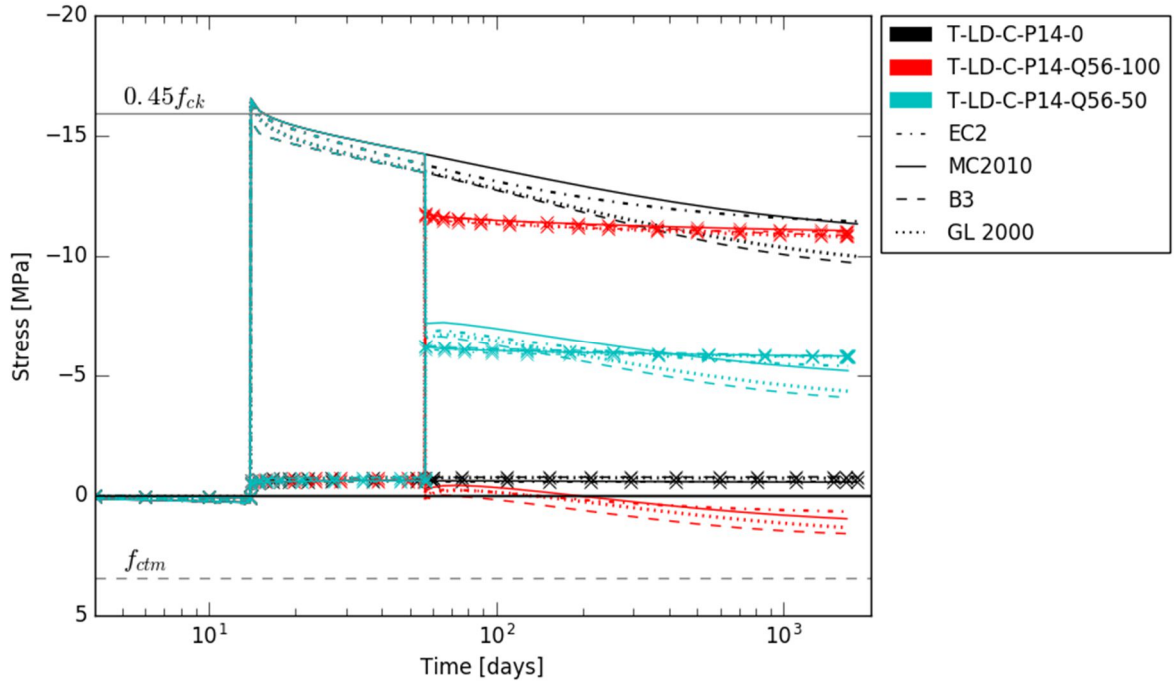

Figure 8.19. Prediction of the stress at the bottom fibre and the top fibre (marked by an x) at midspan of the post-tensioned T-shaped beams which are loaded at 28, respectively 34 days (constant aging coefficient equal to 0.8 and no correction for relaxation of prestress).

The stresses of all the other beams can be found in Appendix G. Their behaviour can be explained similarly to the pre-tensioned I-beams. Note that the stress in all beams surpasses the boundary value of $0.45f_{ck}(t_0)$. However, the stress in the prestressed beams exceeds this boundary in a much less pronounced way than the stress in the reinforced beams. The overstepping of the boundary is most distinct for the post-tensioned I-shaped beams. The stress in their bottom fibres exceeds the boundary by approximately 6 MPa. This is a similar value as obtained for the reinforced beams of type II loaded at 52%. The influence of a nonlinear creep calculation for the reinforced beams was studied in section 7.3.4. Figure 7.17 showed that the influence on the deflection of a nonlinear creep calculation was limited. Moreover, the method which was developed in section 7.3.4 assumed that a tensile zone was present in the cross-section. This is not the case for the prestressed beams immediately after loading. Considering that a new method would have to be developed, and considering that the influence of this method on the results would be limited, it was decided to not study the nonlinear effects of creep for the prestressed beams.

Studying all the stress graphs, it can be concluded that in none of the beams the stress goes below the mean concrete tensile stress at 28 days f_{ctm}. NBN EN 1992-1-1 (2005) prescribes this value as the boundary for cracking; as long as the tensile stress in a concrete member stays below f_{ctm} the member can be considered uncracked. It is thus concluded that the assumption of uncracked calculations, which was made in section 8.4.1, is valid.

8.4.2.3. Strain

The predicted strains near the top fibre of the unloaded rectangular beams are shown in Figure 8.20. The location of the measuring point for the strains was 10 mm below the top fibre, see Appendix C. Before the time of prestressing the beam exhibits a small amount of compressive strain due to shrinkage. At the moment of prestressing there is an instantaneous compressive strain

increase. Note that this increase is small. The transfer of prestress has not much influence near the top fibre, as was already reasoned in the previous section. For the other beam shapes the influence of prestressing is even more limited (near the top fibre), see Appendix H. For the post-tensioned I-shaped beams the influence is even hardly noticeable. After prestressing, the concrete strain increases under creep and shrinkage. Note that there is not a lot of difference between the prestressing at 14 days and the prestressing at 45 days.

The lowest prediction of the strains are done by the B3 model. Since the creep deformation is small, the time-dependent deformation is dominated by the shrinkage deformation. This shrinkage deformation is small for the B3 model compared to the other models, see section 8.1. The strain predicted by MC90-99 is almost indistinguishable from the strain predicted by MC2010. Since their shrinkage models are identical, this indicates that there is a small amount of creep deformation. The shape of the strain predicted by EC2 is different from the shape of the other models. It is very similar to the pure shrinkage strain predicted by EC2, see Figure 8.1.

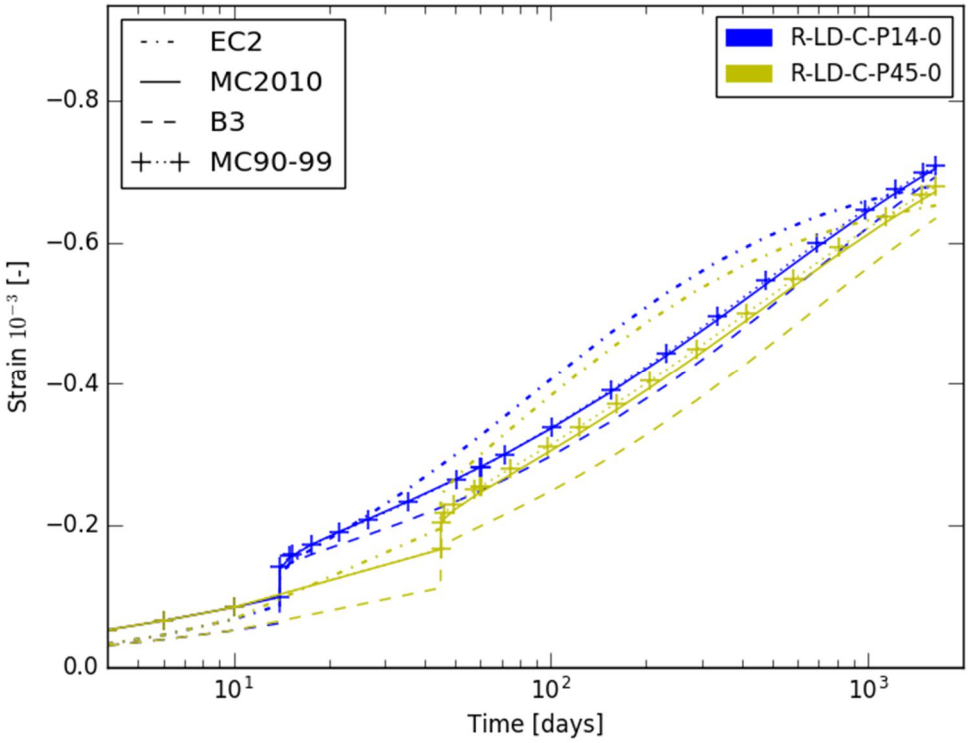

Figure 8.20. Predictions of the strain near the top fibre at midspan of the post-tensioned unloaded rectangular beams (constant aging coefficient equal to 0.8 and no correction for relaxation of prestress).

The predictions of the strains near the top fibre of the I-shaped beams prestressed at 7 days are compared against measurements in Figure 8.21. Similar as for the previous two beams there is some shrinkage strain before prestressing. At prestressing there is a slight increase in the strain and there is a more pronounced increase in the strain when the loading is applied. Note that the rate in which the strain increases after loading is proportional to the loading level. This is explained by the fact that creep deformations are higher for higher loaded beams.

The influence of the creep can also be deduced from the strain predictions of the B3 model. For the unloaded beam the strains predicted according to B3 are the lowest. From the comparison in Figure 8.8 it was concluded that the creep coefficient for B3 is much higher than the creep coefficient of

MC2010. Since for the loaded beams both the absolute value of the strain, as well as the rate of the strain, are higher for the B3 model than for MC2010, this thus proves that the concrete creeps.

There is even a third observation proving the fact that the loaded beams creep. For the unloaded beam the strain predictions according to the different models are very similar. As the load increases, the difference between the predictions of the models increases. Since the shrinkage predictions for all the models are very similar, this needs to be caused by the diverging creep predictions.

Observe that the highest strain predictions are the ones from GL 2000. This is the result of a mediocre shrinkage predictions, as well as a mediocre creep coefficient for loading at 28 days and a low modulus of elasticity throughout the entire time domain. The strain predictions of MC2010 are the lowest. This is caused by its mediocre shrinkage predictions, in combination with a low creep coefficient and a high modulus of elasticity (compared to GL 2000).

The measurements of the beams, which are shown in Figure 8.21, are smaller than the predictions. This is related to the behaviour of the deflections, which were also slightly overestimated by the predictions. Since the deflections are calculated out of the deformations, also the strain in the bottom fibre is required to make a more complete link between the deflections and the strains.

Unlike for the reinforced beams, it can be deduced from the provided measurements, that the assumption of a linear relationship between stress and strain is valid for the prestressed beams. This is explained by the lower levels of loading which are applied on the prestressed beams.

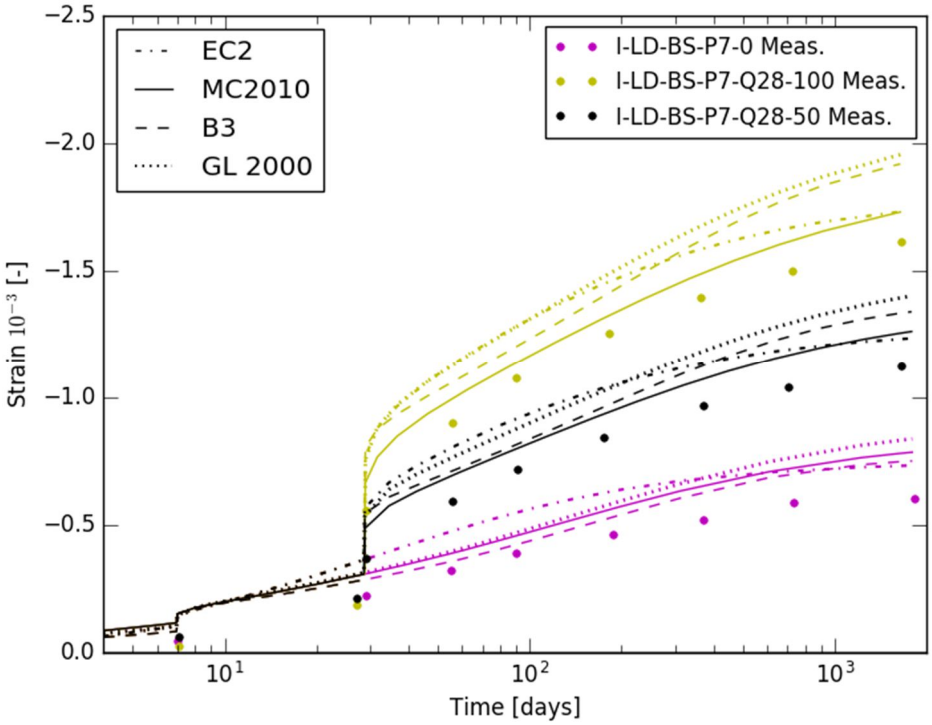

Figure 8.21. Predictions and measurements of the strain near the top fibre at midspan of the pre-tensioned I-shaped beams prestressed at 7 days (constant aging coefficient equal to 0.8 and no correction for relaxation of prestress).

In Figure 8.22 the predictions of the strains near the top fibre of the T-shaped beams loaded at 56 days are compared against measurements. The strain predictions according to the ACI model have a

similar trend as the strain predictions of EC2. This is logical since both their creep coefficients and their shrinkage predictions are similar for the studied beams. At a medium age the strain predictions of the ACI model are larger than the predictions by GL 2000. This is considered to be because the ACI model has a larger shrinkage prediction as well as a larger creep coefficient compared to the GL 2000 model at medium age. At later age, both the shrinkage prediction and the creep coefficient according to the ACI model come close to their asymptotic value. This causes the rate of the strain development to decrease significantly. The creep coefficient of the GL 2000 model has no asymptotic value, explaining why its rate of strain development decreases only slightly over time.

The models severely underestimate the measurements of the unloaded beam in Figure 8.22. The measurements even show that there is a tensile strain in the concrete near the top fibre which is induced by the prestress. Due to shrinkage (and creep) this tensile strain decreases and becomes a compressive strain. Note that the models do not predict a tensile strain. The reason that a tensile strain is measured but is not predicted can be related to the modulus of elasticity. When analysing the deflections, it was already noted that the reported modulus of elasticity was probably too high and not representative for the beams. With a lower modulus of elasticity the beams would behave less stiff and would deform easier. Allowing for example for tensile strains to be induced due to the application of prestress. Despite the overestimation of the models, the rate of strain development of the unloaded beam is decently predicted by MC2010, B3, and GL 2000.

Due to the bad prediction of the unloaded beam, the instantaneous strains due to loading are also badly predicted. Because of the creep underestimation just after loading, the strain predictions of the loaded beams do not differ that much from the measurements at later age. Note that at a later age the rate of strain development is predicted quite good by MC2010, B3, and GL 2000.

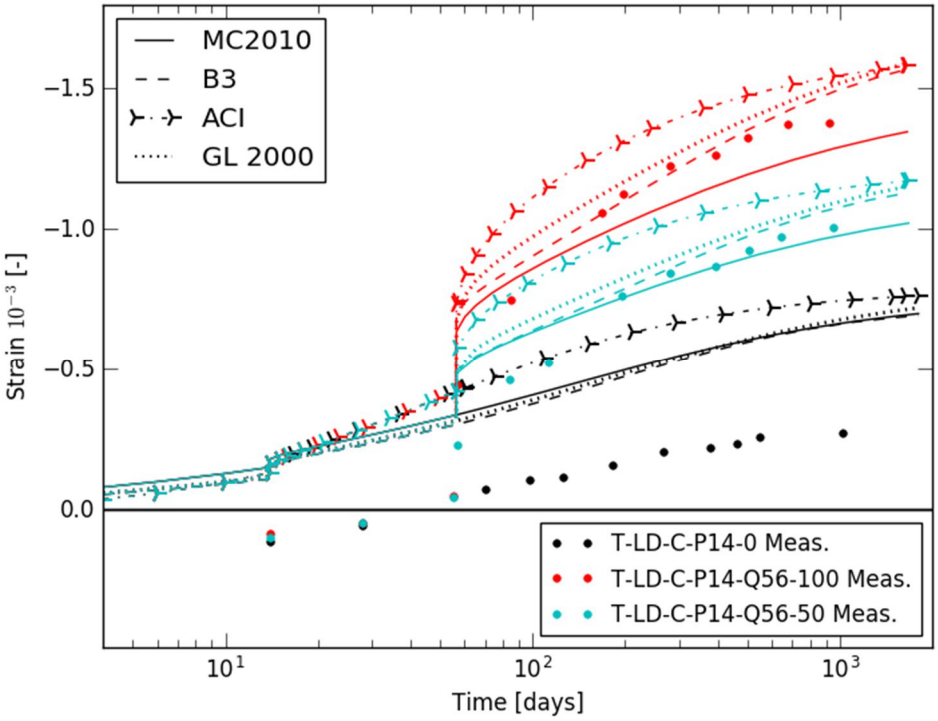

Figure 8.22. Predictions and measurements of the strain near the top fibre at midspan of the post-tensioned T-shaped beams loaded at 56 days (constant aging coefficient equal to 0.8 and no correction for relaxation of prestress).

8.4.2.4. Axial shortening

The strains at mid height of the beams (200 mm from the bottom fibre) were integrated over the length of the beams, using formula (6.27), to calculate the axial shortening. Figure 8.23 shows the axial shortening for the unloaded rectangular beams. Up until the moment of prestressing the axial shortening in the beams builds up due to shrinkage. At the moment of prestressing the beams undergo an elastic shortening because the cross-section is placed in compression. Afterwards, the shortening increases due to shrinkage and creep (note that the predictions by MC90-99 and MC2010 are not identical). The differences between the models for the elastic shortening step are the result of the deviations of their moduli of elasticity. All the remarks made about the models in the previous section are also valid here.

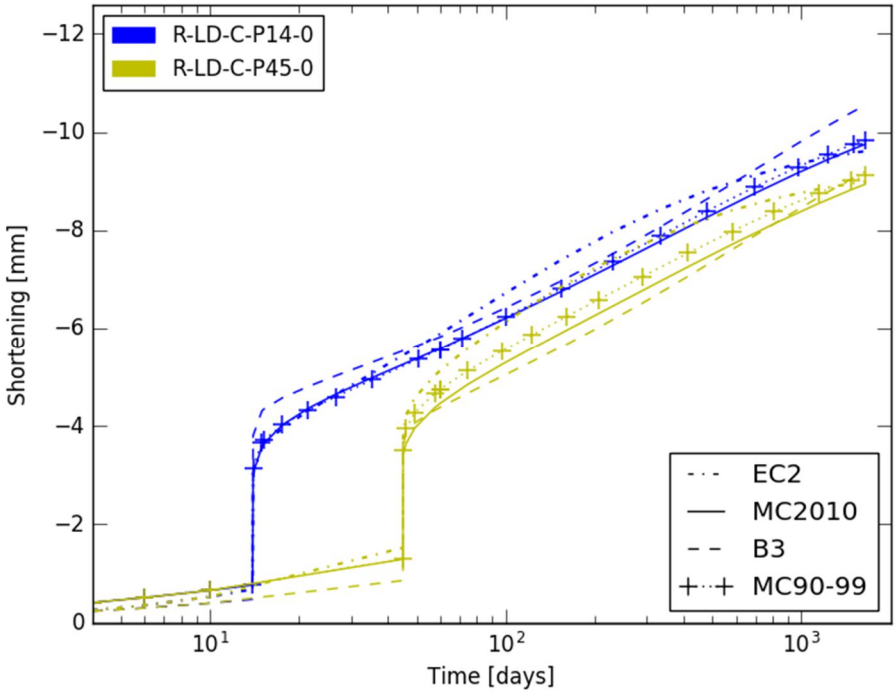

Figure 8.23. Axial shortening at mid height of the unloaded post-tensioned rectangular beams (constant aging coefficient equal to 0.8 and no correction for relaxation of prestress).

The axial shortening of the I-shaped beams pre-tensioned at 7 days is illustrated in Figure 8.24. Up until the moment of loading the predictions of the shortening are identical for the three beams. The behaviour up until that moment is comparable to the behaviour of the unloaded rectangular beams. At the moment of loading the predictions of the three beams start to deviate slightly from each other. The difference is however minuscule. The bending moment which is applied causes the top fibre to gain compressive stress and the bottom fibre to loose compressive stress. Near the middle fibre the influence of the bending moment is limited, explaining why the difference between the shortening predictions of the beams is so minuscule after loading.

For the post-tensioned T-shaped beams loaded at 56 days in Figure 8.25 the behaviour is completely analogue. The beams slightly extend at the moment of loading, but this extension is small and is almost immediately superseded by the time-dependent shortening due to shrinkage and creep. The shape of the predictions done by the ACI model deviate from the other predictions. This is related to the creep coefficient and shrinkage prediction of ACI, as was already previously explained.

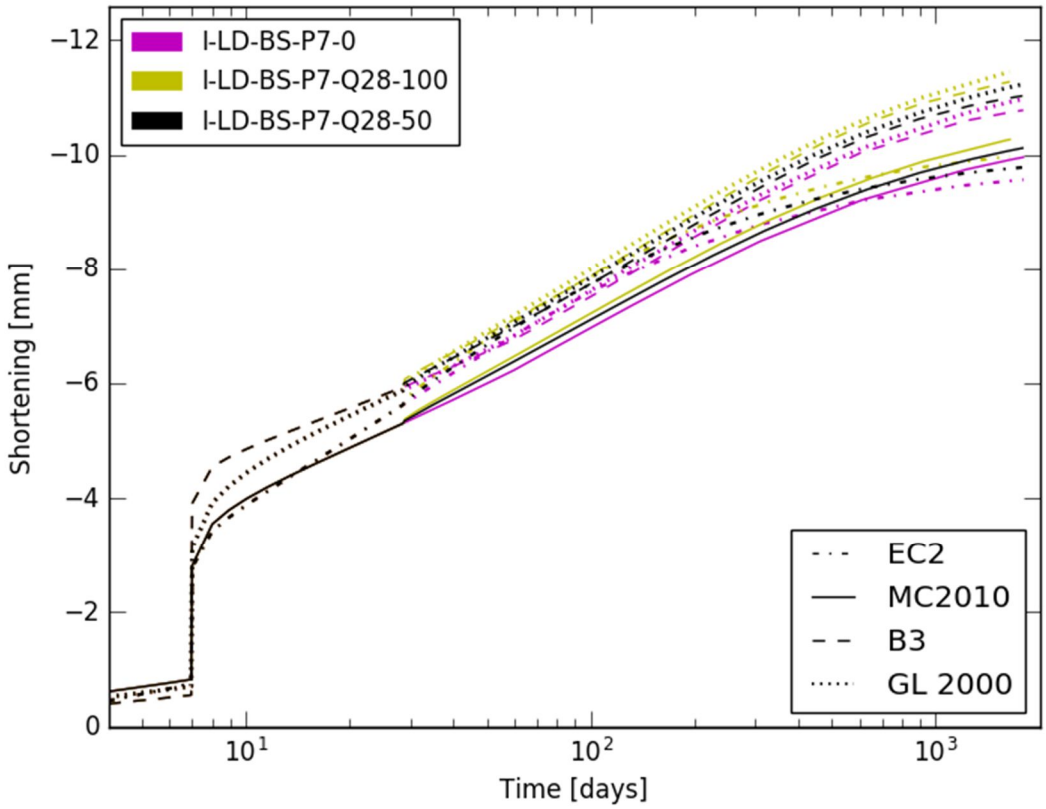

Figure 8.24. Axial shortening at mid height of the I-shaped beams pre-tensioned at 7 days (constant aging coefficient equal to 0.8 and no correction for relaxation of prestress).

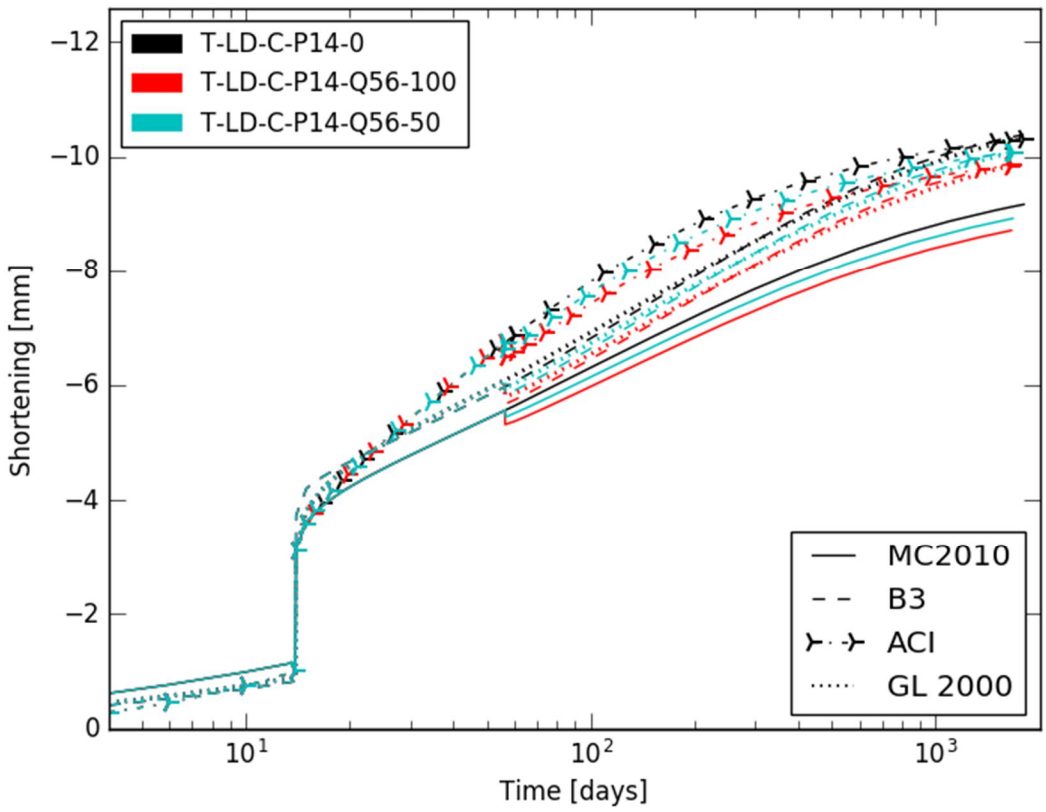

Figure 8.25. Axial shortening at mid height of the post-tensioned T-shaped beams loaded at 56 days (constant aging coefficient equal to 0.8 and no correction for relaxation of prestress).

8.4.2.5. Deformation

In this section some deformation graphs will be discussed. Similar as for the reinforced beams, the predicted values according to one of the models are represented by a solid line. The measured values are represented by a pair of dots: a dot near the top fibre and a dot near the bottom fibre. The dashed line is merely a visual aid that connects the pair of dots. The actual deformation was only approximately linear. It showed (one or more) kinks. The lines do not start at a height of 0 m (they start 10 mm higher) and they also do not end at 0.400 m (they stop a 10 mm lower). Similar as for the reinforced beams, this is related to the location of the measuring point, see Appendix C.

The predictions according to MC2010 for the unloaded I-shaped beam pre-tensioned at 7 days are compared against the measurements in Figure 8.26. The predictions underestimate the curvature throughout the entire testing period. This is due to an overestimation of the strains near the top fibre and an underestimation of the strains near the bottom fibre. This underestimation of the curvature relates to the deflections. The rate of deflection increase was underestimated by MC2010 throughout the entire testing period for this beam.

From the figure it can be seen that the main deformation is located near the bottom fibre. The deformation near the top fibre is caused mainly by shrinkage and in a small degree by creep, as was explained in section 8.4.2.3. The bottom of the beam is subjected to higher stresses than the top. This causes the creep component to be more important, resulting in higher deformations. The creep and shrinkage deformation causes time-dependent prestress losses. This results in a quicker decrease of the time-dependent deformations than in an ideal case of constant prestress.

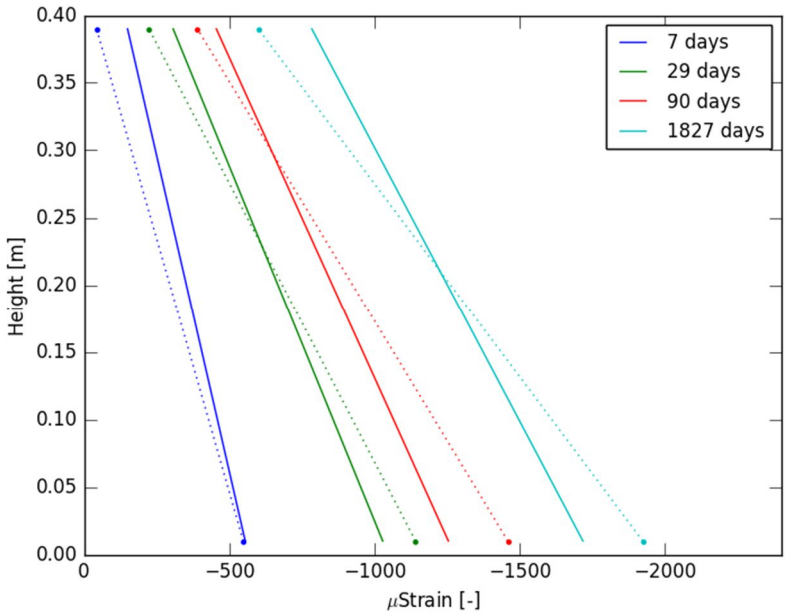

Figure 8.26. Predictions (MC2010) and measurements of the deformation at midspan of the unloaded I-shaped beam pre-tensioned at 7 days (constant aging coefficient equal to 0.8 and no correction for nonlinear creep).

The same beam is also shown in Figure 8.27, only now the beam is loaded at 28 days at 100% of the service load. MC2010 predicts the deformations reasonably well, and the predictions of the curvature become better over time. Similarly, in Figure 8.12, the predictions of MC2010 lie very close to the measurements.

Up until loading, the beam deforms identical as in Figure 8.26. When the loading is applied, the strain in the beam becomes approximately equal over the entire height of the beam. From Figure 8.18 it is know that the top of the beam is in compression, while the bottom of the beam is nearly stress free. The top of the beam will thus start to deform more than the bottom of the beam, resulting in a sign switch of the curvature. Note that there is still some deformation at the bottom of the beam, even though the stresses are small and the creep deformations are thus negligible. This is caused by shrinkage. The free shrinkage deformation between 28 days and 1642 days would approximately be 550 µm. The strain in the bottom fibre is lower due to the presence of passive reinforcement and the time-dependent loss of prestress. This time-dependent loss of prestress causes the induced compressive stress to decrease over time, resulting in a small extension. This also explains why the (compression) strain near the bottom fibre is lower at 90 days than at 29 days.

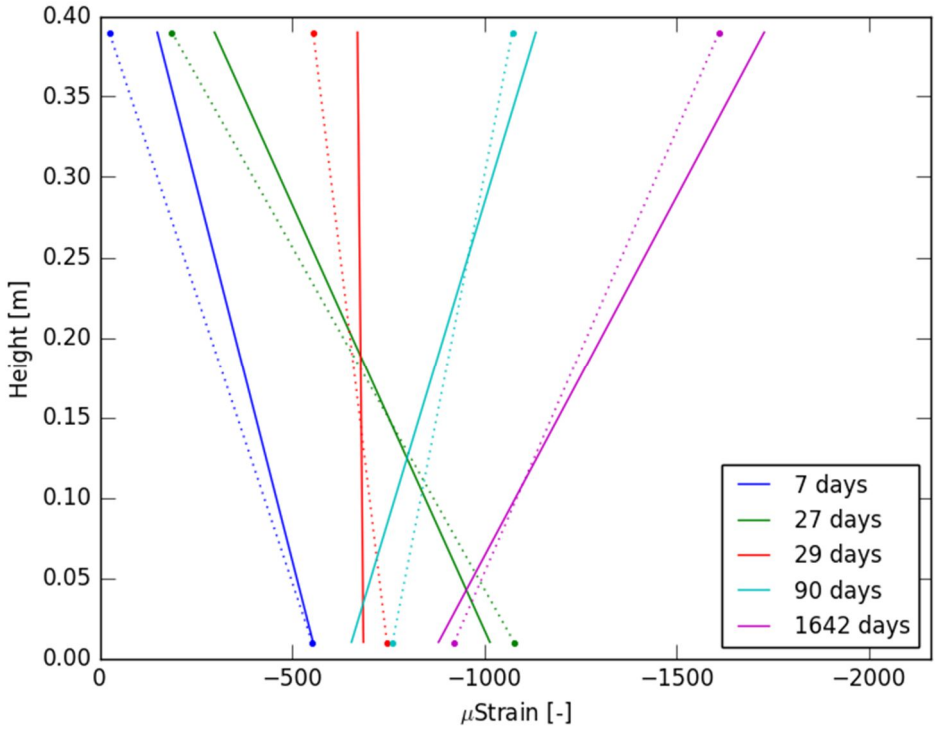

Figure 8.27. Predictions (MC2010) and measurements of the deformation at midspan of the I-shaped beam pre-tensioned at 7 days and loaded at 100% at 28 days (constant aging coefficient equal to 0.8 and no correction for nonlinear creep).

Figure 8.28 shows the same beam. The predictions of the deformation in this figure are however done according to the B3 model. It is clear that the B3 model's predictions are more inaccurate than the ones from MC2010. At prestressing and just after prestressing the predictions of the strain in top fibre are similar to those of MC2010; however, the predictions of the strain in the bottom fibre are significantly higher than the predictions by MC2010 and the measurements. This is related to a relatively low modulus of elasticity of the B3 model at early ages, in combination with a high creep coefficient. This causes the deflections at prestressing and just after prestressing to be significantly higher than the measurements, see Figure 8.12. At loading and just after loading the predictions of top fibre are severely overestimated, due to the high creep coefficient of the B3 model. This results in a higher deflection increase than the measurements, see Figure 8.12.

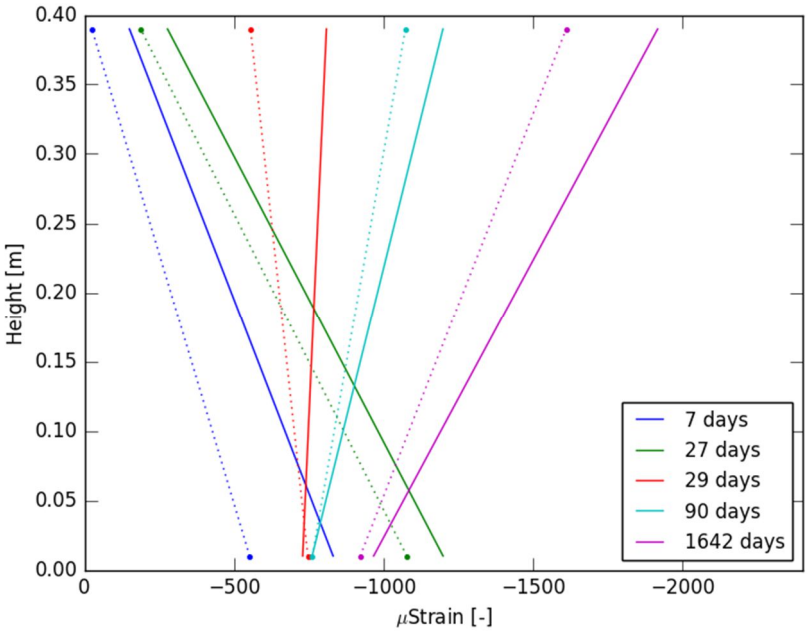

Figure 8.28. Predictions (B3) and measurements of the deformation at midspan of the I-shaped beam pre-tensioned at 7 days and loaded at 100% at 28 days (constant aging coefficient equal to 0.8 and no correction for nonlinear creep).

The predictions according to MC2010 for the unloaded T-shaped beam post-tensioned at 14 days and loaded at 50% of the service load at 28 days are compared against the measurements in Figure 8.29. The strains near the top fibre are all overestimated, except for the strain at the end of loading. Contrarily, all the strains near the bottom fibre are underestimated. This results in an underestimation of the curvature throughout the entire testing period. Looking at Figure 8.15, it is clear that also the deflection of this beam was underestimated throughout the entire testing period. The small curvature of the predictions explains why the deflection of this beam is almost constant after loading.

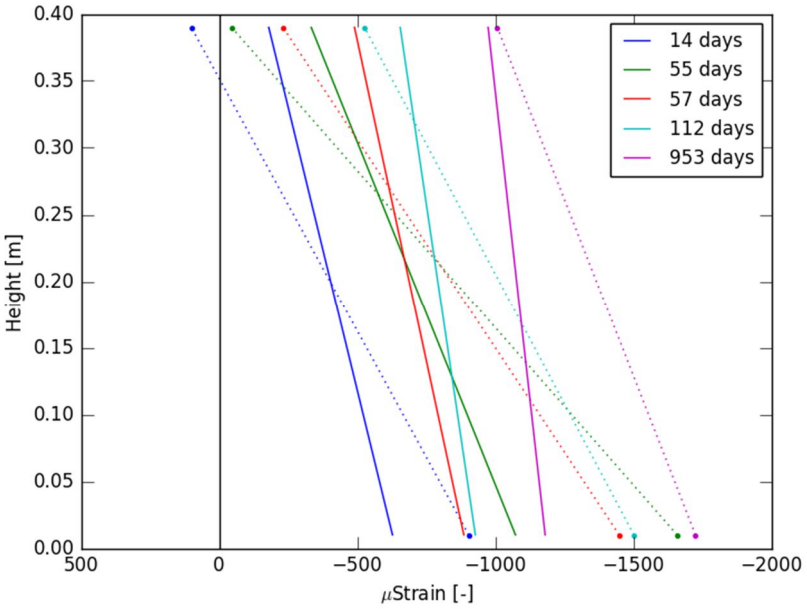

Figure 8.29. Predictions (MC2010) and measurements of the deformation at midspan of the T-shaped beam pre-tensioned at 14 days and loaded at 50% at 56 days (constant aging coefficient equal to 0.8 and no correction for nonlinear creep).

As already explained before, the bad predictions of this beam can be related to a too high reported modulus of elasticity. If the modulus would be smaller, the strains in the bottom fibre would be higher and the strains in the top fibre would be lower.

8.4.2.6. Summary

In this section, the results of a cross-sectional linear calculation, using the age-adjusted effective modulus with a constant aging coefficient equal to 0.8, were compared against measurements on prestressed beams. In the analysis, it was assumed that these beams remained uncracked throughout the entire testing period. Based on the predictions of the stresses, it was concluded that this assumption is indeed valid. From these stress predictions and based upon the results of the previous chapter, it was also concluded that a correction for nonlinear creep would not improve the results significantly. Therefore, a nonlinear creep prediction has not been performed for these prestressed beams.

Out of the evaluation of some of the unloaded beams it was noticed that there is quite some variation between the predictions of the different models. The B3 model and the GL 2000 model predict the deformations more severely than the other models, which have relatively comparable predictions. These more extreme deformation predictions are attributed to large variations in the moduli of elasticity and creep coefficients of the different models at early age. This also explains why the predictions of later prestressed beams are more similar to one another.

For the loaded beams it was noticed that the variation between the predictions according to the different models is smaller than in the case of the unloaded beams. This observation is explained by the superposition of opposing deformations. Take for example the B3 model, this model usually overestimated the deflections in the unloaded stage due to its low modulus of elasticity at an early age and its high creep coefficient. When loading was applied, deformations happened in the opposite direction. Despite the later age, the creep deformations of the B3 model are still significantly higher than the creep deformations of other models like MC2010. Due to superposition the high downward creep and the high upward creep balance each other out, resulting in predictions after loading which are more comparable to the other models.

From a visual investigation it can be concluded that at a later age the deformations and their rate are best described by either GL 2000, B3 or MC2010. None of the models prescribes all beams accurately.

8.4.3. Influence of non-centric placement of prestressing wires in duct

In all the previous calculations it was assumed that the post-tensioning wires were located in the centre of the duct. In reality, the wires will be positioned in the top of the duct as a result of the prestressing force. A formula to calculate the loss of eccentricity of the prestress due to the non-centric placement of the prestressing wires Δe is given hereunder (Taerwe, 1999):

$$\Delta e = \frac{3}{7} \cdot \phi_i \cdot \left(1 - 1.25 \cdot n \cdot \frac{\phi_{nom,wire}}{\phi_i}\right) \tag{8.1}$$

in which ϕ_i is the internal cable duct diameter, n is the number of prestressing wires, and $\phi_{nom,wire}$ is the nominal wire diameter. An overview of the calculations of the beams which were

post-tensioned is shown in Table 8.5. Note that the prestressed beams do not have a cable duct and this phenomena is thus not applicable for them.

Table 8.5. Overview of the calculation of the loss of eccentricity Δe.

Shape	n [-]	ϕ_i [mm]	$\phi_{nom,wire}$ [mm]	Δe [mm]
Rectangular	24	60	7	15.2
T-shaped	14	50	7	14.0
I-shaped (post-tens.)	16	50	7	13.0
I-shaped (pre-tens.)	N/A	N/A	N/A	N/A

It was assumed that the eccentricity did not change near the ends of the beams due to restraining of the anchorage blocks. Note that the upward shift of the wires results in a decrease of the moment applied by the prestressing force; the positive effect of prestressing is thus somewhat reduced.

A comparison of the deflection predictions calculated by taking into account the non-centric placed wires with respect to centric placed wires is given in both Figure 8.30, Figure 8.31, Figure 8.32. For the displayed rectangular beams in Figure 8.30 the upward deflections due to prestress were already underestimated. The correction for non-centric placed wires increases this underestimation drastically due to a loss of the upward bending moment.

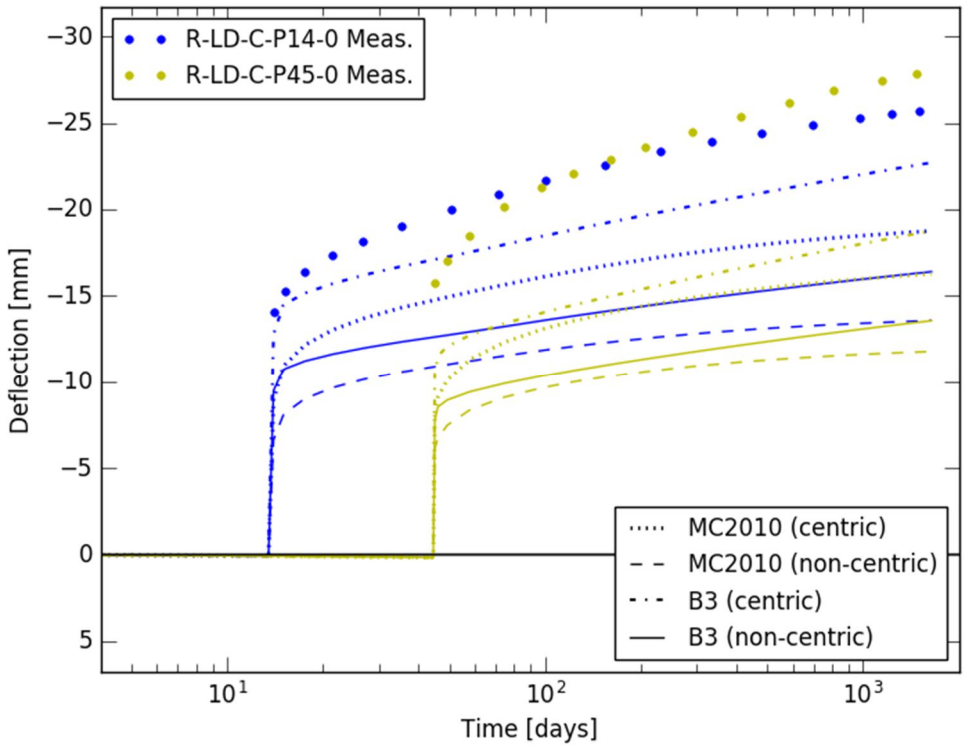

Figure 8.30. Comparison between the deflection predictions with centric placed wires, respectively with non-centric placed wires for the post-tensioned rectangular beams which are not loaded (constant aging coefficient equal to 0.8 and no correction for relaxation of prestress).

The deflection of the unloaded I-shaped beam in Figure 8.31 was overestimated for centric placed wires. The correction for non-centric placed wires ameliorates the predictions. The predictions of the loaded I-beams were underestimated. Due to the correction, the instantaneous deflection at time of loading is overestimated. This in combination with a more pronounced downward deflection rate results in better predictions.

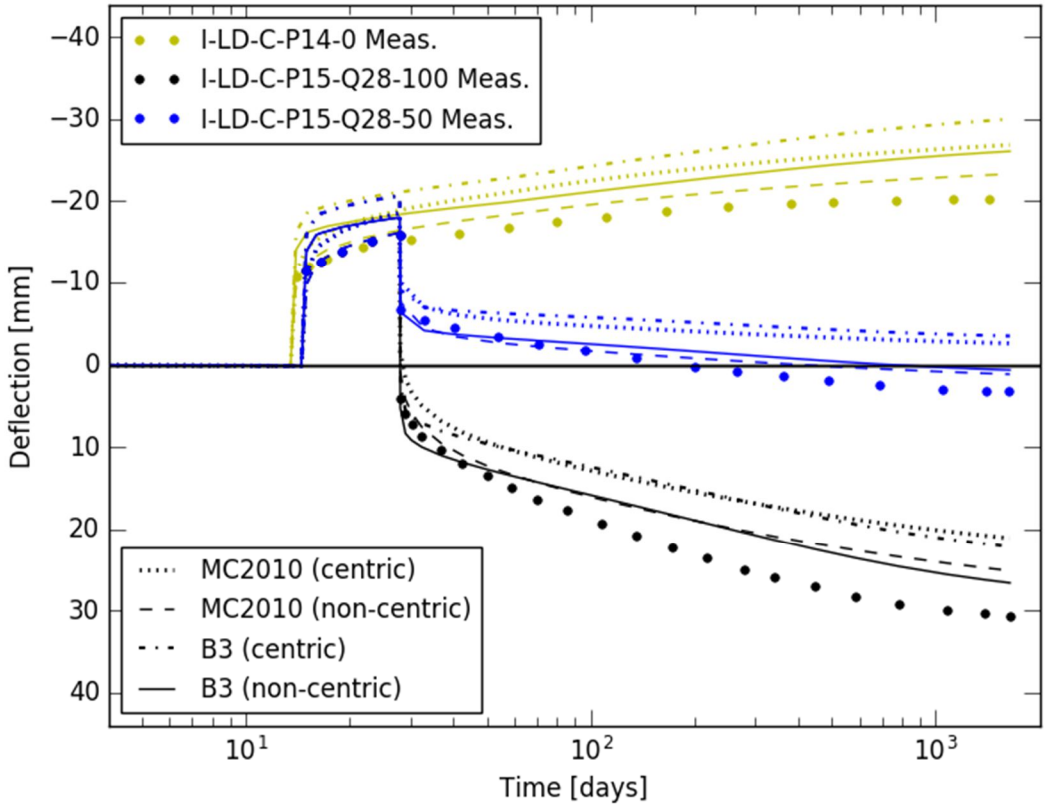

Figure 8.31. Comparison between the deflection predictions with centric placed wires, respectively with non-centric placed wires for the post-tensioned I-shaped beams which are loaded at 28 days (constant aging coefficient equal to 0.8 and no correction for relaxation).

The T-shaped beams were in the previous sections inaccurately predicted. The correction worsens the prediction of the time-dependent behaviour of the unloaded T-shaped beam in Figure 8.32. Yet, the time-dependent rate of the beam loaded at 50% is better predicted, even though the absolute difference between the measurements and predictions has increased. Using the correction, MC2010 predicts the end deflection of the beam loaded at 100% perfectly. The rate of the B3 prediction is also improved compared to the case without the correction.

From the above, it is clear that no general conclusion, with regards to the effectiveness of this method, can be drawn. The effectiveness needs to be checked for each beam separately. A general guideline is that if the deflections of the unloaded beams are overestimated and/or if the deflections of the loaded beams are underestimated, the correction ameliorates the predictions. In the other case, the accuracy of the predictions worsen.

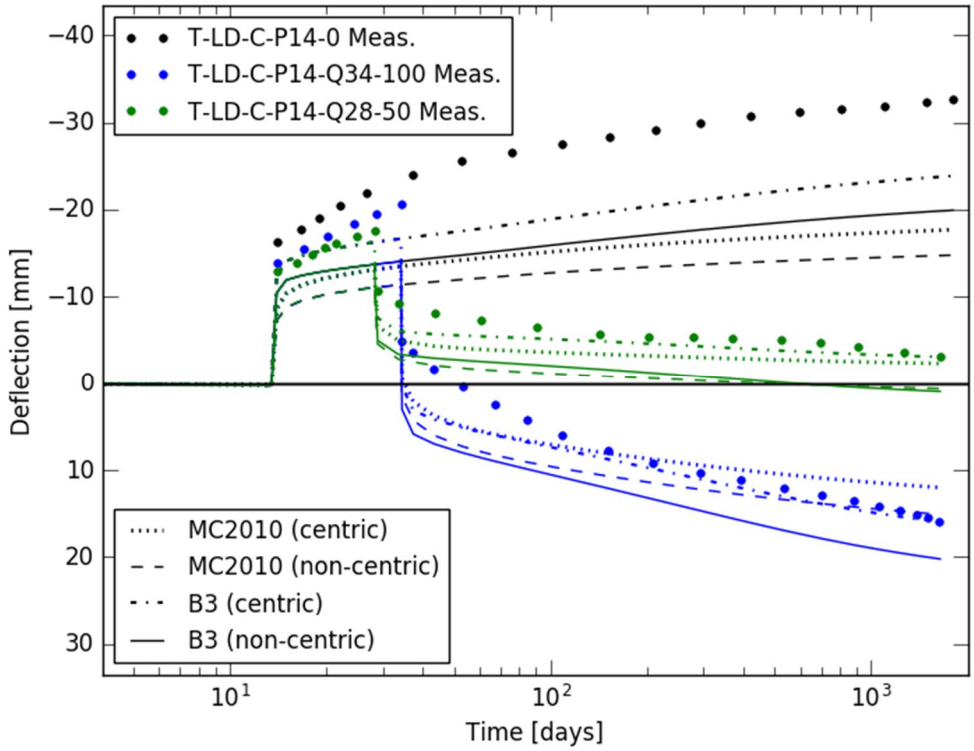

Figure 8.32. Comparison between the deflection predictions with centric placed wires, respectively with non-centric placed wires for the post-tensioned T-shaped beams which are loaded at 28 days (constant aging coefficient equal to 0.8 and no correction for relaxation).

8.4.4. Influence of relaxation of prestressing steel

Up until now, the loss of prestress due to relaxation has been neglected. Relaxation tests were performed on both the post-tensioning wires and the pre-tensioning strands. The results can be seen in Table 8.6. The table gives the percentage, relative to the ultimate load, at which the steel was tested. Table 8.7 shows an overview of the calculation which was performed to calculate the percentage at which the beams were loaded in the long-term tests. In Table 8.7 P is the total prestress, A is the area of one wire or one strand, n is the number of wires or strands, σ is the stress in one wire or one strand, f_{ptk} is the ultimate load of a wire or a strand, and λ is the ratio of the stress over the ultimate load. Comparing the ratio calculated in Table 8.7 with the test values in Table 8.6, it can be seen that the maximum theoretical relaxation will be no higher than 2%. Due to creep and shrinkage deformation the relaxation will be smaller, as was already explained in section 2.4.3.

The influence of the relaxation was, in a simplified way, studied by lowering the initial prestress force by 2%. The result of this calculation is compared against the original predictions in Figure 8.33. It can be seen that the influence of lowering the initial prestress force by 2% is limited. The deflections which are given for the relaxation in the figure are an extreme case; in reality the relaxation will be lower due to creep and shrinkage and will be induced over time, resulting in a smaller influence on the deflections. Based on this observation it can be concluded that the influence of a detailed relaxation calculation will have a minimal influence on the results.

Table 8.6. Results on relaxation tests performed on the prestressing steel, the values are given in percent.

	24 h	120 h	300 h	1000 h	3000 h	5000 h	7000 h	10000 h
post-tensioning wire at 60%	0.55	0.86	1.06	1.32	-	-	-	-
post-tensioning wire at 70%	0.89	1.21	1.43	1.84	-	-	-	-
post-tensioning wire at 80%	2.73	3.64	4.15	5.05	-	-	-	-
pre-tensioning strand at 60%	0.89	1.19	1.34	1.60	1.88	2.00	2.03	2.05
pre-tensioning strand at 70%	0.97	1.31	1.50	1.85	2.16	2.28	2.30	2.30
pre-tensioning strand at 80%	1.60	1.92	2.11	2.46	2.85	3.02	3.05	3.08

Table 8.7. Calculation of the prestressing percentage.

Shape	P [kN]	A [mm²]	n [-]	σ [MPa]	f_{ptk} [MPa]	λ [-]
Rectangular	1120	38.48	24	1212.6	1753	0.69
T-shaped	684	38.48	14	1269.5	1753	0.72
I-shaped (post-tens.)	750	38.48	16	1218.0	1753	0.69
I-shaped (pre-tens.)	757	126.68	6	996.0	1916	0.52

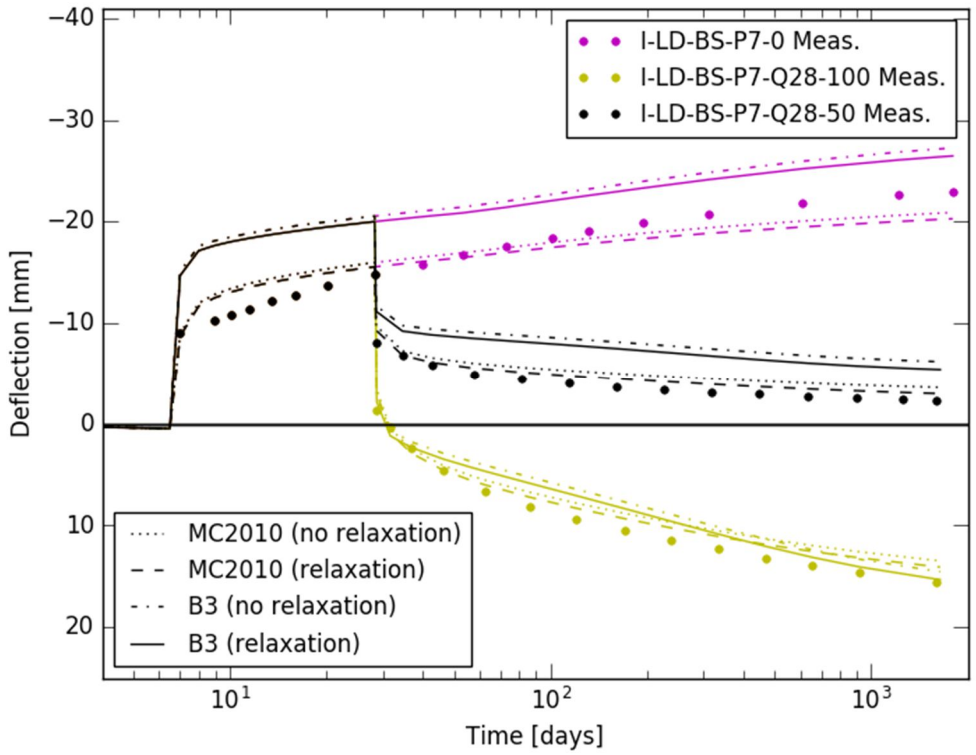

Figure 8.33. Comparison between the deflection predictions with and without a constant relaxation loss of 2% for the I-shaped beams prestressed at 7 days (constant aging coefficient equal to 0.8).

9. Conclusions

In this master dissertation, the time-dependent behaviour according to six different material models was analysed. This was done by comparing their predictions for reinforced and prestressed beams against measurements. The following material models were studied : CEB-FIP Model Code 1990-1999 (MC90-99), FIP Model Code 2010 (MC2010), Eurocode 2 (EC2), Bažant's and Baweja's model B3 (B3), Gardner Lockmann 2000 (GL 2000), and ACI 209 (ACI). Their predictions were calculated using a cross-sectional calculation method which implemented the ag-adjusted effective modulus. This age-adjusted effective modulus is, among others, dependent on an aging coefficient. The calculation time of this aging coefficient is computationally intensive. Therefore, in a first analysis, the aging coefficient is assumed to be constant and equal to 0.8.

The measurements which were used are part of an extensive research programme. The goal of this programme was to study the influence of the duration of different levels of permanent loading on the behaviour of concrete elements, reinforced concrete elements and prestressed concrete elements. The programme focused on the testing of beams with practical dimensions subjected to sustained loading up to four and a half years, making the results quite invaluable and unique.

The lower loaded reinforced beams were reasonably well predicted by the different material models; the measurements were only slightly underestimated. For the higher loaded beams, the predictions severely underestimated the time-dependent behaviour. In the calculations, a linear relationship was assumed between stresses and strains. From the measurements it was clear that this assumption was only valid for lower loaded beams. For higher loaded beams the relationship became nonlinear, explaining the underestimations made by the material models. Another source of error was the fact that the material models are only valid in the service stress range. From an analysis of the stress in the top fibre, it could be concluded that most of the beams were outside of this service range.

From all the studied models, the ACI model gave the best predictions at early and medium age. At a later age the predicted values according to the GL 2000 model fell closest to the measured values. The rate of creep at this later age was best described by the B3 model, followed by the GL 2000 model.

The deflections of the reinforced beams were also computed using a calculated aging coefficient. It was concluded that the deflections which were calculated using a constant aging coefficient equal to 0.8 hardly differed from the deflections computed using a calculated aging coefficient.

Since the stresses in the reinforced beams were outside of the service range, the creep could no longer be assumed linear. A method, taking the nonlinearity of the creep into account, was proposed. It was concluded that this method greatly improved the accuracy of the predictions. The use of this method resulted in a slight overestimation of the measurements. This is more desirable than an underestimation since it provides safer and more conservative values.

Using this nonlinear creep method, MC2010 predicted, on average, the absolute values of the deflection the most accurate (except for the absolute value at the end of loading). The rate of the time-dependent behaviour is on average best predicted by the GL 2000 model, followed by the B3 model at later ages. GL 2000 gave on average the best prediction for the absolute deflection at the

end of loading. The most inaccurate predictions were provided by the ACI model. For this model correcting for nonlinear creep resulted in more inaccurate predictions, except for the rate of creep at later ages, which is predicted better. These results were found to be comparable to what is reported in literature.

In the analysis of the prestressed beams it was noted that there was quite some variation between the predictions of the different models. The B3 model and the GL 2000 model gave higher predictions of the deflection than the other models. This was attributed to large variations in the moduli of elasticity and creep coefficients of the different models at early age.

By comparing the loaded and unloaded prestressed beams, it was observed that the predictions are less divergent for the loaded beams. This observation was explained by the superposition of opposing deformations. Due to superposition, a diverging downward deflection and a diverging upward deflection balance each other out, resulting in a total deformation which is comparable to other models.

It was concluded that none of the material models predicted all beams accurately. However, in general, the deformations and their rates at later ages are best predicted by GL 2000, B3, and MC2010.

For the post-tensioned beams, the influence of a non-centric placement of the prestressing wires in the cable duct was studied. It was concluded that if the deflections of the unloaded beams are overestimated and/or if the deflections of the loaded beams are underestimated, the correction for a non-centric placement of the prestressing wires ameliorates the predictions. In the other case, the accuracy of the predictions worsen.

In all the calculations of the prestressed beams, the relaxation of the prestress was neglected. Using a simplified but conservative method it was concluded that the influence of relaxation on the deformations is limited.

Further research

The data contained in the followed research programme is not yet exhausted. The programme also contains measurements on partially prestressed beams. Similar as for what was done here, the deformation of these beams can also be analysed. This analysis can extend the comparison which was done here, resulting in a complete comparison for all types of concrete.

The calculation tool which was used should be extended with a module to take the nonlinear relation between stress and strain, under higher stress levels, into account. This will provide more accurate predictions for the higher loaded beams. The tool could also be expanded to deal with the geometry of the end blocks of the prestressed beams and the fact that the reinforced and prestressed beams extend beyond their supports. These changes will make the calculation more computationally intensive. Therefore, it should be reasoned if an analysis in a finite element software package could be more desirable, since it will take secondary effects into account.

Concrete technology has advanced greatly over the years, resulting in new types of concrete, e.g. self-healing concrete. The time-dependent behaviour of self-healing concrete is still largely uncharted terrain. The chemical (and biological) admixtures which are added to the concrete can influence its time-dependent behaviour. In order for self-healing concrete to gain credibility, a detailed time-dependent analysis is required.

Appendix A. Detailed reinforcement scheme of reinforced beams

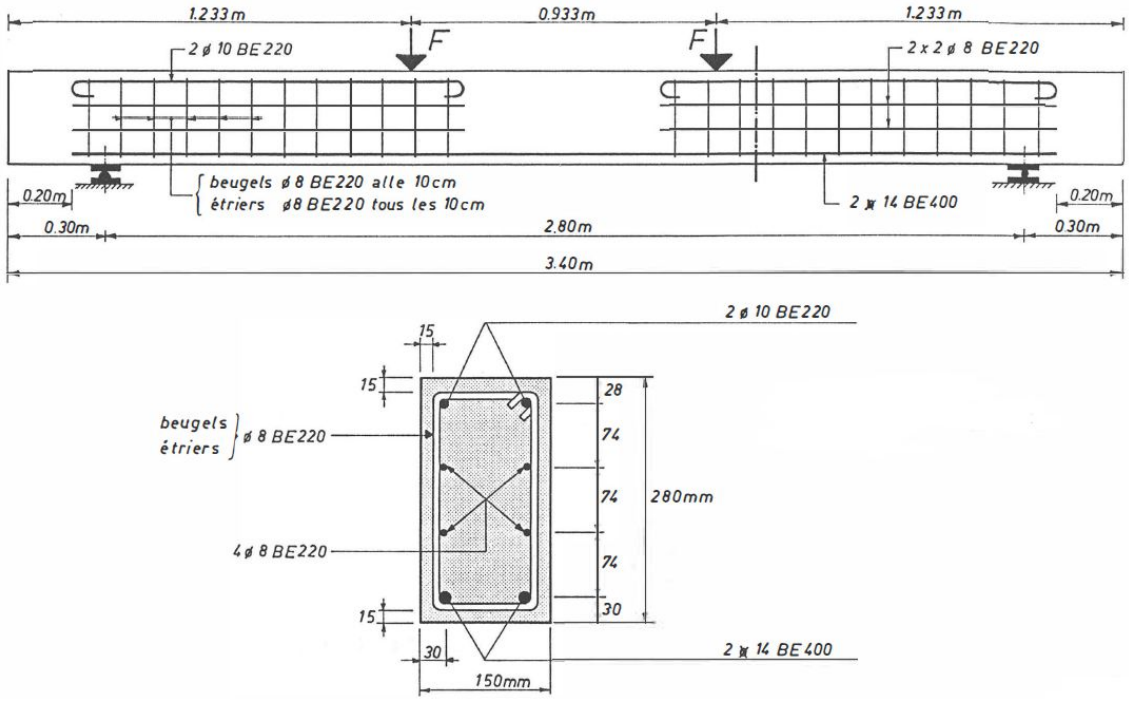

Figure A.1. Detailed reinforcement scheme of reinforced beam type I. The drawing in the top shows a side view of the beam. The bottom drawing shows the cross-section of the beam. For your information: "beugels" is the Dutch word for stirrups (FKFO no. 547).

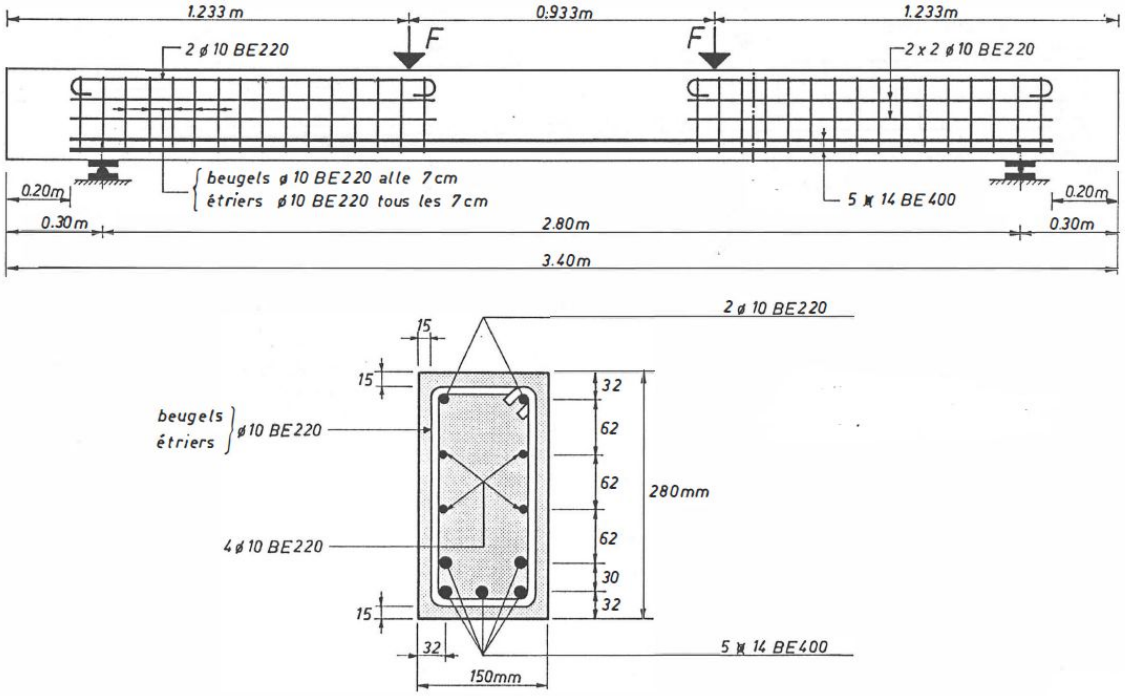

Figure A.2. Detailed reinforcement scheme of reinforced beam type II. The drawing in the top shows a side view of the beam. The bottom drawing shows the cross-section of the beam. For your information: "beugels" is the Dutch word for stirrups (FKFO no. 547).

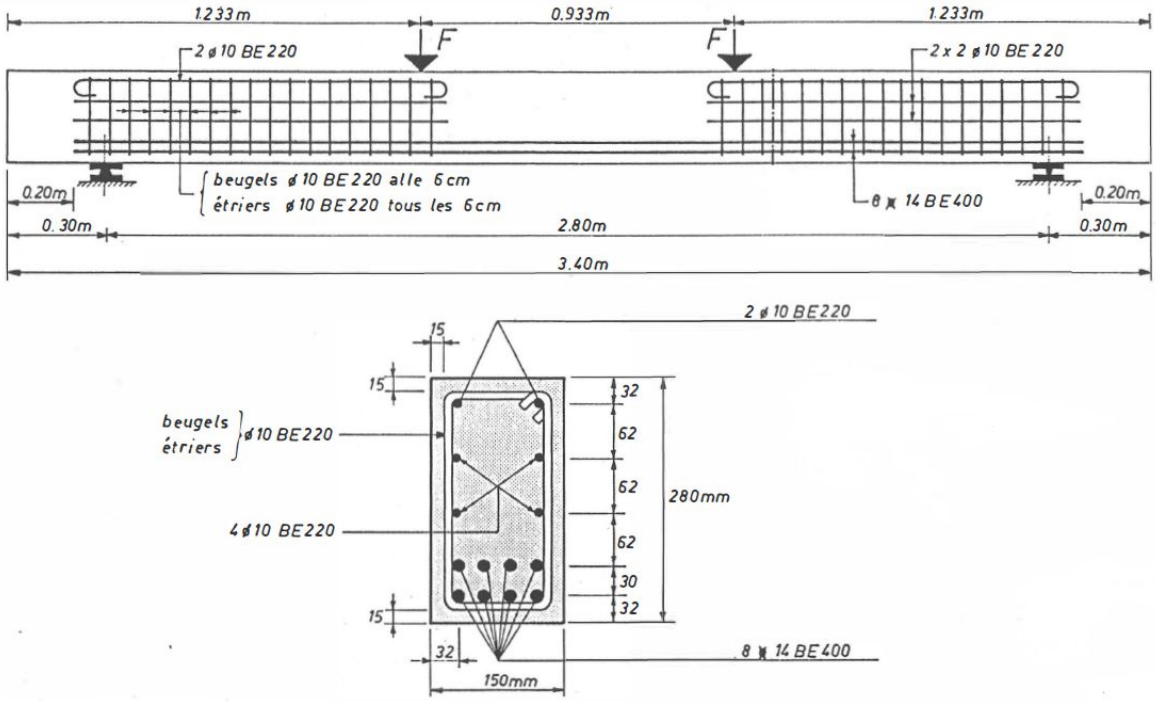

Figure A.3. Detailed reinforcement scheme of reinforced beam type III. The drawing in the top shows a side view of the beam. The bottom drawing shows the cross-section of the beam. For your information: "beugels" is the Dutch word for stirrups (FKFO no. 547).

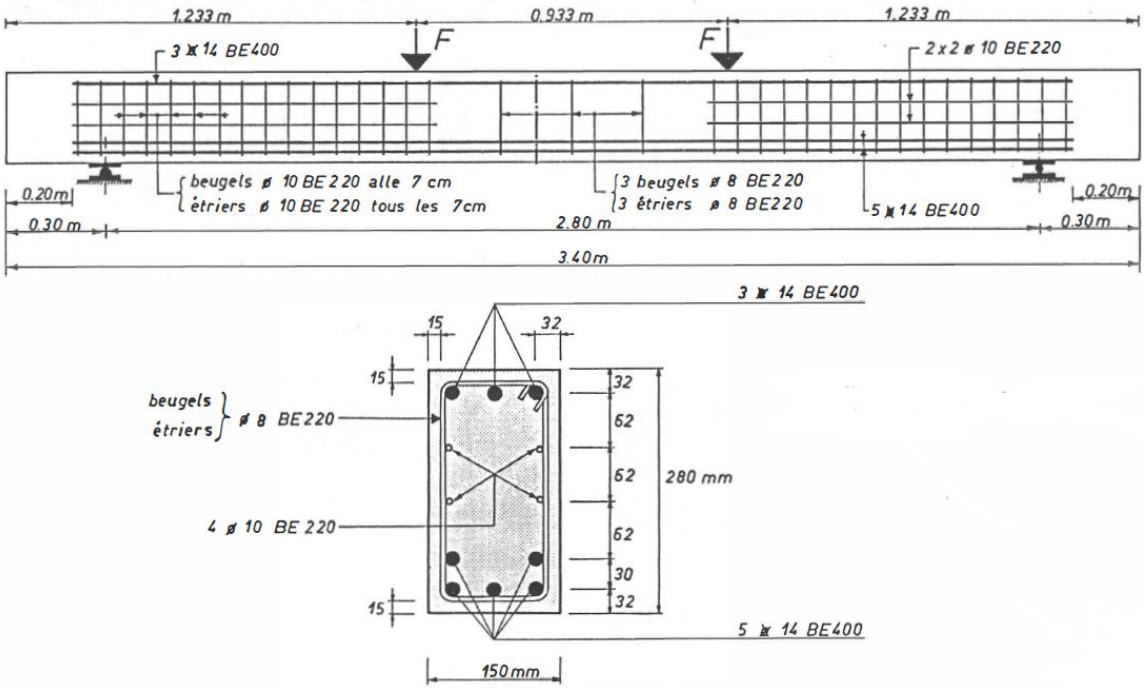

Figure A.4. Detailed reinforcement scheme of reinforced beam type IV. The drawing in the top shows a side view of the beam. The bottom drawing shows the cross-section of the beam. For your information: "beugels" is the Dutch word for stirrups (FKFO no. 547).

Appendix B. Location of the measuring points of the strains of the reinforced beams

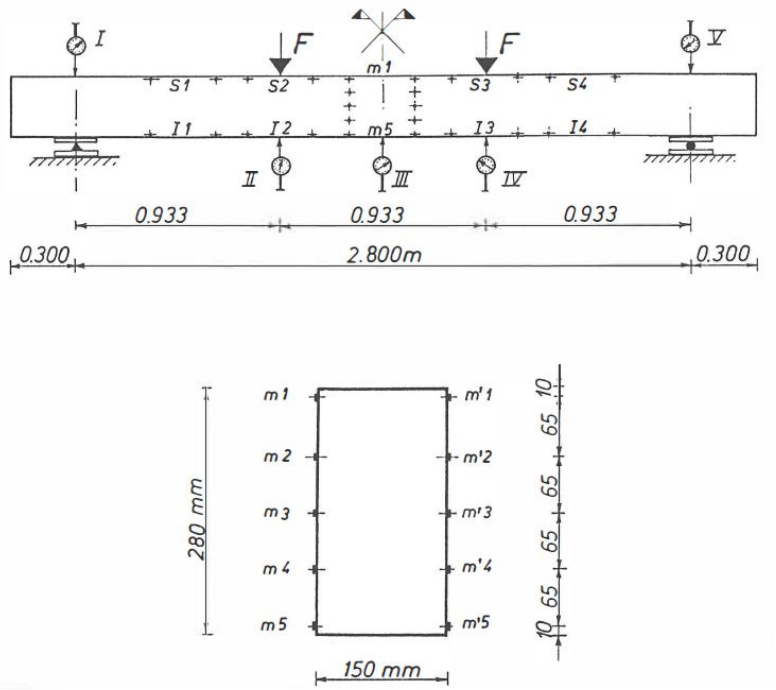

Figure B.1. Locations of the measuring points of reinforced beam type I (FKFO no. 547).

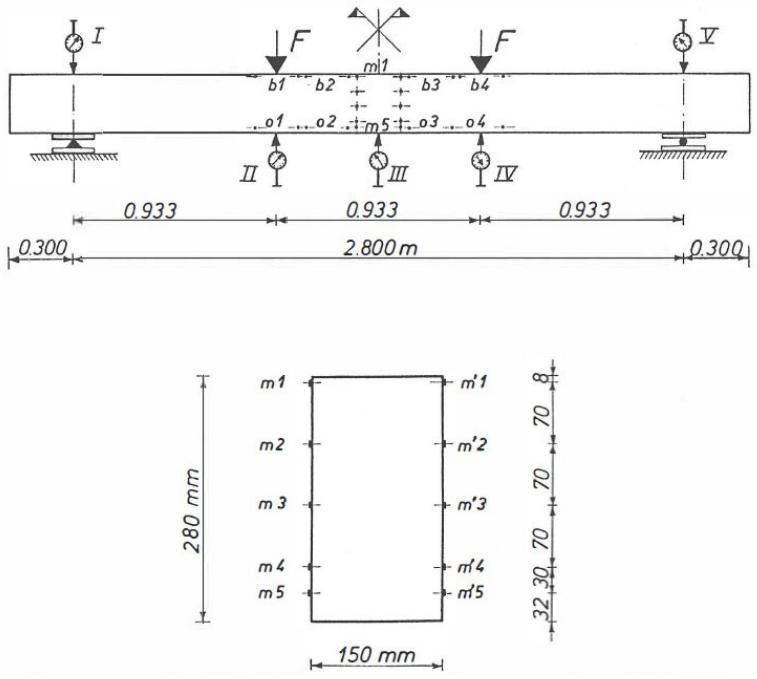

Figure B.2. Locations of the measuring points of reinforced beam type II (FKFO no. 547).

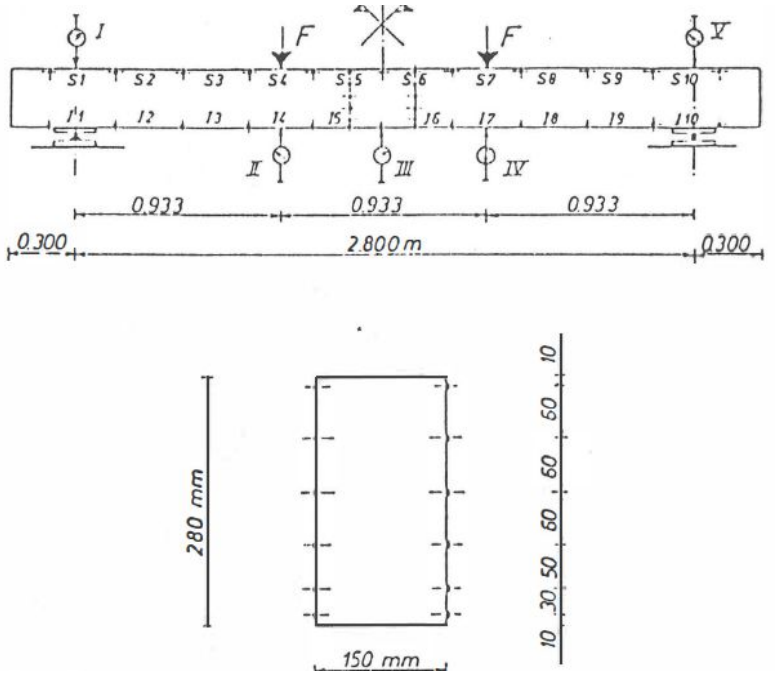

Figure B.3. Locations of the measuring points of reinforced beam type III (FKFO no. 547).

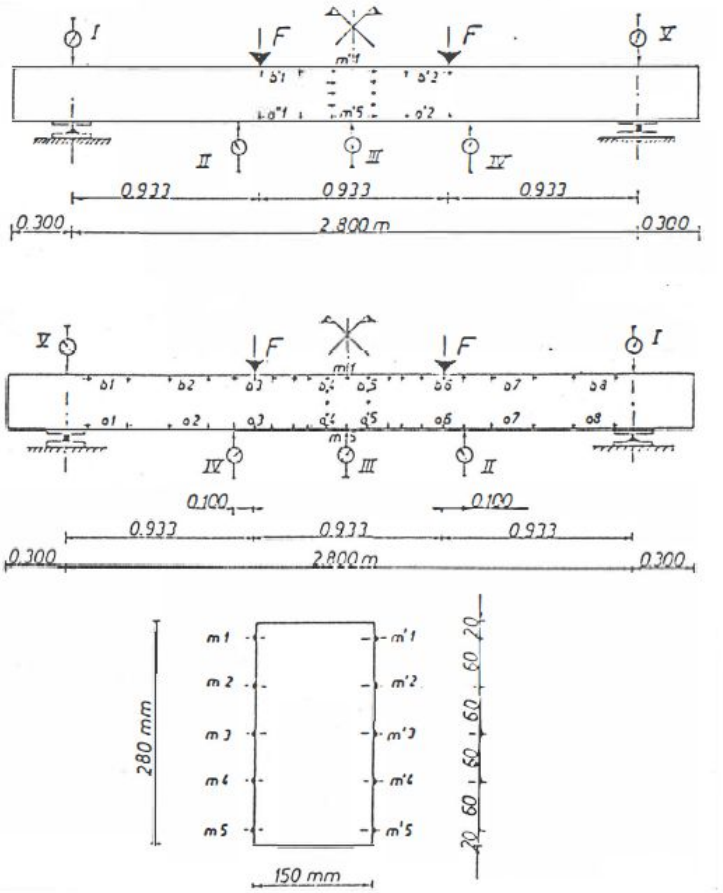

Figure B.4. Locations of the measuring points of reinforced beam type IV. The tope side view is the back of the beam, and the other side view is the front of the beam (FKFO no. 547).

Appendix C. Location of the measuring points of the strains and deflections of the prestressed beams

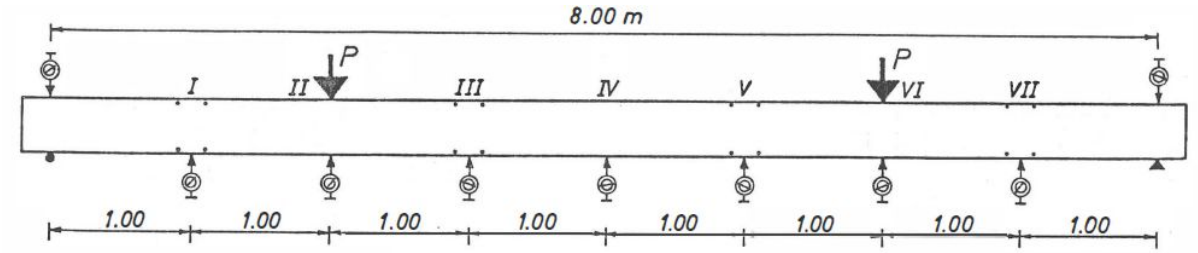

Figure C.1. Location of the dial gauges for the static tests on prestressed beams (FKFO no. 547).

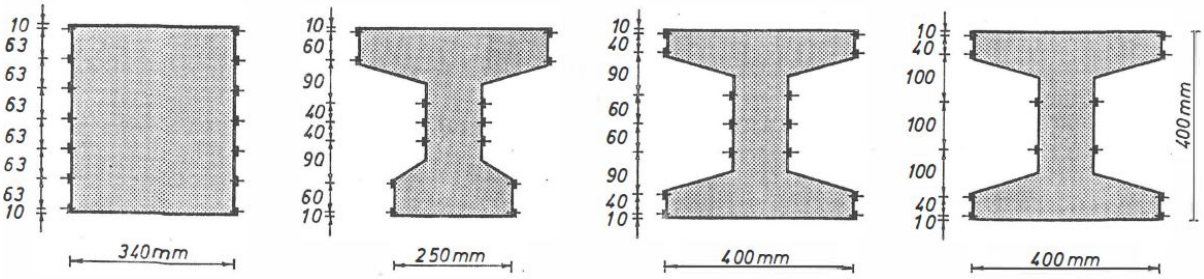

Figure C.2. Location of the deformation measurements in section II, IV, and VI (see Figure C.1). From left to right: rectangular beam type, T-shaped beam type, I-shaped beam type with post-tensioning, and I-shaped beam type with pre-tensioning.

Appendix D. Results of the long-term tests on prestressed beams

Table D.1. Results of the static tests after long-term loading of the beams with a rectangular cross-section.

	$M_{ser.,cal.}$ [kNm]	M_r [kNm]	$M_{u,t}$ [kNm]	$M_{u,t}/M_{ser.,cal.}$ [-]	$M_{u,t}/M_{u,o,m}$ [-]
R-LD-C-P14-Q31-100%	127.5	130	350	2.75	0.99
R-LD-C-P14-Q31- 50%	127.5	160	330	2.59	0.93
R-LD-C-P14- 0%	127.5	163	350	2.75	0.99
R-LD-C-P14-Q56-100%	127.5	130	370	2.90	1.05
R-LD-C-P14-Q56- 50%	127.5	-	360	2.82	1.02
R-LD-C-P45- 0%	127.5	163	360	2.82	1.02
Mean	127.5	149	353	2.77	1.00

Table D.2. . Results of the static tests after long-term loading of the beams with an I-shaped cross-section which are post-tensioned.

	$M_{ser.,cal.}$ [kNm]	M_r [kNm]	$M_{u,t}$ [kNm]	$M_{u,t}/M_{ser.,cal.}$ [-]	$M_{u,t}/M_{u,o,m}$ [-]
I-LD-C-P15-Q28-100%	125.6	165	292	2.32	0.90
I-LD-C-P15-Q28- 50%	125.6	145	324	2.58	1.00
I-LD-C-P14- 0%	125.6	165	324	2.66	1.03
I-LD-C-P14-Q56-100%	125.6	160	324	2.58	1.00
I-LD-C-P14-Q56- 50%	125.6	145	304	2.42	0.94
I-LD-C-P56- 0%	125.6	145	347	2.76	1.07
Mean	125.6	154	321	2.56	0.99

Table D.3. Results of the static tests after long-term loading of the beams with an I-shaped cross-section which are pre-tensioned.

	$M_{ser.,cal.}$ [kNm]	M_r [kNm]	$M_{u,t}$ [kNm]	$M_{u,t}/M_{ser.,cal.}$ [-]	$M_{u,t}/M_{u,o,m}$ [-]
I-LD-BS-P7-Q28-100%	109.8	-	324	2.95	0.96
I-LD-BS-P7-Q28- 50%	109.8	145	320	2.91	0.95
I-LD-BS-P7- 0%	109.8	130	316	2.88	0.94
I-LD-BS-P14-Q28-100%	109.8	-	320	2.91	0.95
I-LD-BS-P14-Q28- 50%	109.8	140	326	2.97	0.97
I-LD-BS-P14- 0%	109.8	140	317	2.89	0.94
Mean	109.8	136	321	2.92	0.95

Appendix E. Prediction of time-dependent behaviour of reinforced beams versus measurements

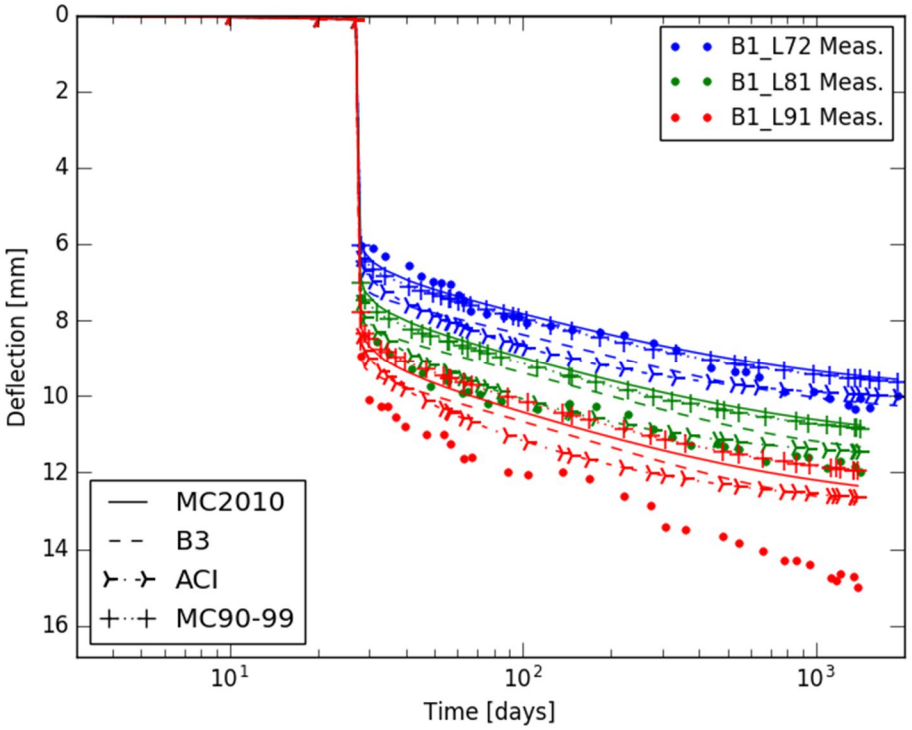

Figure E.1. Predictions and measurements of the deflection at midspan of the reinforced beams of type I (constant aging coefficient equal to 0.8 and no correction for nonlinear creep).

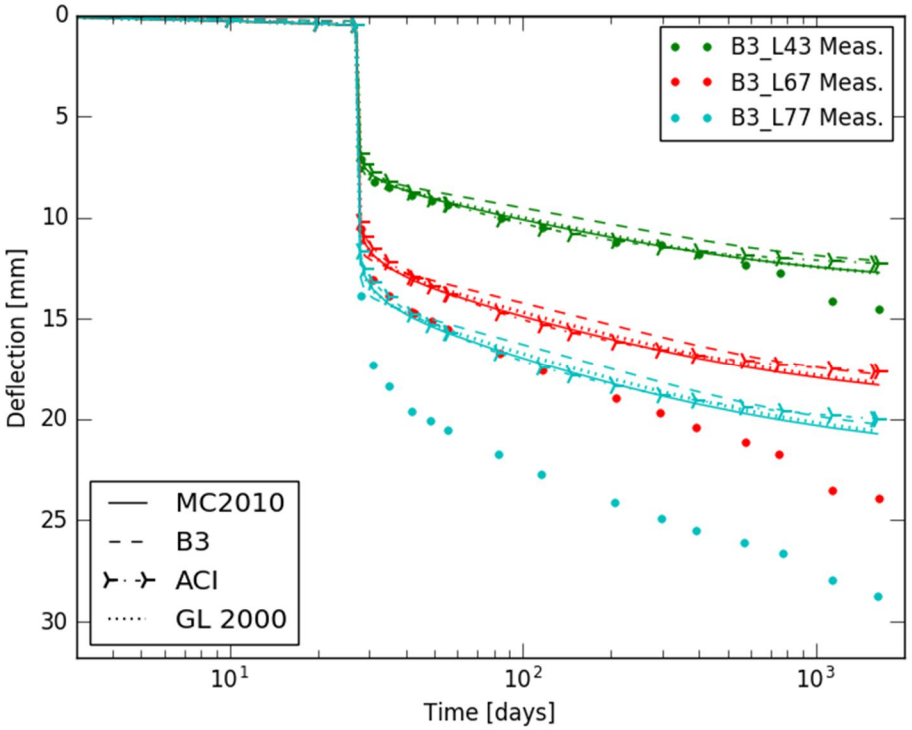

Figure E.2. Predictions and measurements of the deflection at midspan of the reinforced beams of type III (constant aging coefficient equal to 0.8 and no correction for nonlinear creep).

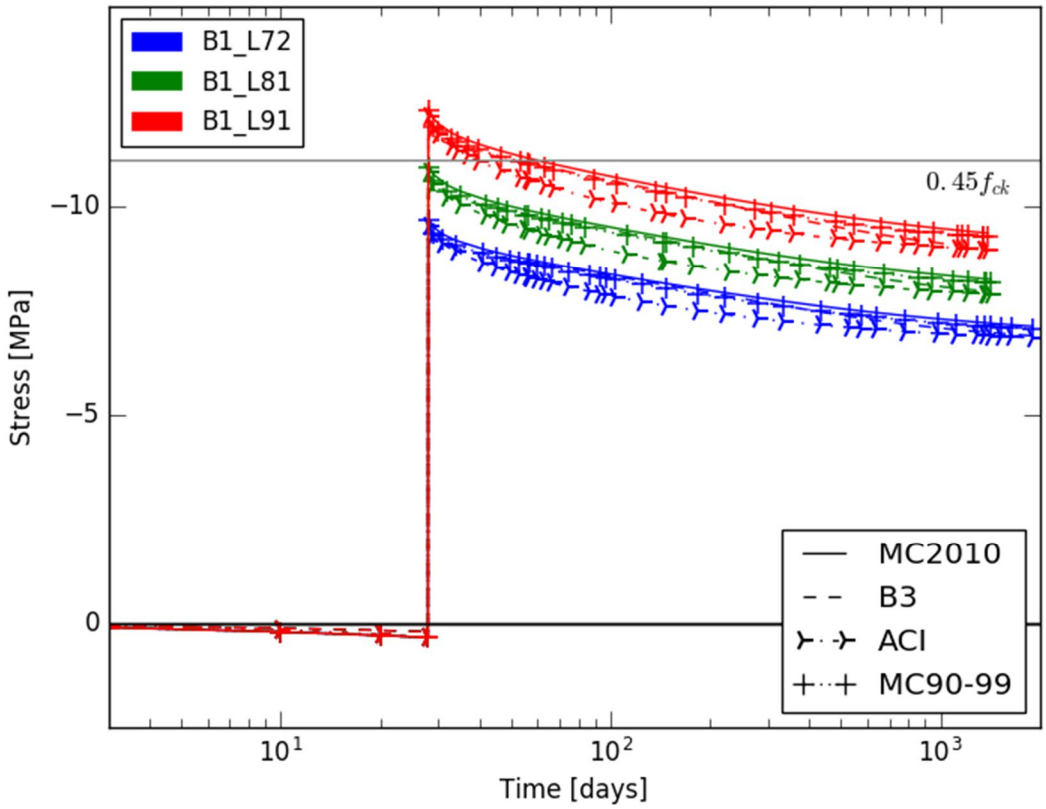

Figure E.3. Prediction of the stress at the top fibre at midspan of the reinforced beams of type I (constant aging coefficient equal to 0.8 and no correction for nonlinear creep).

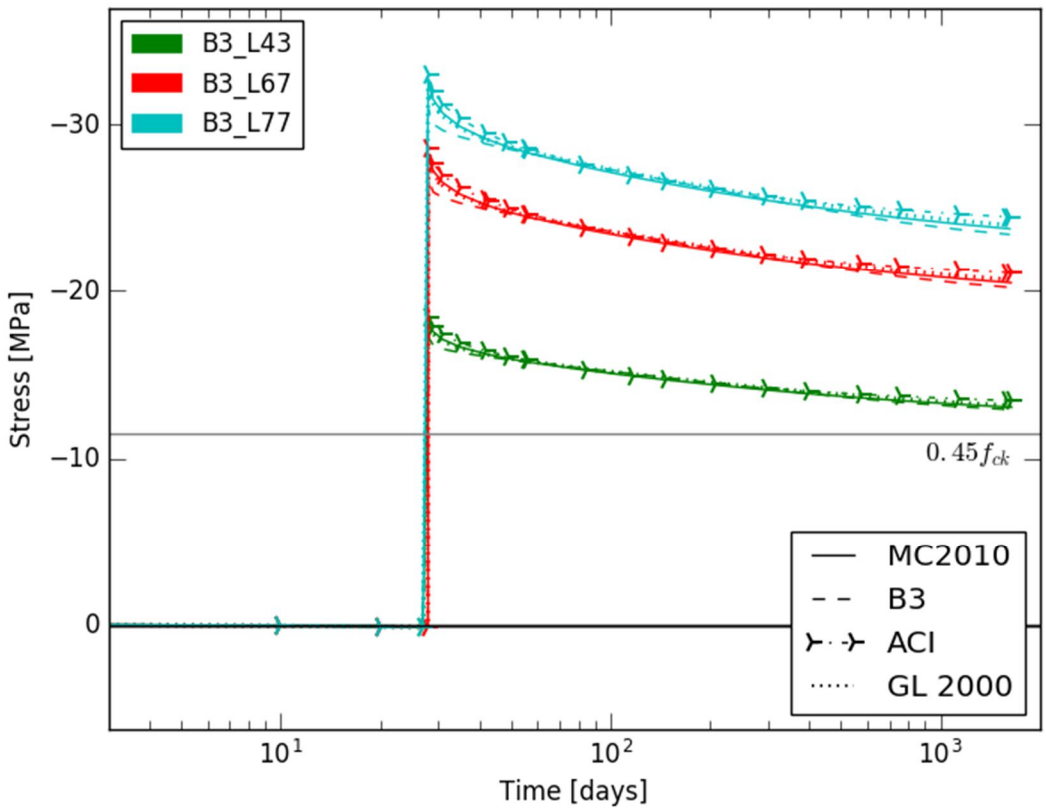

Figure E.4. Prediction of the stress at the top fibre at midspan of the reinforced beams of type III (constant aging coefficient equal to 0.8 and no correction for nonlinear creep).

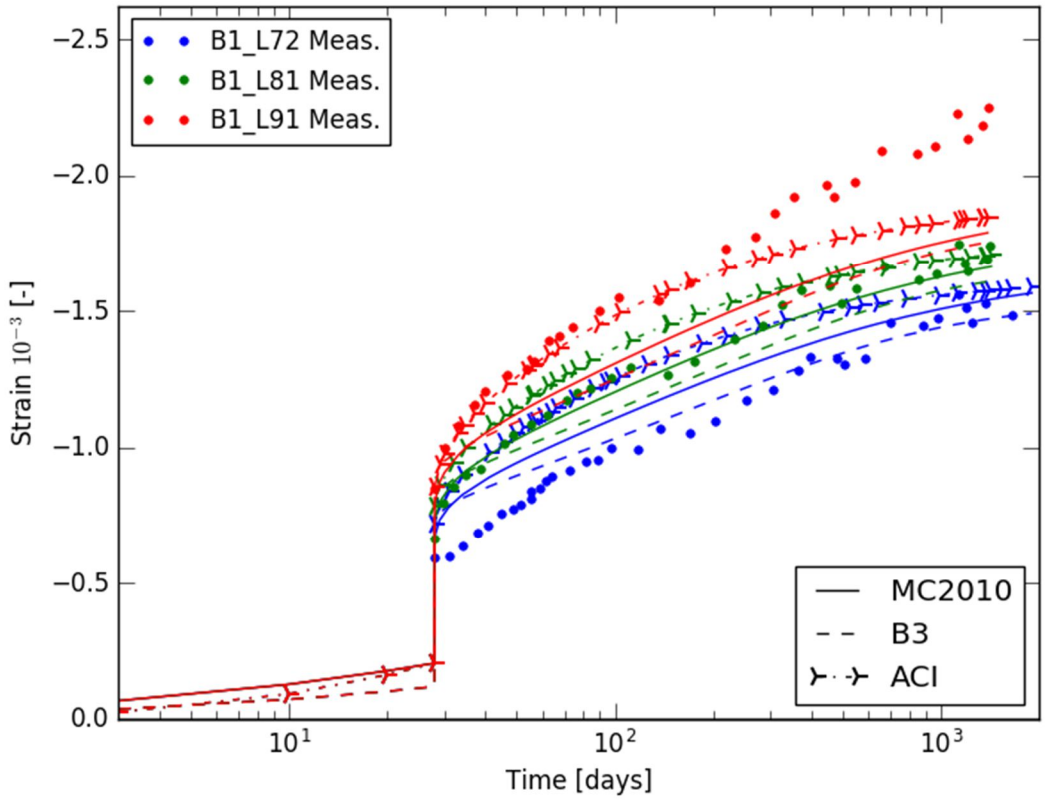

Figure E.5. Predictions and measurements of the strain near the top fibre at midspan of the reinforced beams of type I (constant aging coefficient equal to 0.8 and no correction for nonlinear creep).

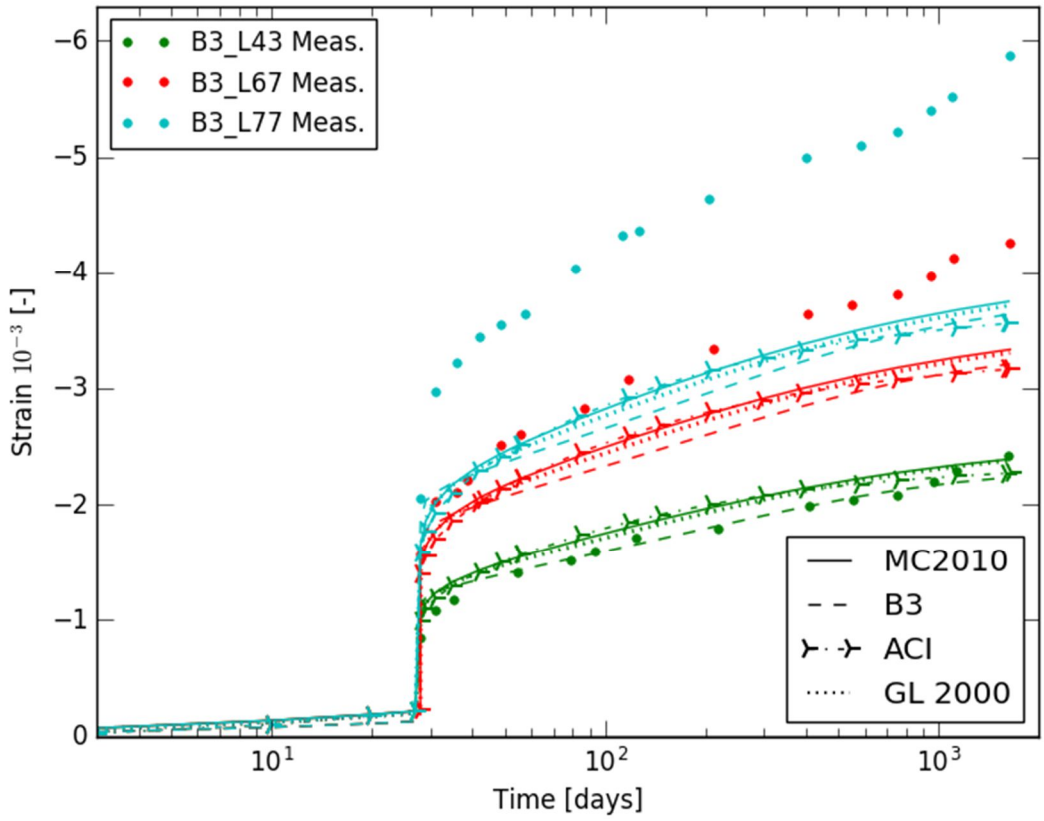

Figure E.6. Predictions and measurements of the strain near the top fibre at midspan of the reinforced beams of type III (constant aging coefficient equal to 0.8 and no correction for nonlinear creep).

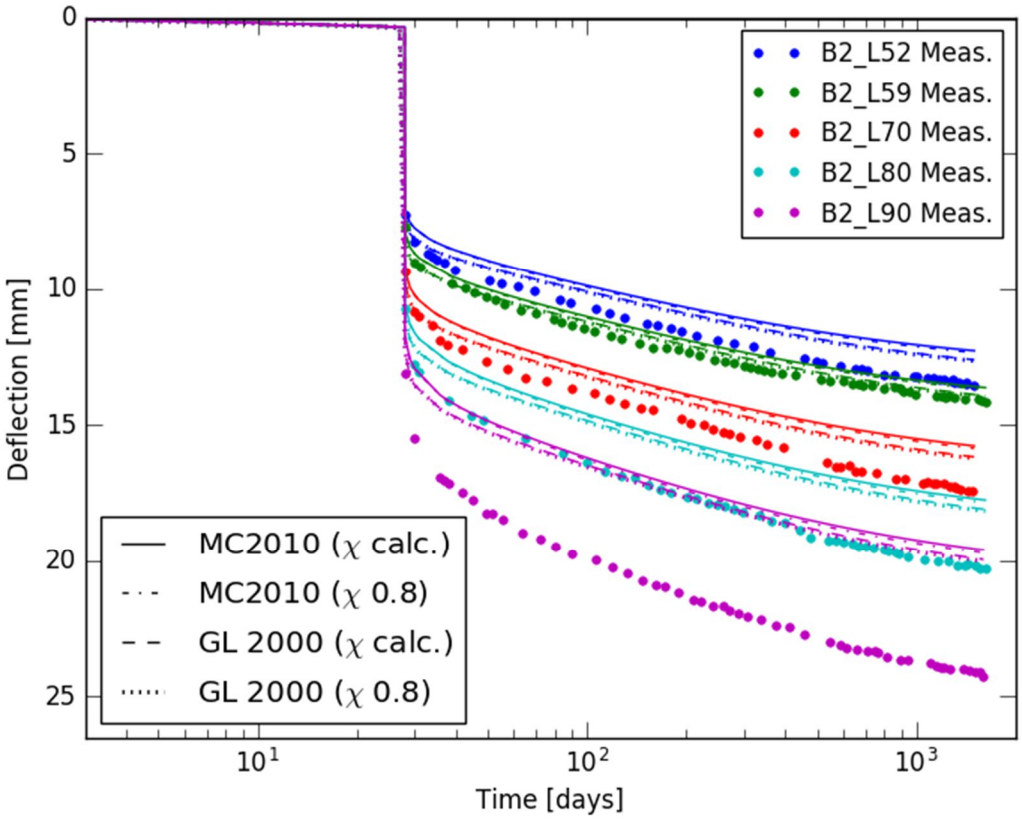

Figure E.7. Comparison of predicted values with a calculated aging coefficient against predicted values with a constant aging coefficient for beams of type II.

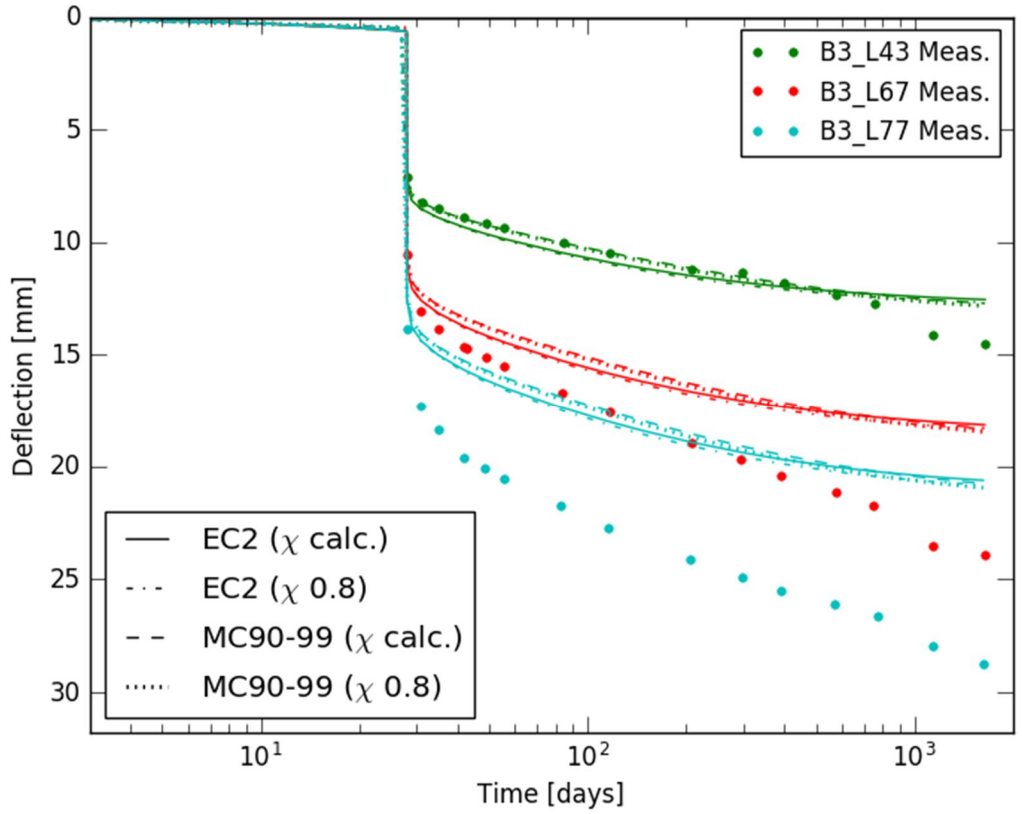

Figure E.8. Comparison of predicted values with a calculated aging coefficient against predicted values with a constant aging coefficient for beams of type III.

Appendix F. Prediction of time-dependent deflections of prestressed beams versus measurements

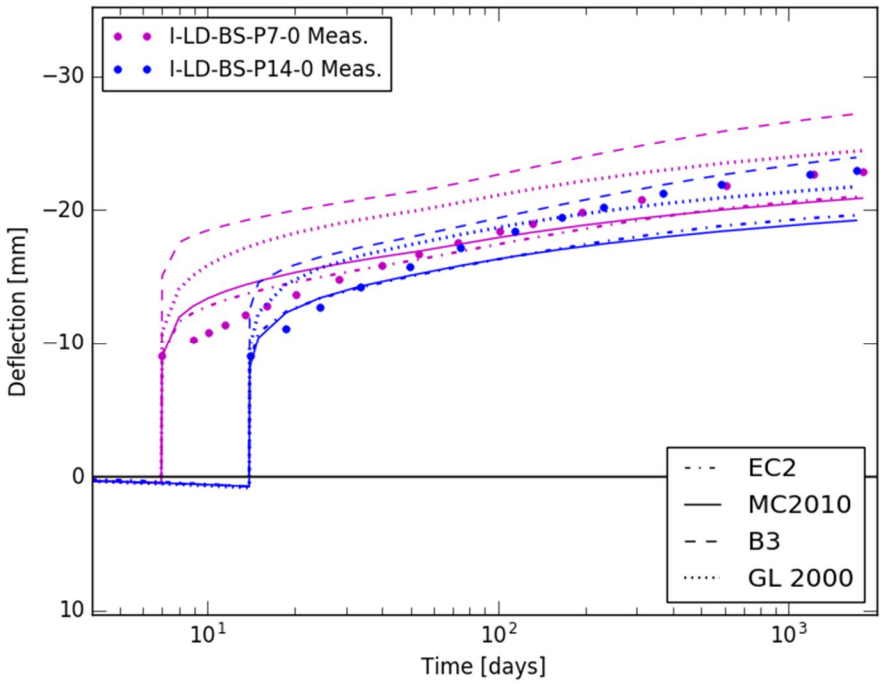

Figure F.1. Predictions and measurements of the deflection at midspan of the pre-tensioned I-shaped beams which are not loaded (constant aging coefficient equal to 0.8 and no correction for relaxation of prestress).

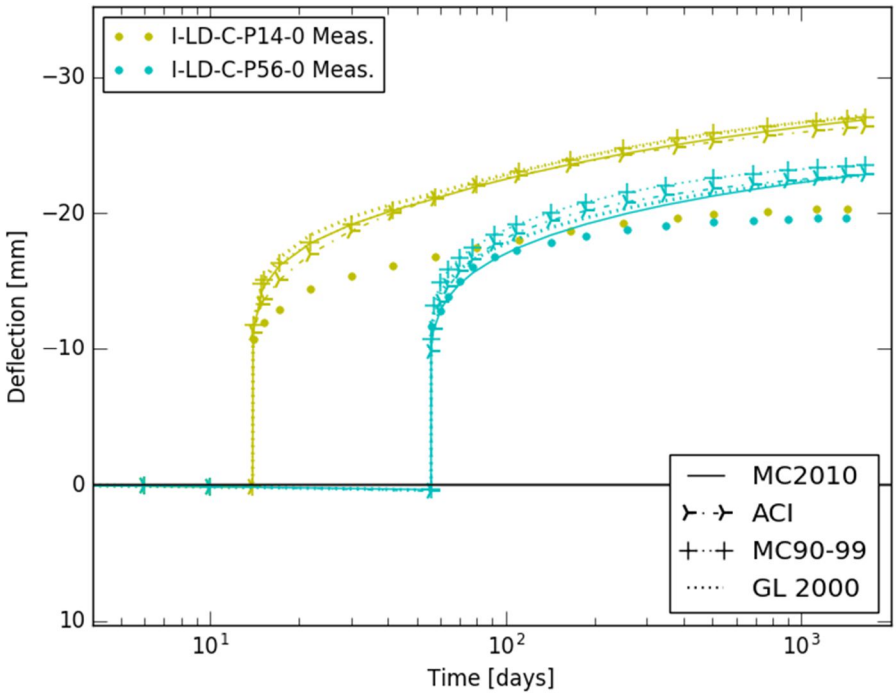

Figure F.2. Predictions and measurements of the deflection at midspan of the post-tensioned I-shaped beams which are not loaded (constant aging coefficient equal to 0.8 and no correction for relaxation of prestress).

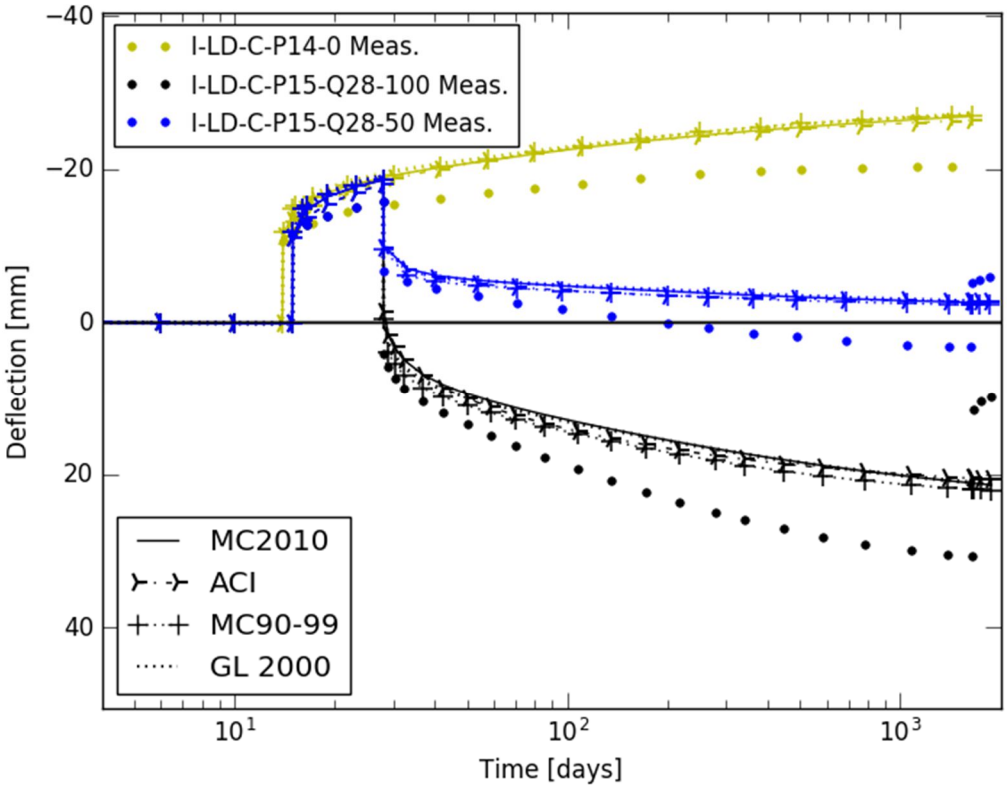

Figure F.3. Predictions and measurements of the deflection at midspan of the post-tensioned I--shaped beams loaded at 28 days (constant aging coefficient equal to 0.8 and no correction for relaxation of prestress).

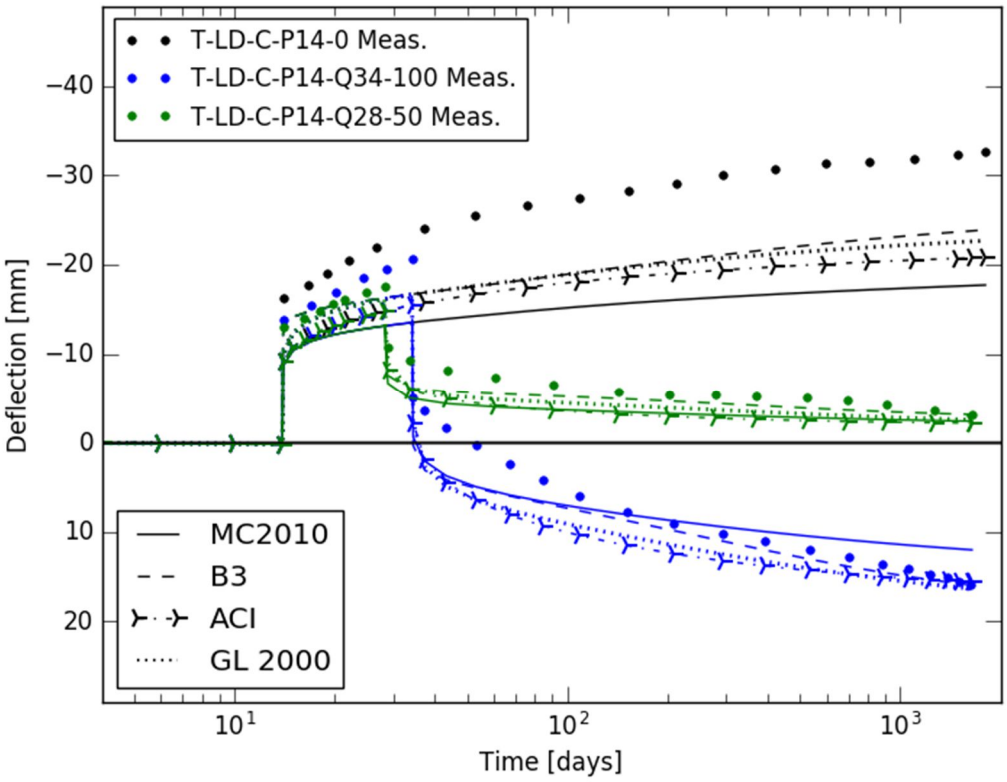

Figure F.4. Predictions and measurements of the deflection at midspan of the post-tensioned T-shaped beams loaded at 28/34 days (constant aging coefficient equal to 0.8 and no correction for relaxation of prestress).

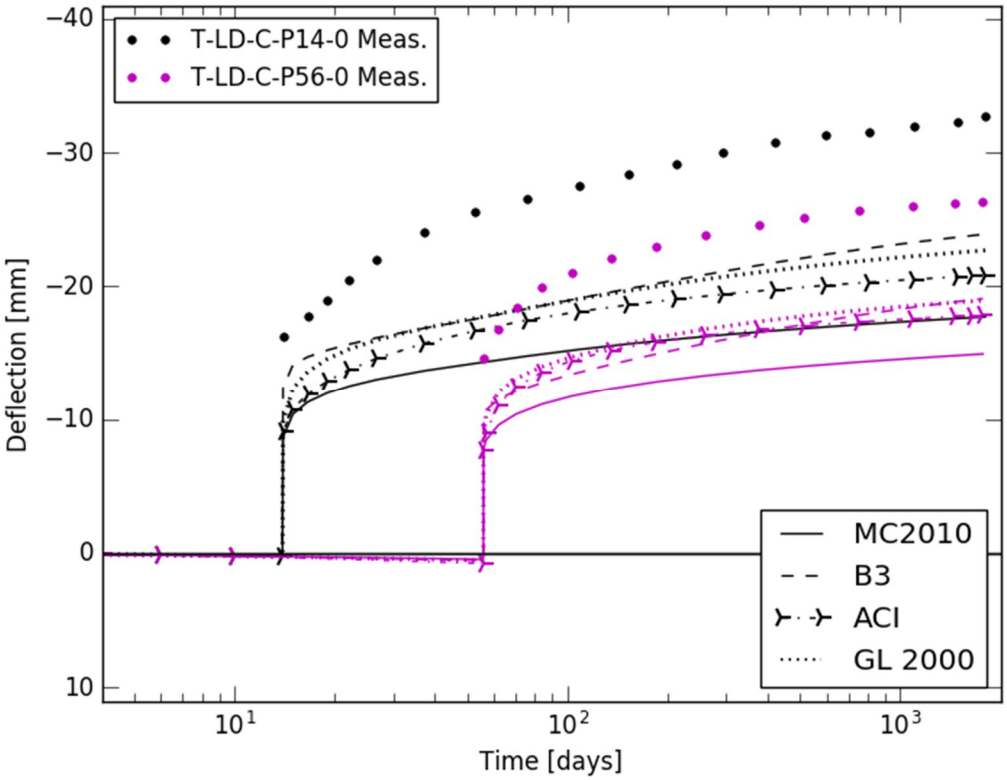

Figure F.5. Predictions and measurements of the deflection at midspan of the post-tensioned T-shaped beams which are not loaded (constant aging coefficient equal to 0.8 and no correction for relaxation of prestress).

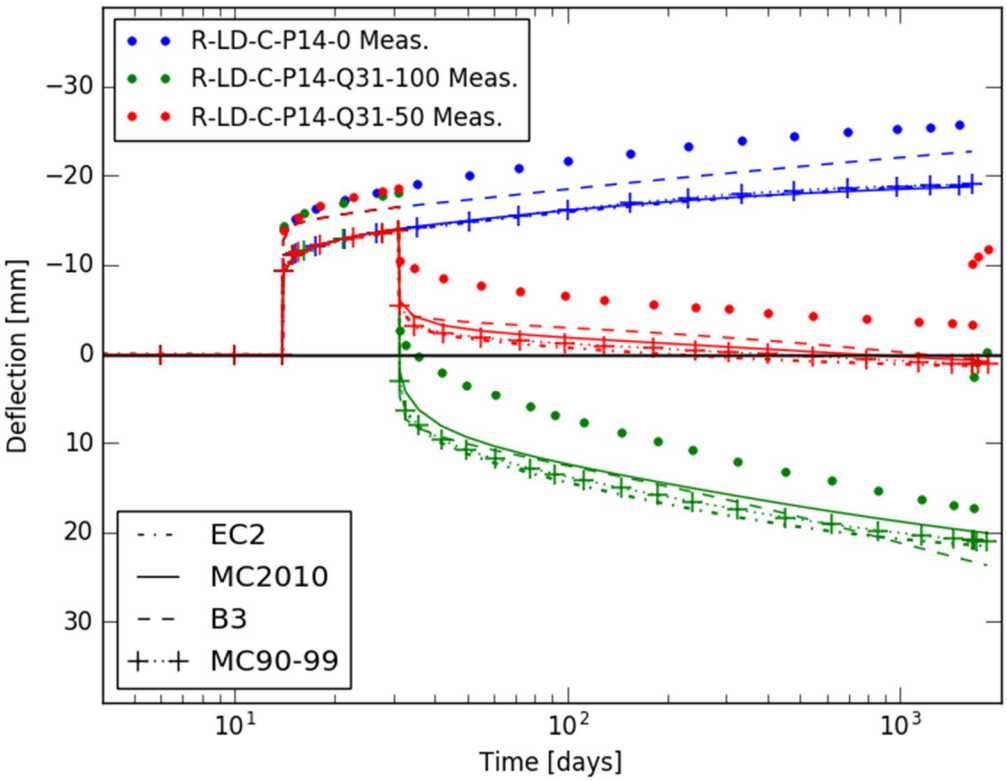

Figure F.6. Predictions and measurements of the deflection at midspan of the post-tensioned R-shaped beams loaded at 31 days (constant aging coefficient equal to 0.8 and no correction for relaxation of prestress).

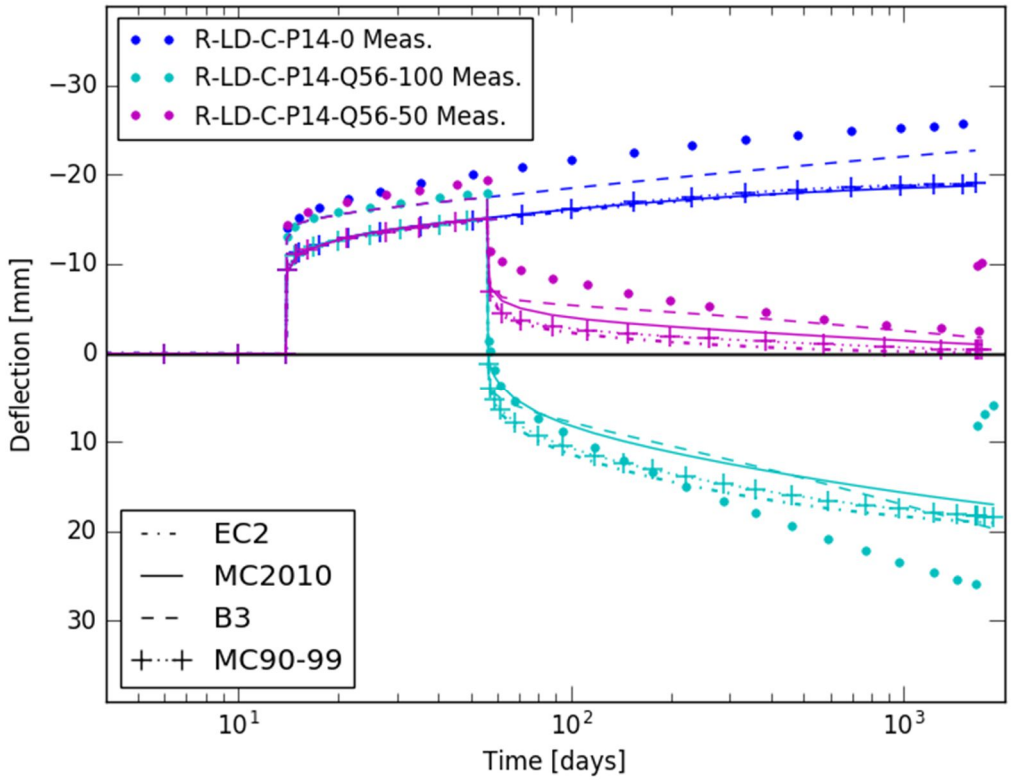

Figure F.7. Predictions and measurements of the deflection at midspan of the post-tensioned R-shaped beams loaded at 56 days (constant aging coefficient equal to 0.8 and no correction for relaxation of prestress).

Appendix G. Prediction of time-dependent stresses of the prestressed beams

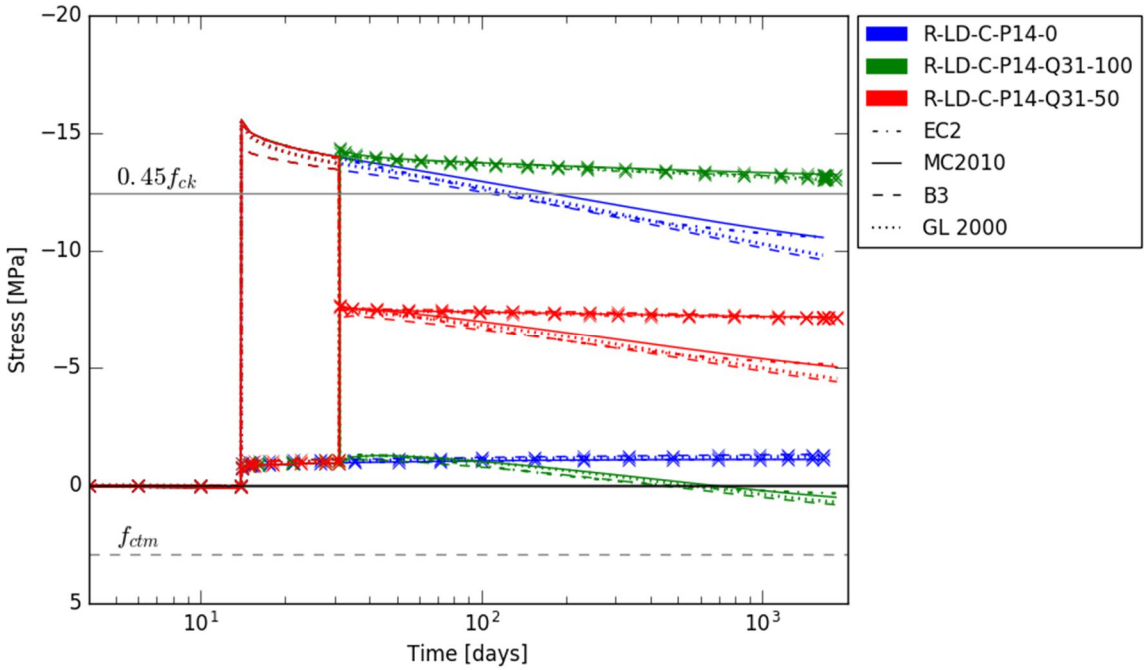

Figure G.1. Prediction of the stress at the bottom fibre and the top fibre (marked by an x) at midspan of the post-tensioned rectangular beams loaded at 31 days (constant aging coefficient equal to 0.8 and no correction for relaxation of prestress).

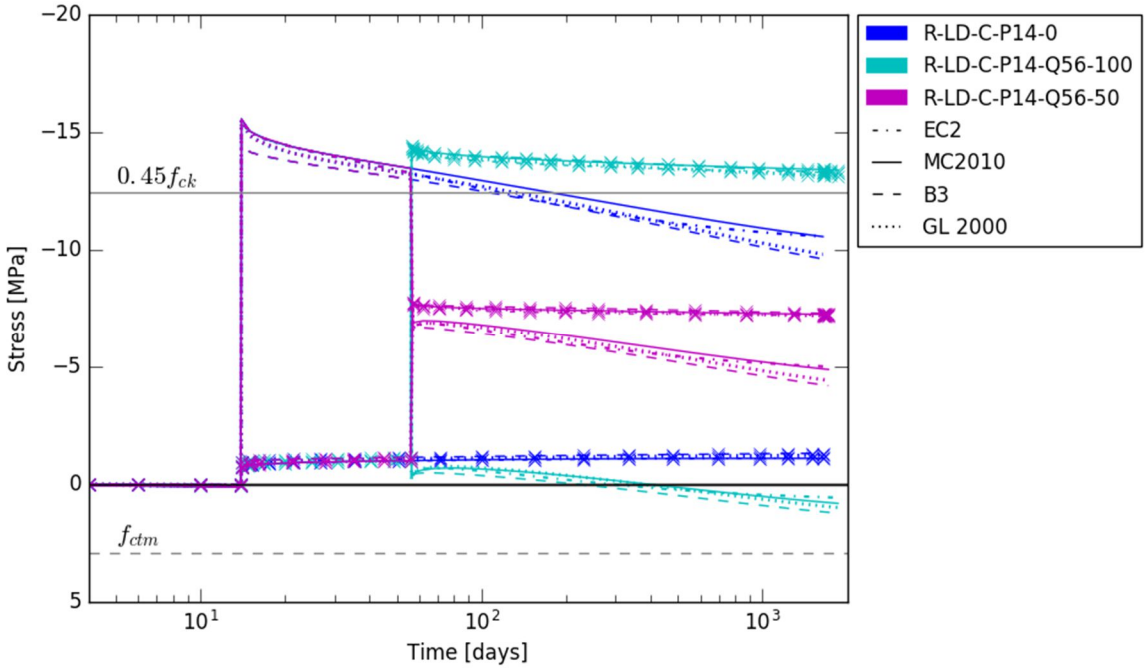

Figure G.2. Prediction of the stress at the bottom fibre and the top fibre (marked by an x) at midspan of the post-tensioned rectangular beams loaded at 56 days (constant aging coefficient equal to 0.8 and no correction for relaxation of prestress).

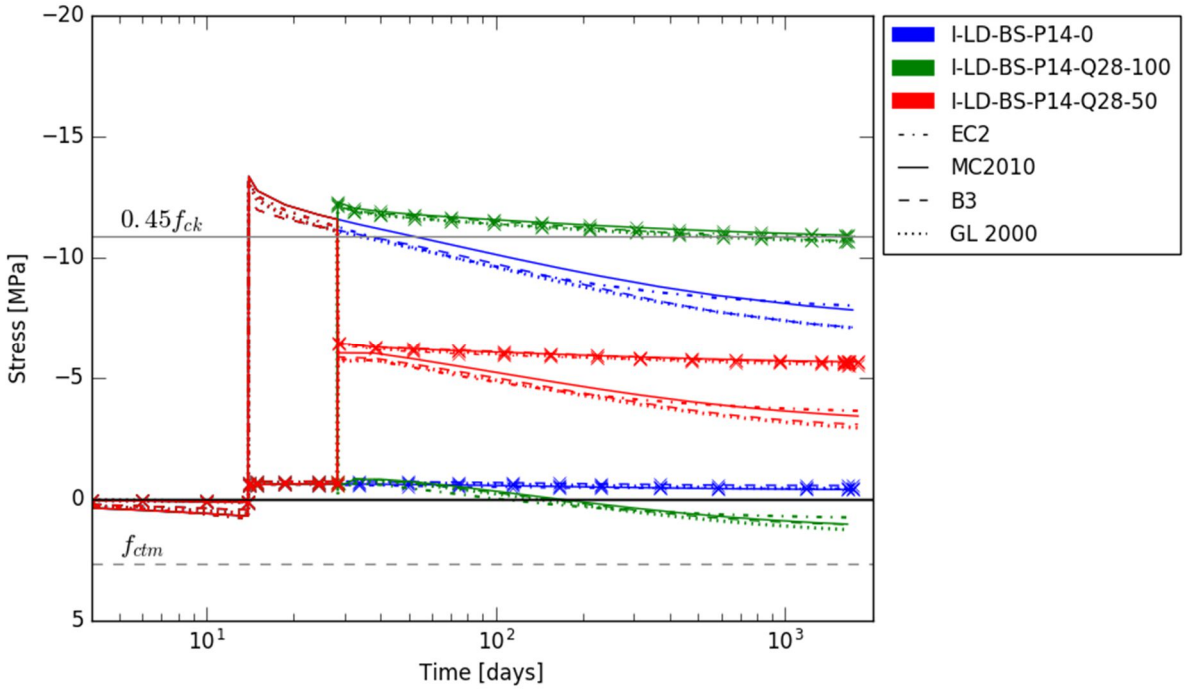

Figure G.3. Prediction of the stress at the bottom fibre and the top fibre (marked by an x) at midspan of the pre-tensioned I-shaped beams prestressed at 14 days (constant aging coefficient equal to 0.8 and no correction for relaxation of prestress).

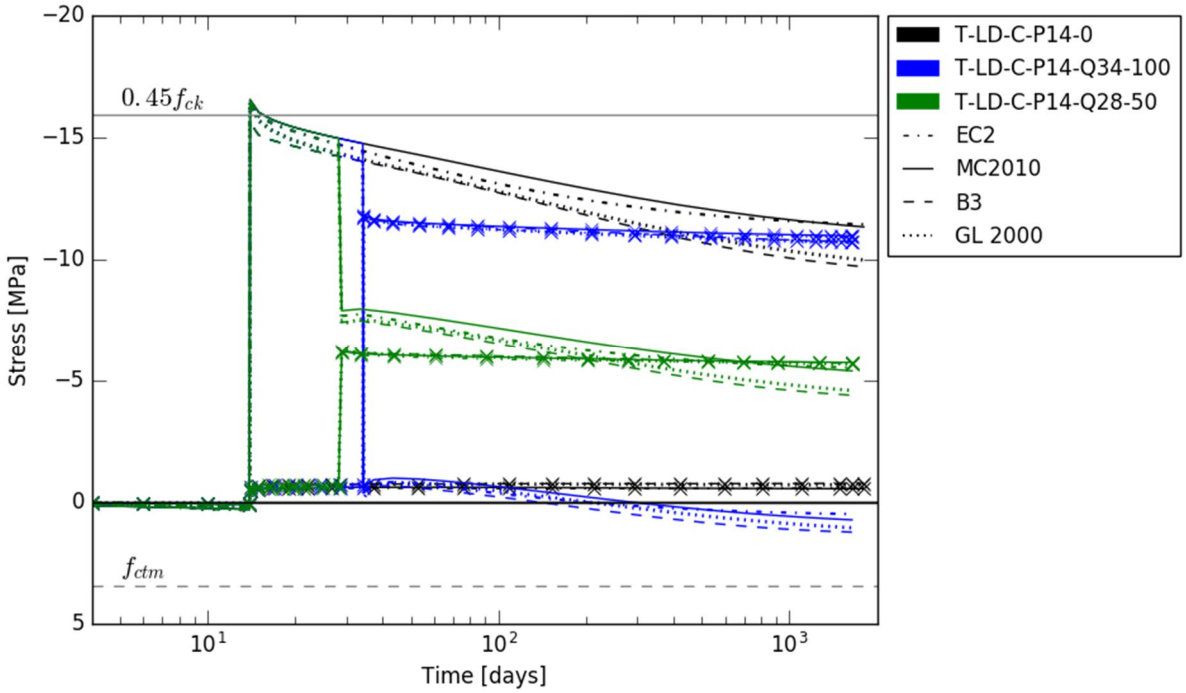

Figure G.4. Prediction of the stress at the bottom fibre and the top fibre (marked by an x) at midspan of the post-tensioned T-shaped beams loaded at 28/34 days (constant aging coefficient equal to 0.8 and no correction for relaxation of prestress).

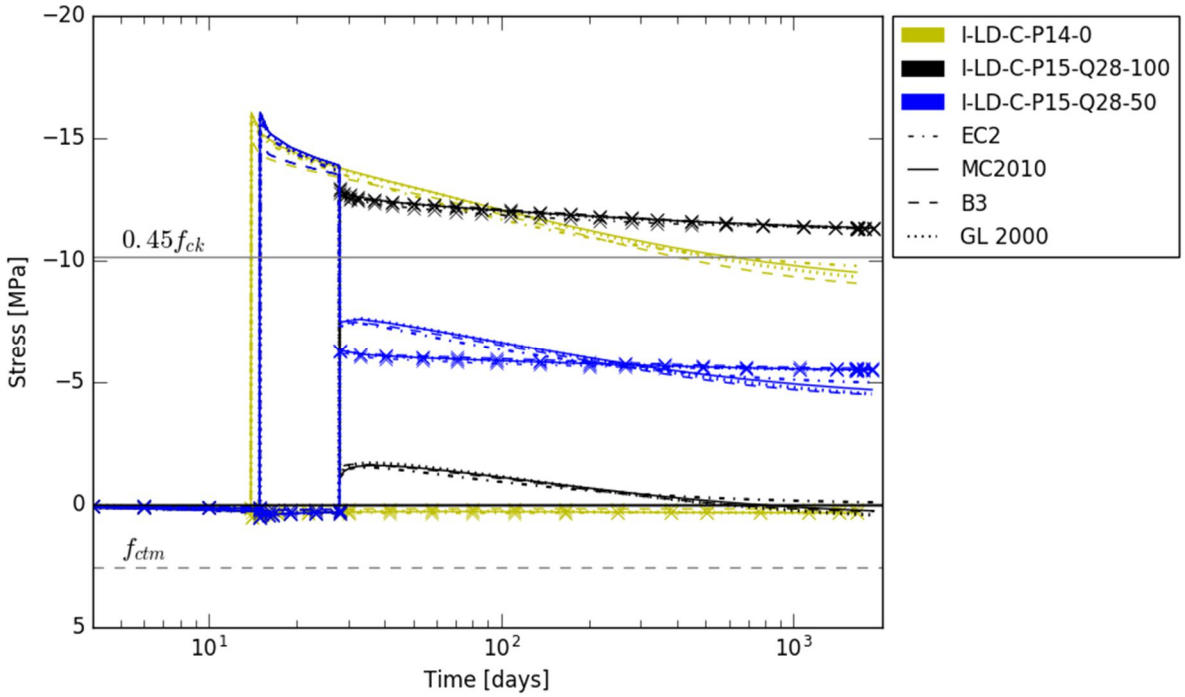

Figure G.5. Prediction of the stress at the bottom fibre and the top fibre (marked by an x) at midspan of the post-tensioned I-shaped beams loaded at 28 days (constant aging coefficient equal to 0.8 and no correction for relaxation of prestress).

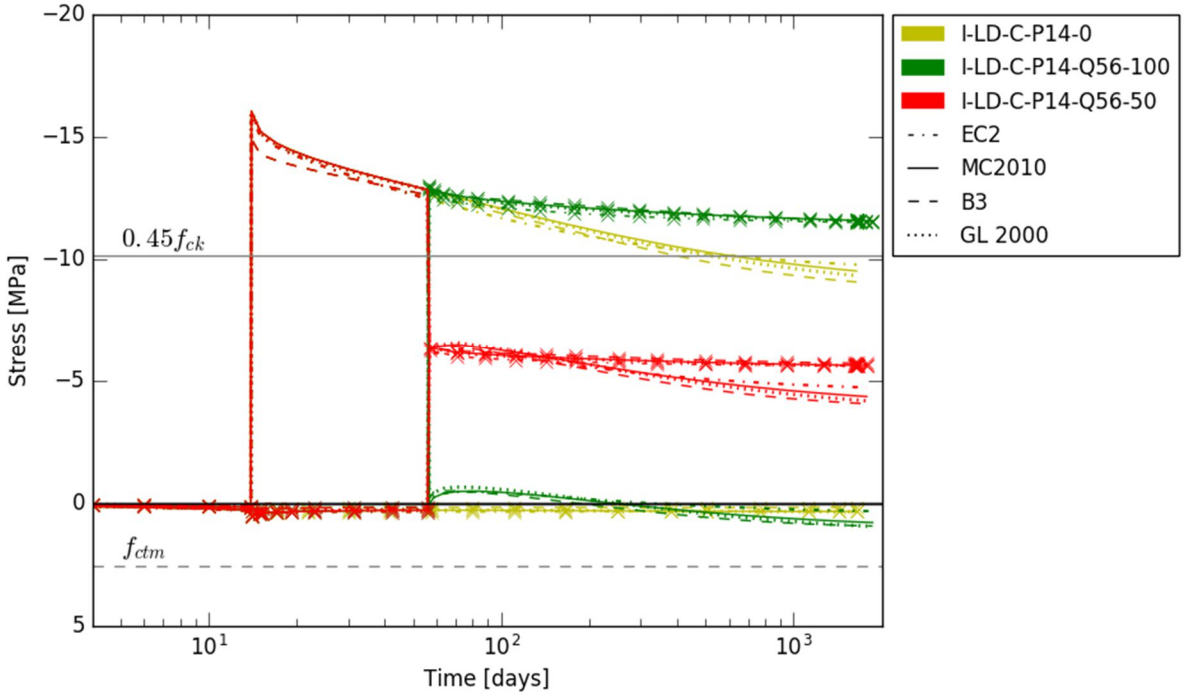

Figure G.6. Prediction of the stress at the bottom fibre and the top fibre (marked by an x) at midspan of the post-tensioned I-shaped beams loaded at 56 days (constant aging coefficient equal to 0.8 and no correction for relaxation of prestress).

Appendix H. Prediction of time-dependent strains near the top fibre of the prestressed beams

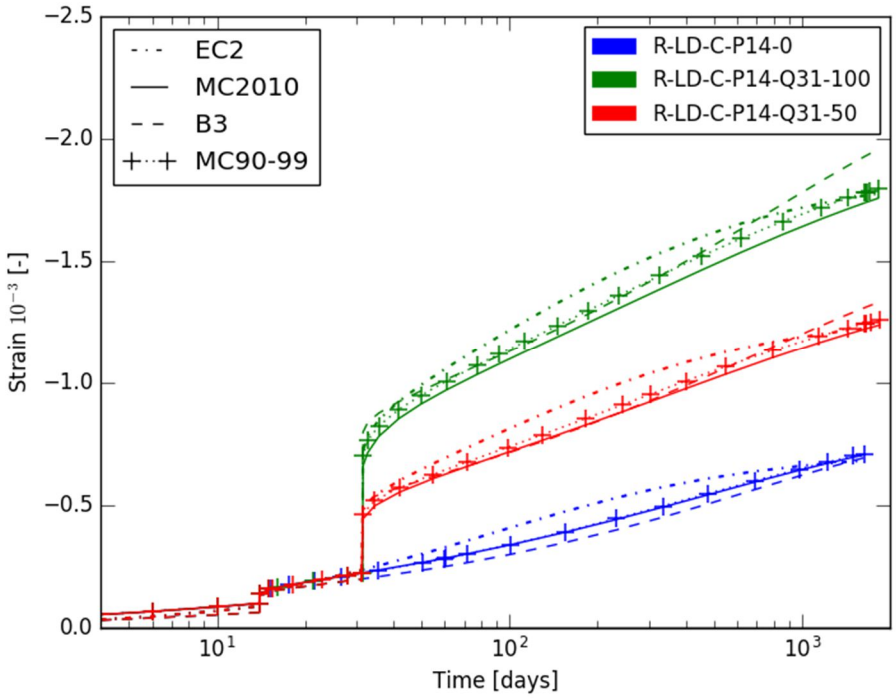

Figure H.1. Predictions of the strain near the top fibre at midspan of the post-tensioned rectangular beams loaded at 31 days (constant aging coefficient equal to 0.8 and no correction for relaxation of prestress).

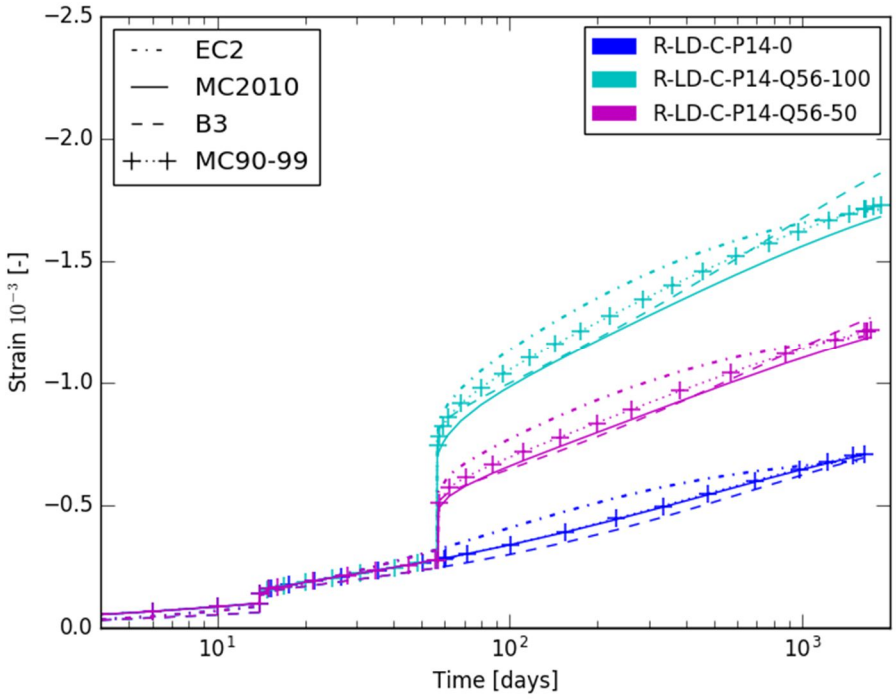

Figure H.2. Predictions of the strain near the top fibre at midspan of the post-tensioned rectangular beams loaded at 56 days (constant aging coefficient equal to 0.8 and no correction for relaxation of prestress).

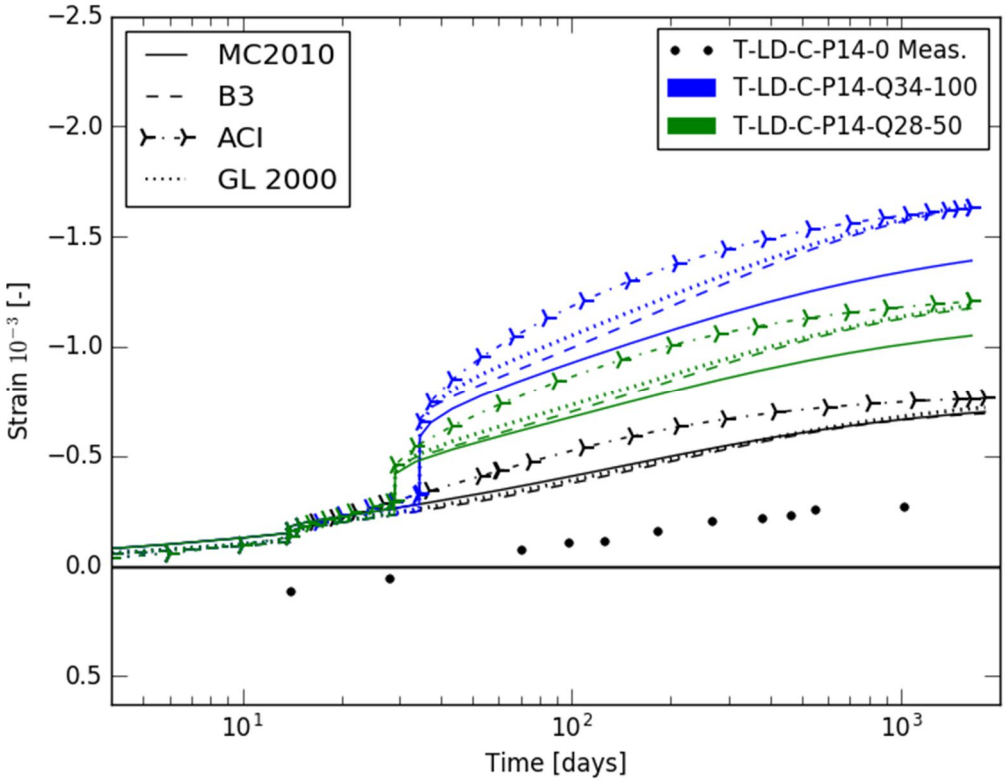

Figure H.3. Predictions of the strain near the top fibre at midspan of the post-tensioned T-shaped beams loaded at 28/34 days (constant aging coefficient equal to 0.8 and no correction for relaxation of prestress).

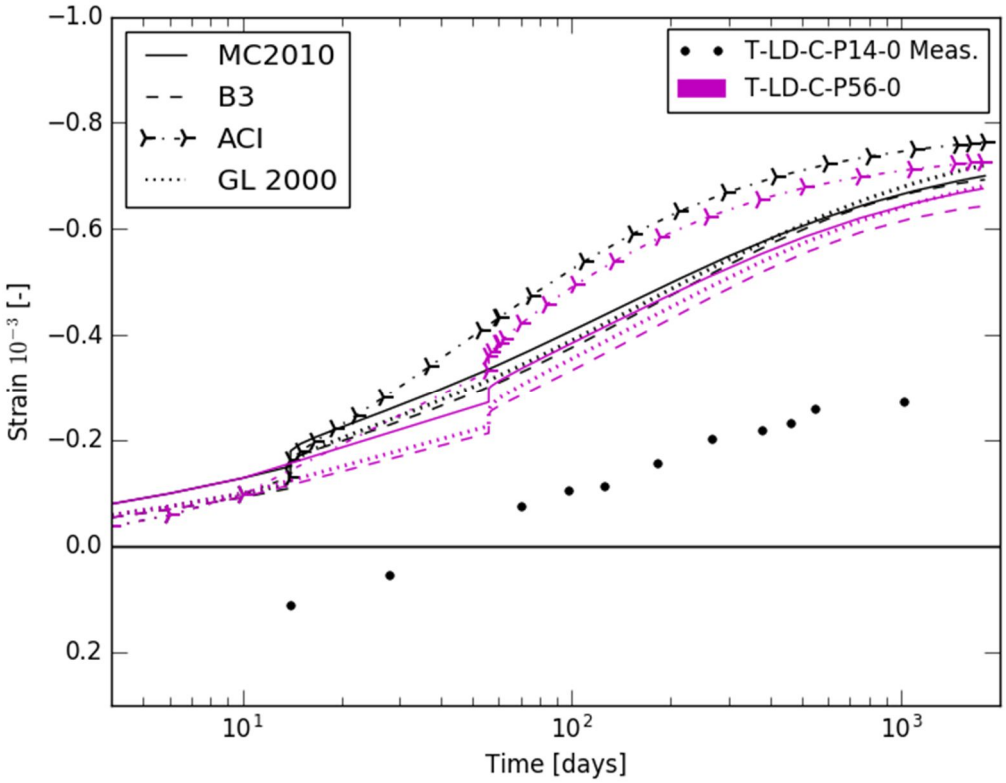

Figure H.4. Predictions of the strain near the top fibre at midspan of the unloaded post-tensioned T-shaped beams (constant aging coefficient equal to 0.8 and no correction for relaxation of prestress).

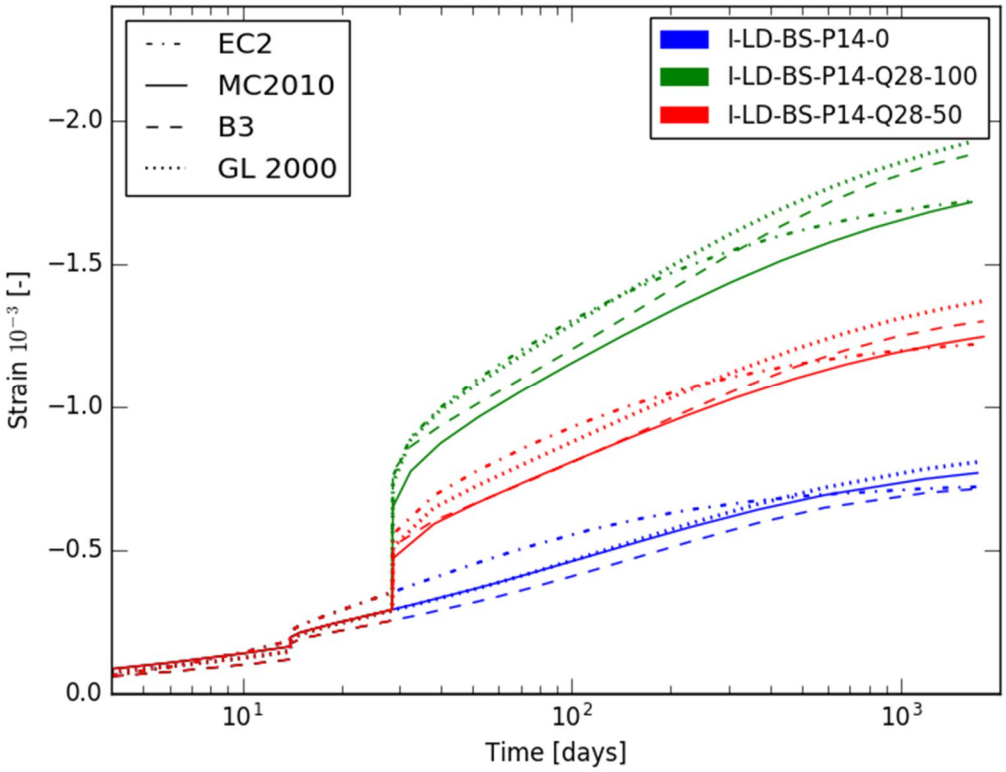

Figure H.5. Predictions of the strain near the top fibre at midspan of the I-shaped beams pre-tensioned at 14 days (constant aging coefficient equal to 0.8 and no correction for relaxation of prestress).

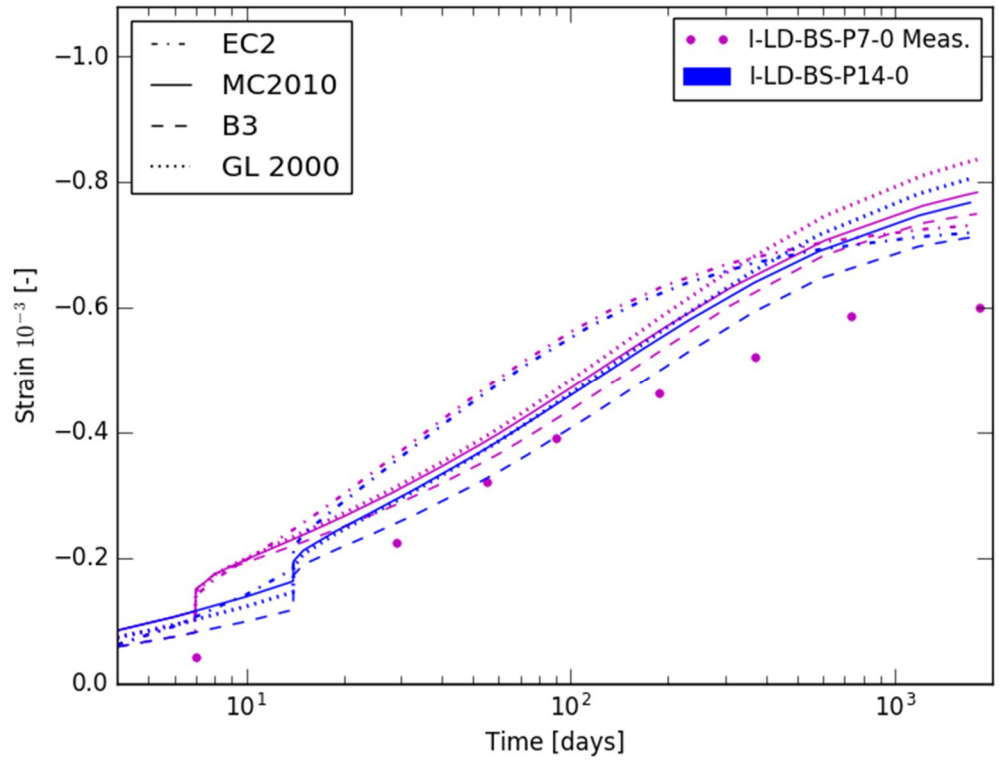

Figure H.6. Predictions of the strain near the top fibre at midspan of the unloaded pre-tensioned I shaped beams (constant aging coefficient equal to 0.8 and no correction for relaxation of prestress).

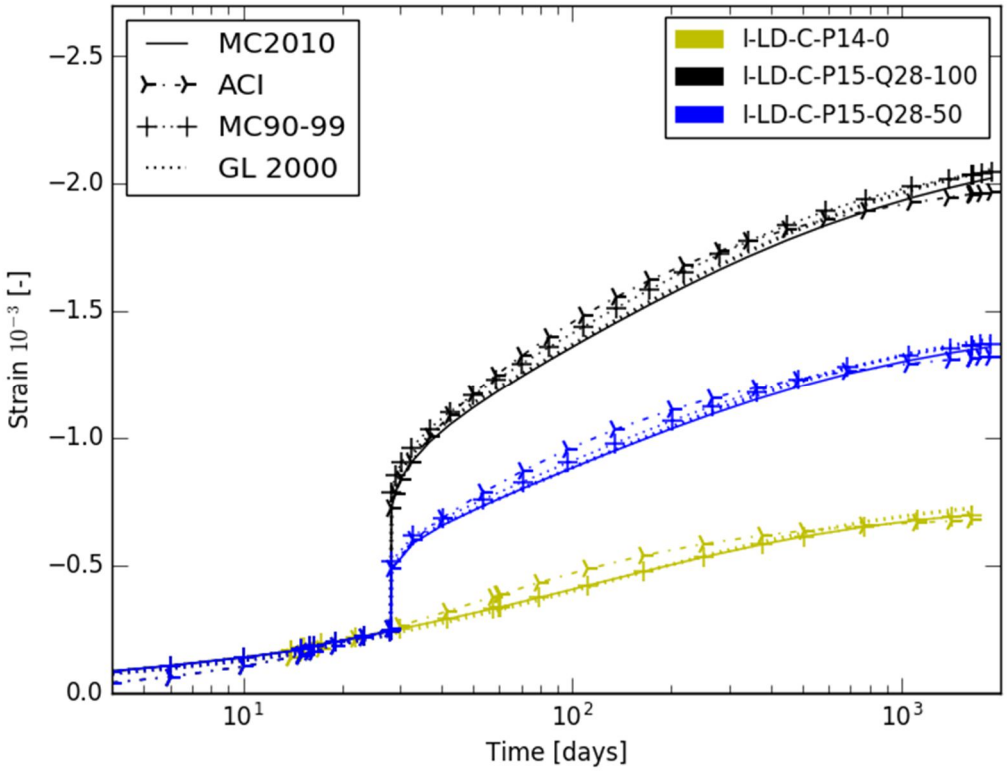

Figure H.7. Predictions of the strain near the top fibre at midspan of the post-tensioned I-shaped beams loaded at 28 days (constant aging coefficient equal to 0.8 and no correction for relaxation of prestress).

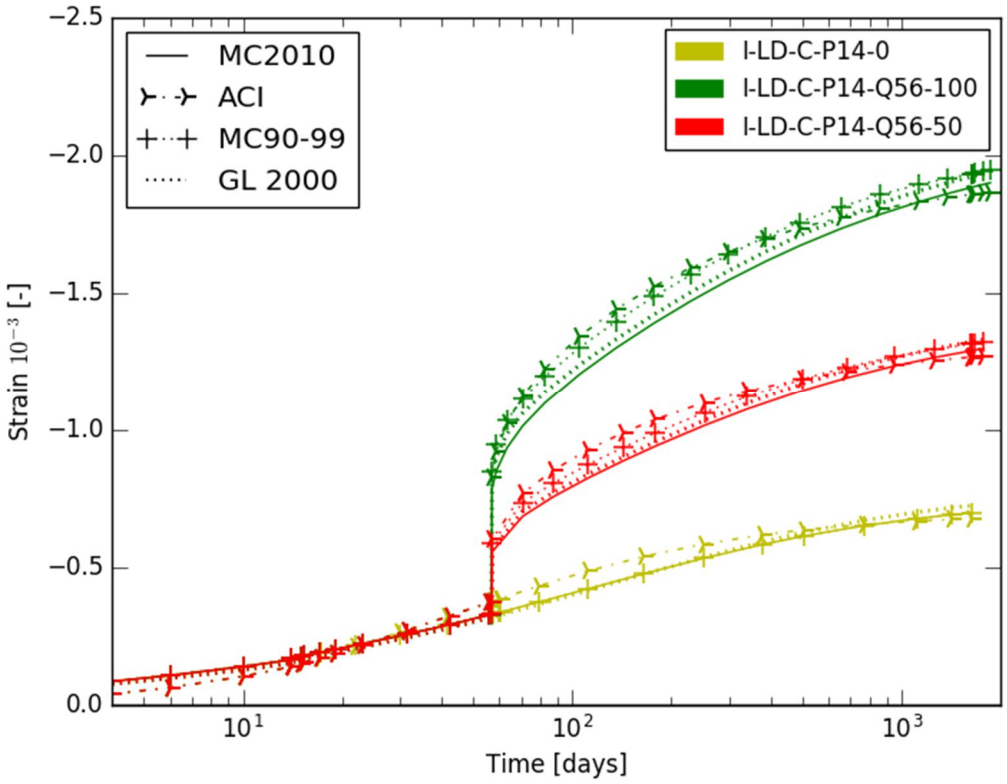

Figure H.8. Predictions of the strain near the top fibre at midspan of the post-tensioned I-shaped beams loaded at 56 days (constant aging coefficient equal to 0.8 and no correction for relaxation of prestress).

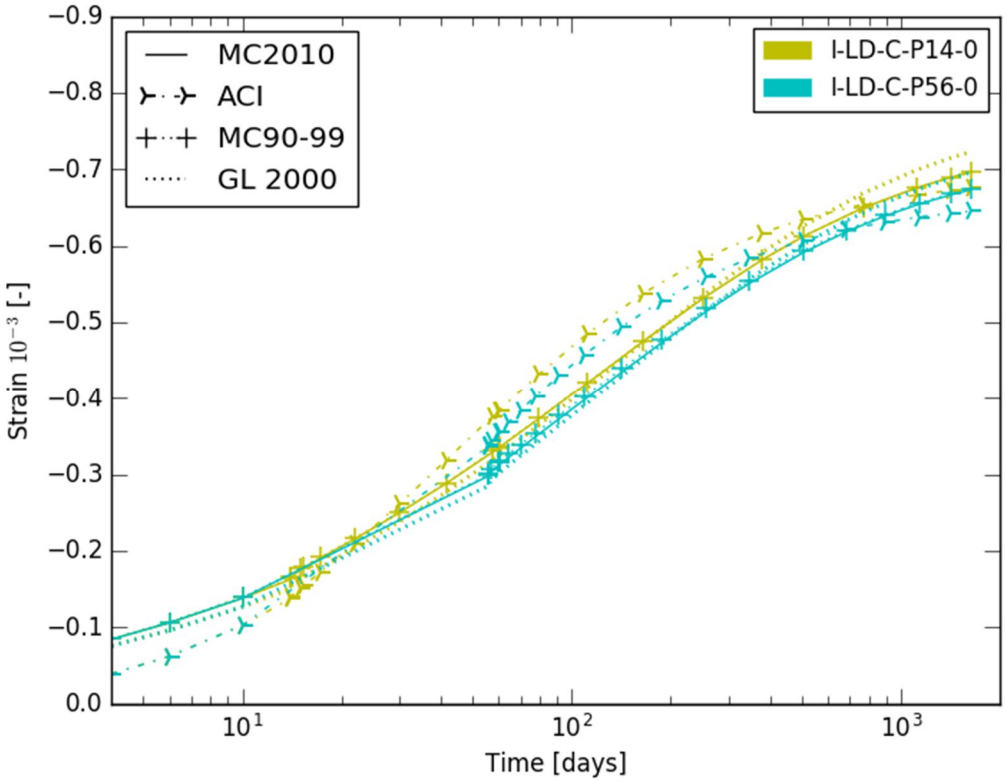

Figure H.9. Predictions of the strain near the top fibre at midspan of the unloaded post-tensioned I-shaped beams (constant aging coefficient equal to 0.8 and no correction for relaxation of prestress).

Appendix I. Prediction of time-dependent deformations of prestressed beams vs measurements

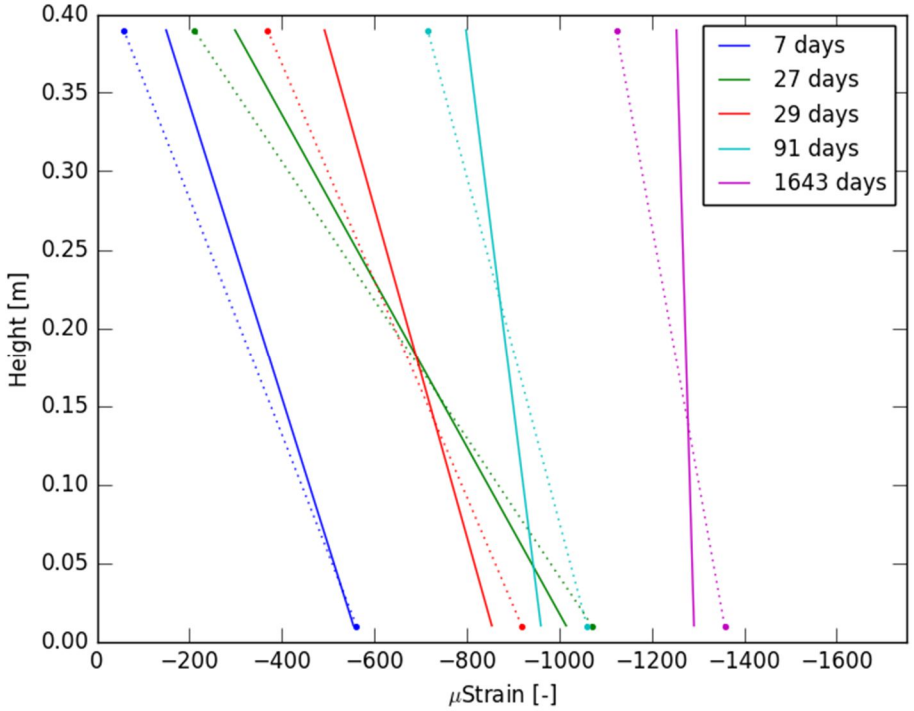

Figure I.1. Predictions (MC2010) and measurements of the deformation at midspan of the I-shaped beam pre-tensioned at 7 days and loaded at 50% at 28 days (constant aging coefficient equal to 0.8 and no correction for nonlinear creep).

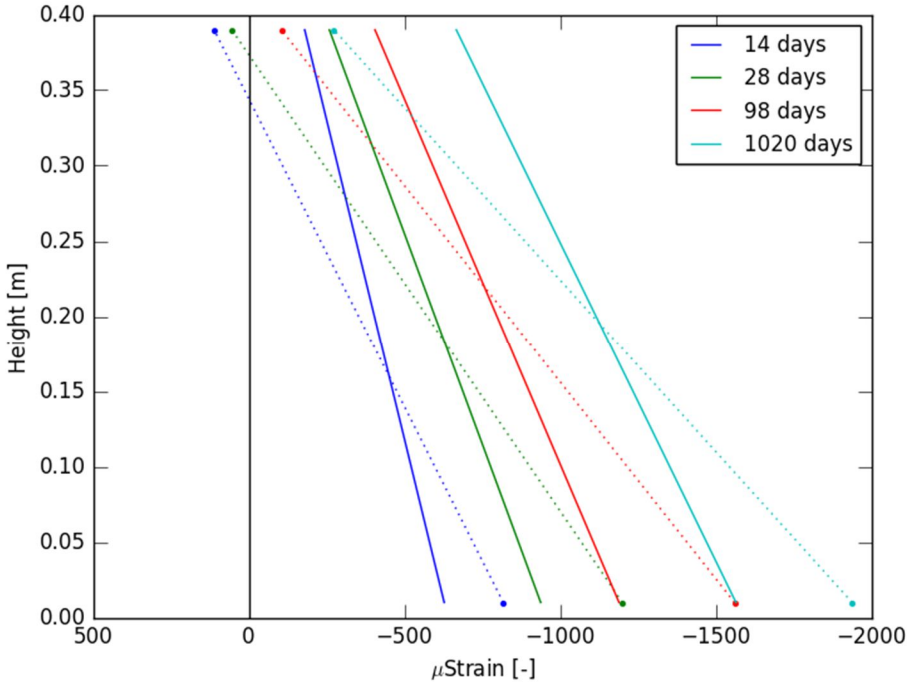

Figure I.2. Predictions (MC2010) and measurements of the deformation at midspan of the unloaded T-shaped beam pre-tensioned at 14 days (constant aging coefficient equal to 0.8 and no correction for nonlinear creep).

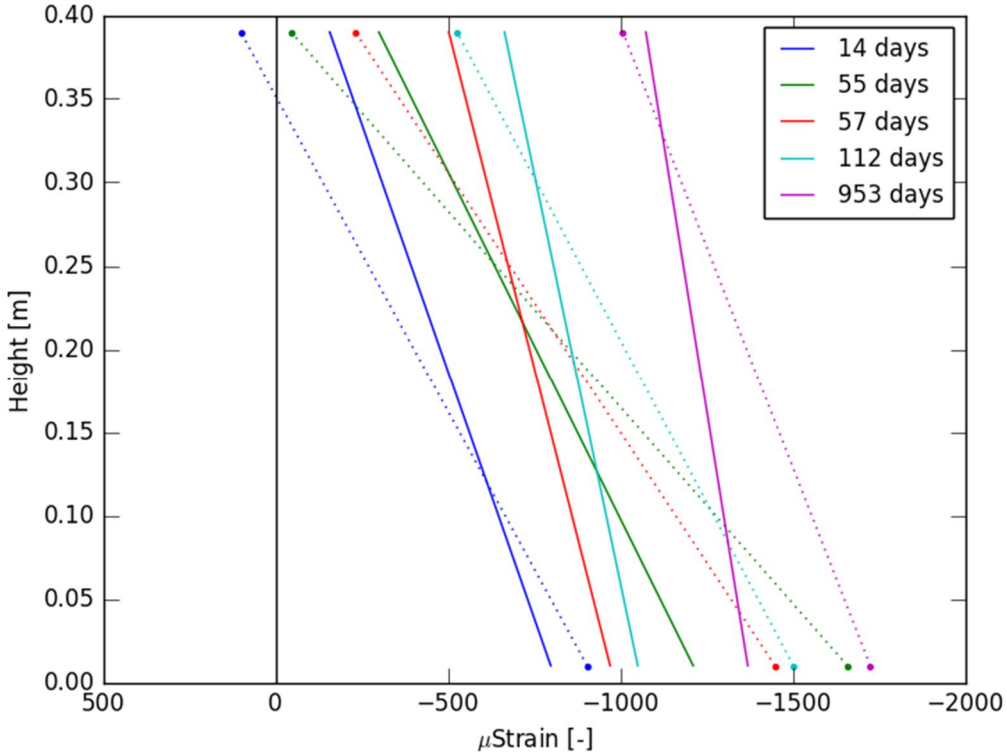

Figure I.3. Predictions (B3) and measurements of the deformation at midspan of the T-shaped beam pre-tensioned at 14 days and loaded at 50% at 56 days (constant aging coefficient equal to 0.8 and no correction for nonlinear creep).

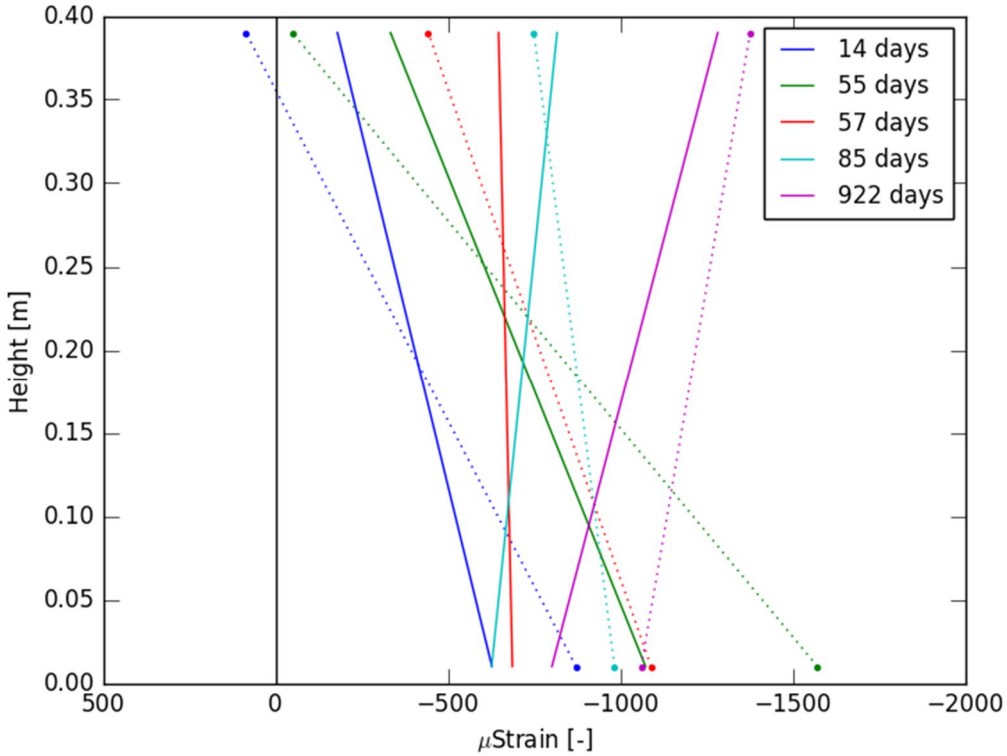

Figure I.4. Predictions (MC2010) and measurements of the deformation at midspan of the T-shaped beam pre-tensioned at 14 days and loaded at 100% at 56 days (constant aging coefficient equal to 0.8 and no correction for nonlinear creep).

References

ACI Committee 209. (1982). *Prediction of creep, shrinkage and temperature effects in concrete structures. Standard ACI 209-82*. Detroit: American Concrete Institute.

ACI Committee 209. (1992). *Prediction of Creep, Shrinkage, and Temperature Effects in Concrete Structures (ACI 209R-92)*. Farmington Hills: American Concrete Institute.

ACI Committee 209. (2008). *ACI Report 209.2R-08: Guide for Modeling and Calculating Shrinkage and Creep in Hardened Concrete*: American Concrete Institute.

Bažant, Z. P. (1972). Prediction of Concrete Creep Effects Using Age-Adjusted Effective Modulus Method. *Journal of the ACI, 69*, pp. 212-217.

Bažant, Z. P. (1982). Chapter 7: Mathematical Models for Creep and Shrinkage of Concrete. In Z. P. Bazant & F. H. Wittman (Eds.), *Creep and Shrinkage in Concrete Structure*: John Wiley & Sons.

Bažant, Z. P. (1988). Chapter 2: Material Models for Structural Creep Analysis. In Z. P. Bazant (Ed.), *Mathematical Modeling of Creep and Shrinkage of Concrete*: John Wiley & Sons Ltd

Bažant, Z. P., & Baweja, S. (1995). Creep and shrinkage prediction model for analysis and design of concrete structures— model B3. *Materials and Structures, 28*(6), 357-365. doi:10.1007/bf02473152

Bažant, Z. P., & Baweja, S. (2000). *Creep and Shrinkage Prediction Model for Analysis and Design of Concrete Structures: Model B3*. Paper presented at the Adam Neville Symposium: Creep and Shrinkage—Structural Design Effects, Michigan, USA.

Bažant, Z. P., Hauggaard, A. B., & Baweja, S. (1997). Microprestress-solidification theory for concrete creep. II: Algorithm and verification. *Journal of Engineering Mechanics, 123*(11), 1195-1201.

Bažant, Z. P., Hauggaard, A. B., Baweja, S., & Ulm, F.-J. (1997). Microprestress-solidification theory for concrete creep. I: Aging and drying effects. *Journal of Engineering Mechanics, 123*(11), 1188-1194.

Bažant, Z. P., Hubler, M. H., & Yu, Q. (2011). Pervasiveness of Excessive Segmental Bridge Deflections: Wake-Up Call for Creep. *ACI Structural Journal, 108*(6). doi:10.14359/51683375

Bažant, Z. P., & Li, G.-H. (2008a). Comprehensive database on concrete creep and shrinkage. *ACI materials Journal, 105*(6), 635-637.

Bažant, Z. P., & Li, G.-H. (2008b). Unbiased statistical comparison of creep and shrinkage prediction models. *ACI materials Journal, 105*(6), 610-621.

Bažant, Z. P., & Prasannan, S. (1989a). Solidification theory for concrete creep. I: Formulation. *Journal of Engineering Mechanics, 115*(8), 1691-1703.

Bažant, Z. P., & Prasannan, S. (1989b). Solidification theory for concrete creep. II: Verification and application. *Journal of Engineering Mechanics, 115*(8), 1704-1725.

BBR VT International Ltd. (2016). Other BBR PT systems.

Branson, D. E., & Christiason, M. L. (1971). Time Dependent Concrete Properties Related To Design-Strength and Elastic Properties, Creep, and Shrinkage. *Creep, Shrinkage and Temperature Effects, 27*. doi:10.14359/17187

Brown, N. H., & Hope, B. B. (1976). The creep of hydrated cement paste. *Cement and Concrete Research, 6*(4), 475-485. doi:http://dx.doi.org/10.1016/0008-8846(76)90076-4

CEB-FIP. (1993). *CEB-fip model code 1990 : design code*. London Thomas Telford.

CEB-FIP. (2013). *fib Model Code for Concrete Structures 2010*: John Wiley &Sons.

CEB. (1964). *CEB recommendations*: S.l. : s.n.

CEB. (1999). Structural Concrete - Textbook on Behaviout, Design and Performance. Updated Knowledge of the CEB/FIP Model Code 1990 *fib Bulletin 2*. Lausanne, Switzerland: Federation Internationale du Beton.

Coutinho, A. S. (1977). A contribution to the mechanism of concrete creep. *Matériaux et Construction, 10*(1), 3-16. doi:10.1007/bf02473583

Criel, P., Caspeele, R., Reybrouck, N., Matthys, S., & Taerwe, L. (2015). Stress Redistribution of Concrete Prisms Due to Creep and Shrinkage: Long-Term Observations and Analysis *CONCREEP 10* (pp. 138-146).

De Schutter, G. (2012). *Damage to concrete structures*: CRC Press ; Taylor & Francis Group 2012.

De Schutter, G., & Taerwe, L. (2000). Fictitious degree of hydration method for the basic creep of early age concrete. *Materials and Structures, 33*(6), 370-380. doi:10.1007/BF02479646

EN 1992-1-1. (2004). *Eurocode 2: Design of concrete structures. Part 1-1: General – common rules for buildings and civil engineering structures*. London: British Standards Institution.

Fanourakis, G. C. (2011). Validation of international concrete creep prediction models by application to South African concretes. *Journal of the South African Institution of Civil Engineering, 53*, 23-30.

Feldman, R. F., & Sereda, P. J. (1968). A model for hydrated Portland cement paste as deduced from sorption-length change and mechanical properties. *Materials and Structures, 1*(6), pp. 509-519.

Gardner, N. J. (2004). Comparison of prediction provisions for drying shrinkage and creep of normal-strength concretes. *Canadian Journal of Civil Engineering, 31*(5), pp. 767-775.

Gardner, N. J., & Lockman, M. J. (2001). Design Provisions for Drying Shrinkage and Creep of Normal-Strength Concrete. *Materials Journal, 98*(2). doi:10.14359/10199

Ghali, A., Favre, R., & Elbadry, M. (2002). *Concrete Structures: Stresses and Deformations*

Glucklich, J., & Ishai, O. (1962). Creep Mechanism in Cement Mortar. *ACI Journal Proceedings, 59*(7), 923-948. doi:10.14359/7946

Goel, R., Kumar, R., & Paul, D. K. (2007). Comparative Study of Various Creep and Shrinkage Prediction Models for Concrete. *Journal of Materials in Civil Engineering, 19*(3), 249-260. doi:doi:10.1061/(ASCE)0899-1561(2007)19:3(249)

Hellesland, J., Aas-Jakobsen, A., & Green, R. (1972). A stress and time dependent strength law for concrete. *Cement and Concrete Research, 2*(3), 261-275. doi:http://dx.doi.org/10.1016/0008-8846(72)90069-5

Holcim. (2010). Gids voor de vakman.

Jirásek, M., & Havlásek, P. (2014). Microprestress–solidification theory of concrete creep: Reformulation and improvement. *Cement and Concrete Research, 60*, 51-62. doi:http://dx.doi.org/10.1016/j.cemconres.2014.03.008

Keulen, H. (2011). Memento cement en beton.

Koenders, E. A. B. (1997). *Simulation of Volume Changes in Hardening Cement-Based Materials.* (PhD thesis), Technical University of Delft, the Netherlands.

L'Hermite, R. (1959). What do we know about plastic deformation and creep of concrete? *RILEM Bulletin, 1*, pp. 21-25.

Müller, H., & Hilsdorf, H. K. (1990). *Evaluation of the time dependent behavior of concrete: summary report on the work of General Task Group 9. Bulletin d'information No. 199.* Lausanne, Switzerland: Comité euro-international du béton (CEB).

NBN B15-220. (1970). *Proeven op beton; Drukproef: Invloed van de afmetingen en vormen van het proefstuk op de druksterkte van het beton*.

NBN EN 1992-1-1. (2005). Eurocode 2: Ontwerp en berekening van betonconstructies - Deel 1-1: Algemene regels en regels voor gebouwen. In B. v. Normalisatie (Ed.).

Neville, A. M., Dilger, W. H., & Brooks, J. J. (1983). *Creep of plain and structural concrete*. United States of America: Longman Inc.

Pham, S., & Prince, W. (2014). Effects of Carbonation on the Microstructure of Cement Materials: Influence of Measuring Methods and of Types of Cement. *International Journal of Concrete Structures and Materials, 8*(4), 327-333. doi:10.1007/s40069-014-0079-y

Reybrouck, N., Criel, P., Caspeele, R., & Taerwe, L. (2015). Modelling of Long-Term Loading Tests on Reinforced Concrete Beams *CONCREEP 10* (pp. 745-753).

Ritzen, J. (2006). Betonbouw. Berekenen-Dimensioneren–Constructie. Deel 3: Voorgespannen beton, Basisbegrippen, Theorie en praktijk. Gent: Uitgeverij Academia Press.

Rossi, P., & Acker, P. (1988). A new approach to the basic creep and relaxation of concrete. *Cement and Concrete Research, 18*(5), 799-803. doi:http://dx.doi.org/10.1016/0008-8846(88)90105-6

Rossi, P., Tailhan, J.-L., & Le Maou, F. (2013). Comparison of concrete creep in tension and in compression: Influence of concrete age at loading and drying conditions. *Cement and Concrete Research, 51*, 78-84. doi:http://dx.doi.org/10.1016/j.cemconres.2013.04.001

Rossi, P., Tailhan, J.-L., Le Maou, F., Gaillet, L., & Martin, E. (2012). Basic creep behavior of concretes investigation of the physical mechanisms by using acoustic emission. *Cement and Concrete Research, 42*(1), 61-73. doi:http://dx.doi.org/10.1016/j.cemconres.2011.07.011

Russel, H. G., & Larson, S. C. (1989). Thirteen Years of Deformations in Water Tower Place. *Structural Journal, 86*(2). doi:10.14359/2681

Taerwe, L. (1999). *Voorgespannen beton*: Universiteit Gent - Faculteit Ingenieurswetenschappen.

Taerwe, L. (2013). *Gewapend beton; Analyse, modllering en ontwerp; Deel 1: Lineaire elementen*: Universiteit Gent - Faculteit Ingenieurswetenschappen.

Taerwe, L. (2015). *Prestressed Concrete*: Universiteit Gent - Faculteit Ingenieurswetenschappen.

Taerwe, L., & De Schutter, G. (2006). *Betontechnologie*: Universiteit Gent - Faculteit Ingenieurswetenschappen.

Tazawa, E.-I. (1999). *Autogenous shrinkage of concrete.* Paper presented at the Proceedings of the International Workshop organized by JCI, Hirshima.

List of figures

List of tables

Happiness can be found, even in the darkest of
times, if one only remembers to turn on the light.

Dumbledore,
Harry Potter and the Prisoner of Azkaban
J.K. Rowling,